Department of Mechanical Engineering
University College London

Characterisation of Laser Induced Spark-Ignited Flame Kernels in Premixed Fuel/Air Mixtures

Emmanuel, Sunny Okara

A thesis submitted in partial fulfilment of the requirement for the Degree of Doctor of Philosophy (PhD) Award in Mechanical Engineering

16 September 2021

Declaration

I, EMMANUEL Sunny Okara confirm that the report presented here is based on a personal effort. Where information has been derived from other sources, I confirm that this has been indicated in the report.

Abstract

Gaseous alternative fuels are promising solution for today's increasing demand for clean and reliable power. The wide number of fuel types and sources implies that engine designers need to develop fuel flexible combustors. Also, to meet tightening emission laws, these combustors would be required to operate under ultra-lean, high pressure and high temperature environments. Such extreme conditions make ignition difficult to achieve especially with current spark plugs which has been the primary ignition source during the last one hundred years. Laser ignition has been proposed as an alternative ignition system capable of providing stable combustion under these conditions. The advantages provided by laser ignition over electric spark system include: the absence of flame quenching effects of electrodes which enhances the ignition of lean mixtures, less energy requirement for ignition at higher pressures, precise timing, and choice of suitable ignition location. To explore the benefits offered by the Laser ignition in practical combustors, there is a need to characterise the propagation behaviour of the laser flame kernel since successful ignition requires the transition from an ignited spark kernel to a self-sustained flame.

The present thesis contributes to existing knowledge on laser ignition through investigation of different development characteristics of the ignited flame kernel. The first investigation involves high-speed imaging of the flow field characteristics of the flame kernel based on combined 2D Laser tomography and PIV techniques. The ignition was achieved by focussing a laser beam of 1064 nm wavelength on an atmospheric co-axial straight tube burner through which stoichiometric CH_4/Air was flowed. The resulting flame kernel and its flow field were visualized through laser-sheet illumination and then captured using a high-speed camera. The observed flame kernel features from the tomographic images were consistent with previous research observation and provided insight to other phenomena such as induced vortex motion in the developing kernel. Additionally, the PIV data provided insight on how the local flow field velocities were changing during development of the flame kernel.

The second investigation involves direct imaging of the flame kernel chemiluminescence to understand both the fluid dynamics and chemical reactivity of the laser flame kernel. The atmospheric burner used in this setup is made of co-axial contracting nozzles in which flowing fuel/air mixtures were repeatedly ignited by a focused laser beam of 1064 nm wavelength and 2 Hz frequency. To characterise the resulting flame kernel, 2D projection images of the kernel OH* chemiluminescence was captured using intensified CCD camera. The observed geometric features of the kernel were similar to the earlier observation. Additional data on the OH* luminosity provided insight on the reactivity of the kernel at various transition points during its development and the reason for the variation in growth rate of the flame kernel at different stages. The investigation was extended to include the effects of varying physical parameters such as laser pulse energy and flow velocity. The observation showed that the effect of increasing the pulse energy within a certain threshold limit is an enhanced early kernel growth, but the ultimate effect was insignificant. Although, a higher flow velocity had no remarkable effect on the size of the kernel, it resulted in faster propagation of the flame front downstream due to the combined effect of convection and increased turbulence.

In the final study, the sensitivity of the kernel characteristics to changes in the fuel thermochemical properties was investigated based on direct imaging of the OH* chemiluminescence. The investigation comprises the effect of changing equivalence ratio, variation in fuels at constant Adiabatic Flame Temperature and variation in fuels at constant Laminar Flame Velocity. The results of the analysis showed linear dependence of most characteristics with equivalence in laminar flow regime but not in turbulent flows. For both constant temperature and constant laminar velocity mixtures, the results showed differences in the flame kernel characteristics depending on the fuel. This shows that no single thermochemical property is enough to uniquely define different fuel/air mixtures. Hence, further study on the inter-dependencies of the different thermochemical properties would be necessary for development of more robust model that would characterise flame kernel propagation in flexible combustion systems.

Thesis Impact

My PhD research has provided new set of data that could help explain how the choice of fuel and selection of appropriate ignition parameters can either improve or hinder stable combustion. These are important considerations that has direct impact on the emission of harmful substances from known combustion devices. The direct application of results from this work is in modelling premixed combustion process which is the combustion mode prevalent in most internal combustion engines as well as in accidental fire explosions.

As part of my PhD work, I developed two unique experiment measurement solutions which enabled me acquire data on the developing flame kernel geometry, the associated radical intensity level as well as the flow field velocity data. The first solution comprises a system of optical instruments combining Laser tomography and PIV techniques to enable simultaneous measurement of the laser-ignited flame kernel and its flow field in an atmospheric burner. The second solution involves a direct capture of the flame kernel using intensified CCD camera by filtering out radiations from the background. The selected techniques are well established and widely used in research.

Some results from this work have been presented locally in the annual UCL Mechanical Engineering PhD conference. My next plan of action is to present this work to wider audience by attending major international conferences and publishing papers. I am passionate about educating young students in primary and secondary schools about how they can impact their environment through knowledge of optics which is the science from which my research technique is based. While doing my PhD, I have been doing voluntary work with the STEM Ambassadors Network where I encourage students to take on STEM subjects. I have also been a member of The Combustion Institute UK and Institute of Physics (IOP) where I engage actively with fellow professionals in topics related to using science to solve emission problems.

Acknowledgement

I wish to thank my supervisors Prof. Alistair Greig and Prof. Rama Balachandran for their expertise guidance and direction through this research work. Prof. Greig, you supported me from onset when I brought my research idea, fine-tuned it to what it is today, and you did not give up on me even in the most difficult times. Prof. Balachandran, you inspired and directed my work, helping me with technical knowledge in the field and supported me with the platform to conduct my experiment.

Due thanks to Dr. M. Talibi, Dr. K. Ajabofu, Mr. Peter Kelly and all other departmental staff and colleagues who supported and assisted me in building the experimental setup used in this study. I will not forget to mention my closest colleagues within and outside the Thermo Lab: Amanda, Chris, Nonso, Ade, Ahmed, Tunde, and others who helped me with different aspects of my work.

I wish to also acknowledge PTDF (Petroleum Technology Development Fund) for funding my PhD which has resulted in this work.

I am forever indebted to my family whose love, prayers and encouragement has kept me going. My wife, Ify has been my greatest source of strength during this period. My kids, Salem and Eunice, who were born during this period made my daily life to be fun and without a dull moment. My elder sister, Mrs. Blessing Youdiowei, who looked after me while growing up and has always been there for me. My siblings, Evans, Iya, Kate, Priscillia and Happi, who always go the extra mile in their support for me through sacrificial giving and relentless prayers. I also cherish the continuous love received from nephews, cousins, aunties, and in-laws.

A special appreciation to all who inspired and supported me through the years. To Mr. and Mrs. Adewumi, who first inspired me to pursue a PhD and has been good role models to Ify and myself. To Dr. Jude Chukwuma, who inspired in me courage to deal with my fears. To Dr. Evans Shed-Okara, my elder brother, who has always been my inspiration to pursue excellence in my academic career. To Mr Alaba Obayori, who inspired my love for science through his mentorship in my secondary school years.

To my parents and role models, Mr. and Mrs. Emmanuel, who are now with the angels, I dedicate this work in your honour because you were the best dad and mum anyone could pray for. You will continue to live in my heart.

Table of Contents

List of Tables

List of Figures

Nomenclature

Symbols

α	Thermal diffusivity	m^2s^{-1}
c_p	specific heat of the mixture at constant pressure	$kJkg^{-1}K^{-1}$
D	mass diffusivity	m^2s^{-1}
δ_f	Flame thickness	m
ε	Dissipation rate of turbulent kinetic energy	m^2s^{-3}
E, E_p	Pulse energy	mJ
E_{min}	Minimum Ignition Energy	mJ
f	Pulse frequency	Hz
hv	photon energy	eV
I	Integral length scale	m
I	radiation intensity	AU
I_0	intensity threshold	AU
k	Thermal conductivity	$Wm^{-1}K^{-1}$
K	Stretch rate	1/s
L	characteristic length	m/s
ℓ	Markstein length	m
Le	Lewis Number	
λ	Laser wavelength	nm
N_e	electron density	m^{-3}
$N_{e,0}$	starting electron density	m^{-3}
η	Kolmogorov length scale	m
$\emptyset, \boldsymbol{\varphi}$	Mixture Equivalence ratio	
ρ	fluid density	kg/m^3
$\boldsymbol{\rho_u}$	Unburnt gas density	Kg/m^3

$\boldsymbol{\rho_b}$	Burnt gas density	Kg/m^3
Q	heat released per unit mass fraction of the deficient reactant	kJ/kg
Re	*Reynolds Number*	
S_{y+}	Flame front propagation rate along Y_+ $\left[\frac{\mathrm{dY_+}}{\mathrm{dt}}\right]$	m/s
S_{y-}	Flame front propagation rate along Y_- $\left[\frac{\mathrm{dY_-}}{\mathrm{dt}}\right]$	m/s
S_{x+}	Flame front propagation rate along X_+ $\left[\frac{\mathrm{dX_+}}{\mathrm{dt}}\right]$	m/s
S_{x-}	Flame front propagation rate along X_- $\left[\frac{\mathrm{dX_-}}{\mathrm{dt}}\right]$	m/s
S_L	Laminar flame propagation rate	m/s
S_f	Stretched flame speed	m/s
T_{ad}	Adiabatic flame temperature	K
T_u	unburned gas temperature	K
T_f	Flame temperature	K
T_g	Gas temperature	K
τ	Integral time scale	s
τ_e	time constant	s
U	mean velocity	m/s
u	instantaneous velocity	m/s
$\bar{u}$	mean velocity	m/s
u'	fluctuating velocity	m/s
$\boldsymbol{u_L}$	Unstretched laminar flame speed	m/s
U_0	Bulk flow velocity	m/s
μ	dynamic viscosity	m/s
v_d	diffusion rate of electrons	s^{-1}
X	Flame kernel width	mm
X_+	flame tip location away from Laser source	mm
X_-	flame tip location towards the Laser source	mm
x_a	mole fraction of the air	
x_f	mole fraction of the fuel	
Y	Flame kernel height	mm
$\mathrm{Y}_t, \mathrm{Y}_+$	Downstream flame tip location	mm

$\mathrm{Y}_b, \mathrm{Y}_-$	Upstream flame tip location	mm
Y_u	mass fraction of the deficient reactant	

Abbreviations

AFT	Adiabatic flame temperature
CH*	CH radical
CH_4	Methane
C_3H_8	Propane
C_2H_4	Ethylene
CCD	Charged Coupled Device
CNG	Compressed Natural Gas
FF	Flame front
FFT	Fast Fourier Transform
IE	Ionization Energy
LFL	Lean flammability limit
LFV	Laminar flame velocity
LPG	Liquified Petroleum Gas
LNG	Liquified Natural Gas
LI	Laser ignition
LISI	Laser induced spark ignition
MARPOL	Maritime Pollution
MIE	Minimum Ignition Energy
MPE	Minimum Pulse Energy
MW	Mega watts
NG	Natural Gas
OH*	Hydroxyl radical
PIV	Particle Image Velocimetry
PLIF	Planar Laser Induced Fluorescence
TL	Threshold Level
TTL	Transistor–transistor logic

UFL	Upper flammability limit
UV	Ultraviolet

Chapter 1 Introduction

1.1 Thesis Background

1.1.1 The Global emissions challenge.

The global community is threatened by the effects of rising emissions from the combustion of fossil fuels used in the transport and energy sector. A 2009 study by the International Maritime Organisation [1], showed a rising annual trend in shipping emission of CO_2 and other greenhouse gases (GHGs). As shown in Figure 1.1, projections reveal that future CO_2 emissions could rise between 50% and 250% from 2012 to 2050 depending on what the future economic and energy developments scenario will look like [2]. This increased concentration of CO_2 and other GHGs is the main cause of global warming, and the resulting effects includes loss of ice cover near the poles, global average rise in sea levels, etc. In addition to global warming effects, the burning of fossil fuels in most IC engines pose a threat to human health due to the release of poisonous gases like unburnt hydrocarbons (HCs), oxides of nitrogen (NO_x), oxides of sulphur (SO_x) and carbon monoxide (CO). Hydrocarbons are harmful to humans, affecting internal organs. Hydrocarbons together with oxides of nitrogen form ground level ozone, which is the primary component of smog [3]. Carbon monoxide is very dangerous, with human exposure to high levels being fatal.

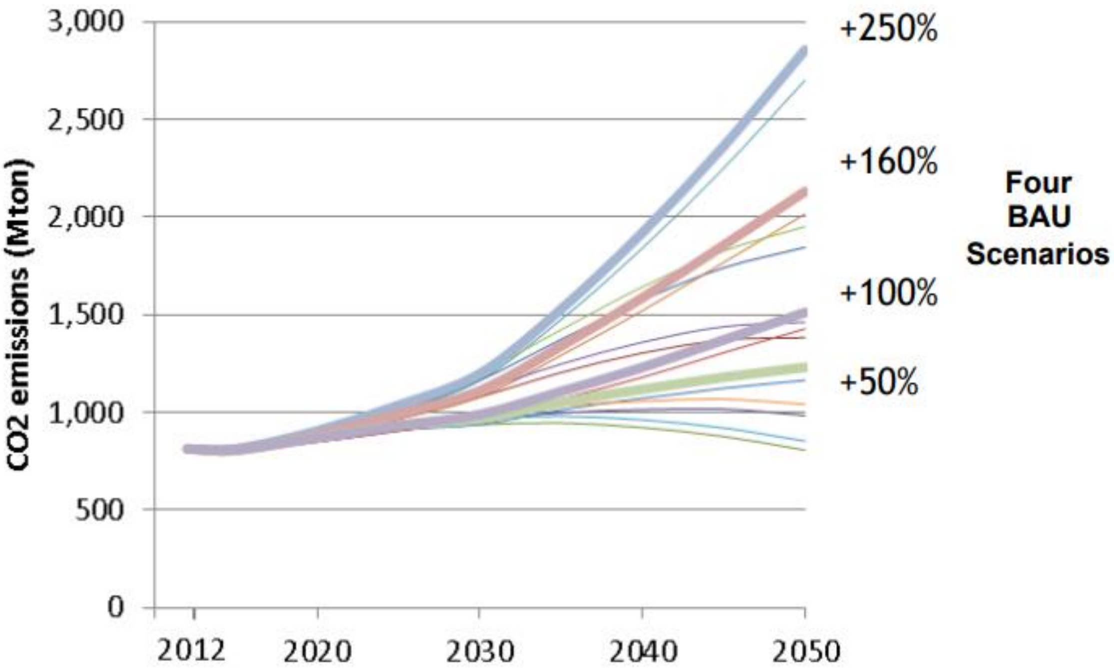

Figure 1.1: Projection of CO_2 emission under four Business-As-Usual (BAU) Scenarios [2]

As counter measures to these threats, stringent emission regulations have been imposed in different sectors. In the maritime industry, the MARPOL Annex VI set limits on NO_x and SO_x emissions from ship exhausts and prohibits deliberate emissions of ozone-depleting substances. Figure 1.2 shows the NO_x emission limits for different ship categories which depends on the vessel's construction date and engine rated speed. According to this regulation, ships constructed before 1 January 2000 installed with diesel engines above 5000kW are required to comply with Tier I standards while ships built after 2015 must comply with either Tier III or Tier II standards depending on the zone of operation. Another legislation aimed at combating pollutant emissions from SI engines is the European Passenger Car Emissions Legislation for Gasoline IC engines (Table 1.1)originally specified in Directive 70/220/EEC which was later replaced by Regulation 715/2007 (Euro 5/6). Both legislations trends show an increasing strictness on emissions due to growing environmental concerns, highlighting the need for alternative fuel sources and development of advanced ignition technologies for IC combustion engines.

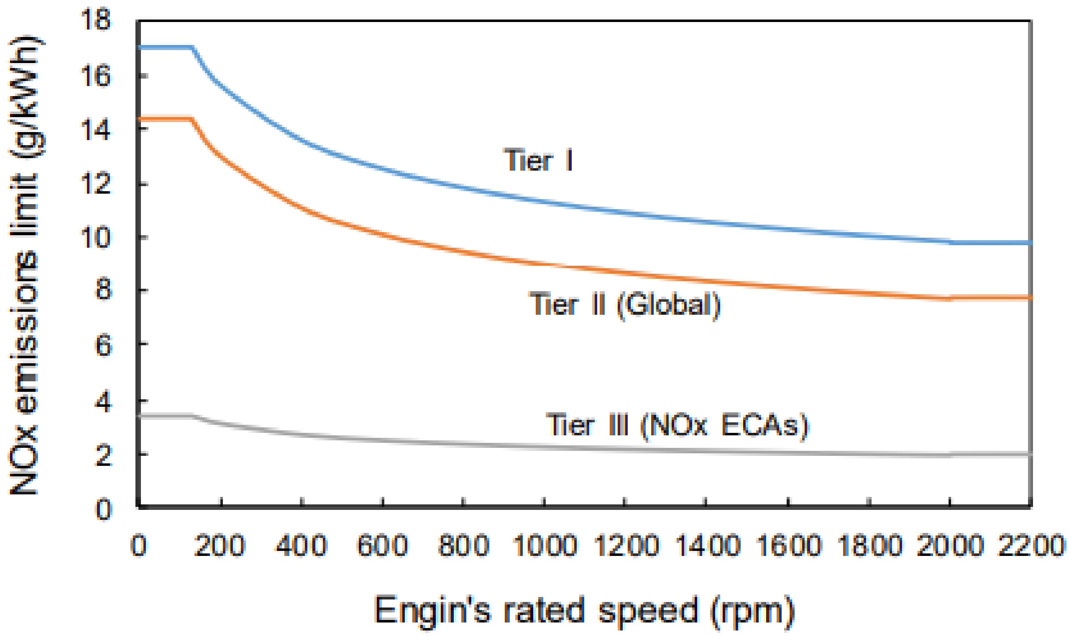

Figure 1.2: NOx emissions regulations in marine shipping based on rated engine speed [10]

Table 1.1: European Passenger Car Emissions Legislation for Gasoline IC engines [4]

	Year	CO	*HC*	NOx
			g/km	
Euro IV	2005	1.0	0.10	0.08
Euro V	2009	1.0	0.10	0.06
Euro VI	2014	1.0	0.10	0.06

1.1.2 Gaseous fuel solution and its challenges

One of the temporary measures being used to cope with the challenges of emissions and regulations is by shifting to gaseous fuels. Although these fuels have established usage in sectors like power generation and aviation, their popularity is beginning to gain ground in the automobile and marine sectors. The advantage of gas-phase fuel over liquid-phase fuel is that they have high combustion efficiency over wide firing ranges. This is due to their ability to form homogenous fuel-air mixtures in less time. They also form cleaner combustion products with hardly any solid pollutants (e.g., ash, particulates, or soot) compared to liquid-phase fuels.

Natural gas (NG) is one of the promising gaseous fuels with cleaner combustion products compared to other commercially available liquid fuels. The number of engines powered by NG has been growing rapidly in both automobile [5] and marine sectors [6]. Figure 1.3 is a recent DNV report which shows that are currently 247 confirmed LNG fuelled ships with additional 110 ready ships. Methane, which is the main component of NG (~ 90% CH_4) stands out as an ideal experimental fuel for demonstrating ignition performance of gaseous fuel sources because of its unique properties. For example, due to its large C-H bond energies, methane has a relatively high ignition temperature and low laminar flame speed. In addition, it has unity Lewis number which means its data can be easily applied to modelling validation by neglecting Lewis number effects.

Liquefied Petroleum Gas (LPG), a product of petroleum refining is a feasible alternative to petrol which could lower CO_2 and other pollutant emissions in SI engines. Propane which is one of the liquefied petroleum gases (LPG) is a readily available and adaptable engine fuel which can be liquefied and stored at low pressures; hence its transportation is more convenient than other gaseous fuels. Like other LPGs (e.g., butane), propane has relatively high calorific value and octane number. Its use as an alternative transport fuel is rising with about 17 million vehicles worldwide [7].

Ethylene which is a by-product of steam cracking of longer chain hydrocarbons (an energy intensive process that involved temperature of between 750-950 degrees Celsius) has thermo-physical properties comparable to gasoline which are strong indications that the gas can be easily combusted. For example, both the enthalpy of combustion (49.46 MJ/kg) and autoignition temperature (490^0C) indicates better combustibility of the gaseous fuel in conventional gasoline in SI engines[8]. It is commonly used in agriculture to enhance the ripening of fruits and to stimulate rubber tree to yield more latex. Also used in petrochemical industry for polythene production by polymerization. In 2005, the global production ethylene exceeded 75 million metric tonnes per year [8].

The present study includes an investigation of the combustion of three hydrocarbon fuels (methane, propane, and ethylene) with unique properties. One issue of concern with the wide number of fuel types and sources is the impact of fuel composition variation on flame stability of combustors. Combustion instability due to fuel variation is caused by differences in the laminar burning velocities (S_L) and adiabatic flame temperatures (T_{ad}) of the fuels. Therefore, the impact of fuel variability on combustion needs to be looked at to minimise the impact of engine pollutant emissions.

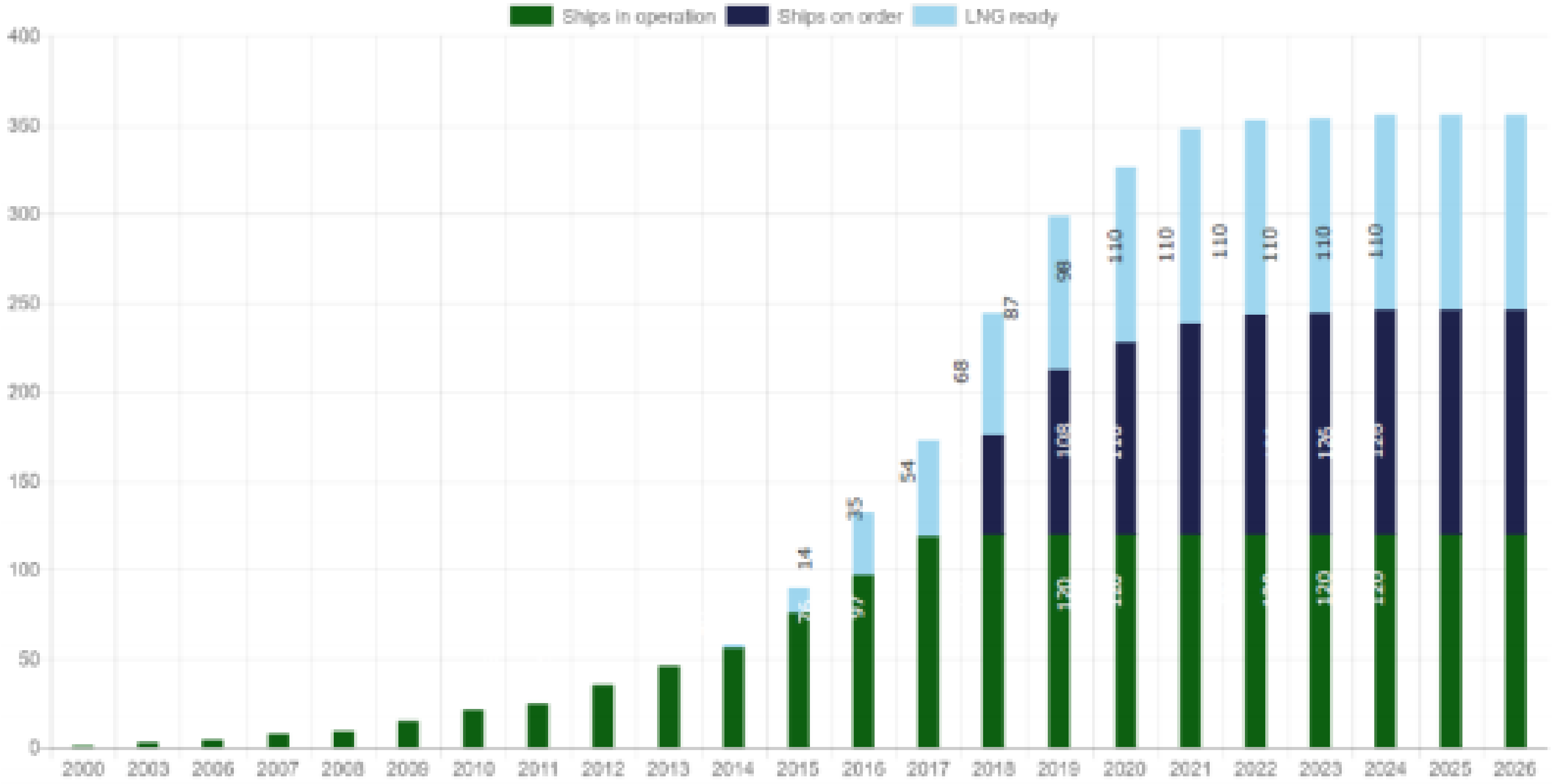

Figure 1.3: Existing and planned LNG Fleet [6]

1.1.3 Lean premixed operation and the challenges with spark plugs

Emissions from gas-fuelled engines are further improved by lean premixed operation [9], [10]. By igniting with leaner fuel–air mixtures, NO_x emissions are reduced due to the combustion temperatures being lowered, however this leads to considerable reduction in power density of the engine. To compensate for this, lean mixture combustion requires higher compression ratios (CR) as shown by Equation 1.2 [11].

$$\eta = 1 - \frac{1}{(CR)^{\gamma-1}} \tag{1.2}$$

$\gamma =$ the gas adiabatic coefficient$\left(\gamma = \frac{C_p}{C_v}\right)$ which is related to the leanness or richness of the fuel/air mixture.

The resulting higher efficiency however comes at a cost due to reduced lifespan of ignition spark plugs. Figure 1.4 shows the required voltage for ignition as a function of spark plug lifetime for brake mean effective pressures of 22 bar and 17 bar in a gas engine. As shown by the figure, a higher spark plug voltage would be required for ignition which significantly reduces the lifespan of spark plugs. This trend can be explained by Paschen's law [12] which states that the breakdown voltage (V) for a uniform electric field at constant temperature is a function of the product of the gas pressure and the spark gap [i.e. $V = f(p, d)$].

The above situation is compounded by the push for more stringent emissions regulation form the basis for research towards the development of alternative ignition sources to the spark plug system which has been the main ignition sources for combustion engines in the past one hundred years. To tackle this problem, a number of novel ignition concepts like high-energy spark plugs, plasma jet igniters, rail plug igniters, flame jet igniters, torch jet igniters, pulsed-jet combustion and laser ignition systems are currently under development [13], [14]. In the current thesis, the focus is on laser ignition which has been proposed as viable alternative to spark plug system capable of providing stable combustion under extreme environmental conditions.

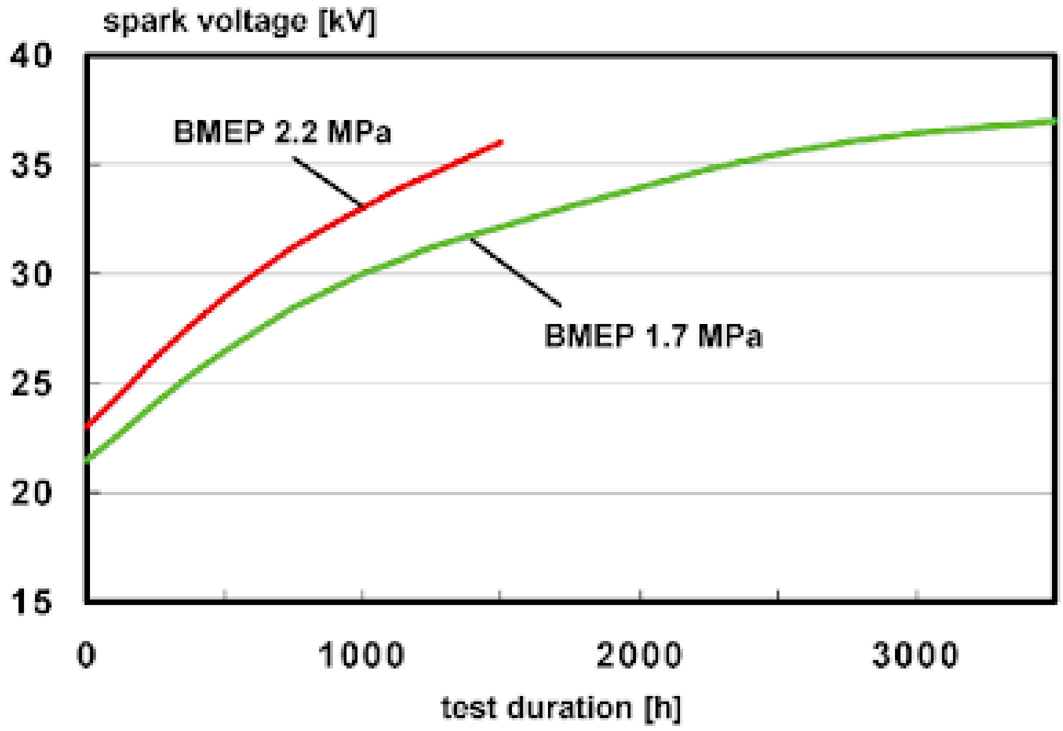

Figure 1.4: Breakdown Voltage of Gas engine Spark Plugs at two BMEP levels [15]

1.1.4 Laser ignition and its benefits

An alternative ignition source for gas-fuelled engines is the use of a laser beam for ignition. Laser ignition involves focusing a laser beam to a small volume of fuel-air mixture until the peak intensity of the focal volume exceeds a certain threshold (known as the breakdown intensity threshold). When this happens, a breakdown of the medium occurs leading to the formation of a spark plasma, whose size depends on the Numerical Aperture of the focused laser beam. If the energy content of the spark plasma is higher than a certain value (known as the Minimum Ignition Energy), the mixture ignites which can result in the propagation of a self-sustained flame. This process differs from spark ignition in many ways. For example, the ignition time scale is much shorter, and the breakdown process is photon driven unlike dielectric breakdown obtainable with spark electrodes.

Ronney [10] discussed four possible ways a laser can ignite a flammable mixture: thermal initiation, non-resonant breakdown, resonant breakdown and photochemical ignition. Thermal initiation (TI) involves using a laser source to heat up a flammable mixture beyond its threshold ignition temperature [16]. The method is most suitable for fuel/oxidizer mixtures with strong absorption at the laser wavelength, but it involves long ignition delay times [14]. Photochemical ignition (PCI) involves use of laser energy to dissociate target molecules within the mixture into highly reactive radical species, leading to ignition[14], [17]. The method requires less energy, and the mixtures can be ignited at lower pressures and closer to their flammability limits. However, it requires a close match between the laser excitation wavelength and the target molecules absorption wavelength; hence a tunable laser is required. Resonant breakdown ignition (RB) process involves, first, a non-resonant multiphoton dissociation of molecules resulting in free atoms, followed by a resonant photoionization of these atoms[18], [19]. This process generates sufficient electrons needed for gas breakdown. Theoretically, less input energy is required due to the resonant nature of this method. Of all the mechanisms, non-resonant breakdown ignition (NRB) is the most feasible in terms of practical implementation. It involves using a focused laser beam to create an electric field of sufficient intensity within a flammable mixture thereby leading to breakdown of the medium[10], [14]. Unlike PCI and RB, it does not require a close match between the laser wavelength and the absorption wavelength of target molecules, hence it can easily be implemented in practical combustion systems[14]. It is also the most similar to the electric spark ignition involving production of a spark plasma which emits light, heat and shockwave; hence, it is also called Laser Induced Spark Ignition (LISI).

There are several potential benefits which laser ignition systems provide over electric spark plugs due to differences in their physical configurations. For example, lasers are non-intrusive which eliminates problems associated with the presence of electrodes which act like heat sink and tend to quench the flame kernel especially in lean mixtures. Due to its flexible nature, laser ignition can be achieved with precise timing and choice of suitable ignition location. Additionally, the differences in plasma parameters (initial temperature, pressure, electron parameters, etc.) of both systems results in differences in their performance. For example, in contrast to electric sparks which is governed by Paschen's law, laser ignition requires lower energy at higher pressures. Previous studies also found that the laser ignited flame speed at early times, exceed the laminar flame speed, thereby providing a clear indication of plasma-assisted flame propagation[20].

Due to its benefits, the implementation of laser ignition is highly sought in a host of combustion applications including: stationary engines [21], [22], internal combustion engine [23], aircraft engines and rocket engines [24]. In stationary gas engines, high cyclic variation which results from slow burning of lean mixtures can be reduced via multipoint ignition or choosing an appropriate ignition location. It is also known that unlike the electric spark, the dependence of laser ignition energy on flow pressure is the opposite of Paschen's law, which means less energy is required for ignition. In spray-guided direct injection Otto-engine, where charge stratification is critical for achieving fuel economy at low loads, optimization of the ignition process is extremely difficult due to fixed spark plug location. Laser ignition makes this easy through flexible spark location. In addition, the formation of the spark plasma is adaptive with respect to the occurrence of fuel droplets near the focus because condensed matter reveals lower breakdown thresholds than gases ($\sim 10^9$ vs. 10^{11} W/cm^2, respectively) [25],[23]. In homogenous charge compression ignition engine, the self-starting reactions with a high temporal jitter is a common problem that severely affects the smooth running of the engine. Laser ignition allows triggering of the start of "self-ignition" by introducing nearly negligible energy into the cylinder with optimum timing. In this way it can help substantially to overcome such drawbacks [26], [27]. In aircraft gas turbine, high altitude flame extinction is a common problem which can be caused by transient disturbances of the air flow through the engine, or by severe ingestion of ice, water, and dust [28]. When the engine is extinguished, the temperature and pressure in the combustor are low, causing a significant decrease in vapour pressure of fuel and the decreased air flow rate may lead to poor atomization, both of which imply the need for large amount of spark energy to initiate a flame kernel. Therefore, there is rising interest in using laser plasmas for ignition of turbines used in aircraft engines primarily in order to achieve rapid relight [29], [30], to capitalize on the possibility of more optimal spark locations along the centreline of the combustor or in flow reversal zones near the fuel nozzle [31], and to avoid the reliability limitations of conventional igniters.

1.1.5 Practical implementation of laser ignition and associated difficulties

Despite the benefits offered by laser ignition, the concept is yet to be adopted in most practical combustion systems. One drawback towards the practical implementation of laser ignition is the huge cost and size of equipment needed to generate high power pulsed laser beams. From inception of laser ignition research, conventional flash-pumped solid-state lasers (e.g. neodymium-doped yttrium aluminium garnet or Nd:YAG lasers) have been used to generate fundamental lasing frequencies in the near infrared region. This fundamental frequency can be doubled to produce visible beam, and further doubling can produce ultraviolet beam. In recent decades, considerable progress has been made in laser technology to reduce the size and cost of potential lasers for ignition much of which stems from improvements to laser diodes and diode pumped solid state lasers. Research efforts has shown that it is now possible to create diode pumped solid state micro-lasers with an energy output of several millijoules; enough to cause laser-induced breakdown [32],[33]. Some researchers have suggested that the use of diode pumped laser sources has advantages over flashlamp pumped lasers, which usually result in variation in the output beam properties across the operating range, limitation of beam repetition frequencies and a shorter life cycle [34],[35].

The most common research technique employed in the initiation of laser ignition is open-path beam delivery which uses mirrors and lenses to create gas breakdown within the combustion location. Such configurations may work over short distances; however they are not practical for commercial implementation owing safety, maintenance, thermal and vibrational issues which can cause misalignment problems [14]. There are two promising concepts by which the commercial delivery of a laser beam into the combustion chamber can be realized, namely the laser mounted on the cylinder or located at a remote location [27]. Both concepts are possible through adoption of optical fibre delivery which could be used to transport either the ignition pulse or pump pulse. Yalin et al. [36], [37] was the first to demonstrate ignition in a natural gas engine using a hollow fibre optic cable (Figure 1.5a)coupled to a remote flash lamp pumped Nd:YAG laser source. The tests showed that the hollow fibre delivery system met the goal of providing a robust and successful means of engine ignition. Engine data showed that the fibre coupled system yielded 100% reliability in ignition and reduced combustion durations compared to conventionally ignited cylinders [38]. A potential advantage of the hollow fibre spark delivery approach is the ability to use a single laser source multiplexed via multiple fibres (Figure 1.5b) to a series of engine cylinders. Thus, the development of a flexible optical fibre system for practical implementation in internal combustion engines is highly desirable. However, it can be quite challenging to bring laser ignition into a realistic application due to the high peak power required to generate laser sparks, however, there are many research efforts which focussed on addressing this problem [39], [29] .

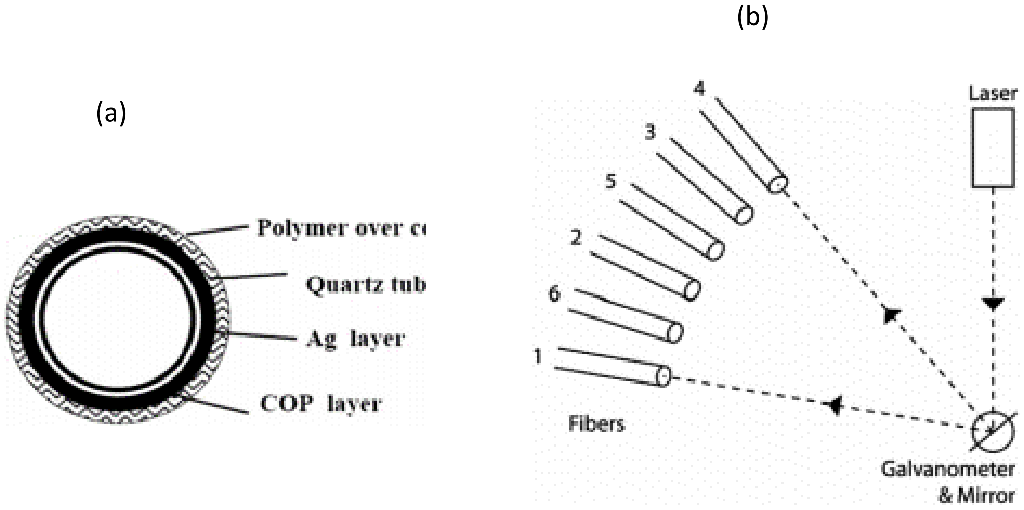

Figure 1.5: Fibre optic beam delivery: (a) cross-sectional view of hollow core coated fibre, (b) Step and hold multiplexing employing mirror attached to galvanometer [14].

1.1.6 Important Characteristics of the Flame Kernel

The processes involved in laser ignition are very complex, therefore optical diagnostics are usually employed by researchers to gain insight into the key events. The choice of a particular technique is based on what information is of interest to the researcher. For example, while some techniques (e.g., shadowgraph, schlieren) provide information related to the fluid dynamics of the flame kernel others (e.g., chemiluminescence, PLIF) provide additional details of the chemical kinetics. In this research, both the fluid dynamics and chemical kinetics data of interest so as to understand the coupling between the two.

In IC engines, geometric properties of the flame kernel such as the shape and size are often investigated. These are useful for predicting the pressure rise with time which maybe too small to be detected by existing pressure probes [40],[41]. They are also useful for estimating the *burning velocity* which is a fundamental parameter required for the development and validation of kinetic mechanisms for fuels. In the early stage of laser ignition, such measurements are particularly important because the relative expansion speed of the flame kernel is low compared with that of a fully developed flame. Also, the laser flame kernel is subjected to high stretch rates which makes extinction more likely. For gaseous fuels, the risk of quenching is high due to its lower energy density compared to liquid-based fuels, hence the need to understand the coupling between the kernel physical properties and ignition success. In addition, there is the widely held view that most practical ignition problems (e.g. quenching, slow burning, unstable combustion, emissions, etc.) originates at this stage [42],[14],[43].

Another important characteristic of the early flame kernel is the rate of radical generation at the kernel-fluid boundary which determines whether the kernel propagates further or extinguishes. Excited radicals are formed in the flame by thermal excitation and through chemical reactions, with concentrations much higher than their equilibrium values. The main chemiluminescence emitters in hydrocarbon flames are OH^*, CH^*, C_2^* and CO_2^* [44], [45]. Their formation reactions are detailed in Table 1.2, together with the band wavelengths. As shown in the table, these radicals are formed in reactions involving intermediate combustion species, whose concentration in the flame exceed their equilibrium values. Therefore, since de-excitation reactions are proportional to the concentration of the excited radicals and have very short time, chemiluminescence is mainly originated in thin reaction zones. This can be observed in Figure 1.6, representing the spatial distribution of local emission intensities in a laminar premixed flame. The reactions listed in the table strongly depend on temperature and involve stable and intermediate fuel and oxidizing species. All of them are important combustion parameters and, therefore, the resultant chemiluminescence emission might be expected to be closely related to the properties of the flame. In fact, spontaneous flame radiation has been extensively used as a flame diagnostic method.

In the current study, the chemiluminescence of OH* will be used as flame markers to detect flame position, shape, and structure, while its intensity is used to indicate the relative heat release rate. The use of OH* chemiluminescence as flame marker has been demonstrated in many past studies [46],[47],[48]. Also, there are many research evidence of the connection between the chemiluminescence intensity of OH* and equivalence ratio [49],[50],[51]. According to [52], the chemical reactions occurring during an ignition event involves three key steps (chain initiating, chain propagation, and chain termination). Initiation of the chemical reactions usually occurs in a few hundred microseconds after the breakdown. The next step which is the most important is the chain propagating step usually involves production of OH* [52]. Therefore, OH* being a key radical produced during the chain propagating step is an important ignition parameter and a reliable flame marker.

At present, direct measurement of HRR is not practical instead the production rate of certain radicals (e.g. OH* and CH*) are used to indicate HRR [53],[54],[55]. A few works have addressed specifically the existence of a relationship between chemiluminescence and heat release rate. One of the earliest studies is that of Price et al. [56], showing a linear relationship between mean C_2* emission and volume flow rate of combustible, not influenced by the conditions of turbulence. Lawn [57] evaluated the spatial cross-correlation of chemiluminescent emissions and concluded that it might serve as a good indicator of instantaneous heat release rate. Comparison of spatially resolved measurements of OH* and CH* chemiluminescence, flame surface density and heat release rate estimated as the product $[CH_2O]$x[OH] revealed similar patterns and behaviour and, therefore, that either OH* emission or flame surface density serve to estimate heat release rate [58], [59]. Measured trends of OH*, CH* and CO2* chemiluminescence intensity in [60], [61] for variations in equivalence ratio and strain rate suggest that these are good markers for heat release rate whereas C_2* is not a reliable indication. However, Nori and Seitzman [62], [63] noted that due to the influence of equivalence ratio and pressure on OH* and CH* emission, their associated signals may not be fully reliable as heat release markers. Numerical results of Najm et al. [64] suggest that chemiluminescence due to OH*, C_2* and CH* may fail as local markers of heat release in high curvature regions of flames; hence the need for additional work and experimental evidences in order to verify that conclusion. For the case of internal combustion engines, Kim et al. [65] found a good correlation between chemiluminescence in the range 350–390 nm and heat release rate in cool flames.

Table 1.2: Formation routes of excited radicals and characteristic wavelengths[66].

Radical	Reactions	Wavelength (nm)
OH*	R1: $CH + O_2 \rightarrow CO + OH^*$ R2: $H + O + M \rightarrow OH^* + M$ R3: $OH + OH + H \rightarrow OH^* + H_2O$	282.9, 308.9
CH*	R4: $C_2H + O_2 \rightarrow CO_2 + CH^*$ R5: $C_2H + O \rightarrow CO + CH^*$	387.1, 431.4
C_2*	R6: $CH_2 + C \rightarrow C_2^* + H_2$	513, 516.5
CO_2*	R7: $CO + O + M \rightarrow CO_2^* + M$	350–600 (Continuous spectrum)

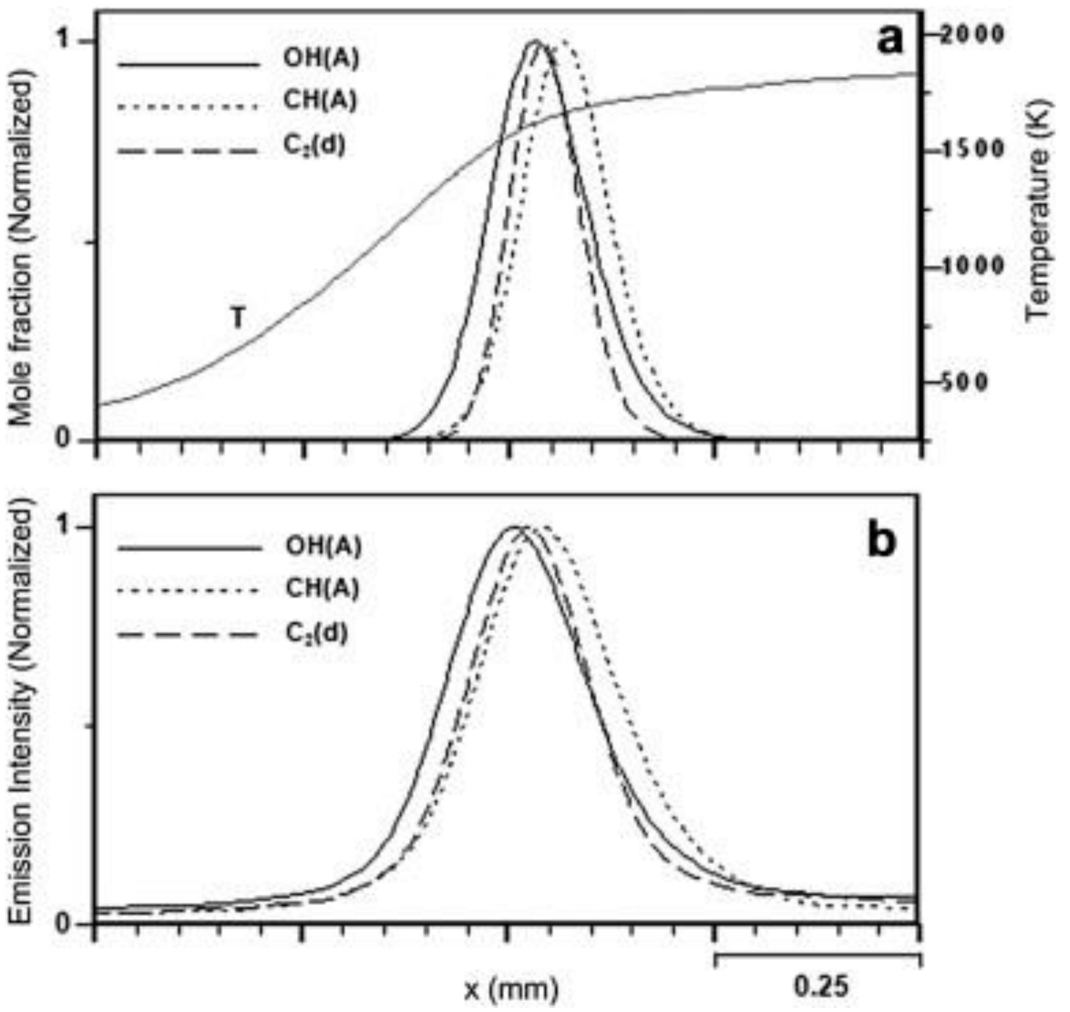

Figure 1.6: Intensity profiles of OH* (306 ± 7 nm), CH* (431.4 ± 0.75 nm) and C2* (516.5 ± 1 nm) chemiluminescence in a laminar methane-air premixed flame (ϕ = 1.1) along the flame normal direction. (a) Simulation (b) Experiment [66]

1.1.7 Survey of Relevant Literature.

The history of Laser Ignition research can be traced back to the time of first discovery of laser-induced optical breakdown by R.W. Terhune and co [67] where a beam of a pulsed Q-switched ruby laser of tens of MW peak power, was focused in air by a single lens to create a spark comparable to an electrical discharge between electrodes. This experimental set-up was dubbed 'the most expensive Spark Plug in automotive history' by Terhune which may have contributed to many researchers abandoning the research due to the belief that it would never be economically feasible. However, the last three decades has witnessed renewed interest in laser ignition research. This no doubt may have been driven by advances in laser technology as well as the current trends towards ultra-lean combustion [68].

Although not exhaustive, the following literature publications deals with laser ignition investigation which relevant to the present study. Early work by Bradley et al. [20] and Phuoc [69] provide extensive reviews on the breakdown and spark evolution process. Reviews by Tauer et al. [27] and Morsy [14] also provided further information on the application of laser-induced ignition and current state of art.

1.1.7.1 Laser induced breakdown and plasma studies.

A Laser Induced Spark Ignition (LISI) event usually involve three development phases (spark generation, development of ignited flame kernel and propagation of self-sustained flame), where failure of any one phase results in ignition failure. The first phase which is the spark generation phase involves focusing a laser beam onto a small volume of fuel/air mixture until the peak intensity of the focal volume exceeds the breakdown intensity threshold of the medium, thus leading to gas breakdown. Growth of the spark is accompanied with shock waves which leads to loss of spark energy.

Following the development of lasers in the early 1960s, initial research effort was focused on the parameters affecting this breakdown threshold. One of the earliest studies by Mitsuk et al. [70] was the effect of focal length and pressure on breakdown threshold of xenon and krypton at low pressures (0.06 - 0.75 atm). They found that the threshold field intensity strongly depends on the focal distance for low pressures where plasma diffusion losses are present.

A later study by Chan et al. [71] investigated the effects of focal length and pressure for an additional number of gases, showing a similar trend.

Of importance to combustion system applications is how the breakdown threshold varies in fuel/air mixtures of various compositions. Hickling and Smith [72] studied the breakdown energy of various combustible fuels (isooctane, cyclohexane, n-heptane, n-hexane, clear-indolene, and No. 1 diesel) in air mixtures.

They reported no significant differences between the breakdown energy of air and the energies of the fuels studied.

Morgan [16] presented a theoretical and experimental study of the processes involved during laser-induced breakdown in air. He identified the necessity of using high spatial and temporal resolution to capture the phenomena, in order to characterize the processes leading to the breakdown and presented a partially unified theory to explain the phenomena in air. The process is described as a competition between multi-photon absorption and inverse Bremsstrahlung with deionization by diffusion, recombination, and radiative energy losses.

YalKcin et al. [73]examined the influence of ambient conditions on the laser air spark and studied laser-induced breakdown under different conditions (humidity, laser energy, particulate level, etc.). They found that the laser spark characteristics were not very sensitive to the ambient conditions or the laser energy. This is encouraging for the quantitative use of laser-induced breakdown spectroscopy (LIBS) and is also of interest when applying laser-induced breakdown for ignition. They found a good correlation between the radiative expansion of the laser spark, using results obtained from a laser-supported radiation wave model. LIBS is an optical diagnostic technique widely used in quantifying the atomic and molecular species present in gases, liquids and solids details of which can be found in [74], [75].

Minowa et al. [76] investigated the earliest stages of laser-induced air optical breakdown using the Mie scattering theory and three different wavelengths: 1064, 532, and 355 nm. These results were in good agreement with the plasma that forms with highly ionized plasma balls.

Dors et al. [77] analysed the fluid dynamic effects following laser-induced optical breakdown. These authors identified the importance of the plasma shape on the shock wave formation. The shock wave formation process is of first-order importance to explain the toroidal shape observed after the plasma cooling phase.

Although this is outside the scope of the present study, understanding the laser plasma development dynamics will help explain some of the characteristic features of the flame kernel.

1.1.7.2 Ignition studies: Measurement of Minimum Ignition Energy (MIE).

Many experimental studies on laser ignition involved measurement of the Minimum Ignition Energy (MIE). Growth of the spark is always accompanied with shock waves which leads to loss of energy. A means to investigate ignition success during the plasma development stage is through measurement of the spark energy which must be higher than the MIE of the combustible mixture. In practical terms, a minimum pulse energy (MPE) greater than the MIE must be supplied by the laser source to achieve successful ignition.

One of the first measurements of minimum ignition energy (MIE) of laser ignited methane-air mixtures was by Weinberg & Wilson [78] using a ruby laser of pulse energies of 2 J and duration 20 ns full width at half maximum (FWHM). Here, the pulse energy was measured by focusing the laser beam through a small aperture into an absorbing spherical calorimeter. For the first time, it was shown that MIE and the plasma dimensions decreased with increasing pressure.

Kingdon & Weinberg [79] analysed the effect of pulse duration and plasma constitution on MIE where they found out that for short pulse duration, the MIE was independent of plasma constitution, while for longer duration pulses (1 ms) the presence of inhibitors in the plasma could lead to flame extinction.

Syage et al. [80] measured the ignition energy of Hydrogen/air mixtures of different equivalence ratios using output at 1064, 532, and 355 nm of a Nd-YAG laser operating either as a Q-switched nanosecond laser or a pulse-mode-locked picosecond laser. They reported minimum ignition energies that are higher than the electric-discharge ignition energies and that increase toward the fuel-lean and rich side of the stoichiometry. Also, MIE dependence on gas composition and equivalence ratio for different combustible gases have been measured by both Phuoc [81] and Beduneau et al. [81], [82]

Other published data on MIE by Huang et al. [83], Shy et al. [79] and Cardin et al. [85] reveal the occurrence of key ignition transition events (in terms of increasing MIE) for different experimental conditions.

There are many other experimental studies based on measurement of MIE or MPE which shows they are highly influenced by: the mixture ratios [81], flow velocity

[86],[87],[84],[85], focal volume [88],[89],[82] and pulse duration [79], however the present study does not involve measurement of MIE.

1.1.7.3 Ignition studies: Flame kernel investigations

The particular focus of this study is the flame kernel development which is the transition from an ignited spark kernel to a self-sustained flame. Understanding the characteristic behaviour of the flame kernel is of high importance because a successful ignition event relies on the survival of the flame kernel.

In one of the first laser ignited flame kernel propagation studies, Santavicca et al. [90], used pulsed laser shadowgraph to visualize the flame kernel development of methane-oxygen flows (at atmospheric pressure) at different equivalence ratios for laminar to turbulent flows. In this study, they measured the flame kernel radius as a function of time and equivalence ratio and compared laser ignition results with that obtained from a General Motors electric ignition system. From their results, they concluded that the laser ignition system performed better than the electric ignition system. In addition, they observed that the measured initial flame kernel Initial radius correlated well with the predicted Energy from Taylor’s spherical blast wave model [91]. Please refer to equation 2.15 -2.18 in section 2.2.3.2 for details of the spherical blast wave theory.

In Spiglanin et al. [92], OH PLIF was used to measure the flame kernel development in LIS ignited hydrogen-air mixtures as a function of gas compositions and time. In this study, a small Q-switched Nd:YAG laser was used to produce 8 ns pulses. They observed that early flame kernel growth is dominated by gas motion induced by the short duration spark. They concluded that the ultimate fate of an ignition event lies with the chemistry of the reactions which determines whether the gas undergoes a transition from hot plasma to propagating flame.

Phuoc and White [93] measure plasma dimensions as a function air-fuel ration in laser-ignited methane–air mixture at 1 atm. With a MIE of 3-4 mJ, they observed the spark length and radius were about 0.8 and 0.3 mm, respectively. Similar to other studies, the plasma elongated in the direction of laser beam. The shape of laser spark was oval and lean for rich methane–air mixture whereas it becomes cylindrical in shape for stoichiometric and near stoichiometric methane–air mixture.

Bindhu et al. [94] investigated the flame kernel development from a laser-induced spark in argon. They found out that at increasing gas pressures, the plasma can absorb the incident laser energy more effectively. This means that the transmitted energy through the focal volume is less, and the laser ignition and flame kernel propagation is more effective.

Lackner et al. [95] characterized flame kernel development in stoichiometric and lean CH_4/Air at 10 bar using Schlieren photography and OH PLIF. From the Schlieren results, a faster evolution was observed from the stoichiometric mixture while OH PLIF image showed the toroidal and front lobe shapes in the early flame kernels.

Beduneau and Ikeda [96] investigated the laser-induced spark kernel in a premixed laminar methane–air burner. They observed an asymmetric toroidal shape of the flame kernel, which is caused by the expansion mode of the shock wave. In their explanation, they attributed the asymmetric behaviour to be partly due to the plasma characteristics. In addition, they observed that flame kernel growth initial stages were strongly influenced by spark energy while at the later stages, kernel growth depended mainly on the relative air–fuel ratios. In a later study of basic firing and non-firing phenomena, Beduneau et al., 2009 [97] showed that the level of radical formed inside the flame kernel is a key factor for the sustainability of ignition.

Bradley et al. [20] studied ignition of gaseous propane-air pre-mixture in an explosion bomb using high-speed Schlieren photography. They observed that gas-dynamics of the shock waves and high energy plasma leads to an overdrive in the laminar flame speed to such an extent that it decays from elevated values contrary to normal flames. From this observation, they concluded that near the LFL, the gas-dynamic effects can stretch the flame to extinction and narrow the ignition limits.

Srivastava et al. [98] employed Shadowgraph technique to visualize the flame kernel shape and propagation of laser-ignited CNG–air mixture inside constant volume combustion chamber, with the aim of simulating end of Compression stroke conditions of a SI engine. They observed the flame kernel shape to be structurally identical for all air–fuel ratios measures. However, they observed a decrease in both flame velocity and peak pressures for lean mixtures and concluded that laser ignition system applied engines are unable to deal with CNG/air mixtures leaner than $\frac{1}{\varphi} = 1.6$.

In Dharamshi et al. [99], shadowgraph technique was used to visualize flame kernel evolution and the effect of changing air-fuel (H_2) ratio in a CVCC at initial pressure 10 bar and initial temperature 373 K. From the results, they observed that the flame speed decreased with increasing air-fuel ratio in all directions. Also, they observed multiple wave fronts on the toroidal surface for richer mixtures than leaner mixtures. This explains the comparative difference in intensity of explosion in both rich and lean mixtures. In addition, they observed increase in the required MPE for leaner hydrogen-air mixtures and that by increasing the laser pulse energy, time taken to attain peak cylinder pressure reduced slightly, indicating faster flame speeds, however the peak cylinder pressure remained almost constant. Their conclusion was that laser ignition is a potential enabling technology in realizing the dream of a practical hydrogen fuelled engine.

Mulla et al. [100] of University College London, showed how the influence of mixture composition, flow velocity and equivalence ratio on the flame-kernel perimeter growth of CH_4/air using OH-PLIF technique. From this investigation, they observed a distinct shift in the trends of evolution of kernel perimeter near the lean flammability limit in CH4/air and H2/air mixtures. Also, they observed that the flow velocity (in both laminar and turbulent flow regimes) did not have a significant influence until a certain time was reached. This they attributed to competing effects, between the strain rate and turbulence.

In Yu et al. [101] the effect of increasing laser repetition rate (i.e., 1 Hz, 100 Hz and 250 Hz) on the stabilization of premixed methane-air flame kernel were investigated using CH* chemiluminescence. This study is typical example of plasma assisted combustion where high frequency laser pulse can be used to achieve flame stabilization. Initially, they observed the plasma energy coupling under these conditions and discovered it was not affected by the air flow. From measurements of catch-up distance and time of merging of consecutive flame kernels, they observed continuous combustion flame stabilization for repetition rates of 100 Hz and 250 Hz. In addition, they observed that the flame kernel formed by the last LIP does not affect the evolution of the newly formed flame kernel by the next LIP. Their conclusion was that a higher laser repetition rate will lead to a shorter catch-up distance which is beneficial for flame stabilization.

In another example of plasma assisted combustion, Dumitrache et al. [48] studied the impact of using a dual frequency pulse on the flame kernel growth of laser ignited lean propane-air mixture. By using OH* chemiluminescence, they compared the flame kernel evolution of a dual-pulse LISI (λ = 266 nm and λ = 1064 nm) with that of a single-pulse LISI (λ = 1064 nm). For single-pulse laser-ignited lean mixture, they observed detachment of the third lobe flame kernel due to high strain rates that which may extinguish the flame. For double-pulse case, no detachment was observed due to the existence of a beam waist offset whereby the resulting vorticity suppresses formation of the third lobe, consequently reducing flame stretch. Their conclusion was that the dual-pulse method enables reduced flame speeds (at early times), an extended lean limit, increased combustion efficiency, and decreased laser energy requirements.

1.1.7.4 Research gaps and challenges

The essence of most experimental studies on ignition is to provide validation data for the development of mathematical ignition models which can be extended to simulate real combustion situations. To have accurate models of laser ignition, data on the physical characteristics of the flame kernel must be available for different fuel/air mixtures as well as their parametric dependencies. However, following the extensive literature survey, a number of research gaps and challenges still persist. Below are some of the challenges and gaps identified which this study hopes to address.

- Most laser ignition measurements observed in the surveyed literatures were conducted in either open atmospheric burners [96], [92], [85] or closed combustion vessels [93], [20], [98]. The advantage of combustion vessels is that a quiescent mixture can easily be obtained, however their designs are more complex and providing optical access require very expensive materials. Such complexities are eliminated with the use of atmospheric burners which justifies why it is chosen in the present work.

- A significant number of the reviewed literatures were focussed on performance of the combustion systems whereas knowledge of the flame kernel structure is still limited. This raises the question of what the key features of a developing flame kernel are and how useful are they in predicting ignition success or failure. Although the features of the flame kernel were observed by past researchers [92], [20] through photographic imaging, there is no consensus as to the origin of these features and their link to ignition success or failure which necessitates further investigation of these salient features using robust optical techniques.
- While photographic images may provide proof of an on-going reaction, the observed features may not be enough evidence of a successful ignition since the early kernel growth is mainly influenced by the gas dynamics of the shock wave and the high energy plasma. A necessary feature of an igniting kernel is the production of sufficient quantity of radicals during initiation of chemical reaction. Due to the optical technique employed in most laser ignition studies, only information relating to the fluid dynamics of the flame kernel were provided. To understand the complex processes involved in laser ignition, both the fluid dynamics and chemical kinetics data are required. Therefore, another question which is yet to be answered is what is the coupling between the fluid dynamics of the flame kernel and the chemical reactions occurring?
- Another limitation resulting from optical the optical techniques commonly employed is that most techniques only provide information about the physical characteristics of the kernel with no evidence of how the flame is interacting with the flow-field. Such information will be useful for optimising combustion based on ignition location.
- Any investigation of the flame kernel characteristics that excludes the effects of operational parameters like pulse energy and flow velocity would be incomplete. The laser pulse energy is a key parameter that could affect the

efficiency of the flame kernel formation and its subsequent propagation to a stabilized flame. Although the effects of laser energy on flame velocity has been studied previously [102],[99], its effect on the early flame kernel development has not been properly addressed. In most combustor designs, variability of the combustion process is a continuing problem which arises from high turbulence and high turbulence is associated with high flow velocity. Hence, the need to address the question of the extent of flow velocity influence on the development and propagation of the flame kernel.

- In terms of the fuels investigated till date, there has been more focus on methane [88], [103],[104],[105] which provides a good baseline for gaseous fuels due to its unique properties. There has been some investigations of other fuels like hydrogen [99], propane [20], etc, however this is only a small number considering the large number of available gaseous fuels. Since each fuel differs from the rest in their thermochemical properties, there is also the need to study what impact the fuel properties have on the development characteristics of the laser flame kernel.

1.1.8 Thesis Objectives and Contributions

The current PhD work involves detailed investigation of the development characteristics of a LISI flame kernel in flowing premixed fuel/air mixtures. The goal is to show the possible link between these characteristics and ignition success as well as possible use of these data for development and validation of laser ignition models. The investigation would be explored under three specific objectives, each with the aim of addressing specific questions raised from gaps identified in literature.

- The first objective is to investigate the flow field characteristics of a developing LISI flame kernel in both laminar and turbulent flow regimes. To accomplish this objective methane mixed with Mie-scattered air forming a stoichiometric aerosol mixture is flowed through a co-axial straight tube burner and then ignited by a single pulse laser beam of 1064 nm wavelength and 7 ns pulse width. To enable visualization of the reacting flow field, a combination of Laser sheet tomography and High-Speed Particle Image Velocimetry (HSPIV) techniques was employed. This allowed simultaneous measurement of the flame kernel geometry and the flow velocity with the hope that this would address the problem of shortage of data on how the flow-field is interacting with the developing flame kernel. By observing the flow field features before and during the ignition event, combustion can be optimized based on ignition location which is one of the advantages of laser ignition over the spark plug [69].

- The second objective is to investigate the characteristics of the LISI flame kernel based on the mean OH* chemiluminescence. To accomplish this objective stoichiometric mixture of CH_4/Air flowing through a burner with co-axial contracting nozzles were repeatedly ignited by focused laser beam (1064 nm wavelength and 2 Hz frequency). Through direct capture of the kernel OH* chemiluminescence with CCD camera at different time delays (0.05 – 10 ms), the geometric data which is linked to the fluid dynamics of kernel would be extracted. In addition, the luminosity of the OH* which is linked to the chemical kinetics would be obtained. Both data could be used to address the problem of shortage of data on the coupling between the fluid dynamics and chemical kinetics of the laser flame kernel. The study scope will also include the effect of changing pulse energy and flow velocity with the aim of addressing what influence these operational parameters have on the flame kernel development.

- The third and final objective is to investigate the effect of changing fuel properties on the development characteristics of the flame kernel. The study is divided in three sub-sections. First, the study will characterise the flame kernel based on differences in the equivalence ratios of the fuel which by implication means differences in both the adiabatic flame temperature and laminar flame velocity of the fuel. Next, the sensitivity of the flame kernel characteristics to the fuel composition is investigated for three different fuels (i.e., methane, propane, ethylene) at constant adiabatic flame temperature. Lastly, the sensitivity of the flame kernel characteristics to the fuel composition is investigated for the three fuels at constant laminar flame velocity. The experimental setup and diagnostic technique employed will be the same as that used in achieving the second objective.

1.1.9 Thesis Outline

The entire thesis consists of eight chapters beginning with the current introductory chapter.

- Chapter 2 presents a review of the background theories which form the basis for understanding Laser ignition and its propagation in gaseous fuel/air mixtures. Most of the important flow properties as well as the processes involved in laser induced spark ignition are covered.
- Chapter 3 presents details of the experimental setups and the diagnostic techniques employed in this work. First, a description of the burners and flow system configurations used for the laser ignition study were given. In addition, a description of the optical systems and processing steps used for implementing Laser tomography, PIV and chemiluminescence techniques were also provided.
- 3.6presents a study of the characteristics of the flame kernel development within its flow field. Results of the kernel geometry and its flow field features obtained by 2D Laser tomography are presented. In addition, the flow field structures obtained using PIV are also reported.
- Chapter 5 presents a study of the flame kernel characteristics based on the OH* chemiluminescence. The results include the visual images of the flame kernel as well as quantitative analysis of the flame front propagation and OH* luminosity. This investigation was extended to include effects of laser energy and flow velocity as described in the objectives.
- In Chapter 6 the investigation was extended to include the effects of varying mixtures ratios and fuel types on the chemiluminescence characteristics of the flame kernel.

- Chapter 7 presents a discussion of all the results from the investigation in a coherent and insightful manner.
- Chapter 8 presents the conclusion of the findings from the investigations. A recommendation of possible future requirements to better understand the research is also given.
- The report also includes References and four Appendices. Appendix A: Experimental Procedures provides further information on the experimental procedures adopted while conducting the experiments. Appendix B: Risk Assessment is the risk assessment document developed for the experimental campaign. Appendix C: MATLAB Codes Used to Analyse Laser Tomography Images and PIV Data contains the code developed for analysis of the tomographic and PIV data. Appendix D: MATLAB Code Used to Analyse Chemiluminescence Data contains the code developed for analysis of the chemiluminescence data. Further sensitivity analysis of the kernel characteristic parameters to different test conditions are provided in Appendix E: Sensitivity Analysis.

Chapter 2 **Flow and Laser Ignition Fundamentals**

This chapter provides the theoretical basis for understanding Laser ignition and its propagation in gaseous premixed fuel-air mixtures. It begins with a discussion of the important properties of the flow in both reacting and non-reacting state. Then the fundamental theories of laser ignition and flame propagation are presented.

2.1 Fundamental Properties of Non-reacting and Reacting Gas Flows

Characterization of the flow turbulence structures is very important since they influence both the development and continued burning of the flame. Before any attempt is made to investigate the influence of the gas flow mixture on the propagation of the flame kernel, it is important to understand the fundamental properties of the flow mixture in both reacting and non-reacting state.

2.1.1 Non-reacting Flow properties

Generally non-reacting gas flows are classified into *laminar* and *turbulent* flows. Laminar flow is an ordered motion of the fluid particles along a streamline (or approximately parallel flow contour lines) which occurs when the velocity of flow is sufficiently reduced for a fixed diameter nozzle. In contrast turbulent flow which is the more practical case is characterized by random or irregular motion of fluid particles due to high velocity. In such a flow, the rates of fluid transfer and mixing are several times greater than the rates of molecular diffusion. To distinguish between the two flow types, *Reynolds Number (Re)* is used. The Reynolds Number is defined as the ratio of the inertia force to the viscous force acting on an element of fluid [106]. It relates to the characteristic length (L), mean velocity (U), fluid density (ρ) and dynamic viscosity (μ) in a dimensionless form given by equation 2.1. It is widely accepted that the flow is laminar if $Re<2000$ and turbulent if $Re>4000$.

$$Re = \frac{\rho U L}{\mu} \qquad 2.1$$

In characterizing turbulence flows, statistical properties are used because the flow is usually viewed as random local fluctuating motions superimposed on a uniform or mean motion of the fluid. The main properties of fluid motion are *instantaneous and mean velocity, fluctuating velocity or turbulent intensity, turbulent length scales* and *turbulent time scales*.

Instantaneous velocity: In a steady turbulent flow situation, the instantaneous local fluid velocity, u (in a specific direction) is given as the sum of the mean velocity component, $\bar{u}$ and the fluctuating velocity component, u' (also known as turbulent intensity).

$$u = \bar{u} + u' \qquad 2.2$$

Mean velocity: this is the time average value of the instantaneous velocities obtained in a steady flow situation. In quasi-periodic flows such as obtainable in engine cylinders, the mean flow varies from cycle-to-cycle, hence measurements made over many cycles are *phase-averaged* to obtain the ensemble-averaged velocity [41].

$$\bar{u} = \frac{1}{\tau}\sum_{t_0}^{t_0+\tau} u(t) \qquad 2.3$$

Turbulence intensity: this provides a measure of the turbulence level present in a flow field. It is the root-mean-square, RMS value of the velocity fluctuations, u' divided by the mean velocity of the fluid motion, $\bar{u}$ [41].

$$u' = \sqrt{\sum(u - \bar{u})^2} \qquad 2.4$$

Turbulence length scales: this provides a measure of the size of turbulent eddy structures present in the flow field. The length scales of turbulence include Integral length scale (i.e., largest size eddies), Taylor micro-scale (i.e., medium size eddies) and Kolmogorov length scale (i.e., smallest size eddies). The Integral length scale (I) and Kolmogorov length scale (η) can be approximated as below [107].

$$I = \frac{u'^3}{\varepsilon} \qquad 2.5$$

$$\eta = \left(\frac{v^3}{\varepsilon}\right)^{\frac{1}{4}} \qquad 2.6$$

Turbulence time scales: this provides a measure of the time over which the turbulent structures occur. An example is the Integral time scale (τ) given by [107]:

$$\tau == \frac{integral\ scale\ (I)}{turbulence\ intensity\ (u')} = \frac{u'^2}{\varepsilon} \qquad 2.7$$

2.1.2 Reacting Flow properties

Gas mixtures consisting of fuel and oxidant undergo unsteady reactions when ignited. Ignition is defined as a time-dependent process in which a starting reaction of fuel-oxidant mixture evolves until a steadily burning flame is reached or the mixture has completely reacted [27]. In internal combustion engines, this process can occur in either of two ways: autoignition or spark-induced ignition. In autoignition the mixture is compressed so that its temperature rises above the autoignition temperature where decomposition and radical formation occurs to such an extent that chain branching can start and proceed at a significant rate[27]. In contrast, spark induced ignition involves the generation of a plasma within a small fractional volume of the mixture that yields the initial radicals via ionic processes. At this early ignition stage, the shape of the flame front is called the flame kernel, and it can be described as the transition stage from the plasma to a self-sustaining flame[27].

Depending on the state of the mixture prior to ignition, two distinct forms of ignition reaction occur. The first is premixed charge ignition which occurs when the fuel and oxidant are completely mixed before ignition occurs. The second case in which there is no prior mixing of fuel and oxidant is known as non-premixed charge ignition. This is the ignition type which this work will be focussed on. Below are some of the fundamental properties of a premixed flow mixture which affects its propagation:

Equivalence ratio ($\boldsymbol{\varphi}$): is a fundamental property of the flow mixture that characterizes the composition of fuel and air. It is defined as the given fuel/air mixture ratio divided by the corresponding fuel/air mixture ratio at stoichiometric composition [27].

$$\boldsymbol{\varphi} = \frac{x_f/x_a}{(x_f/x_a)_{stoic}} \qquad 2.8$$

where: x_f is the mole fraction of the fuel, x_a is the mole fraction of the air. Lean mixture has values of φ less than one while rich mixtures have values of φ greater than one. A mixture of stoichiometric composition is defined by a value of φ equal to one.

Flammability limits: define the range of equivalence ratio of fuel/air mixture at specified temperature and pressure within which an ignited flame kernel will continue to propagate even after the ignition source has been extinguished. The maximum value in the rich mixture range is known as the upper flammability limit (UFL) while the minimum value in the lean mixture range is known as the lower flammability limit (LFL). The flammability maps of fuels are usually determined experimentally, and they depend on both temperature and pressure. Table 2.1 shows the results of flammability limits of the investigated fuels, measured in an explosive vessel with temperature and pressure conditions maintained at 35^0C and 5 psi, respectively. A typical fuel flammability map and its dependence on temperature is shown in Figure 2.1. According to the figure, the flammability range for a mixture increases with temperature and finally reaches a temperature beyond which autoignition will occur. At higher pressures, the flammability window will usually exceed the limits shown [27]. These limits are also affected by the nature of the fuel, direction of flame propagation, size and shape of combustion chamber, temperature and pressure [108].

Adiabatic flame temperature ($\boldsymbol{T_{ad}}$): this is the temperature achieved when a combustible mixture of fuel and air burns to completion under isobaric and adiabatic condition. In other words, it is the maximum temperature of the flame in the absence of non-unity Lewis number, differential diffusion and strain effects[109]. According to [109], the adiabatic flame temperature through the Arrhenius kinetics exerts a dominant influence on flame speed. Theoretically, $\boldsymbol{T_{ad}}$ is obtained from the overall energy balance based on the one-step Arrhenius kinetics:

$$T_{ad} = T_u + \frac{QY_u}{c_p} \tag{2.9}$$

where: $\boldsymbol{T_u}$ is the unburned gas temperature, $\boldsymbol{Y_u}$ is the mass fraction of the deficient reactant, $\boldsymbol{Q}$ is the heat released per unit mass fraction of the deficient reactant, $\boldsymbol{c_p}$ is the specific heat of the mixture at constant pressure.

Figure 2.1 shows a comparative $\boldsymbol{T_{ad}}$ versus φ values obtained using GASEQ chemical equilibrium software [110] for the different fuel gases studied in the present work. As shown in the figure, $\boldsymbol{T_{ad}}$ peaks at slightly above $\varphi = 1$ for all the fuels. Of the three fuels, ethylene has the highest flame temperature for a given φ value while methane has the lowest. The difference in values is due to the different enthalpy of reaction required to dissociate the bonds. For example, the respective bond strength of methane and ethylene molecules are 436 and 699 kJ/mol.

Laminar burning velocity ($\boldsymbol{S_L}$): this is the speed at which a planar flame travels into the mixture in the absence of heat losses. It is also defined as the velocity of the combustion wave normal to itself and relative to the unburnt gas [52]. It is a fundamental parameter because it is the only flame speed unique for a gas of a fixed composition, initial temperature and pressure, without further specification of hydrodynamic conditions such as stretch rate, Reynolds number, etc [111]. Hence, accurate determination of $\boldsymbol{S_L}$ is of fundamental importance since it is required for the development and validation of kinetic mechanisms for fuels. Experimental measurement of $\boldsymbol{S_L}$ is based on four main techniques that have proven to be quite versatile and accurate. These includes Bunsen flame approach, Flat flame approach, spherically expanding flame method and Stagnation flame method. Figure 2.2 compares $\boldsymbol{S_L}$ versus φ measurements obtained for the three fuels by using the Stagnation flame method [112]. In addition, $\boldsymbol{S_L}$ can be derived theoretically using the chemical structure of the flame.

Table 2.1: Flammability limits observed from experiment [113]**.**

Property	Methane	Propane	Ethylene
LFL - UFL (%vol)	4.9 - 15.8	2.03 -10.0	2.74 - 31.5
LFL - UFL (φ)	0.50 – 2.00	0.50 – 2.64	0.40 – 6.57

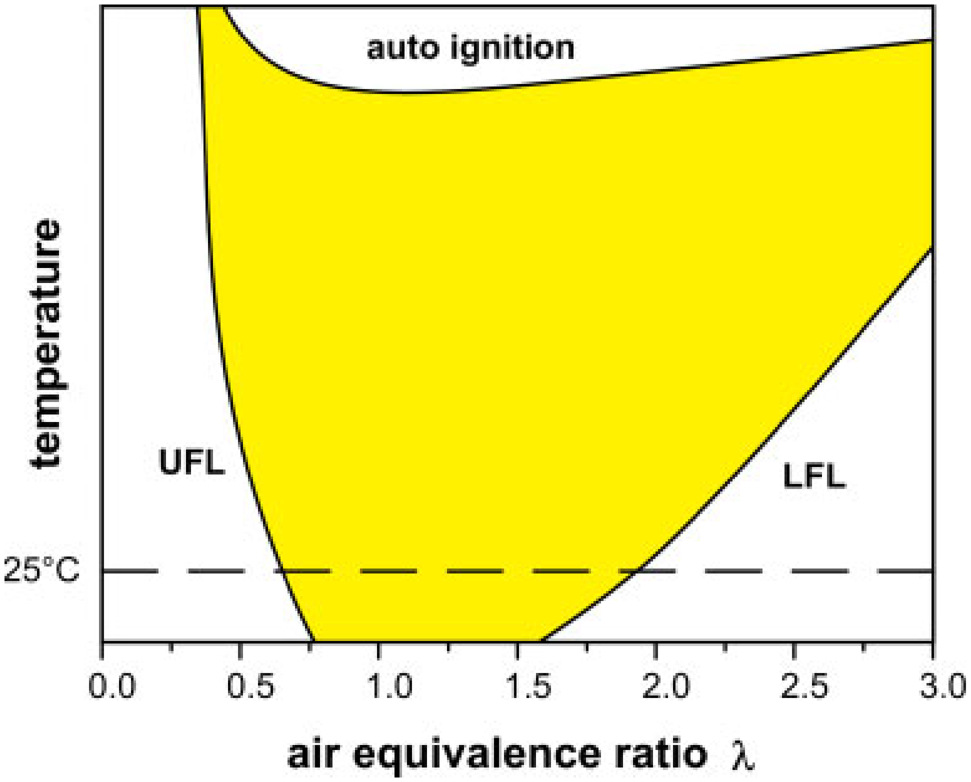

Figure 2.1: Typical flammability map showing its dependence on temperature and the autoignition limits[27]**.**

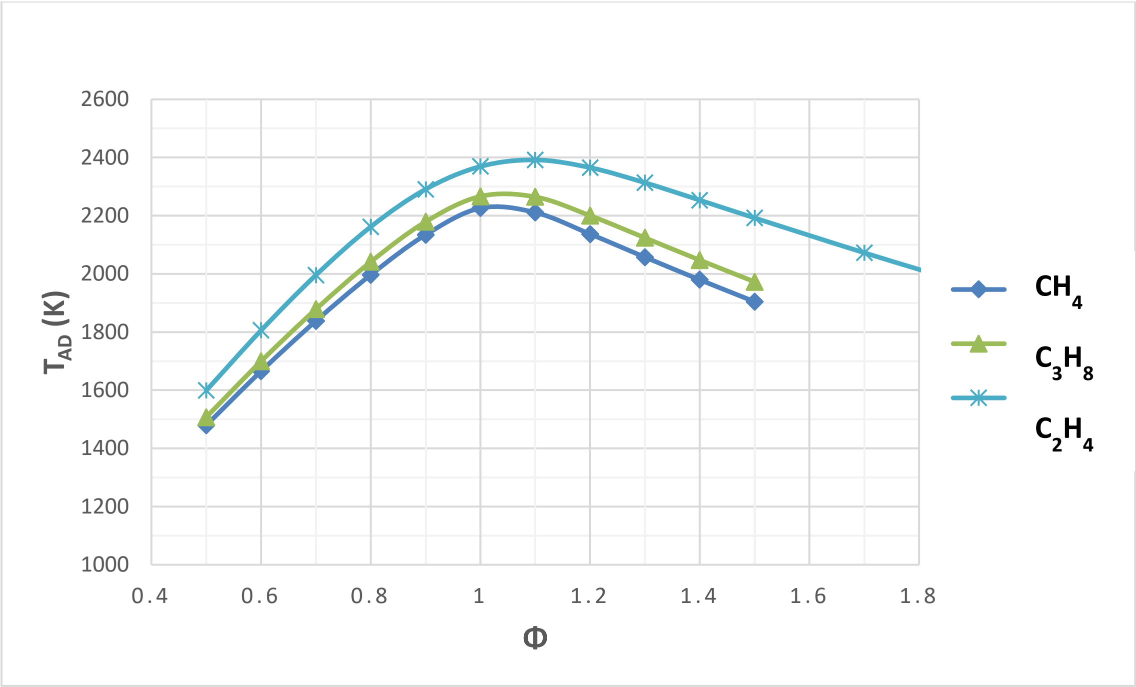

Figure 2.2: Adiabatic flame temp versus Equivalence Ratios for CH_4, C_3H_8 and C_2H_4 (Source: [110]).

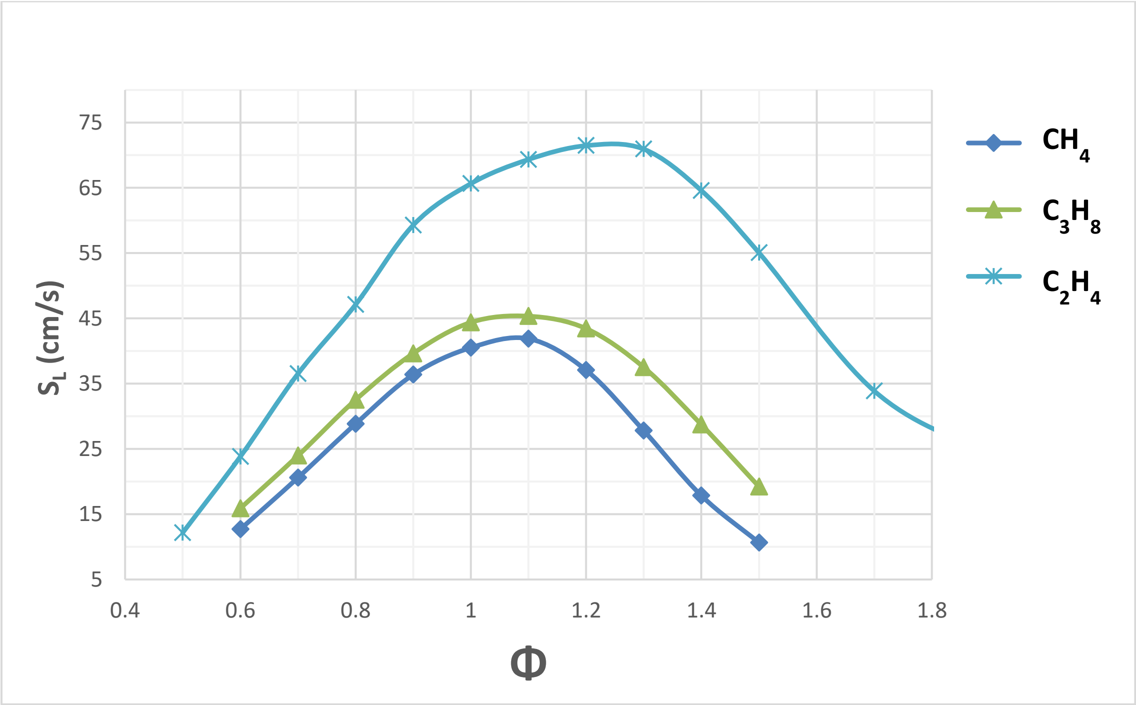

Figure 2.3: Lam flame velocity versus Equivalence Ratios for CH_4, C_3H_8 and C_2H_4 (Data Source: [112])

2.2 Fundamentals of Laser Induced Spark Ignition

2.2.1 Mechanisms of Laser Ignition

According to Ronney [10], there are four known mechanisms by which laser radiation can ignite combustible gas mixtures. These includes thermal initiation, non-resonant breakdown, resonant breakdown, and photochemical ignition. In thermal initiation, no electrical breakdown is required, instead a laser source is used to heat up the mixture beyond its threshold ignition temperature[16]. It is also possible by heating of a target surface in the combustion chamber. Consequently, molecular bonds are broken, and chemical reaction occurs leading to ignition. This mechanism is unique in that it can easily be used to ignite combustibles in combination of solid [114], [115], liquid [116], and gas phases [117], [118],[119],[120]. The method is most suitable for fuel/oxidizer mixtures with strong absorption at the laser wavelength, but it involves long ignition delay times. In photochemical ignition, laser photons dissociate target molecules into highly reactive radical species, leading to ignition (provided radicals production rate is higher than their recombination rates). Various studies on this ignition mechanism have shown that it involves less energy and it does not involve photoionization [121],[122],[123],[124] or direct heating [125]. Compared with other mechanisms, mixtures can easily be ignited at lower pressures and closer to the flammability limits. However, it requires a close match between the laser excitation wavelength and the target molecules absorption wavelength; hence a tuneable laser is required. The resonant breakdown ignition process involves, first, a non-resonant multiphoton dissociation of molecules resulting to freed atoms, followed by a resonant photoionization of these atoms. This process generates sufficient electrons needed for gas breakdown. Theoretically, less input energy is required due to the resonant nature of this method. This mechanism has been demonstrated for successive ignition of H_2/O_2 and H_2/N_2O mixtures at atmospheric pressure using a tuneable UV laser to produce laser pulses near 225.6 nm wavelength and to produce ground state oxygen atoms from the two-photon photodissociation of O_2 and NO_2 molecules [18],[19],[126]. The Non-resonant breakdown ignition is the most widely studied laser ignition method with similar characteristics to the electric Spark Ignition [127]. It involved the use of focused laser beam to create an electric field of sufficient intensity which cause dielectric breakdown of the air-fuel mixture. Like the electric spark system, it involves production of plasma which emits light, heat and shockwave. Hence, it is also referred to as Laser Induced Spark Ignition (LISI) or simply Laser Ignition (LI). In the rest of the thesis, the terms Laser Ignition or Laser Induced Spark Ignition would be used to refer to Non-Resonant Breakdown ignition.

2.2.2 Basic setup and important thresholds for successful laser ignition

The basic setup needed for laser ignition is shown in figure 2.3. It consists of a short laser pulse beam (usually in the *ns* or *ps* time regime) which is tightly focussed within a small volume of a flammable mixture by a converging lens.

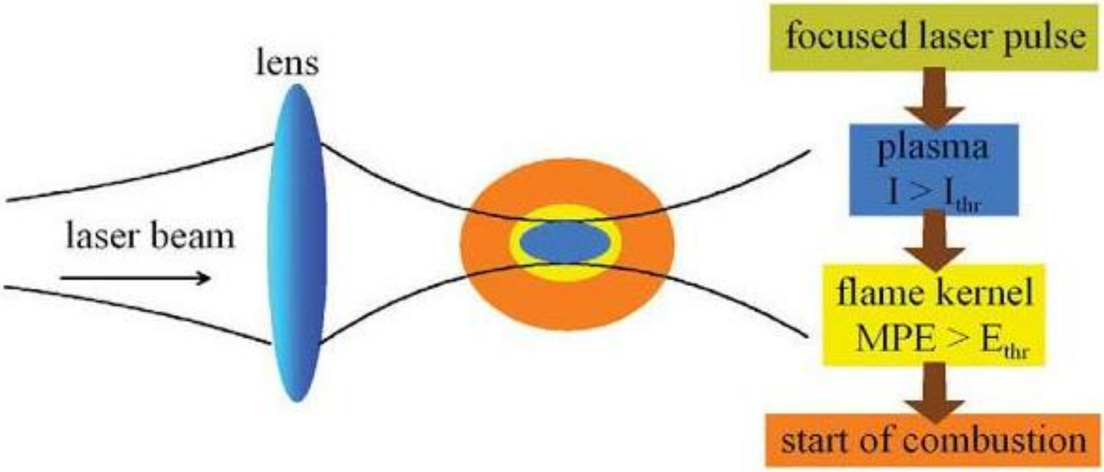

Figure 2.4: Schematic of Laser ignition setup and thresholds for ignition success [11]

Also depicted in figure 2.3 are the important thresholds for successful laser ignition most of which are discussed in the paragraphs below.

Breakdown Intensity threshold (I_o): The first condition for a successful ignition by laser induced breakdown is that in the focal point, a certain intensity threshold (I_o)

has to be exceeded. If the laser pulse exceeds this intensity, a plasma is formed, and it is possible to ignite a stoichiometric mixture with pulse energies below 1 mJ. For most gases under atmospheric condition, the required threshold for plasma generation is of the order of 10^{10} - 10^{12} W/cm^2 [27], [35].

Minimum Ignition Energy (MIE or E_{min}): A second necessary condition for successful ignition is that the energy input from the laser spark must exceed a certain value known as minimum ignition energy. This is the energy required to raise the temperature of a sphere of gas with radius equal to the characteristic flame thickness (δ_f) and temperature equal to the adiabatic flame temperature (T_{ad}) [10],[27]. For deflagrative combustion, the MIE and δ_f can be approximated by the following equations:

$$E_{min} = \frac{4\pi{\delta_f}^3}{3} * \rho_f * c_p * \left(T_f - T_g\right) \qquad 2.10$$

$$\delta_f = \frac{k}{\rho_f * c_p * v_f} \qquad 2.11$$

where: $\rho_f, T_f,\ v_f$ represents the density, temperature, and velocity of the flame, respectively. $T_g,\ c_p$ represents the cold mixture temperature and specific heat capacity at constant pressure.

The concept of MIE had earlier being captured in [128] description of ignition of premixed gases by deflagrations (i.e., flame propagation at sub-sonic speed) as follows:

> “If a subcritical quantity of energy (in the form of heat and/or radicals) is deposited in a combustible mixture (of premixed gas and air), the resulting flame kernel decays rapidly because heat and radicals are conducted away from the surface of the kernel and dissociated away from the surface of the kernel and dissociated species recombine faster than they are regenerated by chemical reaction in the volume of the kernel. The kernel extinguishes after consuming a small quantity of reactant. However, if the ignition energy exceeds a certain threshold (i.e., the minimum ignition energy) at the time when the peak temperature decays to the adiabatic flame temperature, the temperature gradient in the kernel is sufficiently shallow that heat is

> generated in the kernel faster than it is lost due to conduction to the unburned mixture”.

The problem with the above description (also known as Homogeneous hot-gas model) is that it excludes gas breakdown and blast wave processes present in laser ignition. Although, the description by Lewis and von Elbe was originally applied to electrical sparks, it is equally applicable to laser-ignited combustible gas mixtures and has been measured by many authors.

Minimum Pulse Energy (MPE): this is the minimum value of total pulse energy needed to yield ignition. The MPE includes both the MIE and the losses due shock waves, reflections, convections and radiations. It is a more practical term compared with MIE which is prone to experimental errors and uncertainties. For a nanosecond laser pulse, the MPE for methane/air is about 5-10 mJ under lean conditions [11].

2.2.3 The Laser Ignition process

Figure 2.4 gives a picture of the processes involved in a typical Spark Ignition engine and their timescales. As shown in the figure, the processes leading to the formation of a laser-ignited flame can be divided into these four stages:

- Gas breakdown or Spark generation
- Spark evolution
- Flame-kernel development
- Combustion.

While this study is mainly focussed on understanding flame kernel development, efforts will be made in describing some of the other processes. Further details of the processes leading to LIS ignition can be found in [69], [20], [27].

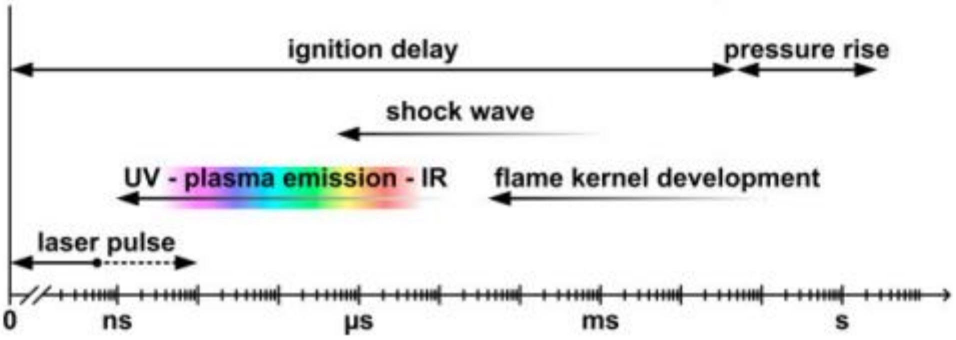

Figure 2.5: Timeline and Sequence of Laser Ignition process [27]

2.2.3.1 Gas Breakdown (Spark generation process)

The first significant event in Laser ignition is the generation of spark plasma by a tightly focused laser beam. Plasma formation is the result of gas breakdown, and this happens when the intensity of radiation within the focal volume exceeds the Breakdown Intensity threshold (I_o) of the gas present. Figure 2.6 shows the steps involved in laser induced breakdown of gases starting from the initial seed electrons to the gas breakdown. As shown in the figure, the presence of initial electrons in the focal volume is a necessary condition for the electron avalanche (i.e., electron density growth) which leads to gas breakdown. The free electron can be supplied either by seed electrons present in the gas as impurities or by multi-photon ionization of gas molecules.

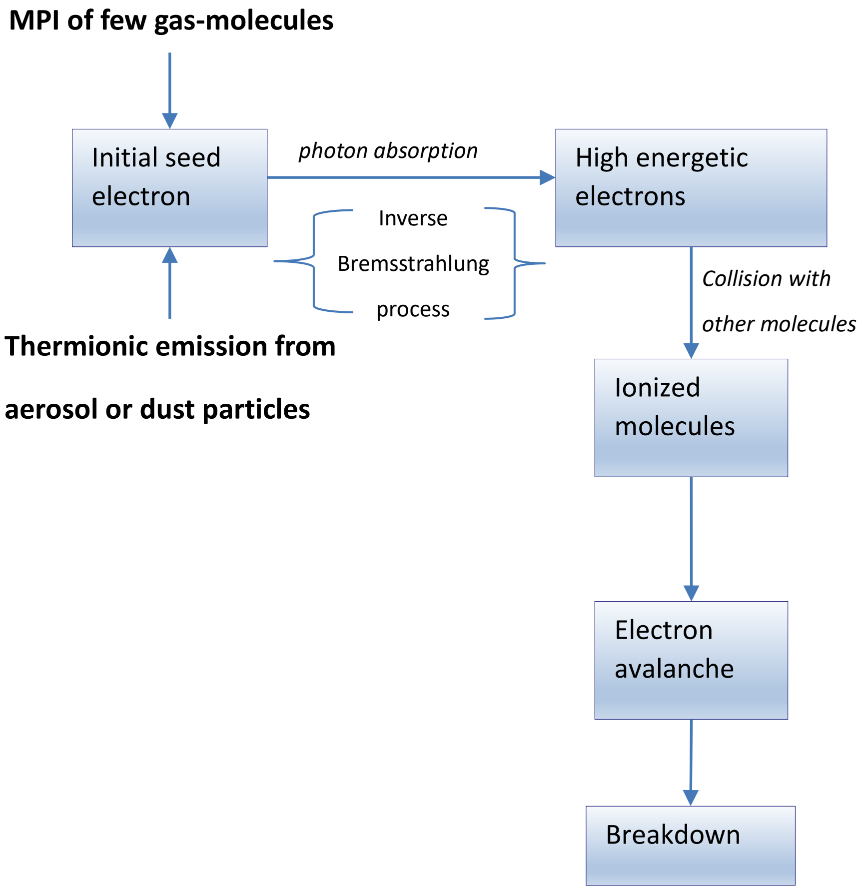

Figure 2.6: The Gas Breakdown process [11].

Initial Seed Electron: Impurities, like aerosol particles, dust or vapor in the focus can be the source of some initial electrons. Such particles typically have a low ionization potential (less than 1eV) and, therefore, can be ionized resonantly by the laser radiation or thermionically due to absorptive heating. Experiments conducted in air at a wavelength of 10.6 µm, showed that the plasma was initiated by aerosols within the focal volume[129]. Under normal atmospheric conditions, there are more than 10^7 particles per mm^3 larger than 0.1 µm[130]. These particles would heat under laser irradiation by absorption and could generate electrons by thermionic emission[131].

Multiphoton Ionization: Another mechanism describing electron generation and growth is multiphoton ionization (MPI) which is illustrated in Figure 2.7. In the MPI process, a gas molecule or atom (M) simultaneously absorbs many photons. If the combined absorbed energy is higher than its ionization potential, then the gas molecule is ionized (M^+). The reaction process is according to the equation [27]:

$$M + m.hv = M^{+} + e^{-} \qquad 2.12$$

where: hv = photon energy, m = number of photons necessary to ionize an atom. For Ionization Energy (IE), m is given as: $m \geq \frac{IE}{hv} + 1$. This process is important only at very short wavelengths (i.e., below 1 μm) or at very low pressures (i.e., below 10 torr), where collisional effects are negligible[132],[35]. It becomes insignificant at visible and near-IR wavelengths because the photon energy at these wavelengths is much smaller than the ionization potentials of most gases. For example, the photon energy for a CO_2 laser is 0.1 eV, and for an Nd-YAG laser at 1.064 mm it is 1.0 eV, while the ionization potentials for most gases are larger than 7 eV. Thus, the multiphoton ionization process would require the absorption of 70 CO_2 photons (or 7 Nd-YAG photons) to ionize most gases.

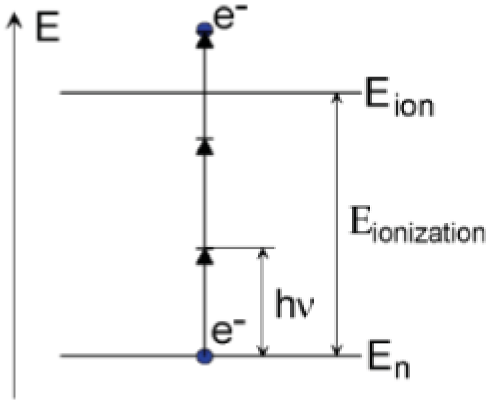

Figure 2.7: Illustration of Multiphoton Ionization[11]

Electron cascade process: After a sufficient number of free electrons have been produced via either (or both) of the above processes, the electron cascade process begins. The electrons gain energy by the absorption of photons which causes them to accelerate. This process is called inverse bremsstrahlung effect [131]. The accelerated electrons on impact with neutral gas molecules causes them to ionize leading to an electron cascade. The reaction process is given as[27]:

$$e^{-} + M = 2e^{-} + M^{+} \qquad 2.13$$

The resulting effect is known as cascade breakdown, where the number of electrons (N_e) increases exponentially with time (t) according to the following equation[27]:

$$N_e(t) = N_{e,0} * e^{\left(\frac{t}{\tau_e}\right)} \qquad 2.14$$

where:	$N_{e,0}$	starting electron density.
	τ_e	time constant given as $\tau_e = \frac{1}{\left[v_d\left(\frac{I}{I_0}-1\right)\right]}$
	v_d	diffusion rate of electrons
	$I,\ I_0$	radiation intensity and intensity threshold of medium

2.2.3.2 Spark Evolution Leading to Ignition

At about 200 ns after the breakdown, the generated spark is completely ionized, containing highly reactive chemical species that provide energy and are a chemical source for combustion initiation. At this time, the plasma has an instantaneous temperature of about 10^5 K and pressure of about 10^3 atm. These extreme conditions relative to the surrounding ambient gas give rise to rapid expansion and dissipation of deposited energy. It is also associated with shock wave generation, which give rise to heat losses in the spark. In the absence of dissociation, the plasma expansion can be modelled using Taylor's spherical blast wave theory [133], [91] given by the following equations:

$$r = (E_k/\rho_0)^{\frac{1}{5}} t^{\frac{1}{5}} \qquad 2.15$$

$$v = \frac{2}{5}(E_k/\rho_0)^{\frac{1}{2}} r^{-\frac{3}{2}} \qquad 2.16$$

$$P = [2/(\gamma+1)]\rho_0 v^2 \qquad 2.17$$

$$T = T_0\left[\left(1-\frac{{v_0}^2}{v^2}\right)\left(\frac{\gamma-1}{\gamma+1}\right)+1\right] \times \left[\left(\frac{v^2}{{v_0}^2}-1\right)\left(\frac{\gamma-1}{\gamma+1}\right)+1\right] \qquad 2.18$$

where: r is distance, E_k is the thermal energy behind the blast front generated by the spark, ρ_0 is the gas density, v and v_0 are the shock and sonic velocities, respectively, $\gamma = c_p/c_v$, and P and T are the pressure and temperature at the blast front. An illustrative model by [92] for a 10 mJ spark deposited in a stoichiometric $H_2/O_2/Ar$ mixture showed that the spark expansion speed decays from supersonic to subsonic in less than 5 μs.

Based on several studies [92],[20],[80], two scenarios have been proposed to be responsible for transition spark evolution to an igniting flame kernel. The first proposal known as the blast wave ignition model states that ignition is a direct outcome of heat of the surrounding mixture to the ignition temperature by the force of the decaying shock wave. However, available experimental data do not support this model [134],[135]. One reason given is that there is a distinct separation of time scales between the shock wave (several microseconds) and the combustion wave (several milliseconds). Another reason based on Semenov's condition for spontaneous ignition shows that even when there is a shock sufficiently strong to ignite the surrounding combustible mixture, the ignition zone does not remain long enough. The second proposal known as hot gas ignition model states that ignition of the surrounding gas mixture indirectly results from the remaining energy of the hot gas after shock wave expansion. This model is supported by [136] who modelled the ignition coupling by adding an adiabatic expansion model to the blast wave theory. Also, this model did not consider energy losses due to shock wave generation. This is also supported by [92], who modelled the coupling between the spark expansion and ignition by adding a simple kinetic model (which considers dissociation of species present) to the blast wave equations.

An important consideration for a transition from a spark plasma of hot gas to a self-sustained flame is the chemistry of ignition reactions. The chemical reactions during this process can be divided in three steps [52]: chain initiating step, chain propagating step, and chain terminating step. This transition begins with the initiation of the chemical reactions and usually occurs in a few hundred microseconds after the breakdown. During the ignition process, the second step must be reached in such a manner as to obtain a self-sustaining flame. According to the hot-gas ignition process, the hot-gas kernel must be sustained longer than the initiation of the chain propagating step. This time corresponds to the ignition delay of the flame, and is very sensitive to the mixture equivalence ratio, mixture type, temperature, and pressure [83],[137]. The shape of the flame front during this transition phase is called the flame kernel and is the focus of the present study.

2.2.3.3 Dynamic features of the Laser-ignited Flame Kernel

Based on photographic images of the early flame kernel acquired by different research groups, the shape of the flame front at different time intervals reveals two distinguishable propagation features. The first distinct feature is a toroidal flame front propagating radially upward and downward in a direction perpendicular to the laser beam axis. The toroidal shaped kernel is usually observed at the early stages (i.e., $t < 100$ μs) and it is present in both laser and electric spark ignition. Computer simulations by [138] shows that the toroidal shape of the kernel is due to an induced inward flow which results from an over-expansion of the shock wave, emanating outward from the region of the discharge at a very high velocity. Figure 2.8a is a pair of LIF images captured at 3 and 22 μs showing transformation from ellipsoidal spark kernel to a toroidal flame kernel [92]. When the two images are superposed, a set of constant velocity streamlines can be drawn (Figure 2.8b) which shows toroidal rings generated by the shock waves expansion. These are indicated by the lengths of the arrowed vectors, the scale for which is indicated by the arrowed line for 25 m/s.

The second distinct feature is a propagation of the flame front back towards the ignition laser. The resulting shape is called the front lobe. The formation of the front lobe follows after the toroidal flame kernel front is formed (i.e., $t > 100$ μs) and it is peculiar only to laser ignition. There are different viewpoints on how the front lobe is formed. One suggestion by [92] is that it may be due to the initial flow field created by the propagation of a radiation transport wave up the laser beam, arising from the high rate of energy transfer at the leading edge of the plasma. However, it is argued that this propagation would cease shortly after the laser pulse is ended (~15 ns duration). Another explanation by [92] attributes the third lobe to asymmetry to the spark with a corresponding asymmetry in the gas flow that follows propagation of the shock wave and ensuing overexpansion. The asymmetry of the spark is evidenced by the formation of an intense spark centre located away from the midpoint of the spark volume, biased towards the spark laser. The resulting shock wave will then propagate outward as discussed above but with an axial component away from the intense spark centre and therefore toward from the direction of the spark laser. Gases rushing to fill the hot, over-expanded region then quickly ignite to form the kernels observed. A third explanation by [20] is that the front lobe formation is due to the asymmetry in the leading edge and trailing edge toroid that generates a centreline velocity towards the laser source. The toroid generated by the rarefaction wave, as proposed in the previous section, would appear capable of generating the lobe, particularly as the toroidal ring at the leading edge would decay more rapidly. Figure 2.9a is a pair of LIF images captured at 52 and 92 μs showing the early transformation leading to appearance of front lobe [92]. By again superposing images, but now after a longer elapsed time, it is possible to infer the direction and approximate magnitude of the induced gas motion. After the weak toroid at the left has dissipated, the gas velocity to the left, up the laser beam, can be high. This results in a flow of hot gas close to the centreline to the left and its displacement by cold gas from the right. The elongated hot gas kernel comprises the third lobe. It is always directed towards the laser and is present in both non-reacting and reacting mixtures. Figure 2.10 represents the sequence of the flame kernel development in three-dimensions which highlight key geometric features of the flame kernel.

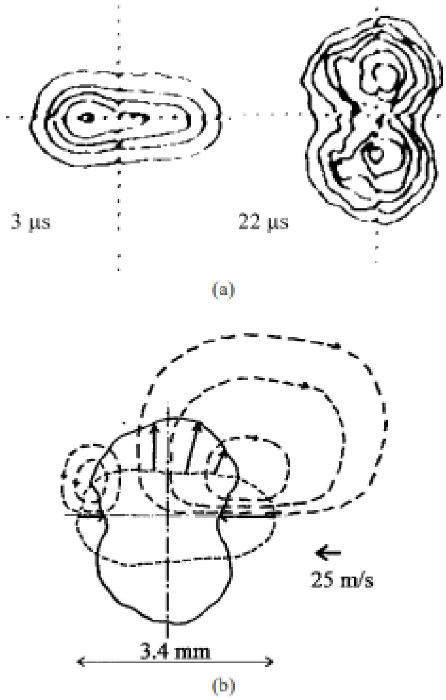

Figure 2.8: Formation of toroidal flame front: (a)LIF images showing transition from spark to toroidal kernel (b) Streamlines showing toroidal rings in superposed images [20].

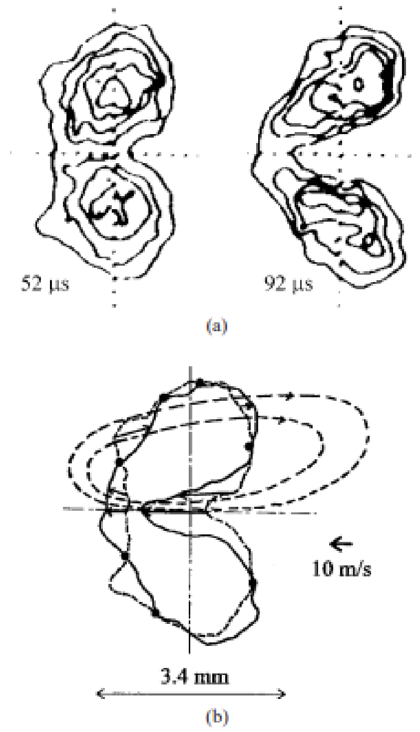

Figure 2.9: Formation of the front lobe: (a)LIF images showing transition from spark to toroidal kernel (b) Streamlines showing toroidal rings in superposed images [20]

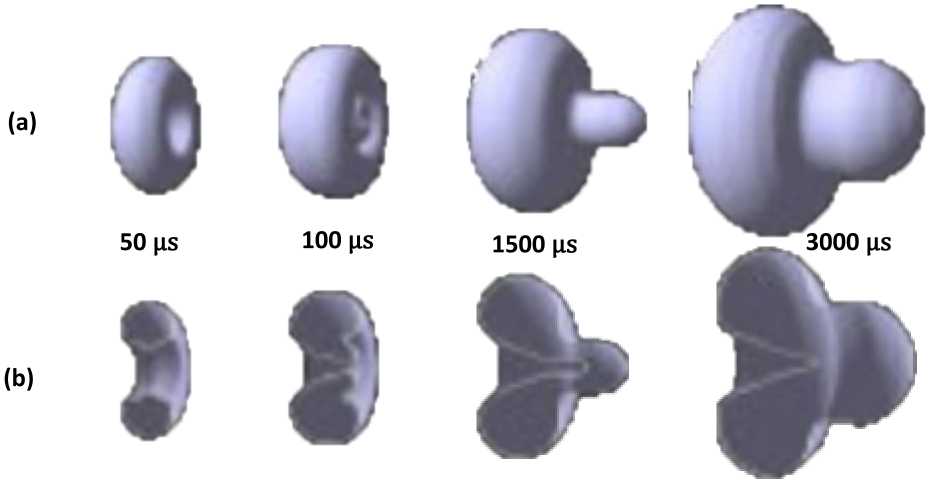

Figure 2.10: Development of the Laser flame kernel: (a) Three-dimensional view, (b) Half-section view. [27]

The above features may not provide enough evidence for a successful ignition since the early kernel growth is mainly influenced by the gas dynamics of the shock wave and the high energy plasma. A necessary feature of an igniting kernel is the production of sufficient quantity of radicals at the moment of chemical reaction initiation. In [96], measurement of the temporal evolution of the OH* emission intensity for two ignition trials (successful and misfiring cases), performed at the same deposited energy, displayed an identical evolution during the first 100 µs. In this measurement, a peak in intensity corresponded to the generation and the cooling of the spark. In the misfiring case, the intensity rapidly decreased to zero after the peak, whereas in the firing case, this peak is followed by a second peak between 400 and 1000 µs, which corresponds to significant production of radicals and thus to the initiation of the chemical reactions.

2.3 Summary

This chapter has provided insight into the theoretical basis for understanding ignition initiation using a Laser beam and the propagation of the resulting flame kernel in gaseous flow environment. It started with a discussion on the fundamental properties of the flow as a foundation for understanding the preparation of premixed flow environment for ignition to occur. Also discussed are the fundamental theories of laser spark generation and the evolution to a propagating flame which would form the basis to develop an understanding of the flame kernel. Therefore, based on the gaps earlier identified from literature survey, this report will further investigate the development characteristics of a LISI flame kernel under premixed flow condition. The investigation will focus on the features related to both the fluid dynamics and reactivity. In the next section, follows with a description of the experimental methods employed.

Chapter 3 Experimental Setup and Measurement Techniques

This chapter gives an overview of the experimental facility and measurement techniques employed in the present study. The components of the experimental facility include the fuel and air supply system, mixture preparation and delivery system, atmospheric burners, laser ignition and various control/data gathering instrumentation. The main diagnostic techniques employed includes High Speed Laser tomography, High speed particle image velocimetry (HSPIV) and chemiluminescence imaging. Also, these experiments required detailed risk assessment and safe experimental procedures details of which can be found in appendices (see Appendix A: Experimental Procedures and Appendix B: Risk Assessment).

3.1 Fuels

Ignition and development of a flame requires the presence of fuel and oxidant mixture, either in premixed or non-premixed state. In all experiments, the fuel and oxidant were introduced as premixed charge before ignition. Three hydrocarbon fuel gases were investigated which includes: methane, propane, and ethylene. Table 3-1 is a summary of the of the three fuel gases investigated and their combustion properties.

Methane used for this study is technical grade CP methane, of 99.9% purity, supplied from a 200 bar BOC Gas Cylinder of 12 m^3 capacity. It is a fuel gas with chemical formula, CH_4 consisting of a single carbon atom linked to four hydrogen atoms by single covalent bonds[139]. Due to its tetrahedral molecular structure, methane exhibits unique combustion characteristics which makes it an ideal fuel for experimental studies. For example, due to its large C-H bond energies, methane has a high ignition temperature and low laminar flame speed. In addition, it has unity Lewis number (*i.e.,* $Le = 1$) which means its data can be easily applied to modelling validation by neglecting *Lewis number* effects. Above all, methane was chosen as the primary (i.e., base) fuel because it is the most widely researched, most understood and most widely implemented of all fuel gases[139]. The **Propane** used is commercial grade propane supplied from a 6 bar BOC Gas Cylinder of 11 kg weight. It is one of the liquefied petroleum gases (LPG) with chemical formula C_3H_8. Propane is produced during natural gas processing and/or petroleum refining. It is economical to store and transport in liquefied form. Due its availability and adaptability as engine fuel, the use of propane as an alternative transport fuel is rising with about 17 million vehicles worldwide. The **Ethylene** used is a research grade ethylene supplied from an 80 bar BOC Gas Cylinder of 15 kg weight. This fuel gas has the chemical formula C_2H_4 consisting of two double-bonded carbon atoms each linked to two hydrogen atoms by single bond. It is a by-product of steam cracking of longer chain hydrocarbons (an energy intensive process that involved temperature of between 750-950^oC). It is commonly used in agriculture to enhance the ripening of fruits and to stimulate rubber tree to yield more latex. Also used in petrochemical industry for polythene production by polymerization. Its thermos-physical properties compared to gasoline are strong indications that the gas can be easily combusted. For example, both the enthalpy of combustion (~49.46 MJ/kg) and autoignition temperature (~490^0C) indicates better combustibility of the gaseous fuel in conventional gasoline in SI engines[8].

The oxidant used for all the fuels studied is **atmospheric air** supplied from the central laboratory compressed air system. It was chosen due to its established usage in combustion systems. The actual composition of dry air is 20.9% oxygen, 78.1% nitrogen, 0.9% argon, with trace amounts of carbon dioxide, helium, neon and hydrogen. However, these can be approximated to just 21% oxygen and 79% nitrogen, hence dry air is usually represented by the formula, $O_2 + 3.76N_2$ in chemical equations.

Table 3.1: Summary of fuel molecular and ignition properties

FUEL	**Mol. wt. (kg/mol)**	**Density @ 20°C (kg/m^3)**	**Dyn. Visc @ 20°C (Pa. s)**	**Min Ign. Energy (mJ)** [140]	**LFL - UFL (vol%)** [113]	**max u_L @ s.t.p. (m/s)** [112]	**max T_A @ s.t.p (K)** [110]
Methane	0.016	0.656	1.03E-05	3.00E-01	4.9 - 15.8	4.30E-01	2.23E+03
Propane	0.044	1.88	7.40E-06	2.60E-01	2.03 -10.0	4.40E-01	2.27E+03
Ethylene	0.028	1.26	9.60E-06	7.00E-02	2.74 - 31.5	6.60E-01	2.37E+03

3.2 Atmospheric Burners

For the experiments presented in this report, two different configurations of co-flow atmospheric burners were employed. The Co-flow burner is a Bunsen-type burner in which the flow mixture exits the system as *co-axial* gas jets. Similar to free gas jets, two distinct regions of flow can be spotted: a potential core region (where the jet velocity of the inner flow is maintained) and a mixing region (where the jet expands and interacts with the co-flow gas or surrounding air). The co-flow burner was chosen instead of a constant volume vessel because it provides complete optical access, allowing the use of any chosen laser diagnostic technique.

The first burner consists of two co-axial straight cylindrical tubes made from a 1.5 mm thick, Stainless Steel. This is the same burner used in [100] with an inner tube diameter of 10 mm and an outer (i.e. co-flow) tube diameter of 25 mm. In the initial study involving characterization of both the flow and flame regions using HSPIV, the reactants (i.e., methane and air) were externally premixed and admitted into the burner through a single inlet port. In the experiment, co-flow was not particularly required due to lower risk of flashback. A schematic of the setup used for HSPIV measurements is shown in Figure 3.1.

The second burner used for the chemiluminescence measurements is also an atmospheric co-flow burner but differs in geometry from the first burner. Unlike the first burner, it has a smoothly contoured nozzle with high contraction ratio. The inner and outer nozzles have exit diameters of 22 mm and 26 mm, respectively. Full details of the burner design can be found in [141]. In the chemiluminescence study of the flame kernel development, the reactants were externally premixed and admitted into the burner via two opposite inlet ports. During the experiment, co-flow was required especially for the laminar flame cases due to high risk of flashback. A schematic of the setup used for the chemiluminescence measurements is shown in Figure 3.2.

3.3 Gas mixture preparation and delivery

Figure 3.1 is a schematic of the burner and mixture delivery setup used for the initial characterization by HSPIV technique. In this study, methane is the only fuel used. As shown in the figure, methane is supplied from a HP Gas Cylinder (200 bar BOC) fitted with a two-stage regulator. The air was taken from a central laboratory compressed air system, fitted with a pressure regulator (range: 0 - 6 bar). Gas delivery from both sources to the burner was via flexible piping and ball valves. The supplied methane was first metered by the digital mass flow meter (MV-304) and then passed through an electrically operated solenoid valve used to shut OFF and ON the fuel line from the control room. Also, the air was metered by a digital flow meter (MV-306) and then piped into a jet atomiser which contains olive oil to generate aerosol-air mixture for laser sheet flow visualization. Both flow meters have an accuracy of 1-2 % full scale. Finally, the metered methane and seeded air were premixed at a T-junction and then sent to the burner through a single inlet port.

Figure 3.2 is a schematic of the burner and mixture delivery setup used for the chemiluminescence measurements of flame kernel. In this study, all three fuel gases (methane, propane and ethylene) were used. All the reactants were prepared in similar fashion as above except that the metered air did not require seeding. After the reactants were premixed at a T-junction, the mixture was passed through a flashback arrestor to prevent back-flow and then sent to the burner through two opposite inlet ports.

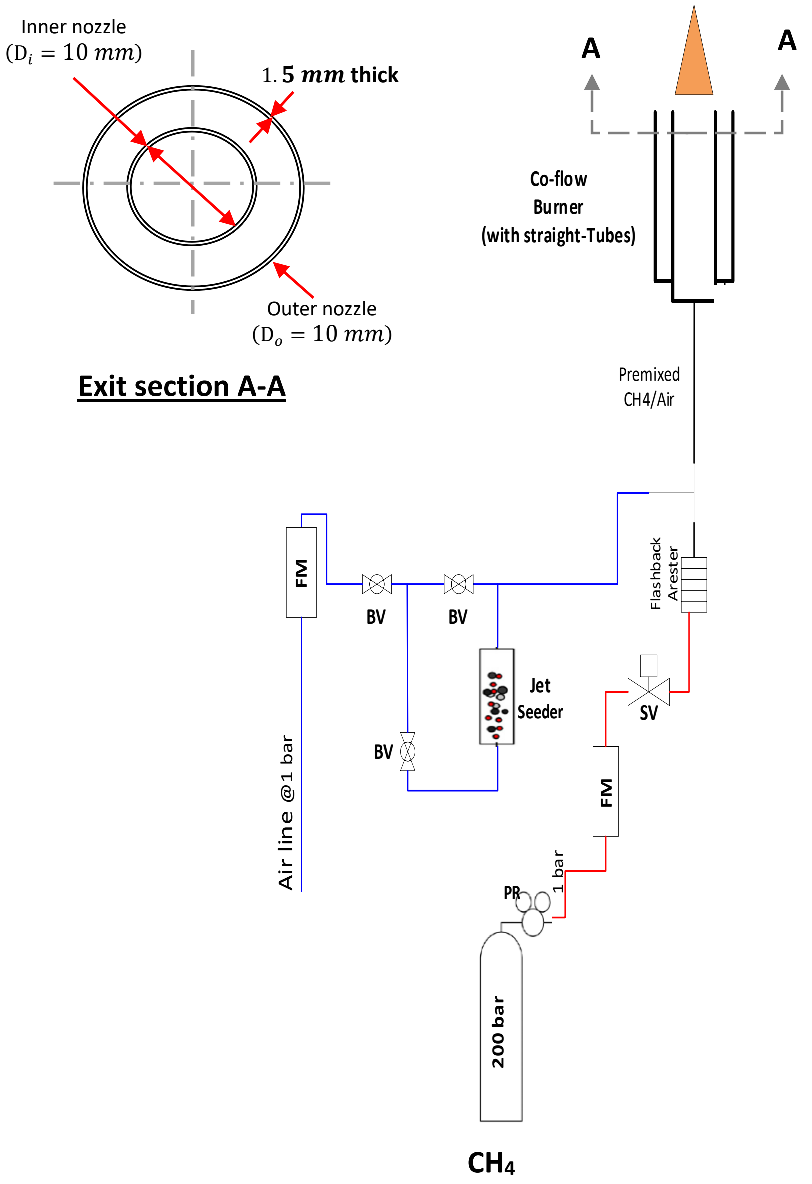

Figure 3.1: Schematic drawing of Burner, Flow Setup used for HSPIV.

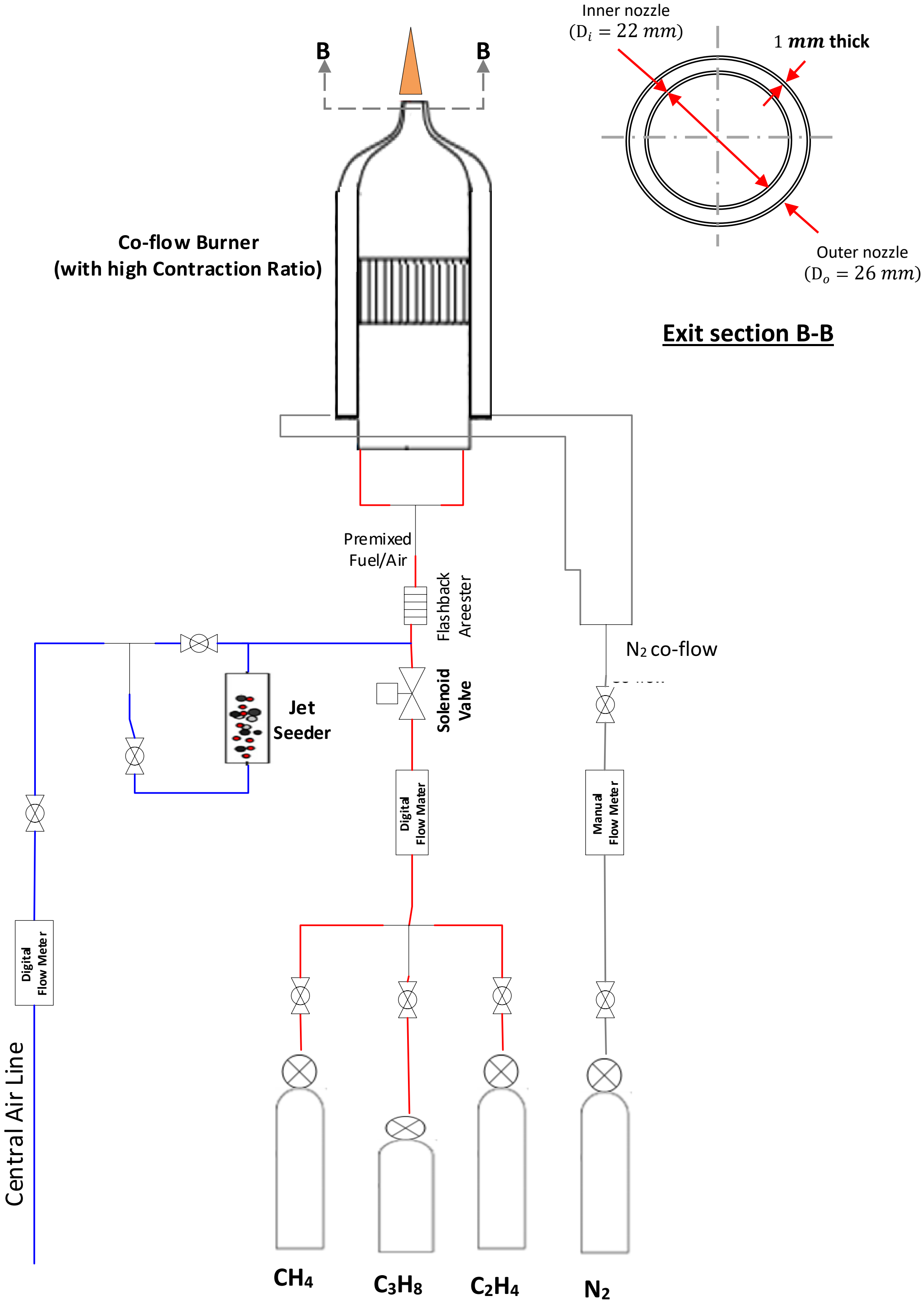

Figure 3.2: Schematic Drawing of Burner, Flow Setup used for Chemiluminescence.

3.4 Instrumentation and Measurement Techniques

3.4.1 Laser ignition, pulse energy and spark spot size

Laser ignition: For all tests, the ignition of premixed fuel gas-air charge was achieved using the spark generated from a Q-switched Nd:YAG laser beam (*Continuum*, Surelite III) which is capable of delivering 500 mJ maximum pulse energy and 7 ns pulse duration (at Full Width Half Maximum) at its fundamental wavelength of 1064 nm. The output laser beam at fundamental wavelength was steered through 90^o by a right-angle triangular prism and then focussed at 20 mm height above the Burner centre using a Plano-Convex lens of 75 mm focal length and 25 mm diameter. This height was chosen to ensure the spark occurred within the potential core region of the gas jet issuing from the burner, as revealed by the velocity profiles obtained from the PIV. Also, it allows sufficient space for development of the flame-kernel. To ensure that each ignition event is time-independent, the laser Q-switch was operated at a pulse rate of 1 or 2 Hz while the flash lamp was operated at its design frequency of 10 Hz.

Pulse energy: Before each ignition, the laser output power per pulse was measured using a pyroelectric laser energy sensor and display meter (*Gentec*, UNO). The energy output is controlled by changing the delay in timing of the laser Q-switch from the flash lamp output. Figure 3.3 is a typical energy profile of the laser at different Q-switch delays. For most of the conditions investigated, a constant energy of 32 mJ was obtained using Q-switch delay 530 μs. This energy is higher than the required minimum ignition energy (MIE) at the selected equivalence ratios of the different fuel–air mixtures.

Beam profile and spark spot size: Using a burn paper, the spot marks produced by the laser beam shows an approximately Gaussian beam profile while the focused beam has a size of about 1 mm diameter. The beam profile gives information about the beam quality. Both parameters are important because they affect the minimum energy required for plasma formation and ignition. For a Gaussian beam profile, the beam quality (defined by the M^2 *factor*) is related to the spot size at its focal point according to the equation:

$$\textbf{spark spot size } (2r) = \left(\frac{4f\lambda}{\pi D} M^2\right) \qquad 3.2$$

where:

where:	D	input beam diameter at the lens (at the 1/e2 point),
	M^2	Beam mode parameter ($M^2 > 1$ except for a perfectly Gaussian beam)
	λ	Laser wavelength
	f	Focal length

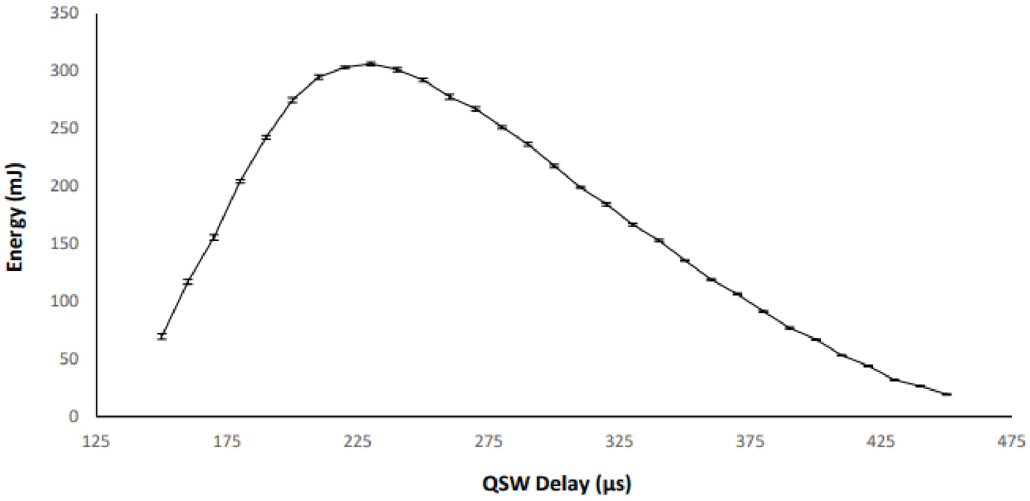

Figure 3.3: Typical Energy profile of the Ignition Laser

3.4.2 Laser sheet flow visualization and velocity field measurement

Characterization of the ignited flame kernel and its flow field was achieved using a combination of high-speed laser sheet tomography and particle image velocimetry (PIV) techniques. Laser sheet tomography enabled visualisation of the and further extraction of the flame kernel characteristics while PIV processing was employed to show the flow field structures such as the velocity vectors and turbulence intensities. The system arrangement used to deploy both techniques is the same.

3.4.2.1 Particle image velocimetry

Particle image velocimetry is a non-intrusive laser diagnostic technique, which provides instantaneous velocity vectors of the flow field. The principle of PIV is based on recording of two separate images with time delay between them as shown in Figure 3.4. Usually seed particles (or traces) are used to seed airflow, which reflect light when illuminated by a laser pulse. The flow seeded with particles is then illuminated twice and two images are recorded with small time separation between them. The velocity vectors are derived through measurement of the particle movement as shown by the acquired images in the two interrogation windows.

The interrogation windows from each image frame are cross correlated with each other. A typically interrogation window has a dimension of 16×16 or 32×32 pixels[142]. The cross-correlation procedure is repeated for each interrogation window over the two images captured by the camera producing a signal peak in each interrogation window. A sub-pixel interpolation is used to measure the velocity with high accuracy. The velocity computation is directly dependent on a number of particles in the flow. It is advised to have at least 10 to 20 particles per interrogation window[143] .

The accuracy of the measurements is dependent on the ability of the particles to follow the flow and adjust their velocity to the flow fluctuations. If the flow is subjected to extreme acceleration, for example just behind the flame front, the inertia of the particles can affect the velocity measurements. This effect can be crucial for application of PIV to combustion [144].

3.4.2.2 Laser tomography

Laser tomography is similar to PIV in the sense that it relies on the illumination of tracer particles seeded in the flow. However, the objective of this technique is not to obtain velocity vectors but to obtain a plane cross section of the flame and to visualize the shape of the flame front [145]. Usually, an oil aerosol is injected into the unburned mixture, and a laser beam formed into a thin sheet illuminates the combustion zone. The oil particles scatter the laser light in the unburned region and thus the beam can be visualised, but in the area where the flame had passed the oil would have evaporated and burned, so do not scatter the light.

A limitation of this technique is that it only allows visualisation of the two-dimensional section of the flow field. Therefore, visualisation of three-dimensional structures is unavailable. The primary use of this technique is for visualisation purposes, however secondary quantitative data can be gathered from each frame of the recordings. Using High Speed Laser tomography for flame propagation studies, secondary data on the flame arrival time, flame position and therefore flame speed can obtained.

The errors involved in this data can result from the collection of high-speed images. Magnification effects of the lens used on the camera can lead to errors in the exact definition of the region of interest. Errors in flame arrival time can also result from delays in the triggering of the recording system.

3.4.2.3 Optical Setup

Figure 3.5 is the optical arrangement used to simultaneously visualize the flow and the flame kernel in a two-dimensional plane. It includes seeded flow, illumination source, beam delivery optics, signal synchronization box and a high-speed camera.

Flow seeding

For both PIV and tomography measurements, air was flowed through a jet atomiser containing olive oil to generate the seeded flow. An important consideration in the selection of seeding material is that the particles must trace the flow with sufficient fidelity to accurately follow the important turbulent structures. For accurate measurement, typical particle diameter required for olive oil seeding is between 0.98 to 3.09 μm [146].

Flow Illumination

An important requirement for the seeding is that individual particle of the material must scatter enough light to allow definition and recording of the flow movement. Based on assumption of circular symmetry of the particle, the theory of light scattering states that the intensity of scattered light depends both on two main characteristics: the size of the particle, and wavelength of the incident light. Based on these characteristics, measurement of light scattering intensity has been classified into three distinct regimes which includes: Rayleigh regime, Geometric optics regime and Mie scattering regime. In Raleigh scattering [147], the radius of the particle is much smaller than the wavelength of the incident beam. This results in a very small light scattering intensity and therefore not suitable for imaging low velocity flows [148]. In Geometric scattering, the particle radius is much greater than beam wavelength. For such particles, the solutions present the use of a large number of terms, which in order to calculate requires the use of a computer. For the study present in this thesis, Mie scattering [149] is the chosen technique. The technique involves the imaging of light scattered by droplet particles whose radius is comparable to the wavelength of the incident beam [149]. In the present setup, illumination of the oil-seeded flow is achieved by a dual pulsed Nd:YLF laser (Litron, LDY304 model), each with wavelength 527 nm, maximum power 30.5 W @ 1 kHz. The PIV laser was mounted on the flat surface of a movable table which was rigidly clamped to the floor to prevent any motion or vibration. For all measurements, the laser pulse setting was 1.3 kHz frequency and 55% energy (corresponding to 15.8 W for laser 1 and 16.1 W for Laser 2).

Sheet formation

The beam from PIV laser was directed to a sheet forming optics device (TSI, 610026) using a flexible light arm (TSI, 1098915 model), with knuckles capable of rotating 360°. Light sheets of 527 nm wavelength exiting the optics were focused on the region of interest in the flow, illuminating the olive oil seeded airflow. The sheet optics device was mounted on an inclined optical bench to prevent any likely damage from the ignition laser beam.

Imaging system

Mie-scattered images of the seeded flow were recorded using a High speed TSI Camera (630106 model, 36 gb memory). The Camera has a resolution of 1 Megapixel (1280 x 800), a pixel size of 20 um x 20 um and a frame rate of 7400 at full pixel resolution. The camera was positioned so that the image plane was perpendicular to the plane of the illuminated flow sheet. A Micro NIKKOR lens (d = 55 mm, f = 200 mm) was fitted to the camera to provide imaging and was operated with an aperture setting of f/32. To filter out chemiluminescence from both plasma and flame, a 527 nm laser-line filter (50mm Diameter, 20 nm Bandwidth) was placed in front of the lens.

Trigger timing and synchronization

Both the laser source and the camera were synchronized using the Synchronizer (TSI, 610036 model) whose function is to control the firing of the laser source and camera frame capturing. A typical timing sequence of the PIV setup used to characterize the flow is shown in Figure 3.6. For the flame kernel development study, both the ignition and the PIV system were initially triggered using the same TTL signal from a *Stanford*, DG535 Function Generator. The PIV software was designed to allow a camera trigger delay time to be set with respect to the external input signal. However, this feature malfunctioned during trial tests, so a TG5011 Delay Generator was included to delay the PIV firing/capture from the ignition.

Software implementation and data acquisition

The Insight software allowed on-screen control of the camera and laser for accurate timing and data acquisition. The software interface is shown in Figure 3.7. The orange triangle with dashed line represents the energy profile of the laser beam which was obtained using varying Q-switch delays. The on-screen window allowed setting of laser pulse separation, dt and the required camera trigger delay, allowing adjustments to the amount of light scattered by the seeding particles for a given camera aperture. For visualization of the flow and flame kernel, the laser pulse repetition rate was set to 6 kHz equivalent to 166 μs total PIV exposure time (or 83 μs per frame for a double-frame CCD camera). The delay from the initial camera synchroniser TTL trigger to the firing of the first laser was set to 75 μs, while a laser pulse separation, 50 μs was applied to allow the capture of the velocity field range in two separate frames. The captured image from the ignition test has an area of 384 by 800 pixel (i.e., 19.2 mm by 40 mm).

The images obtained were stored as TlFF files, which were later processed to obtain flow velocity and flame tomographic information.

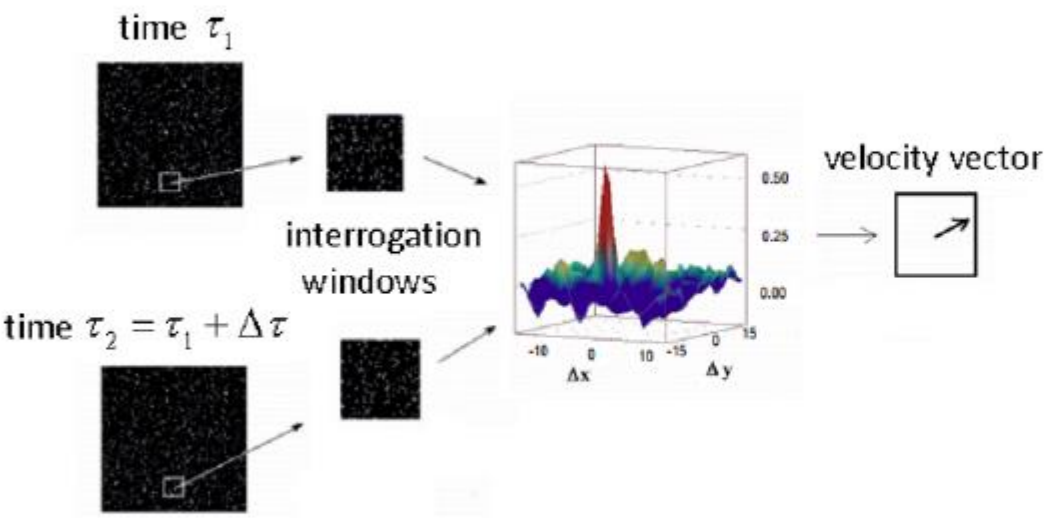

Figure 3.4: PIV cross-correlation technique[150]

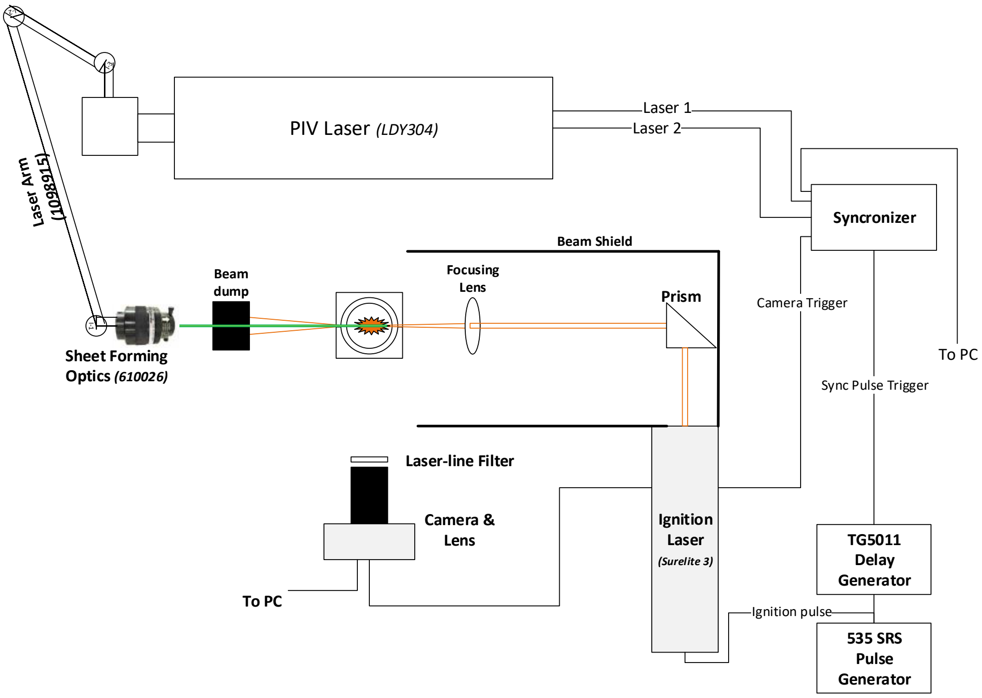

Figure 3.5: Optical Layout for PIV and Tomography Measurements

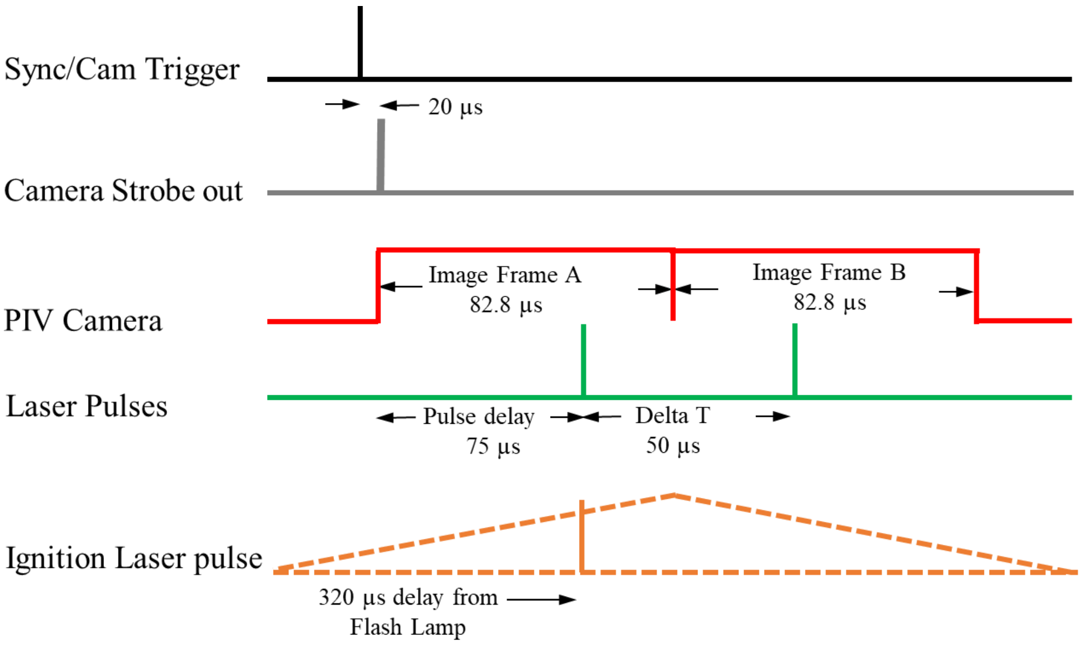

Figure 3.6: Timing Sequence for PIV and Tomography Measurements

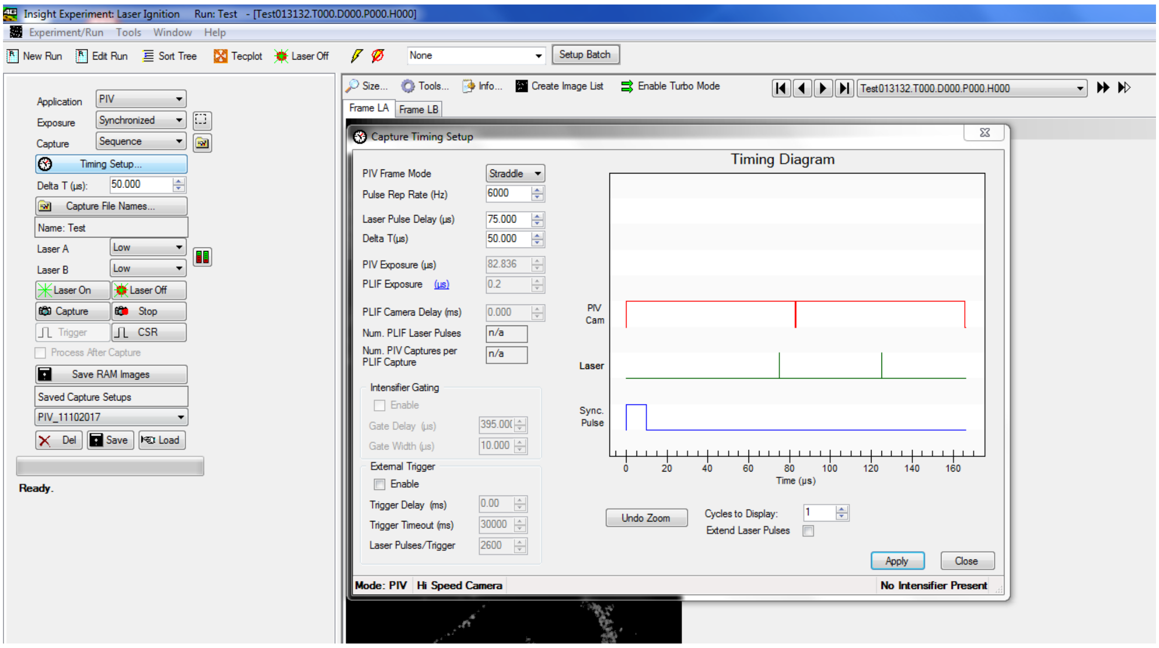

Application: PIV
Exposure: Synchronized
Capture: Sequence
Delta T (μs): 50.000
Name: Test
Laser A: Low
Laser B: Low
☐ Process After Capture
Saved Capture Setups: PIV_11102017
None
Test013132.T000.D000.P000.H000
Ready.

PIV Frame Mode: Straddle
Pulse Rep Rate (Hz): 6000
Laser Pulse Delay (μs): 75.000
Delta T(μs): 50.000
PIV Exposure (μs): 82.836
PLIF Exposure (μs): 0.2
PLIF Camera Delay (ms): 0.000
Num. PLIF Laser Pulses: n/a
Num. PIV Captures per PLIF Capture: n/a

Intensifier Gating
☐ Enable
Gate Delay (μs): 395.00(
Gate Width (μs): 10.000

External Trigger
☐ Enable
Trigger Delay (ms): 0.00
Trigger Timeout (ms): 30000
Laser Pulses/Trigger: 2600

Cycles to Display: 1
Extend Laser Pulses ☐

Mode: PIV Hi Speed Camera No Intensifier Present

Figure 3.7: PIV Software (Insight 4G) Interface

3.4.3 OH* Chemiluminescence Imaging

Chemiluminescence imaging was performed mainly to capture the characteristics of the flame kernel and its dynamics. Chemiluminescence involves capturing the radiations emitted by electronically excited molecules in the flame, while returning to their lower energy states. From emission spectroscopy, it is long known that the radiation wavelength is a characteristic of a particular molecule and the transition the molecule undergoes. As shown in Figure 3.8, the hydroxyl radical (OH*) is one of the most used markers of flame presence in combustion studies because its emission spectrum exhibits major narrowband wave peak around 308.9 nm wavelength. The OH* is an intermediate species which is formed by fast two-body reactions, such as the attack of CH radical on O_2 molecules. Unlike diffusion flames where the OH* tends to occur in thin, tendril-like structures (indicative of reactions occurring at stoichiometric fuel/air interface), OH* appearance in premixed flames can exist over a large spatial region (commensurate with the extent of the reaction zone). Hence, it is a good flame marker for the present study.

Figure 3.9 is a schematic of the experimental setup used for the chemiluminescence studies reported chapters 5-7. OH* chemiluminescence signals from the developing flame kernels were captured using a 16-bit intensified CCD camera (*Princeton Instruments*, P-MAX II) fitted with a UV Camera Lens (78 mm diameter, f/3.8). The camera uses a CCD array size of 512 x 512 pixel, and its spectral range is 180-900 nm, hence it is sensitive in both ultraviolet and visible regions. In order to capture the OH* chemiluminescence, a combination of UG 11 and WG 305 Schott glass filters were placed in front of the UV lens to filter unwanted radiations.

The camera was externally triggered using the laser output signal, **fixed sync out,** which is the same as the Q-Switch signal used for laser ignition. The timing sequence is shown in Figure 3.10. During this test, the laser Q-Switch which was internally triggered and operated at 2 Hz frequency. All camera settings used for data acquisition were remotely controlled via the commercial PC software (*Princeton*, Winspec32) provided by the camera manufacturer. The software platform enabled camera gate width and delay to be set. In all the experiment conducted, a constant gate width of 20 μs was used while ignition delay was varied between 50 μs and 10000 μs. The software also allowed captured images to be saved either as individual TIFF files or in matrix SPE file format. For each delay, a total of 200 images were captured and each capture image has an area of 512 by 512 pixel (i.e., 94.72 mm by 94.72 mm). These images were later processed with codes written in MATLAB to obtain both geometric and radical intensity information of the flame kernel.

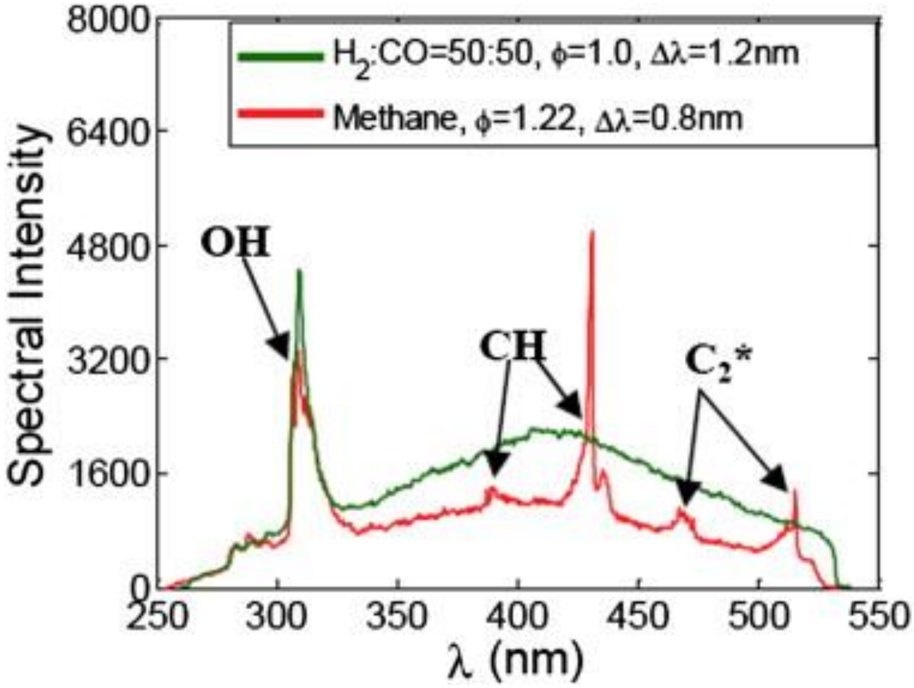

Figure 3.8: Typical flame spectra in syngas and methane flames [66].

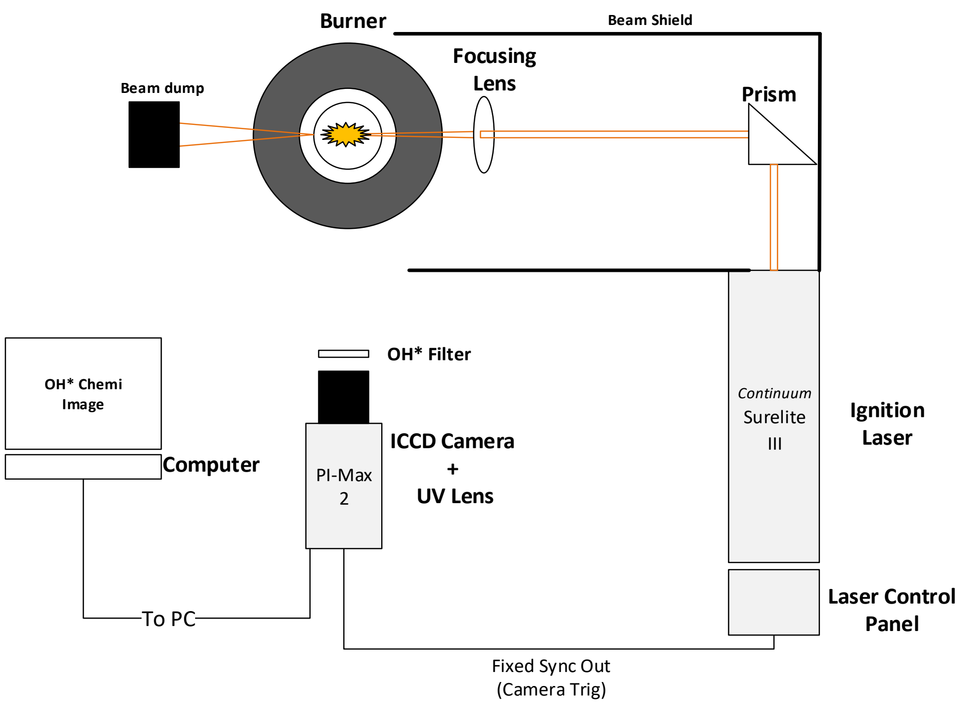

Figure 3.9: Optical Layout for Chemiluminescence Imaging

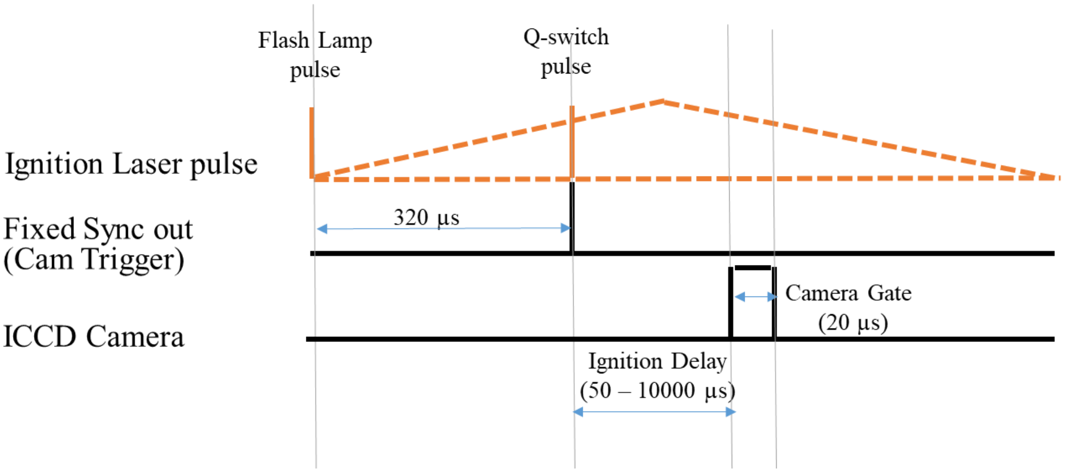

Figure 3.10: Timing sequence used for Chemiluminescence Imaging.

3.5 Data Processing

3.5.1 Processing of Velocity field data

Prior to the measurements, a target image of known dimensions was obtained. Using the calibration function present in the software, the x and y scale was input to allow conversion from pixel to mm. The calibration values obtained were 52 µm per pixel (x scale) by 52 µm per pixel (y scale).

Once the images were captured, the raw image were **pre-processed** with the Insight 4G software. The first pre-processing step involves subtraction of a minimum background image (generated by the Insight 4G software) from the raw images. Due to non-uniformity of the two image frames, background subtraction was done using two pre-processors with the first pre-processor generating the background image and the second subtracting the background image from each image. This was useful for enhanced image quality (by reducing signal-to-noise ratio) and for obtaining a uniform image for the PIV. The second pre-processing step involved masking of the background subtracted image. This was done to separate the flame boundary from the flow. To enable movement of the boundary, a dynamic mask was created by setting the intensity threshold value as one. Also, the images were conditioned to restore intensity in flow areas with low intensities.

After the initial image pre-processing, velocity vectors of the flow were obtained using in-built functions provided in the software. Insight 4G performs velocity field calculation using a two-frame cross-correlation routine, which incorporated an FFT correlation engine and a Gaussian peak search algorithm. This correlation method differs from autocorrelation and single-frame cross-correlation, in that it achieves image particle separation by recording the first laser pulse images on frame 1 and the second laser pulse images on frame 2, thus allowing the velocity to be measured without directional ambiguity. By repeated application of the cross-correlation routine to the interrogation window pairs (Figure 3.4), an intensity spectrum is obtained from which particle displacement and velocity were computed.

For the current analysis, a final grid size of 32 by 32 pixels (i.e., interrogation region) with a maximum displacement limit of 4 pixels. This grid size proved to give good results with reasonable resolution compared to grid sizes of 64 by 64 pixel. No masking was used in processing the results. This is due to the high computational time required when masking is used for processing. The default FFT correlation engine was used due to its speed. The Gaussian peak correlation is the default setting with FFT, and thus it was selected. Insight 4G allows the user to specify the minimum number of particles and the signal to noise ratio of the interrogation spot required for a velocity vector to pass. The defaults of 10 particles per interrogation spot, and a signal to noise ratio of 1.5 were chosen. Table 3.2 lists the settings used for PIV images processing using Insight.

The cross-correlation method of processing PIV images can generally produce over 95% correct velocity vectors [151], however, spurious vectors can also be produced. For the results obtained during this study, good agreement was achieved with the calculated bulk flow velocity, however, as with all experimental investigations using PlV, a small number of false vectors were apparent. Insight 4G provides a number of inbuilt macros, ranging from a standard deviation filter to a smooth filter, which allowed the validation of the computed results. Results presented in this thesis were subjected to a median filter. The local median filter applied, compared each velocity vector in the field with a median value calculated from the surrounding neighbourhood vectors. Full details of the validation scheme can be found in [152].

Finally, the results of the processed data were exported in excel format. A code written in MATLAB was further used in visualising the flow velocity vectors as well as the turbulent intensities. Detail of the code are contained in section C3 of Appendix C

Table 3.2: PIV Processing Settings

Grid Engine	Nyquist	**Grid size**	32 x 32
Mask Engine	No mask	**Signal-to-Noise Ratio**	1.5
Correlation Engine	FFT	**Max. Displ (pixel)**	4
Peak Engine	Gaussian	**Min. # of particles**	10

3.5.2 Processing of flame kernel data from the Raw Tomographic Image

Following the initial pre-processing of captured imaged using Insight 4G software, further processing was done to extract the flame boundary using MATLAB. Figure 3.11 shows the processing steps from the raw to the boundary detected edge of the flame kernel. After pre-processing, the first processing step in MATLAB was binarization and image inversion. To be able to separate the flame region from the flow, it was necessary to create a binary (i.e., black and white) image, where the white part is the flame, and the black part is the flow. This was achieved using two MATLAB functions (a binarization function followed by an inversion function). Finally, the flame edges were detected using another MATLAB function (known as canny edge detection). From the detected edges, the geometric properties of the flame kernel were obtained. The codes written for these processing is contained in section C1-C2 of Appendix C.

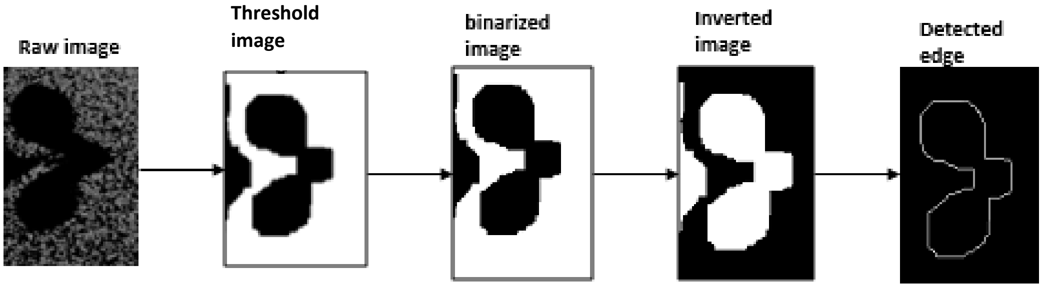

Figure 3.11: Image processing steps

3.5.3 Processing of Flame kernel data from the OH* chemiluminescence Images.

Following acquisition of chemiluminescence images, computer codes written in MATLAB were used to process the images (see Appendix D: MATLAB Code Used to Analyse Chemiluminescence Data). Figure 3.12 shows the main processing steps. The first processing step involved averaging of the 200 images acquired for each ignition delay. This step was necessary to reduce shot-to-shot variation in the analysed data and it formed the basis for further analysis.

To obtain the flame geometric characteristics, image thresholding and binarization which was performed on the mean projection images to distinguish the flame area from the fresh gases. This was achieved by first applying a multilevel thresholding algorithm based on Otsu’s thresholding technique [153]. Next, a binarization function was applied. To smoothen the flame edges, a median filter was applied. Finally, the boundary of flame edges was extracted based on an edge detection algorithm.

From the mean projection image, both qualitative and quantitative data were extracted. The visualisation quality of the images was improved by introducing colour scales as shown by the colour-mapped image. Due to the wide range of data, all the images could not be plotted on the same scale, however comparisons could be made based on the spatial structure and intensity scale of individual images.

Also, quantitative values of the spatially integrated intensity and peak intensity were directly extracted. To investigate the uncertainties in the selected sample size both the integrated intensities and peak intensities were compared for different sample sizes at different time delays. Figure 3.13 shows the normalised distribution of integrated OH* intensities with respect to sample size at various time delays which shows a variation range between 0-1% of the maximum value. Likewise, the normalised distribution of peak OH* intensities with sample sizes shows a variation between 0-5% of the maximum value as shown by Figure 3.14.

From the extracted edges, key geometric information about the flame front locations and propagation rate were obtained.

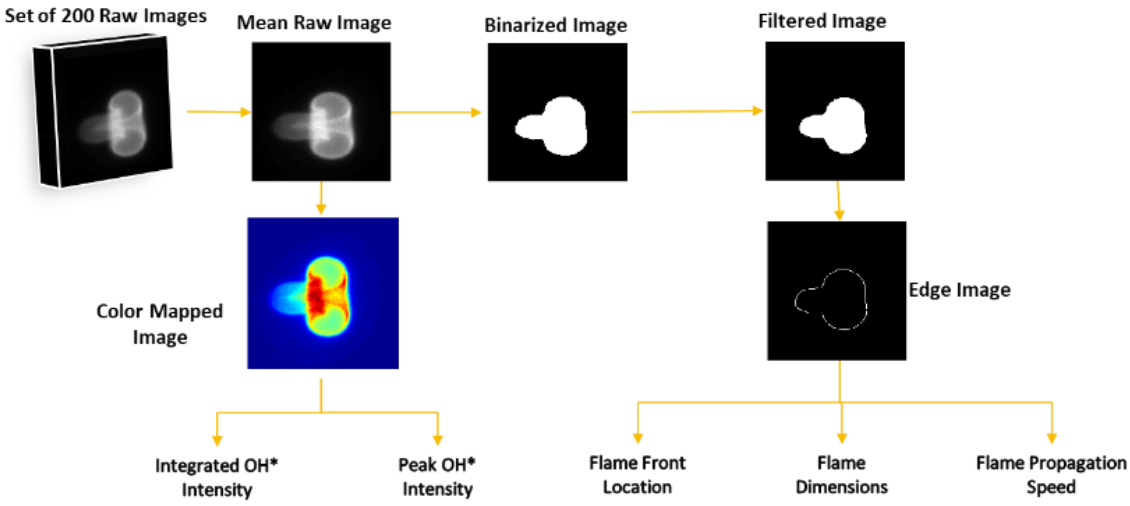

Figure 3.12: Chemiluminescence Image processing steps

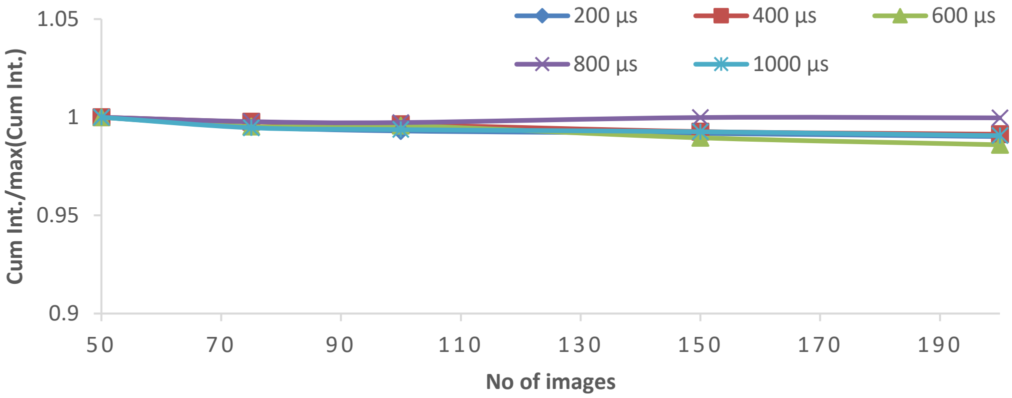

Figure 3.13: Normalised distribution of Integrated OH* intensity w.r.t sample size.

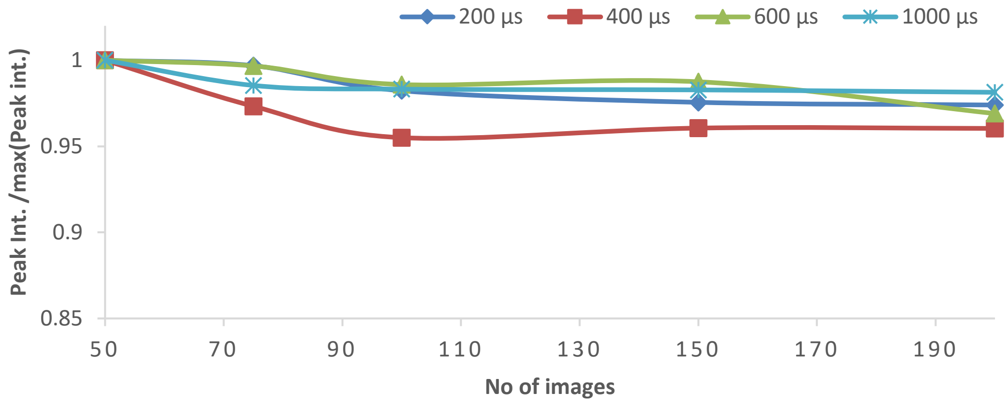

Figure 3.14: Normalised distribution of Peak OH* intensity w.r.t sample size.

3.6 Summary

This chapter presented the experimental setup and measurement techniques used in this work. The measurements were conducted based on two experimental setups and three optical techniques developed during this PhD. The first setup consists of a co-axial straight tube burner in which air-seeded methane was flowed and illuminated by using a double-pulsed PIV Laser. Following ignition of the mixture, high speed tomographic imaging of the flow field was achieved by filtering out the flame chemiluminescence using a laser-line filter. Analysis of the tomographic images would allow simultaneous investigation of the flame kernel features and its flow field. The second setup consists of co-axial contracting nozzles burner with in which different fuel/air mixtures were flowed. Repeated laser ignition and subsequent capture of the natural OH* chemiluminescence of the flame kernel enable analysis of both the fluid dynamics and reactivity of the flame.

Chapter 4 Flame Kernel and Flow-field Characterisation of Laser-Ignited Methane-Air Mixture

4.1 Introduction

The flame kernel represents the transition phase between the initiation of chemical reactions in a flammable mixture and a fully developed or self-sustained flame. In the early stage of laser ignition, measurements of the flame kernel characteristics are particularly important because the expansion speed of the flame kernel is low compared with that of a fully-developed flame [41],[98]. For example, the flame kernel shapes and sizes are useful for predicting the pressure rise with time inside a combustor which maybe too small to be detected by existing pressure probes. These properties are also useful for estimating the burning velocity which is a fundamental parameter required for the development and validation of kinetic mechanisms for fuels. One of the advantages offered by laser ignition is flexible choice of ignition location. To optimize combustion based on ignition location, there is a further need to characterise the properties of local flow field prior to ignition and during the ignition event. There have been numerous studies relating to the fluid dynamics of the laser-ignited flame kernel [92],[134],[20],[154], however there is a lack of data on the effect of the kernel expansion on surrounding flow field structure. In addition to optimizing combustion based on ignition location, such data is important for understanding the interaction between flame generated turbulence and the fluid shear generated turbulence.

In this chapter, high-speed images obtained from the 2D-flow sheet of laser-ignited stoichiometric Methane/Air mixture was used to characterise the flame kernel and its flow field. The study is divided into two main sections. In the first section, the characteristics of the laser flame kernel was qualitatively described based on tomographic images obtained using Laser sheet flow visualization. Further extraction of the flame kernel edges enabled quantitative description of the kernel characteristics such as the flame front location, kernel size and growth rate. The second section begins with characterisation of the burner under cold isothermal conditions. Finally, the flow field properties in the reacting state is described. Visualisation of the flow in both isothermal and reacting state was based on PIV technique from which the flow field quantities like velocity and turbulence intensity were extracted.

4.2 Flow conditions

To characterise the development of the flame kernel and its flow field, two flow conditions of stoichiometric methane-air mixture were selected. The flow conditions were selected based on the Reynolds number of the flows (one laminar flow case and one turbulent flow case). A summary of the test conditions for the two test cases is shown in Table 4.1: Summary of flow conditions. **Methane (CH_4)** was chosen because of its unique combustion characteristics. For example, its high ignition temperature and low laminar flame speed makes it an ideal fuel for experimental studies; It has unity Lewis number (i.e., $Le = 1$) which means its data can be easily applied to modelling validation by neglecting Lewis number effects; It is the most widely researched, most understood and most widely implemented of all fuel gases. In addition, methane is the main component of Compressed Natural Gas (CNG) which is regarded as one of the most promising alternative fuels for major combustion systems. **Atmospheric air** was chosen as the oxidant due to its established usage in combustion systems. Dry atmospheric air is composed of 20.9% oxygen, 78.1% nitrogen, 0.9% argon, with trace amounts of carbon dioxide, helium, neon and hydrogen. However, these can be approximated to just 21% oxygen and 79% nitrogen, hence dry air is usually represented by the formula, $O_2 + 3.76N_2$ in chemical equations.

Table 4.1: Summary of flow conditions

Test case #	**1** **(Laminar)**	**2** **(Turbulent)**
Equivalence Ratio, Ø	1.0	1.0
Air Flow Rate (litres/min)	23.8	100.95
CH_4 Flow Rate (litres/min)	2.5	10.6
Bulk flow velocity, U_0 (m/s)	1.15	4.89
Flow Reynolds Number, R_e (Pa. s)	1694.35	7184.03
Adiabatic flame temperature, T_{ad} (K)	2226	2226
Laminar flame velocity, S_L (cm/s)	41	41

4.3 Flame kernel Characteristics

4.3.1 Visualisation of Flame Kernel Development

This section discusses visual characteristics of the propagating flame kernel based on high-speed images acquired using two-dimensional Laser tomography. Figure 4.1a is a sequence of images showing the time evolution of the instantaneous flame kernel obtained for the laminar case while Figure 4.1b shows the evolution for the turbulent case. As shown by the figures, the first frame of both test cases contains an *elliptically shaped* high intensity plasma (usually observed within the first 1-3 µs) which is usually accompanied with shock waves. As observed by many authors [92],[20][100], in the early stage the plasma usually extends more towards the direction of laser beam and the shockwave centroid is usually displaced from that of the plasma. Its initial size can be inferred from the mechanism of electrical breakdown and energy transfer from the laser beam.

The second common feature of both tests observed in frame 2 (about 50 µs later) is a *toroidal-shaped kernel* with two lobes propagating radially upwards and downwards. As observed in the past [20], the toroidal shaped kernel is the results of two contra-rotating vortices (A and B) of different strengths which are generated through interaction of the shock waves and rarefaction waves from the hot plasma. An illustration of the transformation from ellipsoidal spark kernel to a toroidal flame kernel had been explained earlier using superposed images captured between 3 µs and 22 µs (see Figure 2.8a & Figure 2.8b). As earlier described, the inward flow resulting from these vortices leads to the formation of the toroidal flame front. Computer modelling by [138] had shown the generation of the toroidal flame front during simulation of the discharge from an electric ignition source, thus this feature is not unique to laser ignition.

A third common feature observed at 167 µs, is the appearance of a third feature in frames 3, known as *front lobe* which propagates in the direction of the laser as shown in subsequent frames. The generation of the third lobe has been attributed to many factors by past authors. For example, Spiglanin *et al.*, 1995 [92] suggested that it might be due to the initial flow field created by the propagation of radiation transport wave up the laser beam, due to the high rate of energy transfer at the leading edge (i.e., upstream) of the plasma. While it is true that the plasma kernel created by laser breakdown can result in an ionized front propagating toward the laser [155],[20] this is not expected to continue long after the laser pulse had ceased, hence, there is no evidence of this being the source of the front lobe feature.

As earlier observe in the toroidal kernel, the two contra-rotating vortices (A and B) are of different strength with A, growing stronger and B fast decaying. As suggested in [20], this phenomenon is capable of producing a centreline velocity directed towards the laser source, leading to generation of the front lobe (as shown by C). Figure 4.3 clearly illustrates this transformation in the superposed kernel edges formed between 51 and 168 µs. As shown in the figure, after the weak leading-edge toroid has dissipated, the induced gas velocity moves to the right towards the laser beam. This results in a flow of hot gas close to the centreline to the left and its displacement by cold gas from the right. The elongated hot gas kernel comprises the third lobe. Overall, the evolution of the kernel shape is similar for both laminar and turbulent flow cases, however there is large differences in the number and magnitude of local curvatures at each ignition delays due to the extent of interaction with the flow field. The three-dimensional geometric features of the flame kernel have earlier been illustrated (see Figure 2.10).

With respect to the kernel interaction with the surrounding flow field, it can be seen that for the laminar case, the initial kernel shape is unaffected by the flow in the first 168 μs. As previously stated, the appearance of the front lobe results from the asymmetry in the upstream and downstream toroid rings which generates a centreline velocity towards the laser source. This can be observed in the impinging jet flow moving from left to right (as shown by D) towards the laser as the kernel grows. By 668 μs, the jet catches up with the flame front referred to as the front lobe enabling mixing of the upstream and downstream flows originally separated by the flame kernel. This mixing could lead to many scenarios. The first is local quenching which is observed around the front lobe where stretch effects are usually high. The second is a splitting of the flame kernel into two combustion zones as observed in subsequent images. In addition, the kernel becomes distorted in shape due to interaction with the flow. A better picture of the flow-field effect on the flame kernel is observed in the velocity vector plots.

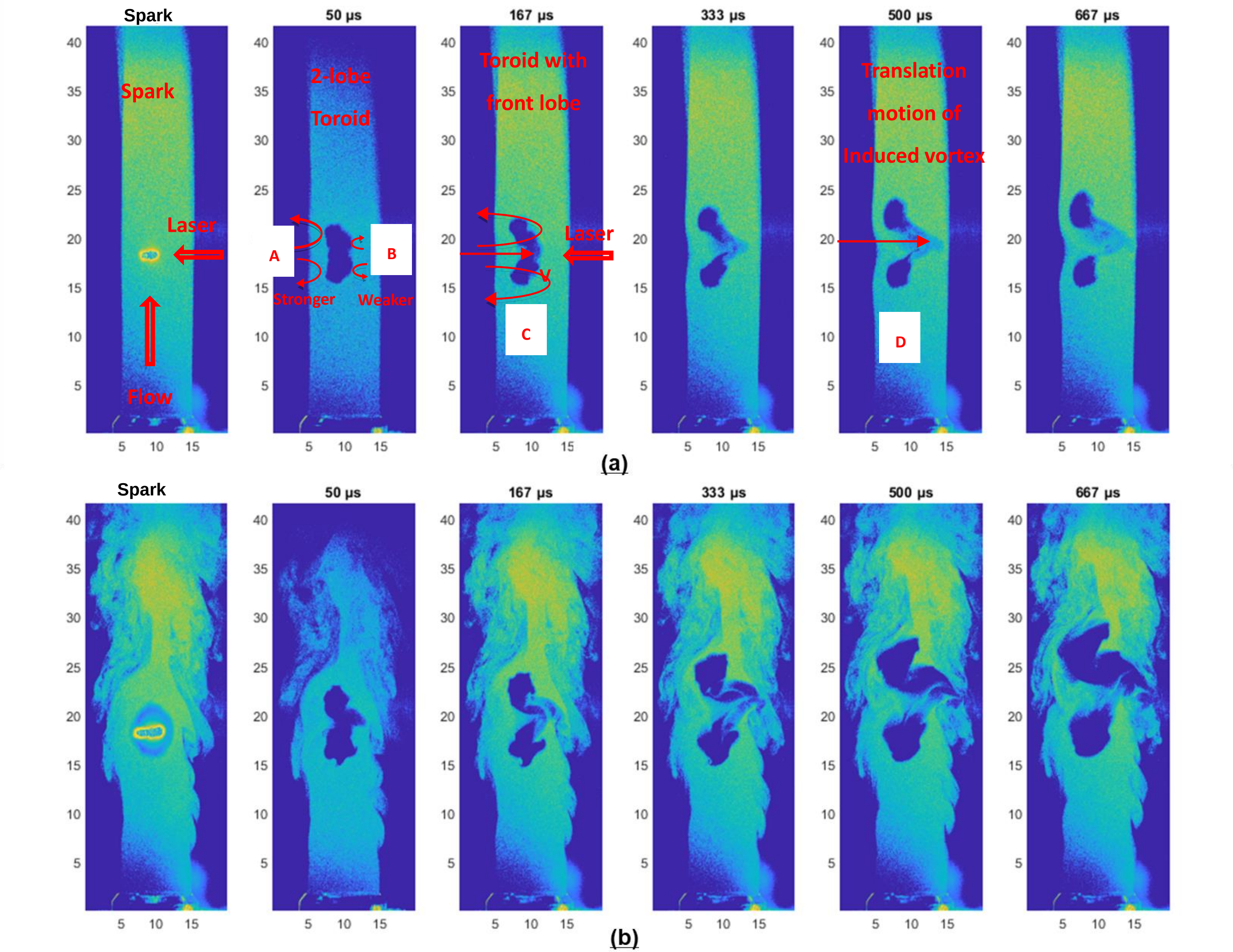

Figure 4.1: Flame Kernel Evolution in: (a) laminar CH_4/Air, and (b) turbulent CH_4/Air

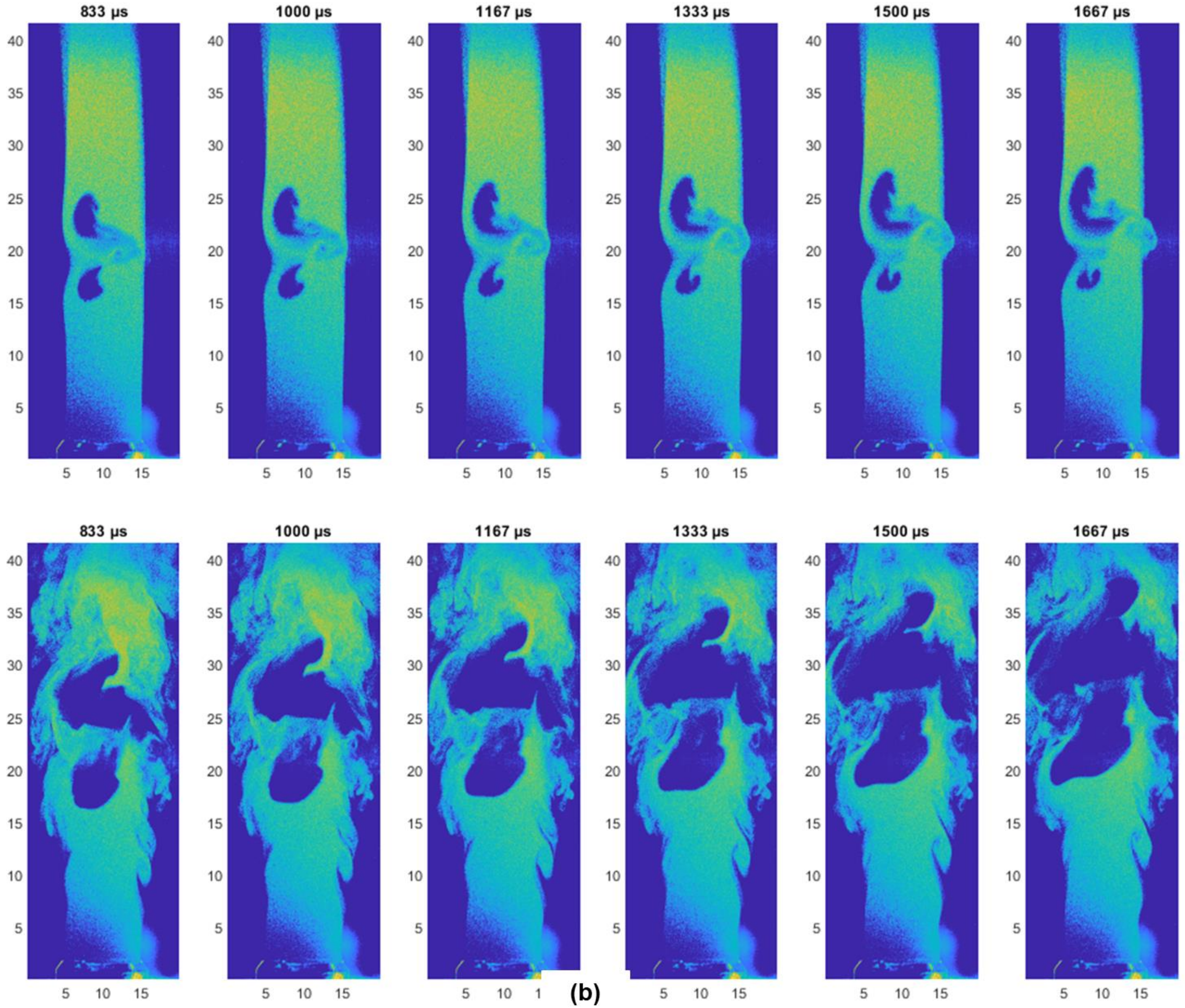

Figure 4.2: Flame Kernel Evolution in: (a) laminar CH_4/Air, and (b) turbulent CH_4/Air {continued}

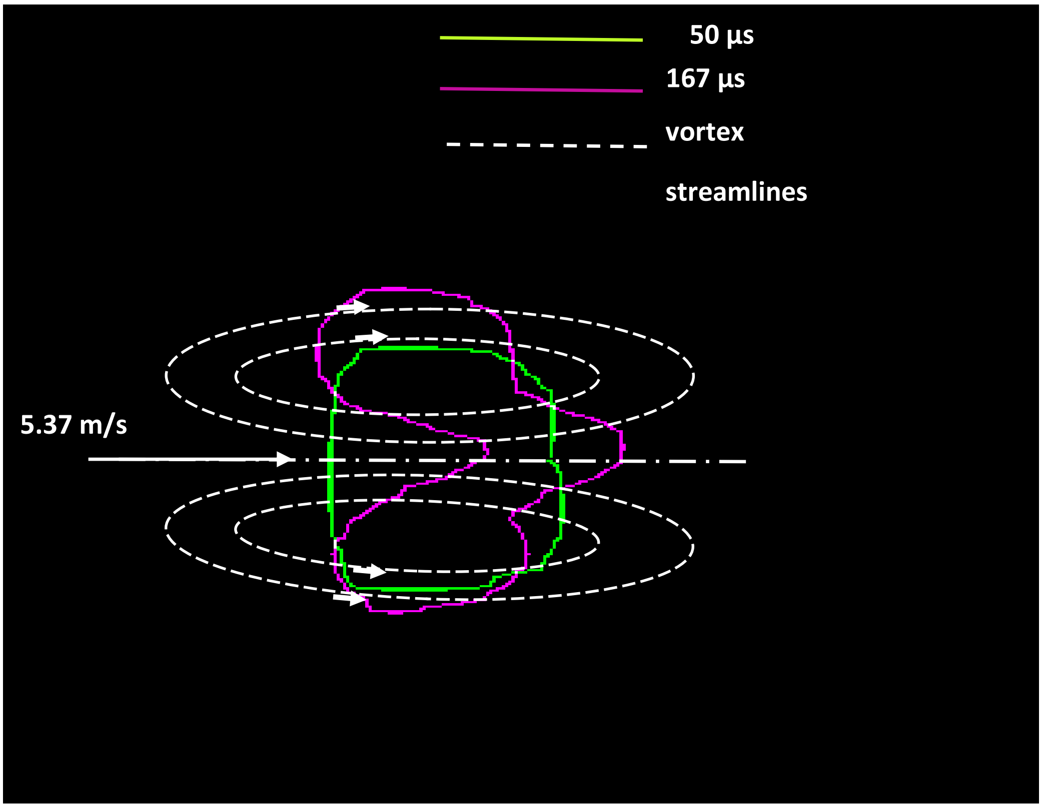

Figure 4.3: Illustration of Front lobe formation

4.3.2 Characterisation of the Flame Kernel

Based on the high-speed images obtained using two-dimensional Laser tomography, geometric characteristics of individual flame kernels were extracted. The first characteristics investigated was the initial size of the plasma for both test cases. As observed in [90], there's nearly an instantaneous growth of the plasma to an initial finite size due to sudden energy deposition at breakdown which generates high pressure in the kernel leading to a rapidly expanding wave. From the equivalent circles of the extracted edges of the initial plasma kernels (i.e. 1 us delay) in Figure 4.4 and Figure 4.5, the initial plasma radii were found to be 1.57 mm for the laminar case and 1.90 mm for the turbulent case. In Table 4.2, comparison is made between the measured values and those predicted using Taylor's Blast wave model (see equation 2.15) assuming 70% spark efficiency. Based on the comparison, the measured radius of the initial plasma for the laminar case is approximately 13.9% less that the predicted radius while that of the turbulent case is 4% more. The observed differences in the initial sizes of the kernel for both conditions despite having similar pulse energy highlights the fact that laser induced gas breakdown is a stochastic process, hence similar pulse energies can produce different spark energies, although the same spark efficiency of 70% has been assumed in the prediction.

Table 4.2: Measured versus predicted initial plasma radius.

Test Case	Measured R (mm)	Predicted R (mm)
1. Laminar	1.57	1.82
2. Turbulent	1.90	1.82

Following determination of the initial sizes of the plasma, the evolution of the flame kernels was characterised based on the *kernel sizes* and *growth rate* at each delay. This time, the kernel size was quantified based on the maximum displacement along the vertical Y-direction (i.e., the flow axis) as shown by Figure 4.4 and Figure 4.5. Figure 4.6 and Figure 4.7 shows the respective sizes and locations (i.e., upstream, and downstream locations) of the flame front along the axis of the flow for both laminar and turbulent flow conditions. As observed in both plots, the initial development of the kernel is marked by rapid growth (i.e., in the first 50 μs), however the growth rate declines before 200 μs. For example, in the laminar flow case, the kernel size increased by 360% (i.e., 1.3 mm to 6 mm) in the 50 μs and by further 8% in 167 μs, while that of the turbulent flow grows from 1.5 mm to 7.5 mm in 50 μs (i.e., 400% increase) and a further 23% increase in 167 μs. This initial rapid growth is mainly due to the gas dynamics of the decaying plasma (i.e., independent of heat release due to chemical reaction) and gives little or no indication of a successful ignition. The large decrease in growth rate by 200 μs shows the dwindling influence of the plasma gas which could mean the end of kernel life for non-igniting mixtures. The second phase of kernel development occurred between 200 μs and 400 μs due to the high stretching of the front lobe. The third phase which starts around 400 μs indicates the end of chemical induction process and the start of actual ignition. During this stage kernel growth is influenced by a combination of gas dynamics and chemical reaction. Around 1.2 ms the influence of plasma gas dynamics is non-existent as kernel growth is mainly as a result of heat release due to chemical reaction. A clearer picture of these stages and the extent of influence of both processes (i.e., plasma gas dynamics and chemical reaction) is shown by the growth rate plots in Figure 4.8 and Figure 4.10. The general trend in growth rate involves reduction from an initial high value to an asymptotic value close to S_L. From the normalized growth rate versus displacement (Figure 4.9 and Figure 4.11), it can be seen that the growth rate drops from an initial stretched value of $1.7S_L$ to about $0.2S_L$ having moved a distance of 10 mm. A similar trend is observed in the turbulent case, however unlike the laminar case there was more fluctuations in growth rate (especially beyond 1 ms) due to turbulence influence.

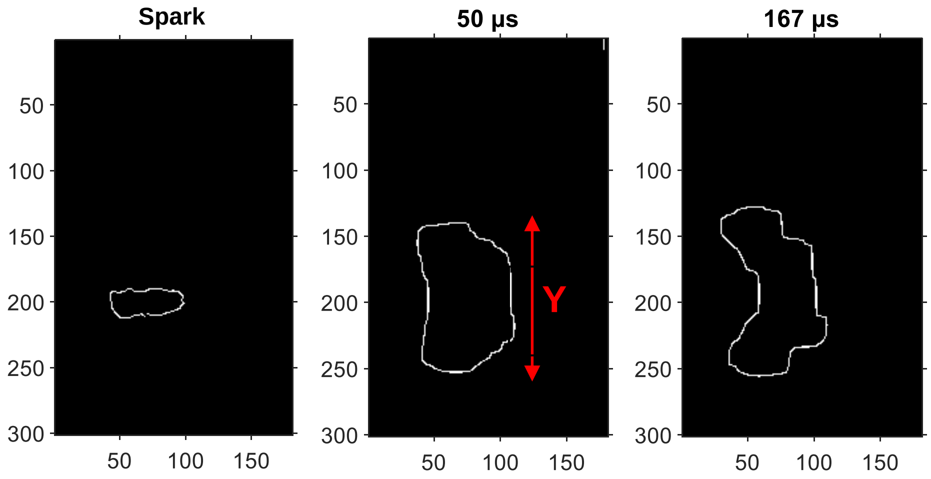

Figure 4.4: Extracted Edges of Flame Kernel in Laminar Flow; Y = max. displacement along flow axis.

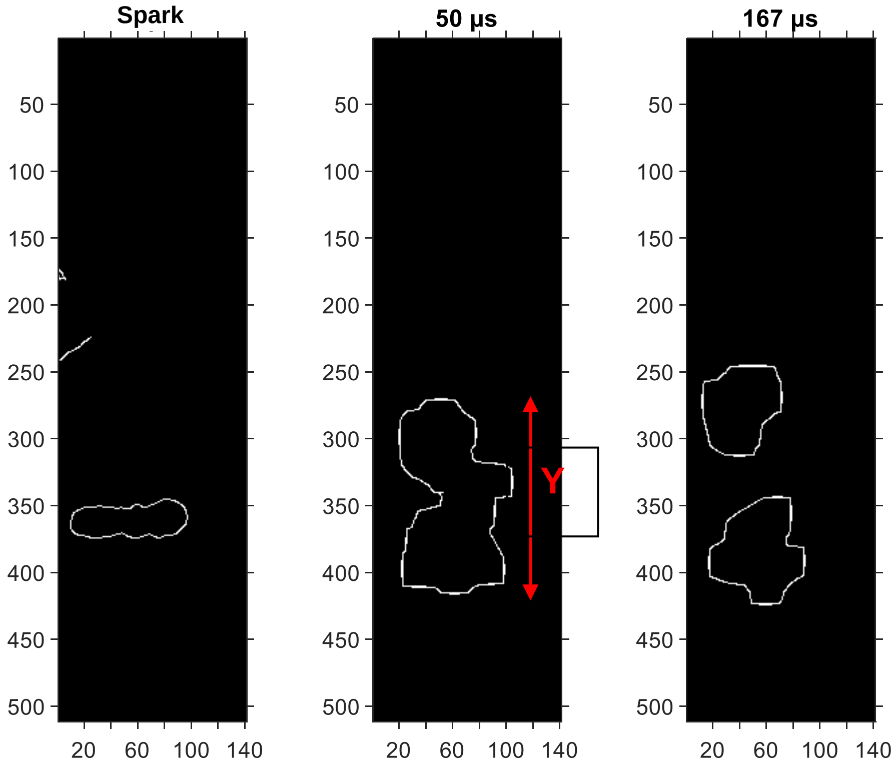

Figure 4.5: Extracted Edges of Flame Kernel in Turbulent Flow; Y = maximum displacement along the flow axis.

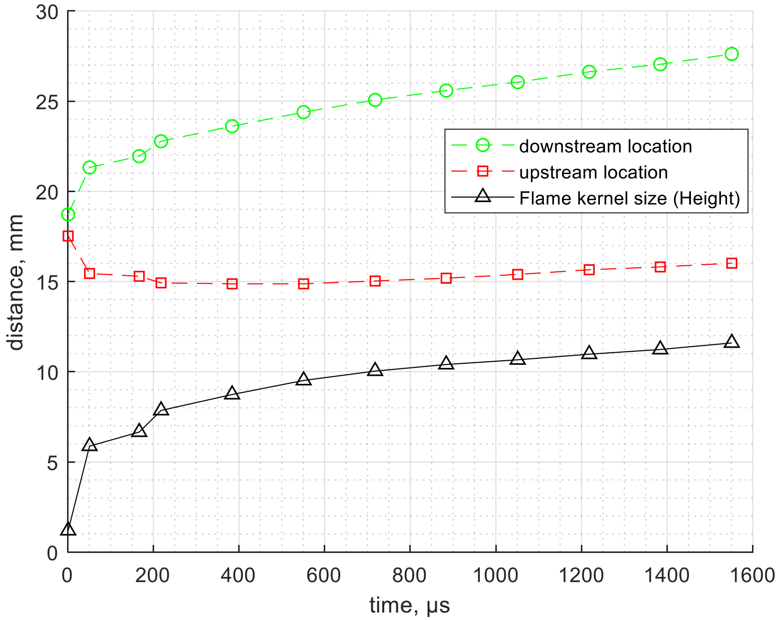

Figure 4.6: Axial Flame Kernel Propagation (Laminar case)

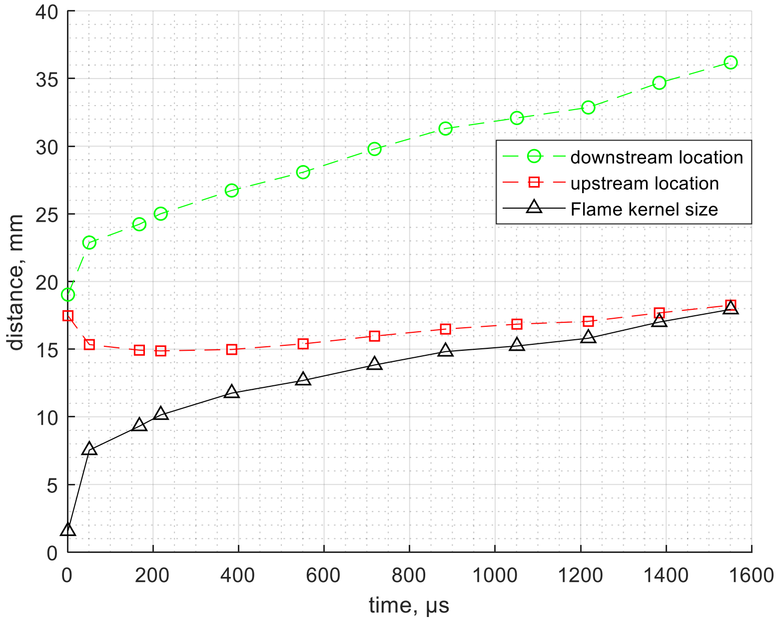

Figure 4.7: Axial Flame Kernel Propagation (Turbulent case)

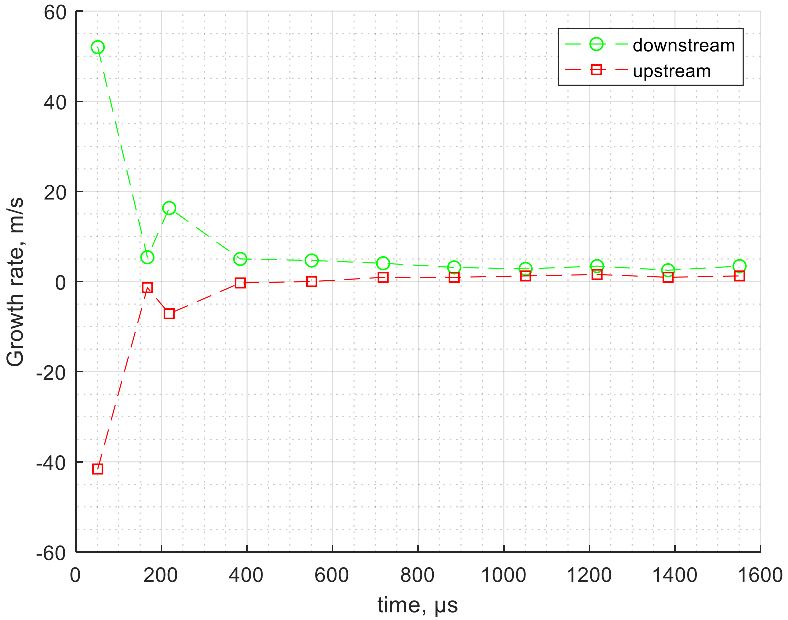

1

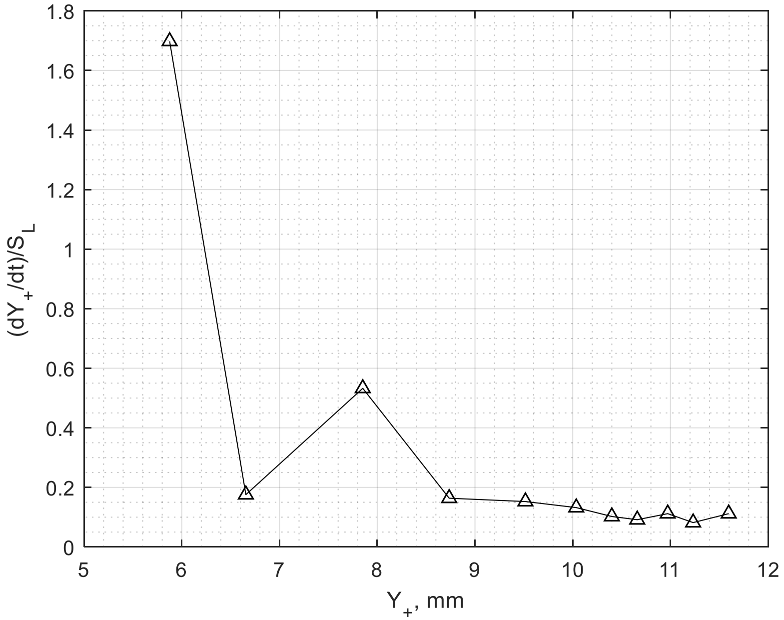

3

2 **Figure 4.8: Axial growth rate of Kernel (Laminar)**

4 **Figure 4.9: Normalised Downstream Growth rate (Laminar)**

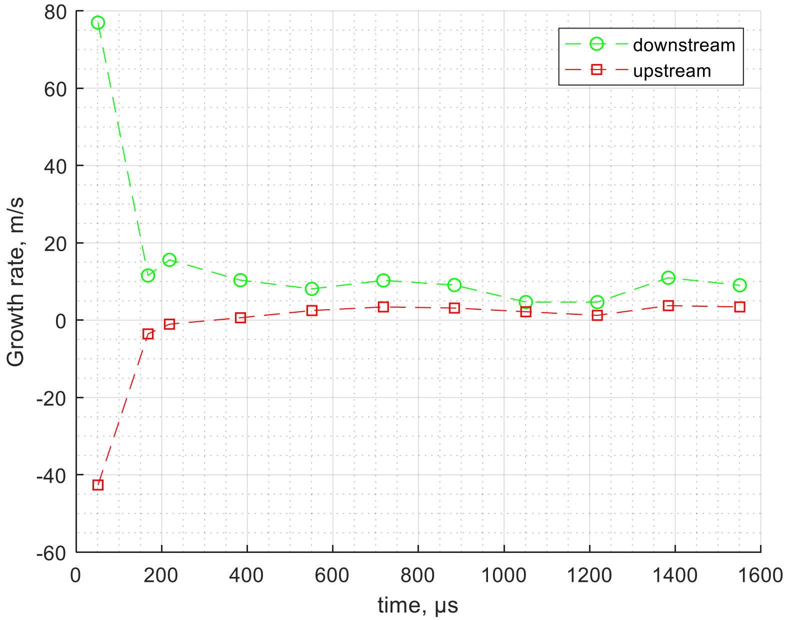

Figure 4.10: Axial growth rate of Kernel (Turbulent)

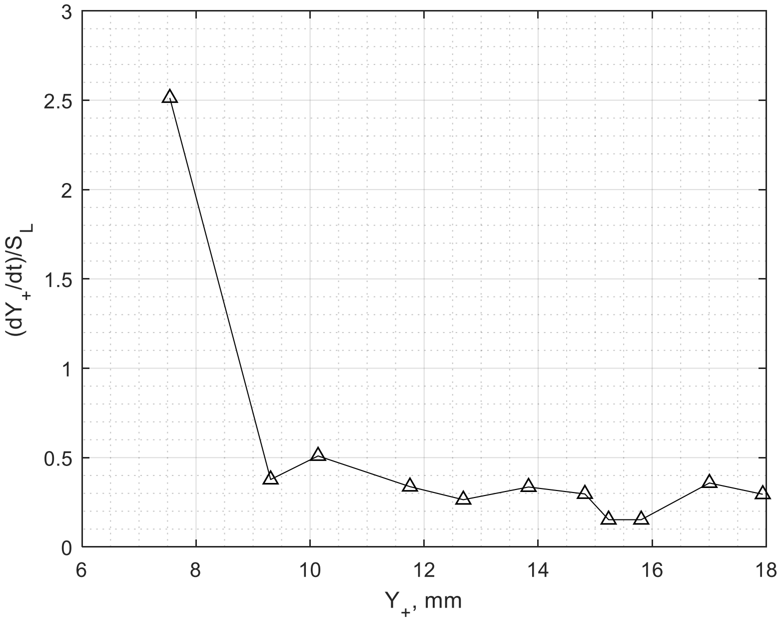

Figure 4.11: Normalised Downstream Growth rate (Turbulent)

4.4 Flow-field Characteristics

4.4.1 Characteristics of the Isothermal cold flow

Figure 4.12a - Figure 4.13a shows the mean velocity vector plots for the laminar isothermal and turbulent isothermal flows whose calculated bulk velocities were 1.15 and 4.89 m/s respectively. As expected, both exhibits a jet-like flow structure with peak velocities in the potential core area which depreciates as you move radially outwards. The jet profile for the laminar flow (Figure 4.14) reveal an axisymmetric parabolic shaped flow structure the velocity along the centreline jet remains nearly constant at all downstream location. In the turbulent flow situation (Figure 4.15), the jet structure is similar, however, the centreline velocity decreased with height. This is due to the jet expansion and interaction with the surrounding air.

Figure 4.12b and Figure 4.13b shows the respective axial turbulence intensities for the laminar and turbulence flows. As expected, the potential core areas were characterized by lower turbulence intensities compared to the outer mixing region. In the laminar case (Figure 4.16), there is nearly a constant low turbulence intensity in core area which persists at different heights considered. In contrast, the turbulence flow experienced higher turbulence (5 -20%) which increased downstream as shown in Figure 4.17.

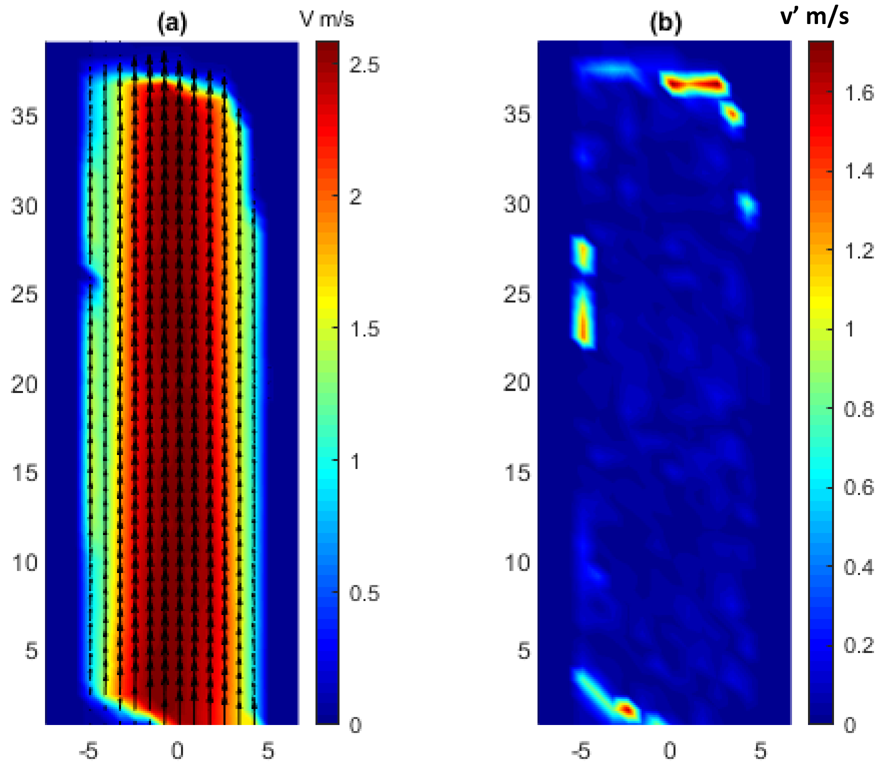

Figure 4.12: Mean flow characteristic of the Laminar jet. (a) Mean velocity b) Mean axial turbulence intensity

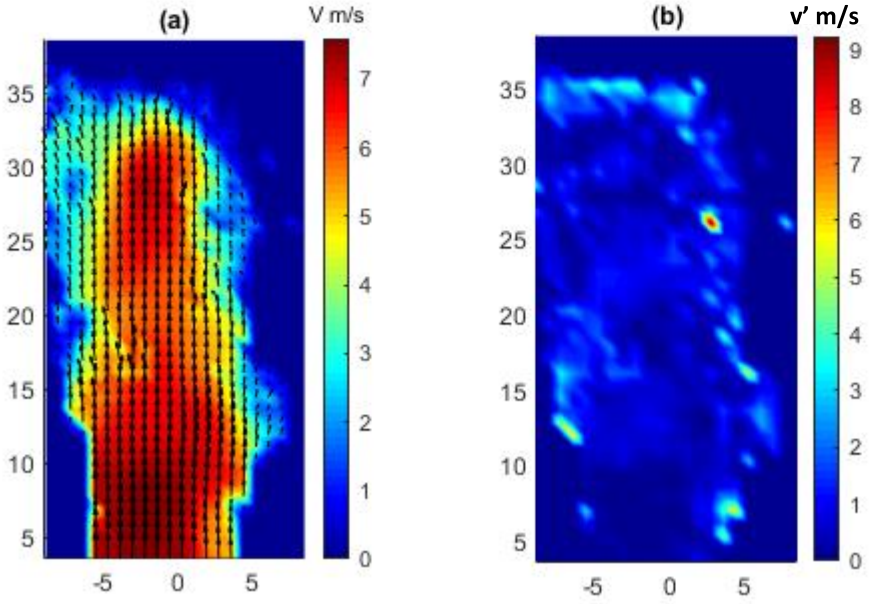

Figure 4.13: Mean flow characteristic of turbulent jet. (a) Mean velocity b) Mean axial turbulence intensity

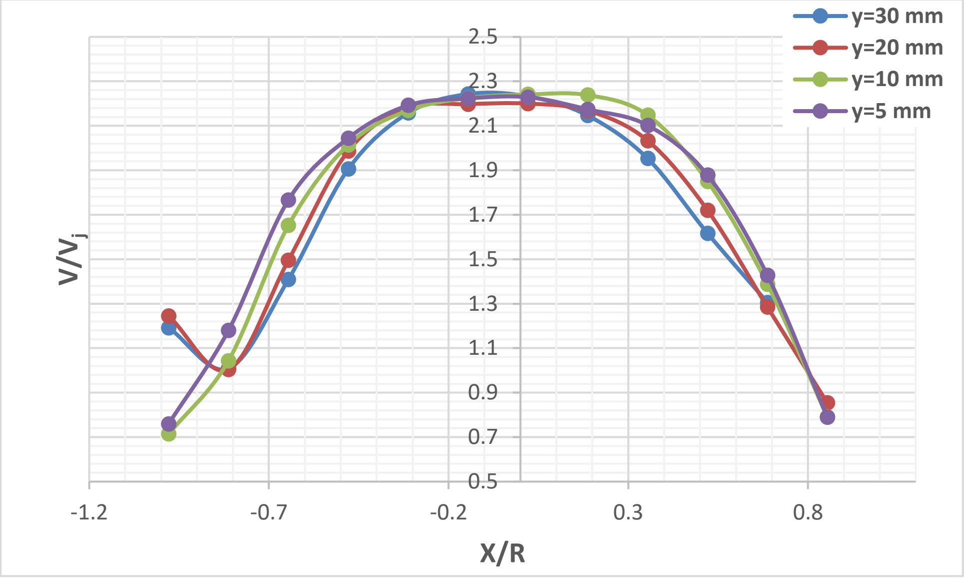

Figure 4.14: Mean Axial Velocity profiles (Laminar flow, V_j=1.15 m/s, R=5 mm)

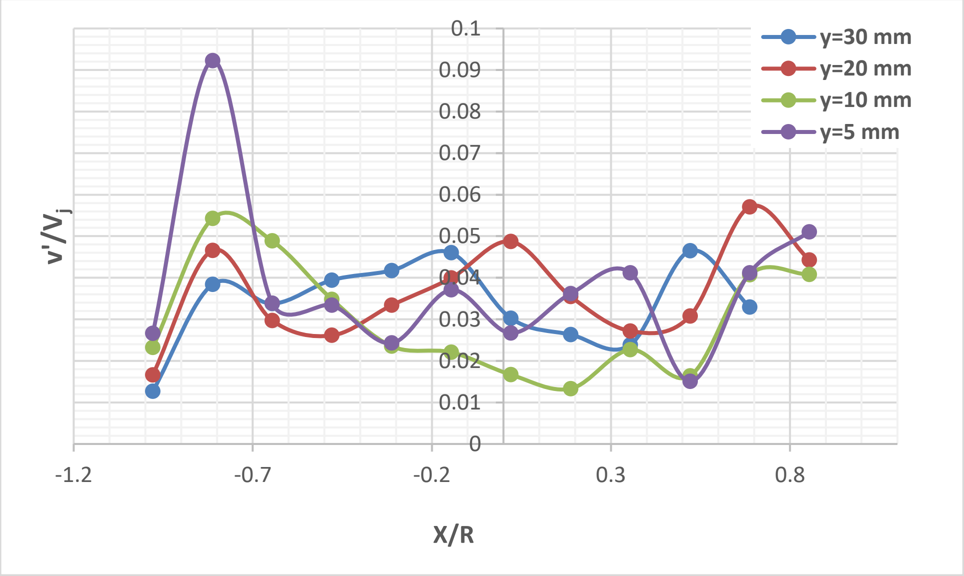

Figure 4.15: Axial Turbulence Intensity profiles (Laminar, V_j=1.15 m/s, R=5 mm)

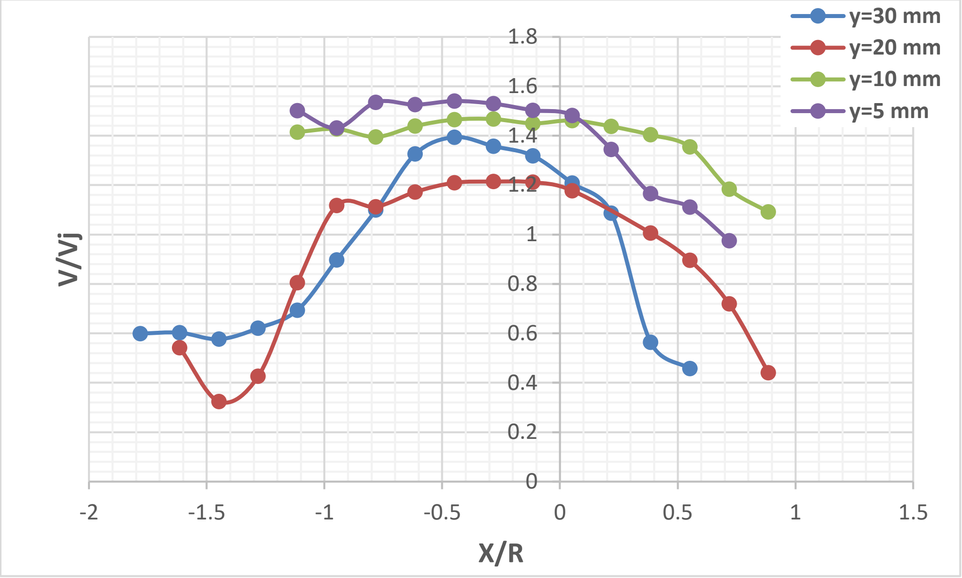

Figure 4.16: Mean Axial Velocity profiles (Turbulent flow, Vj=4.89 m/s, R=5 mm)

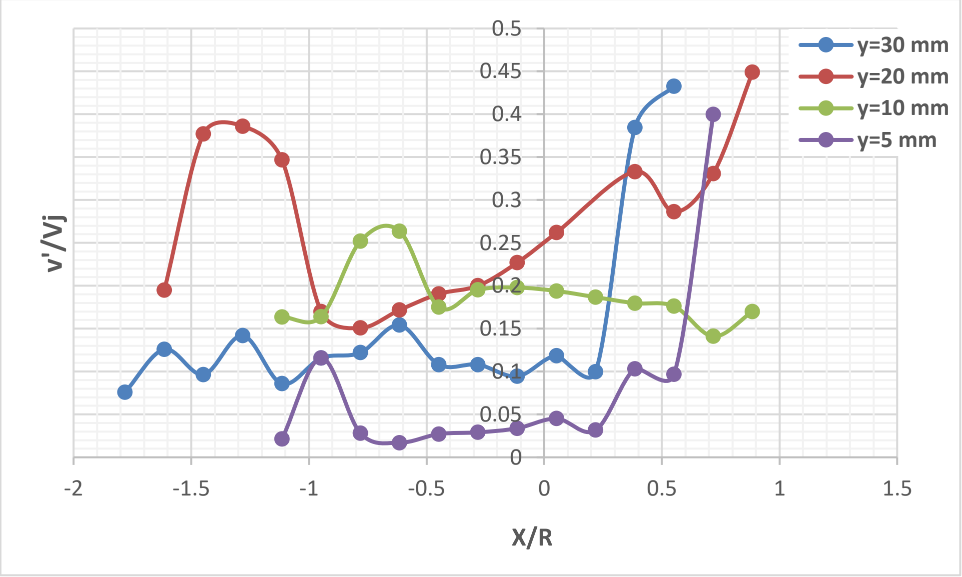

Figure 4.17: Axial Turbulence Intensity profiles (Turbulent flow, Vj=4.89 m/s, R=5 mm)

4.4.2 Characteristic of the reacting flow

Figure 4.18 is the instantaneous velocity vector fields of the burner flow at three different stages of the flame kernel development (217, 550 and 1217 μs) for the laminar case. The first main observation in the first frame (at 217 μs) is the zero-velocity region near the kernel trailing edge due to rotation effect of the vortex generated as the front lobe moves towards the laser. This vortex motion is also responsible for the swirling flow observed due to mixing of the upstream and downstream flow.

The second observation is the significant difference in the velocity field of the upstream and downstream flow. As observed in the three frames, a conspicuous peak in axial velocity (about 3 m/s) is noticed in the downstream flow just ahead of the flame front. This peak is caused by the acceleration of the flow due to rapid thermal expansion of the flame kernel and had been observed previously in a fully developed flame [156]. Additionally, the velocity vectors downstream appear vertical as in the isothermal laminar flow (before ignition). In contrast, the axial velocity of the upstream flow just behind the flame front is significantly reduced especially in the first two frames. The differences in behaviour of the both the upstream and downstream flow is further illustrated by axial profile plots in Figure 4.19. By further investigation of the flow field changes with development of the flame kernel, it was discovered the initial jump in downstream peak velocity decreased with time as the kernel grew in size until it approaches the isothermal flow field velocity (see Figure 4.20). Likewise, the initial drop in upstream velocity increased with as the kernel grew developed until it attains the isothermal flow field velocity (see Figure 4.21)

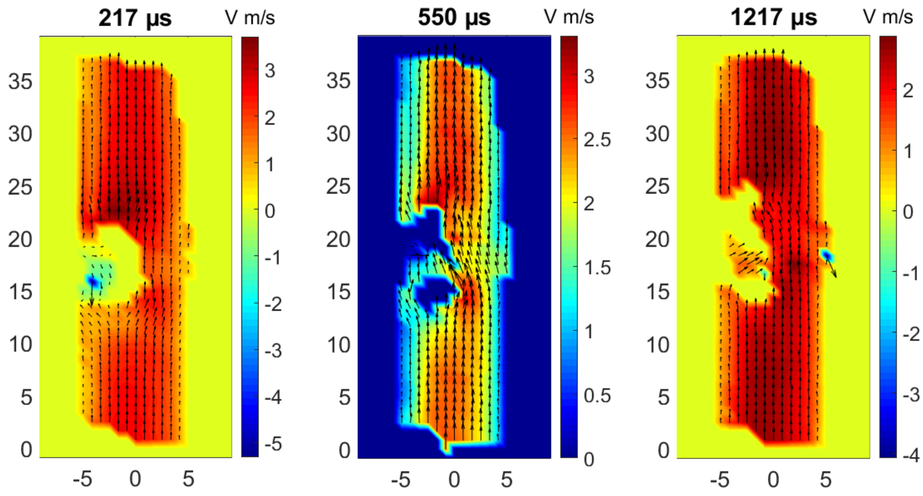

Figure 4.18: Instantaneous Velocity Vector plots in Laminar Reacting flow

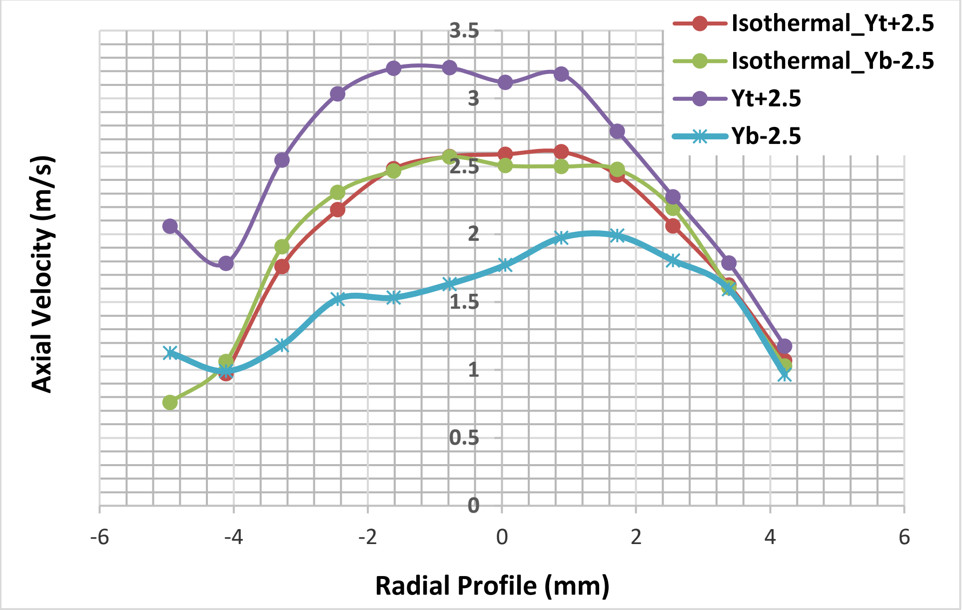

Figure 4.19: Profiles plot of Axial Velocity at 217 μs delay compared with the Isothermal flow. [Yb,Yt] - Upstream and Downstream of Flame front

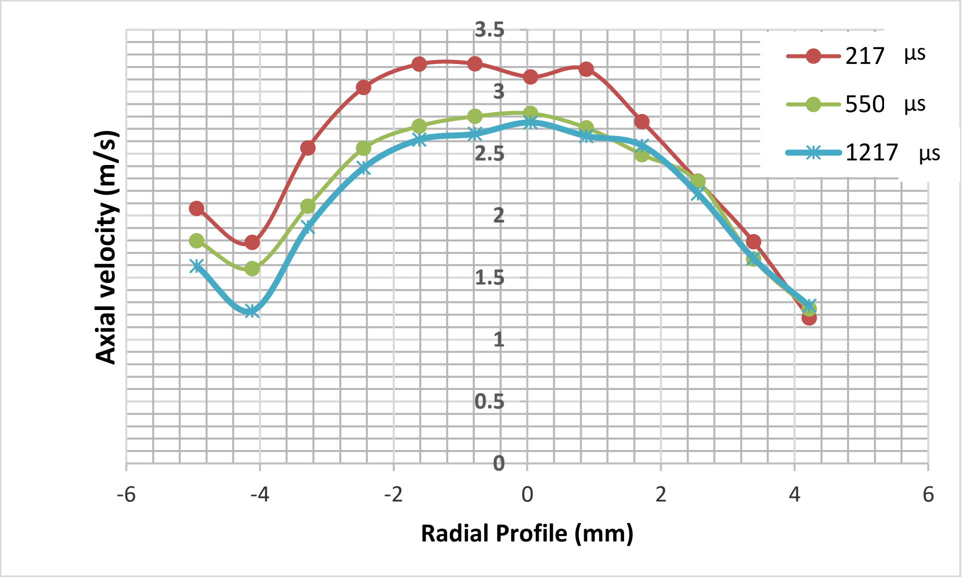

Figure 4.20: Radial profiles of Axial Velocity at location (Yt+2) mm downstream

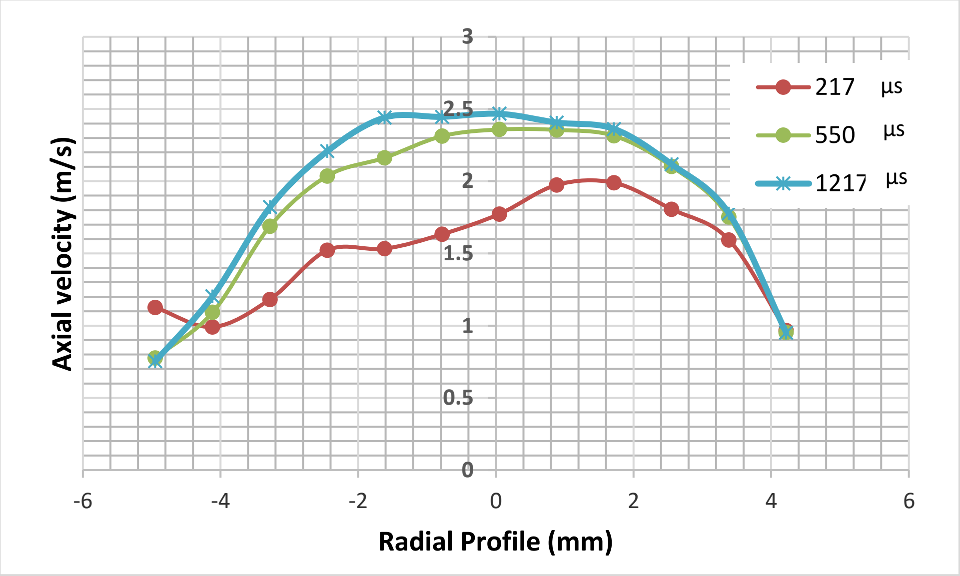

Figure 4.21: Radial profiles of Axial Velocity at location (Yb-2) mm upstream

4.5 A note about the results

It is important to mention that there were gaps in data set owing to limitations. An obvious discrepancy is the lack of symmetry in the radial profile of the axial flow velocity vectors. This resulted from calibration errors. As earlier explained in section 3.51, setting up the High-speed PIV system required a target object of known dimensions which was captured before the actual experiment commenced. Using this target capture dimensions, subsequent images were scaled to determine the x-, y- dimensions in both pixels and mm. The calibration of the flow field also involved setting up the central axis of the flow which ideally should be along the centre of the burner diameter. Therefore, the use of a target object for this exercise instead of an actual flow no doubt created the discrepancy in the measured data.

Another limitation encountered is the fact that only single capture preliminary results were used for this investigation. It was originally planned to acquire a series of cycle ignition measurement which will be compared and average to obtain a true picture of the flame kernel development. However, this was not possible due to equipment breakdown. After months of waiting, the equipment was repaired but then moved to other projects which made it difficult to conclude the experiment coupled with time limitation. It is therefore advised that the results reported in this chapter be used with utmost caution.

4.6 Conclusions

In this chapter, results of the instantaneous flame kernel characteristics and its surrounding flow velocity field were reported based on instantaneous high-speed images acquired during laser-induced ignition of stoichiometric Methane/Air mixture. A summary of the main findings is given below:

- The flame kernel visualization study using laser sheet tomography provided insight on the changes in the geometric features of the flame kernel during its development. At ignition, an elliptically shaped plasma of hot gas was first observed. This then developed into a two-lobe toroidal structure (which is symmetric about the laser axis) by 50 µs. The next feature at appeared before 167 µs was a front lobe resulting in an asymmetric toroidal flame kernel. The images also reveal how the front lobe results from the motion of a centreline jet flow generated by large contra-rotating upstream and downstream vortices.

- Variations between the measured initial plasma radius (at about 1 µs) and the Blast wave theory showed some differences with respect to the flow. For example, in laminar flow case, R was 13.9% less while in the turbulent flow case R was 4% more.

- The displacement locations of the upstream and downstream flame fronts (i.e., Y_+, Y_-) differed depending on the flow condition. For example, in the laminar flow mixture, the kernel flame front locations showed a growth curve nearly symmetric about the laser axis, while for the turbulent case, this symmetry is lost due to displacement of the kernel centroid. In addition, the spatial evolution of the kernel height (Y) shows that in the laminar flow, Y reaches the burner diameter (i.e., 10 mm) in about 0.7 ms while in the turbulent flow, it took only 0.3 ms to reach this height.

- Changes in axial growth rate of the kernel show there were three key development stages. From an initial shock speed 23 times the unstretched laminar value (S_L), the kernel decayed in stages to a stable speed close to S_L in 1 ms. A reasonable deduction from this is that the initial growth was dominated by induced gas velocity of the shock waves, the second phase of growth was the result of both the induced gas velocity and chemical reaction while the final phase was predominantly due to reaction chemistry.

- The velocity field visualization obtained by PIV analysis revealed key information on the structure of the flow field in both reacting and non-reacting state. Prior to ignition, the axial velocity plots reveal an axisymmetric flow structure with maximum velocity in the potential core area which decreased radially to a minimum near the flow edges. In the laminar flow, the axial velocity profiles did not change significantly with height, however in the turbulent flow the velocity profiles decreased with increase in height. Unlike the flow velocity, the turbulence intensity was stronger in the mixing region (i.e., near the flow edges) than in the potential core (i.e., centre of the flow). Moving downstream, the general trend reveals an increasing intensity, already this was somewhat irregular in the turbulent flow.

- Following ignition, the observed flow field velocities were different from the isothermal case. Due to the rapid thermal expansion of the flame, an increased axial velocity peak is observed in the downstream region just ahead of the flame front. Upstream the flow profile shows change in near the flame front which caused a skew in the symmetry of the developing flame kernel. In contrast, a reduced axial velocity peak is observed in the upstream region just behind the flame front. Further investigation of the radial profiles of the axial velocity revealed that this variation in velocity peak existed only within certain distances (below 2.5 mm) from the flame fronts.

Chapter 5 OH* chemiluminescence characteristics of the Flame Kernel and its dependence on physical parameters.

5.1 Introduction

This chapter presents further characterisation of the laser-ignited flame kernel through analysis of the mean OH* chemiluminescence images and its dependence on two physical parameters: pulse energy and flow velocity. The study is divided into three main sections. The first section begins with qualitative characterisation of the flame kernel based on the mean chemiluminescence images obtained at various ignition delays. Further edge extraction of the mean kernel images enabled quantitative description of the kernel characteristics by the flame front location and its propagation rate. In addition, the relative changes in OH* concentration with time was described from the integrated and maximum OH* intensity. While kernel location is useful for predicting the burning rate, the relative OH* concentration gives information about the heat release rate due to chemical reaction. The second included investigation is the effect of pulse energy on the evolution of the flame kernel structure for the flow condition. Finally, the flow velocity effect on the kernel properties were investigated in section three.

5.2 Test conditions

Table 5.1 gives a summary of the test conditions for the three investigations conducted in this chapter. As shown in the table, the initial run (test 1) was conducted with laminar methane-air mixtures ($\emptyset = 1.0, U_0 = 1.15\,\mathrm{m/s}$) to gain a general overview of the flame kernel development characteristics. This was followed by a study of the pulse energy effects (test 2) and finally a study of flow velocity effects (test 3) was conducted. For all the tests, methane-air mixtures of constant stoichiometric composition were used.

Table 5.1: Summary of test conditions

Test	**1**	**2**	**3**
Flow parameters:			
Equivalence Ratio, Ø	1.0	1.0	1.0
Air Flow Rate (litres/min)	23.80	23.80	23.80, 42.86, 61.90, 71.43
CH_4 Flow Rate (litres/min)	2.5	2.5	2.5, 4.5, 6.5, 7.5
Bulk flow velocity, U_0 (m/s)	1.15	1.15	1.15, 2.08, 3.00, 3.46
Flow Reynolds Number, R_E (Pa. s)	1694	1694	1694, 3050,4405,5083
Adiabatic flame temperature, T_{ad} (K)	2226	2226	2226
Laminar flame velocity, S_L (cm/s)	41	41	41
Nitrogen co-flow (litre/min)	3	3	3
Laser parameters:			
Pulse energy, E (mJ)	32	32, 64, 96, 128	32
Laser frequency, f (Hz)	2	2	2
Laser wavelength, λ (nm)	1064	1064	1064

5.3 General OH* chemiluminescence characteristics of the flame kernel

5.3.1 Visual characteristics of the Flame Kernel

Before studying the parametric dependence, it was necessary to first characterise the flame kernel based on the mean OH* chemiluminescence images acquired for a single test condition [CH_4/Air ($\text{Ø} = 1.0, U_0 = 1.15\frac{m}{s}$), Ep=32 mJ].

The first observation from the acquired images is the changes in kernel shape as it develops from a two-lobe symmetric toroid to a three-lobe asymmetric toroid. Figure 5.1 shows the sequence of mean OH* chemiluminescence images acquired between 50 µs and 1.5 ms time delays with respect to the ignition pulse. The first kernel image observed at 50 µs is a butterfly-shaped (or two-lobe) toroidal structure propagating symmetrically above and below the laser axis. Previous studies observed similar shape for both laser ignition and electric spark ignition [92],[100]. The origin of this feature has been attributed to an induced inward flow resulting from an over-expansion of the shock wave, emanating outward from the region of the discharge at a very high velocity [138]. From 100 µs onwards, a third lobe (a.k.a. front lobe) begins to emerge from the edge of the kernel facing the incident laser beam thereby leading to an asymmetric structure. Previous studies [92],[100] has shown that this third lobe is a unique feature of laser ignition and it propagates towards the direction of the incident laser. Hence, for the first 1.5 ms, the kernel shape is predominantly a three-lobe toroid with rapid growth along the central axes of the lobes. Figure 5.2 shows that beyond 1.5 ms, local quenching occurs at the front lobe while growth is continuous along the symmetric (i.e., upper, and lower) lobe axes. The resulting final shape of the kernel is similar to that of a typical flame ball propagating mostly in the upstream and downstream directions of the flow. In this study, the flame is prevented from stabilizing to allow repeated measurement. Therefore, the flame front growth downstream is enhanced by the flow while the flame front growth upstream is restrained by the flow. In addition, propagation of the flame in both directions is marked by changing radius of curvature.

The second observation from the images is the progressive change in reaction intensity and distribution of reaction zones within the kernel as it evolves. Between 50 μs and 100 μs, the peak intensity of OH* dropped from 3800 AU to 2300 AU due to cooling of the hot gases which make up the initial kernel. At 150 μs, a new peak in OH* intensity occurs which is the first indication of the kernel survival. Subsequent kernels showed a continuous decay in peak OH* until a minimum peak is attained beyond which the peak rises again due formation of a self-sustained flame. Further observation the image colourmap shows that the distribution of the OH* within the kernel differs at different stages of development. At the initial stages (50 - 300 μs), the OH* is evenly distributed, hence the kernel is composed of an isotropic reaction zone. A possible explanation for this is that initial kernel growth is predominantly due to the presence of hot gases which originated from the initial hot plasma. At the mid stage of development (450 - 1500 μs), the distribution of OH* reveals the kernel is composed of anisotropic reaction zones with peak intensity within the middle region. A possible explanation for this is that kernel growth during this period is the result of both induced gas flows and chemical reactions. This could also be the result of mixing of the reaction zone with the flow due to vortex induced motion which may lead to multiple flame fronts within the kernel. As shown in Figure 5.2, the colourmap of the late kernels (3 – 10 ms) shows that the reaction zones (i.e., flame fronts) were concentrated at the edges. Unlike the early kernels, the inner region of low intensity may indicate the presence of burnt gases. These observations also give an idea of the two-way interaction involving the flame-flow mixture and flame-burnt products.

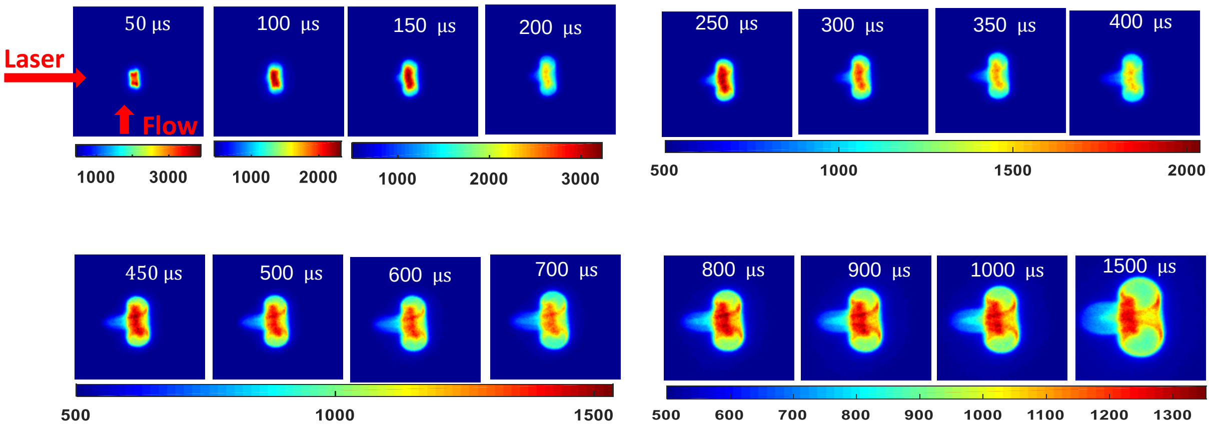

Figure 5.1: Mean OH* chemiluminescence images showing 50 – 1500 μs Kernel Development (Image FOV: 28x28 mm^2)

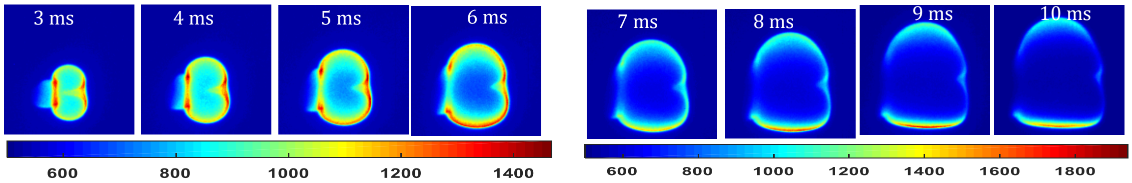

Figure 5.2: Mean OH* chemiluminescence images showing 3 – 10 ms Kernel evolution (Image FOV: 56x56 mm^2)

5.3.2 Analysis of the Flame Kernel Geometric Characteristics

From the extracted edges of the mean OH* chemiluminescence images, geometric analyses were performed to ascertain the growth of the flame kernel with time. The first characteristics investigated is the size and its flame front location in both vertical axis (i.e., flow axis) and horizontal (i.e., laser axis). Figure 5.3 is a schematic of the measurement plane showing the locations of the flame front relative to the spark location. Y_+Y_- represents the flow axis while X_+X_- represents the laser axis.

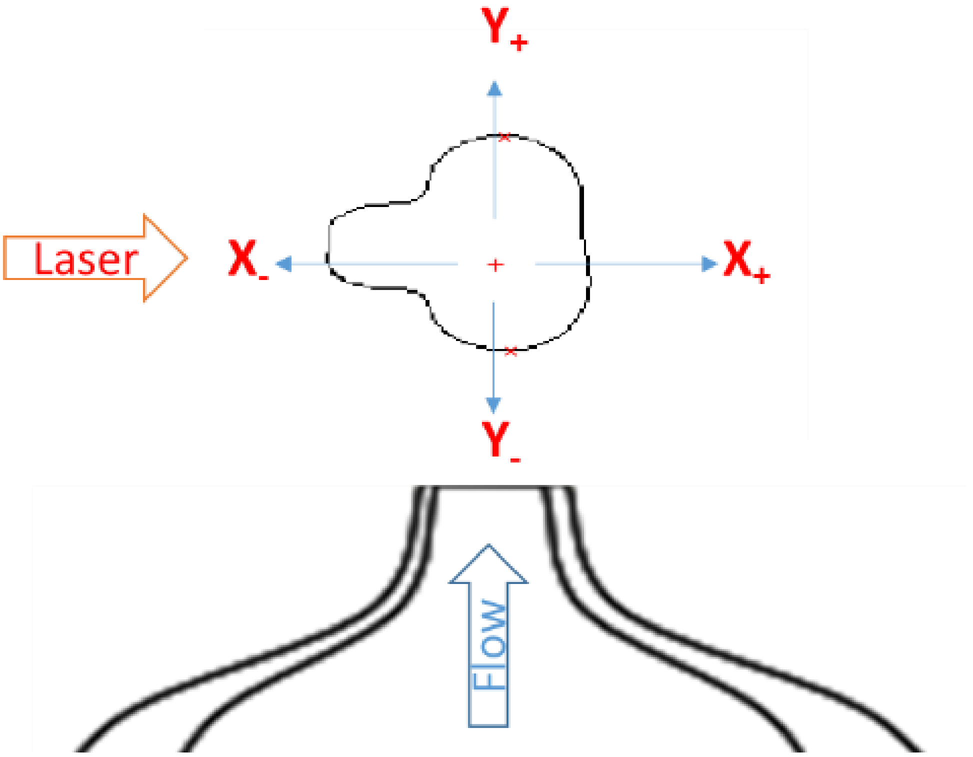

Figure 5.3: Measurement plane showing the flow and laser axes of the Flame Kernel

Figure 5.4 shows the displacement of the flame front tip from the ignition point downstream and upstream the flow axis. Following ignition, the displacements of the upstream and downstream flame fronts reveal a gradually decaying growth up to 0.8 ms when the growth become steady. From this point the downstream flame front maintain a steady linear growth. Likewise, the upstream flame front maintained a steady linear growth until it reached its maximum displacement of 12 mm in about 7 ms. The combined growth of the flame fronts (i.e., Y_+ and Y_-) reveals a nearly symmetric growth about the laser axis. This is however not the true situation as revealed by the two-dimensional scatter plot of axial flame tip displacement (Figure 5.5).

Figure 5.6 shows the displacement of the flame front tip from the ignition point along the laser axis. Unlike the axial flame fronts, the transverse displacement of the fronts (i.e. X_+ and X_-) is clearly non-symmetric. This is expected due to the presence of the front lobe. Following ignition, the displacements of the flame fronts along opposite directions of the laser axis is characterised by an almost linear growth with sudden change in slope at specific instances. For example, the displacement of the flame front away from the laser was marked by sudden decline at 0.1 ms, thereafter the growth was almost linear with very little decay. Kernel was very rapid during the first 1.5 ms. Likewise, displacement towards the laser was relatively steady until 1.5 ms, when an abrupt change in slope occurred and then a steady linear growth onwards. The abrupt change in the slope of X_ at 1.5 ms occurred because of local quenching due to high stretching of the front lobe.

To further compare growth along both axes, the dimensions of the kernel were evaluated from the differences in kernel tip displacement. Figure 5.7 compares the evolution of the kernel height (H) with its width (W). According to the figure, only small differences were observed in the first 1.5 ms between the kernel dimensions with H slightly greater than W. The small difference in the early development is due to the presence of the front. In past studies [97], this has been attributed to the asymmetry in the dimensions of the initial spark kernel. This knowledge may be useful when deciding the best orientation of the incident laser beam for a particular combustion system. Beyond 1.5 ms, the difference between H and W became increasingly wider due to flow velocity effects. In the current setup, it takes about 2 ms for the kernel to reach the spatial size of the burner (i.e., diameter =22 mm) along the flow axis while it takes about 2.5 ms to reach the same dimension along the laser axis.

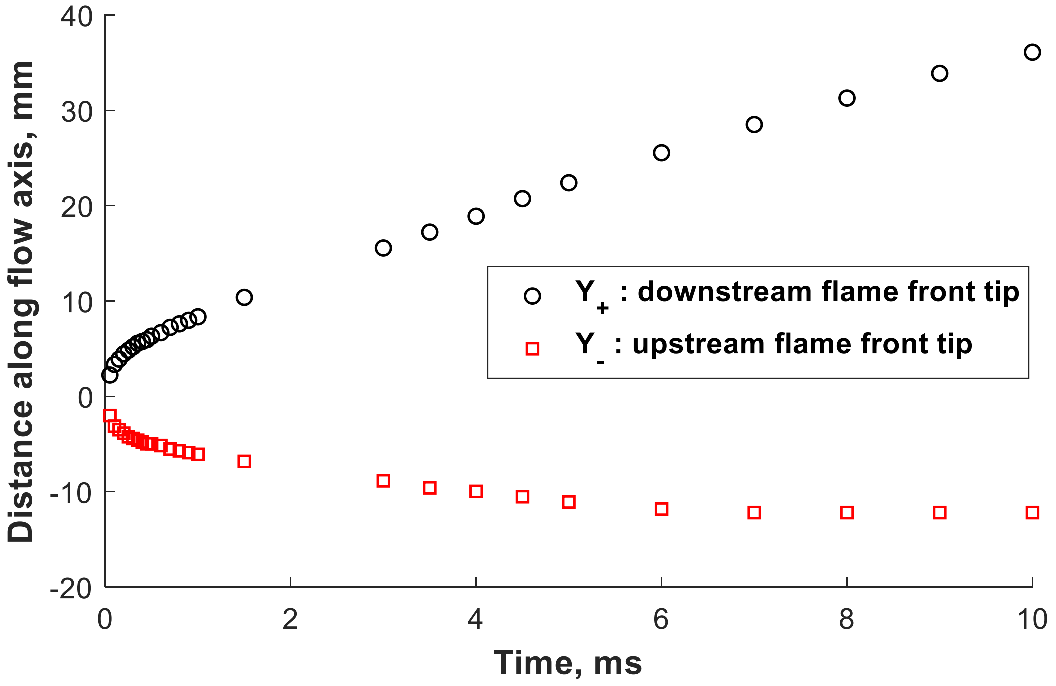

Figure 5.4: Displacement of the flame front tip along flow axis

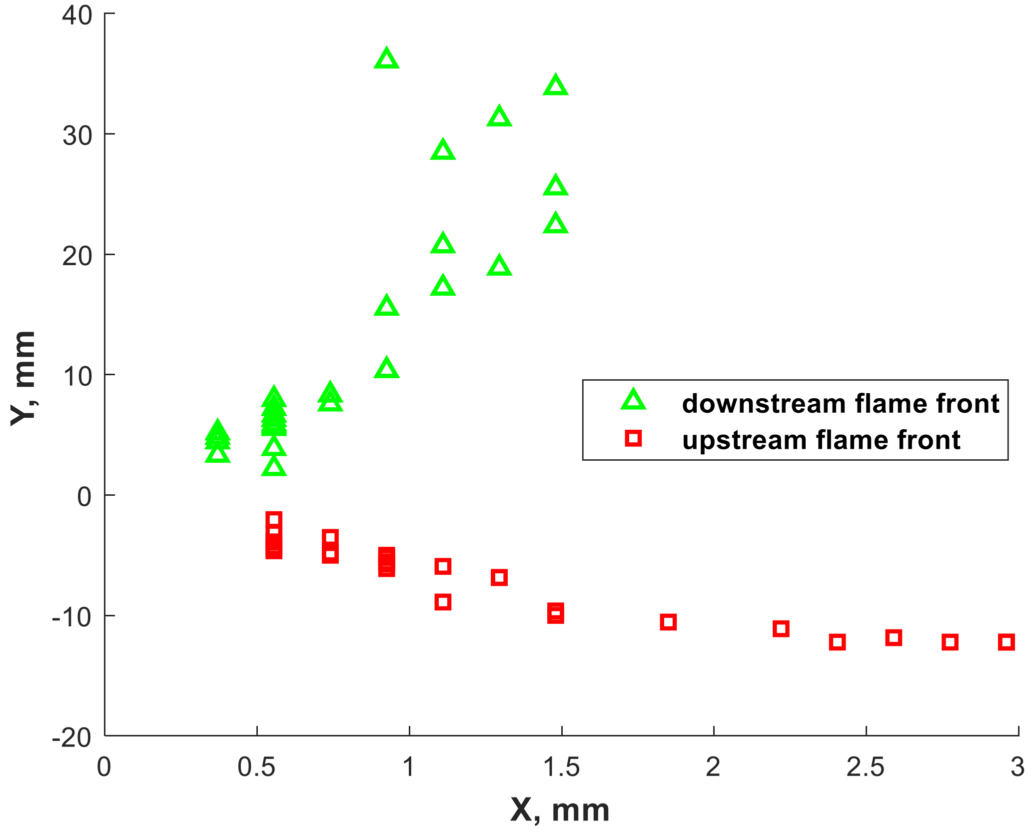

Figure 5.5: Two-dimensional scatter plot of axial flame front tip

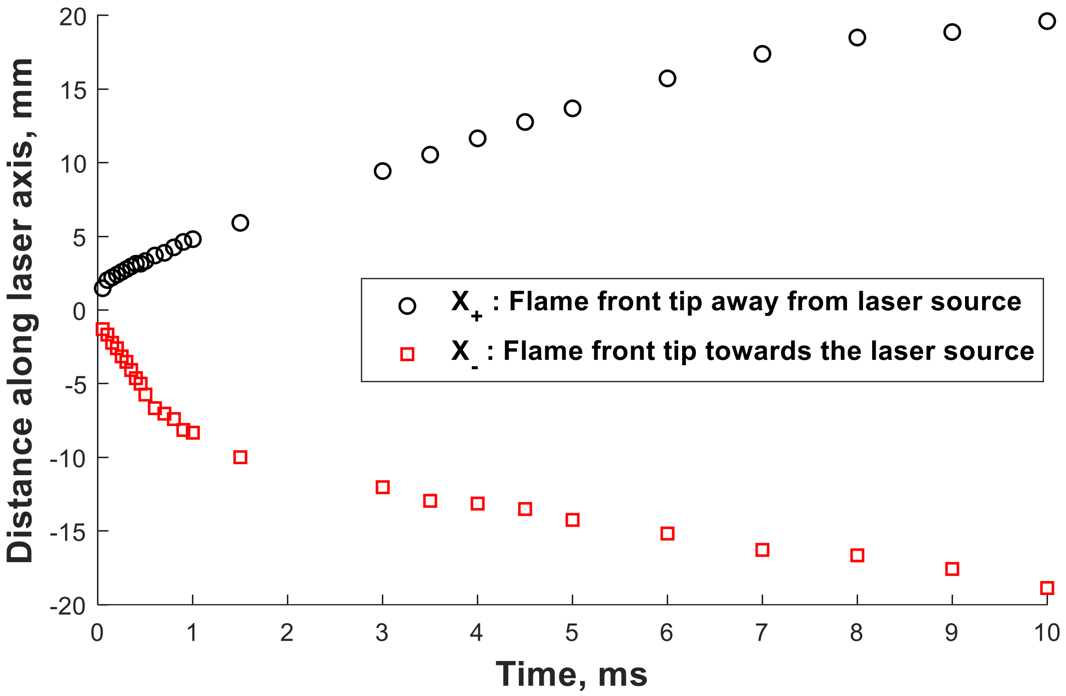

Figure 5.6: Displacement of the flame front tip along Laser axis

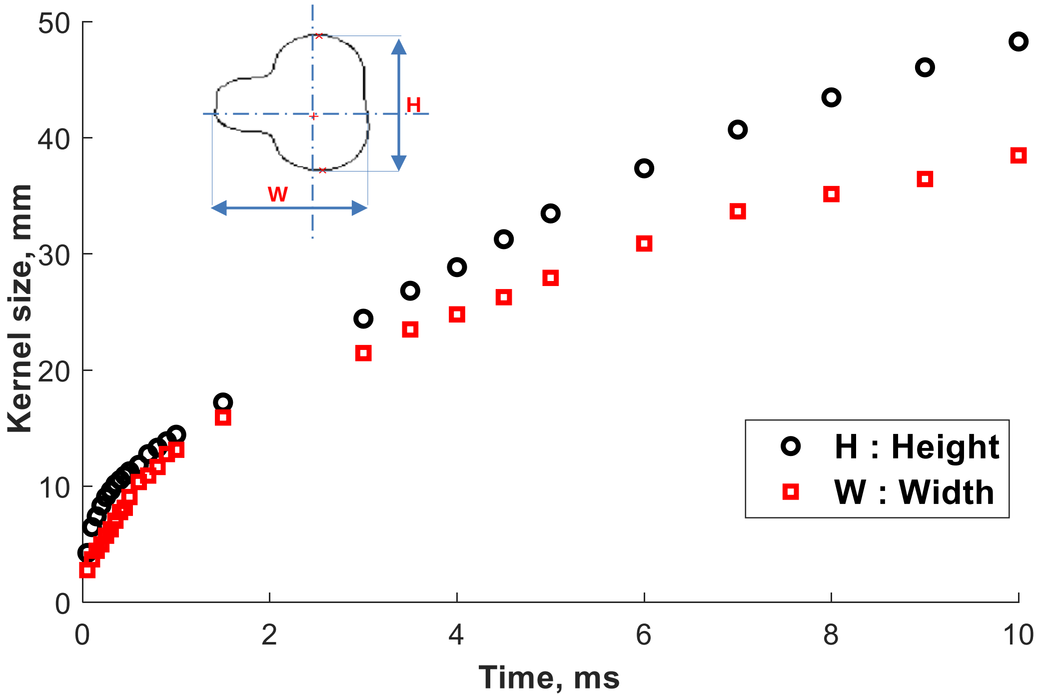

Figure 5.7: Evolution of the Flame Kernel dimensions

Next, an analysis of the growth rates of flame front tips was performed from the measured tip displacements. To determine the kernel growth rates, the time derivatives of the tip displacement were obtained according to the following equations:

$$\mathrm{S}_{y+} = \frac{dY_+}{dt} \tag{5.1}$$

$$\mathrm{S}_{y-} = \frac{dY_-}{dt} \tag{5.2}$$

$$\mathrm{S}_{x-} = \frac{dX_-}{dt} \tag{5.3}$$

Figure 5.8 is a graph showing the kernel propagation rates along the three main directions of propagation. From the graph, the general trend is that the growth rates decay from a highly stretched value to an asymptotic value close to the unstretched laminar flame growth rate (S_L). Where S_L is evaluated from the product of the unstretched laminar flame velocity (u_L) and the expansion coefficient which is the ratio of fresh gas density to the density of the burnt product (i.e. $S_L = \rho_u/\rho_b * u_L$). Analysis of the growth rate of each flame front highlight the existence of three key development stages. For example, S_{y+} dropped from an initial high value of 22 m/s to a steady value of 11 m/s in the first 0.15 ms. This was the first phase of growth dominated by induced gas velocity of the shock waves. Between 0.2 and 0.25 ms, S_{y+} decayed from 11 m/s to a second stable speed of about 7.5 m/s which marked the formation of an igniting kernel. This marked the beginning of the second stage of development when the kernel propagates due to combined influence of chemical reactions and induced gas velocity. The third and final major decay in growth rate occurred between 0.5 and 0.8 ms when S_{y+} dropped to a steady velocity of 3.5 m/s. Beyond this point, the downstream flame front maintained a stable velocity which fluctuated around the mean value of 3.3 m/s when growth is mainly due to chemical reactions. Therefore, it is needful to investigate the sensitivity of the flame front growth to these competing factors under changing test conditions.

Figure 5.9 compares the actual speed of the flame front along the three main directions of propagation. To accurately compare them, a velocity compensation is applied by considering the bulk flow velocity (U_0) which affects growth along the flow axis. Therefore, a value of 1.15 m/s is added S_{y-} to while the same value is subtracted from S_{y+}. Such compensation is based on the assumption that the horizontal component of flow velocity along the flow axis is negligible, hence, it will only be valid under a laminar flow condition. The first observation highlighted by this figure is that the growth rate of each flame front decay from a highly stretched value to the same asymptotic value below the unstretched laminar flame growth rate (S_L). The second observation is that there is variation in stretch between the flame fronts during the early development stage. For example, at 0.1 ms, following the appearance of the front lobe, S_{y+} was 18 m/s higher than S_L while S_{x-} is only 8 m/s higher. At 0.15 ms, the variation reduced to 6.9 m/s for S_{y+} 0.64 for S_{x-}. At the late kernel stage, the same value of growth rate is observed along the different directions of propagation.

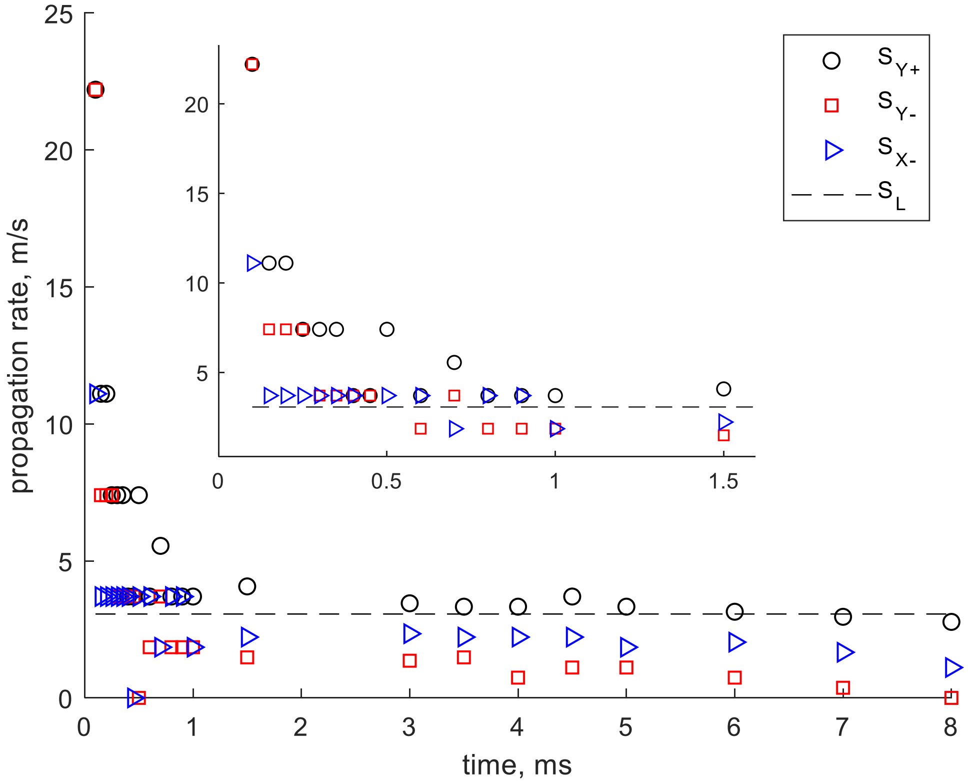

Figure 5.8: Propagation rate along different directions of the flame front.

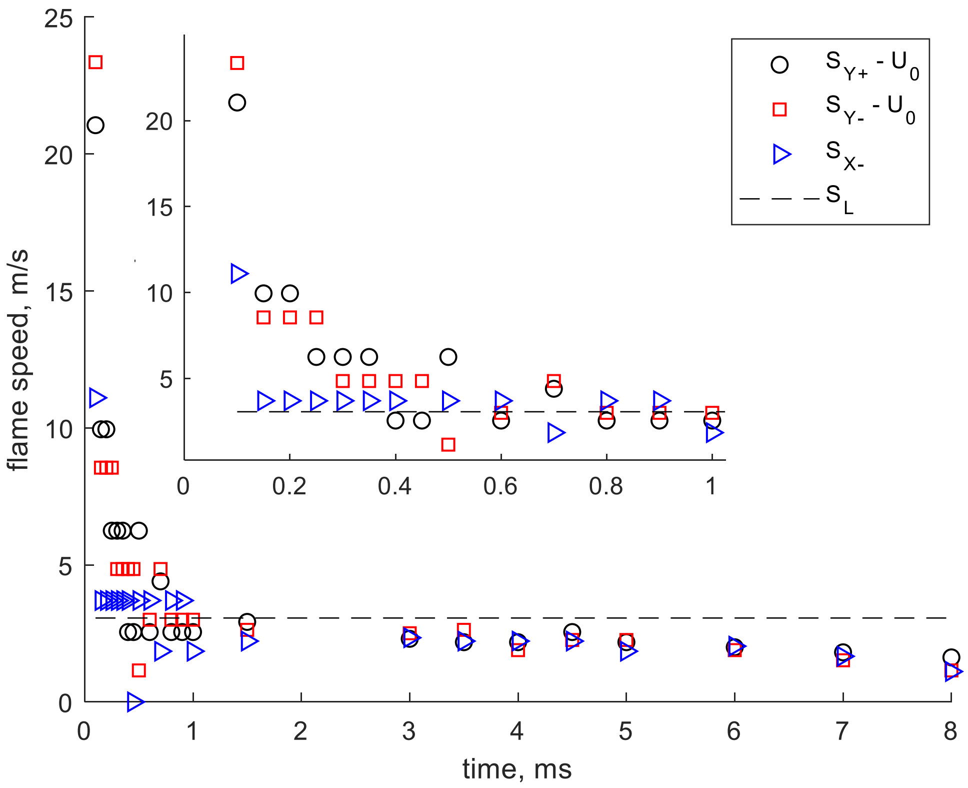

Figure 5.9: Growth rate of the flame front along the three-lobe directions

5.3.3 Analysis of the Flame Kernel OH* Intensity

Having studied the dynamics of the flame kernel geometry, it was necessary to investigate the dynamics of the OH* intensity which could provide an idea of the coupling between the fluid dynamics and chemical kinetics of the flame kernel. From the raw images, a quantitative analysis was also performed to show the general trend in OH* intensity characteristics of the flame kernels. For a reliable measure of the OH* intensity evolution, the images analysed were captured from the same field of view (351x351 pixels) and with an intensifier gain setting of 200.

Figure 5.10 is a plot of the spatially integrated OH* intensity from 150 μs to 10 ms. The evolution of the spatially integrated OH* intensity provided information about the strength of the flame kernel as well as further evidence of the key transition phases of kernel development. The measurement shows that the integrated OH* intensity decreased in value between 0.15 to 0.2 ms. This initial decrease indicates transition from a quenching flame kernel to a more reactive flame kernel. The event could also be interpreted as the chemical induction phase. Beyond this point, the integrated OH* intensity rises continuously in a non-linear fashion. A rising trend in the integrated OH* intensity indicates a developing kernel with a higher chance of survival because the cumulative heat release was increasing with kernel expansion. Between 6 ms and 8 ms, a plateau is observed in the integrated OH* intensity indicating a fully developed flame. Beyond 8 ms, a downward trend is observed in the integrated OH* intensity which may be due to heat losses resulting from interaction of the flame kernel with the Nitrogen used as blow-off gas. By relatively comparing the integrated OH* intensity with the kernel dimensions, it can be deduced that both predicts the key transition points of the early development such as the end of chemical induction and the time when growth is purely due to chemical reaction.

Figure 5.11 is the evolution of peak OH* intensity from 150 μs to 10 *ms* time delay. The peak intensity indicates the measure of heat release due to the balance between radical production rate and consumption rate. Just like the cooling curve of most gases, the observed trend in peak in OH* intensity shows a continuous decay until it reaches a minimum value 1314 AU around 1.5 *ms*. After reaching this minimum value, a slow recovery is observed in the peak OH* intensity reaching a trough value of 1500 AU at 4.5 ms and and a second trough value of 2000 AU at 9 ms. At the developed stage, the kernel's ability to maintain intensity values above the minimum peak is necessary to prevent quenching of the flame kernel and indicates continuous heat release due to chemical reaction. Also, correlation can be made between the time kernel reaches its minimum peak OH* intensity and the period when the propagation rate of the flame fronts reaches an asymptotic value.

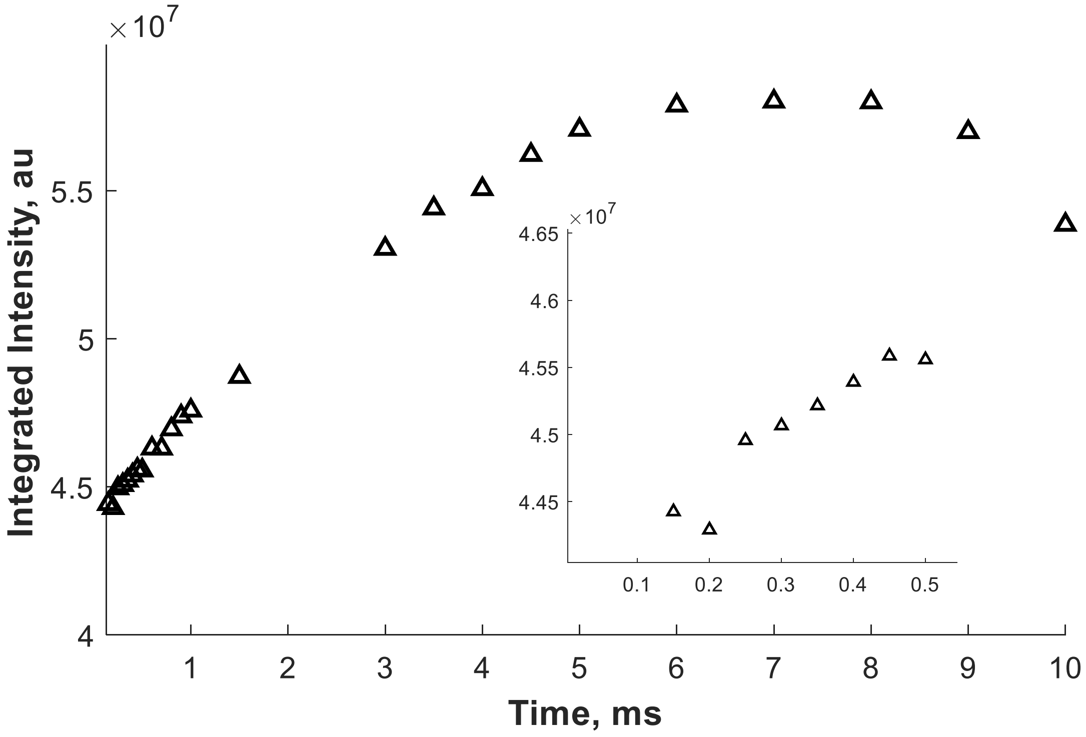

Figure 5.10: Evolution of the mean integrated OH* intensity from 150 µs to 10 ms

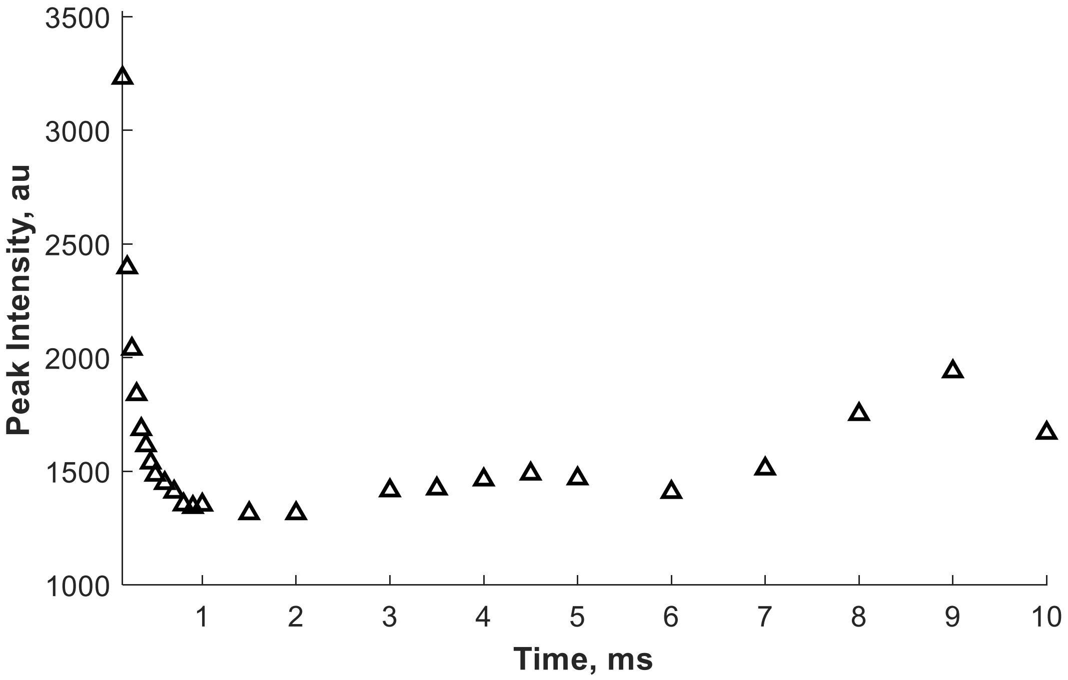

Figure 5.11: Evolution of the mean peak OH* intensity from 150 µs to 10 ms

5.4 Effects of Laser Pulse Energy

Having studied the fundamental characteristics relevant to flame kernel propagation, the next stage of the study was to investigate the effect of the key control parameters. In this section, the effect of laser pulse energy on the flame kernel characteristics was investigated using four variations of pulse energy (i.e., 32, 64, 96 and 128 mJ). For fair comparison, a constant flow condition (same as that used in Test case 1) is maintained throughout.

Figure 5.12 visualizes different development stages of the flame kernel (150 µs, 500 µs, 1500 µs and 3000 µs) due to changing pulse energy. As in earlier observation, the flame kernel shapes were identical for all cases each evolving from a two-lobe symmetric toroid to a three-lobe structure with the late kernels developing into a flame ball shape. Overall, with a higher pulse energy, the upper and lower toroid develops faster producing a bigger sized kernel at a particular time delay from the beginning of an ignition event. This increase in kernel size is attributable to higher plasma induced gas velocity associated with higher pulse energy leading to higher stretching of the kernels. In the late kernels, the impact of increased pulse energy is not so significant compared with the early kernels, especially for higher pulse energies. A second visible effect of higher pulse energy on the early kernels is that the front lobe development is faster for higher energies and their lifespan is shorter due to higher stretch rates. This is due to the stretching effects of high energy pulses which can lead to premature extinction of the kernel. Based on the images captured at 150 µs delay, overstretching resulted in separation of the front lobe flame front from the rest of the kernel at higher pulse energies. A third visible effect of pulse energy can be observed from the color scale of images acquired at the same time delay. For example, at 150 µs each increase in pulse energy produced a corresponding increase in peak OH* intensity. By 1.5 ms, each increase in pulse energy had no effect on the peak OH* intensity. In contrast to the early kernel, a downward trend was observed in peak OH* intensity due to increased energy at 3 ms.

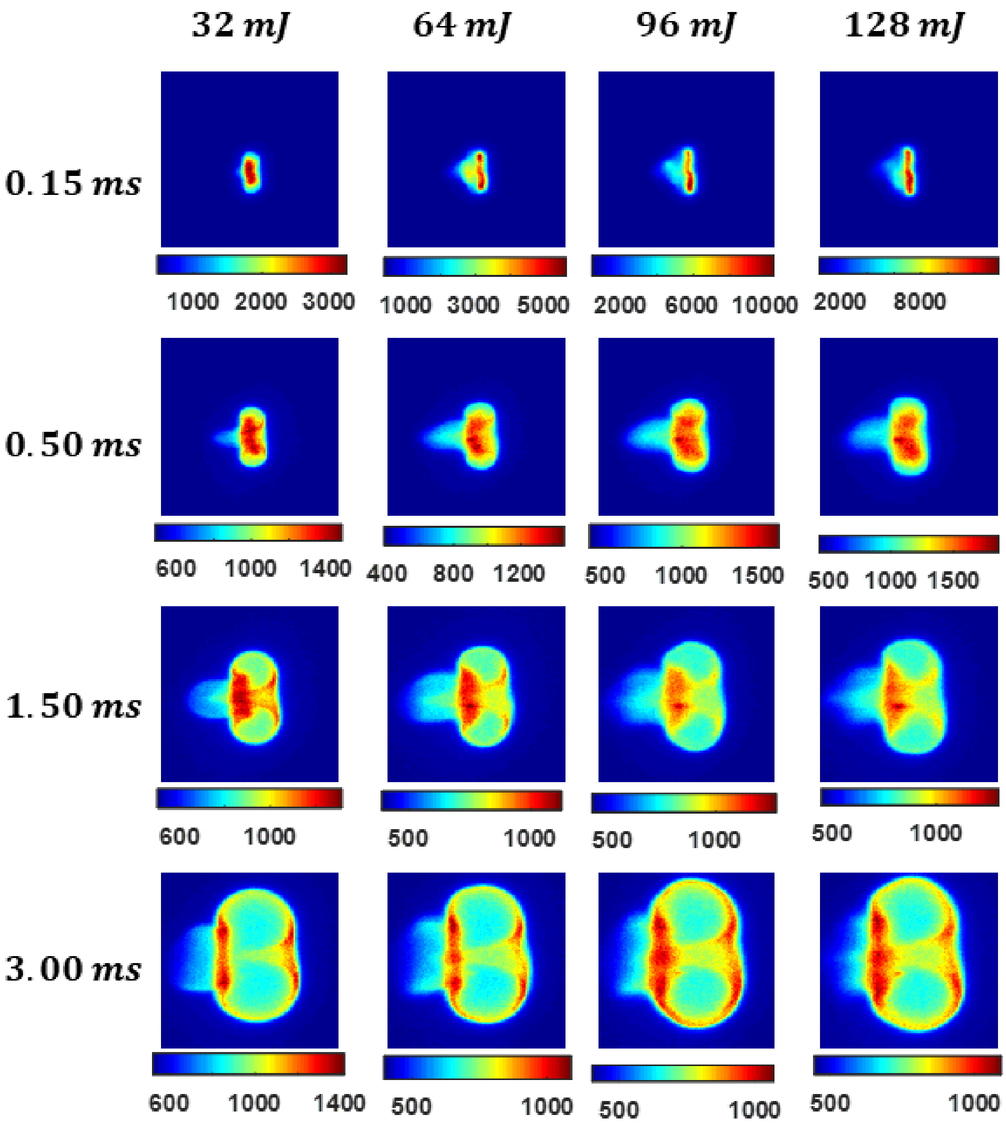

Figure 5.12: Visual comparison of flame kernel development at different pulse energies (FOV: 28x28 mm^2)

Figure 5.13 and Figure 5.14 shows the comparative dimensions of the developing flame kernel due to changing pulse energies. Both plots reveal a noticeable increase in kernel size due to higher energy especially at the early development phase. It is worth noting that there was a significant increase in size (especially W) when the incident energy increased from 32 mJ to 64 mJ, however, further increase in energy had little or no effect on the kernel size. This shows the existence of a threshold incident energy for optimal ignition performance for the selected focusing lens and flow condition. The observation agrees with previous authors that spark energy deposition has a limiting efficiency depending on the lens focal length [90],[157]. The current observation showed that further energy increase beyond the threshold value could lead to premature extinction instead of enhancing flame propagation. Further analysis showed the most enhancement in early kernel growth rate occurred in the first 400 μs along X- when the pulse energy increased from 32 mJ to 64 mJ. This further confirms the existence of a threshold energy above which an increase in pulse energy had no impact on growth rate. No significant changes were observed in the late kernel stage with increase in pulse energy.

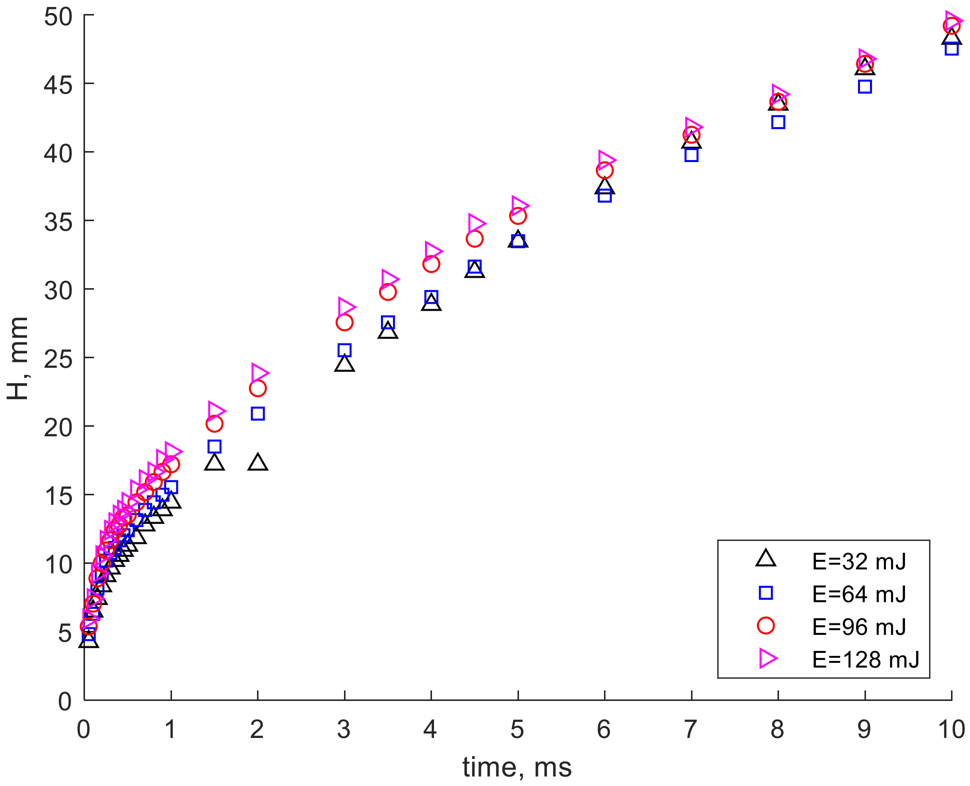

Figure 5.13: Evolution of kernel height compared at different pulse energies

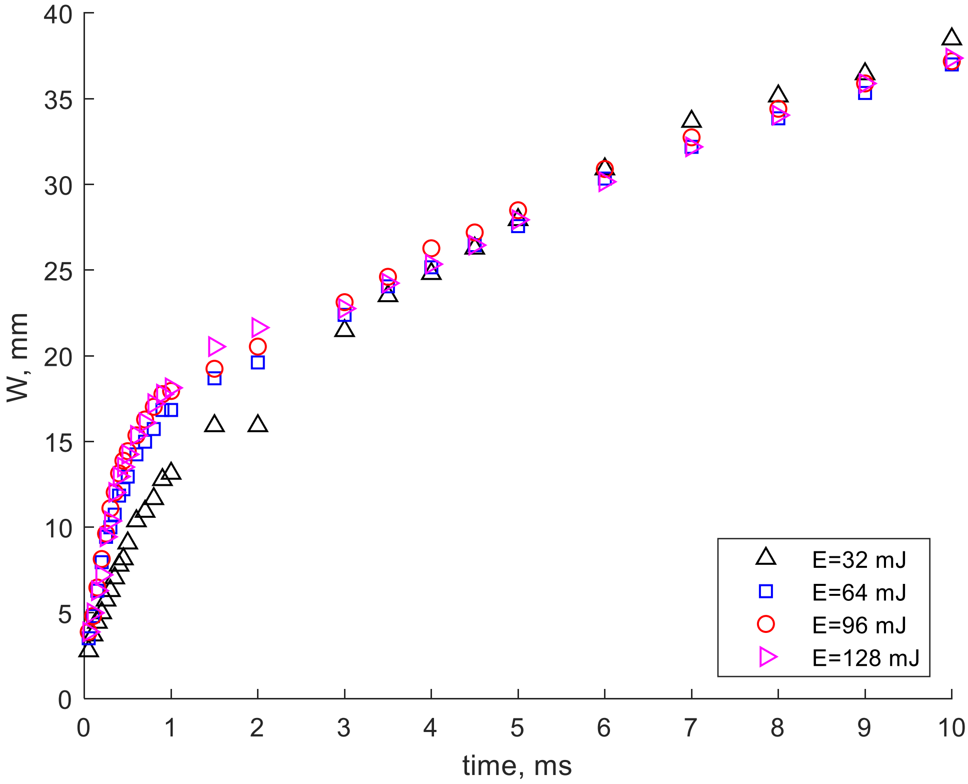

Figure 5.14: Evolution of kernel width compared at different pulse energies

Figure 5.15 compares the propagation rate of the flame front tip along opposite directions of the flow axis at varying pulse energies (i.e., 32, 64, 96 and 128 mJ). A common feature of the plots is that the growth is characterised by decay from a high initial velocity to a stable asymptotic velocity close to the laminar unstretched value. Overall, the kernel propagated faster with higher incident energy, but this happened before 1 ms, during the early kernel development. From 1 ms onwards, all the kernels propagated with the same steady state velocity which implies that stretch effect is only prevalent at the development stage.

To better illustrate the relative changes in propagation rate and stretch effect of the incident energy, the normalised flame front propagation speed downstream is plotted as a function of the displacement as shown in Figure 5.16. As the figure shows, when the incident energy was 32 mJ, $\mathbf{S}_{y+}$ reached its asymptotic velocity after travelling 8.5 mm downstream which makes it the least stretched. On the other hand, when the incident energy was 128 mJ, $\mathbf{S}_{y+}$ reached its asymptotic velocity after travelling 10.5 mm downstream which makes it the most stretched. Furthermore, for the same displacement of 8 mm, the respective stretched speed at 32, 62 and 128 mJ were 20, 20, 30, and 50% more than the upstretched laminar value. The similar stretch between the two flame fronts at 96 and 128 mJ further confirms the existence of a threshold incident energy above which further increase has no impact on the growth. The results also shows that the incident energy has no impact the growth of any of the flame kernels after extending 10.5 mm downstream during which a constant velocity is maintained.

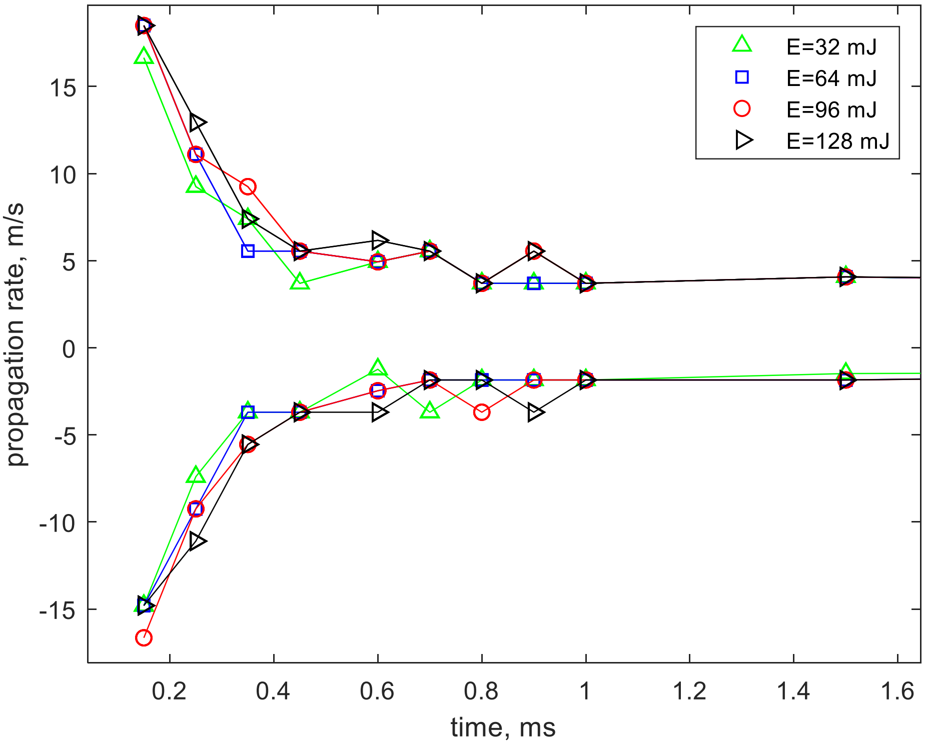

Figure 5.15: Axial propagation rate at changing incident pulse energy.

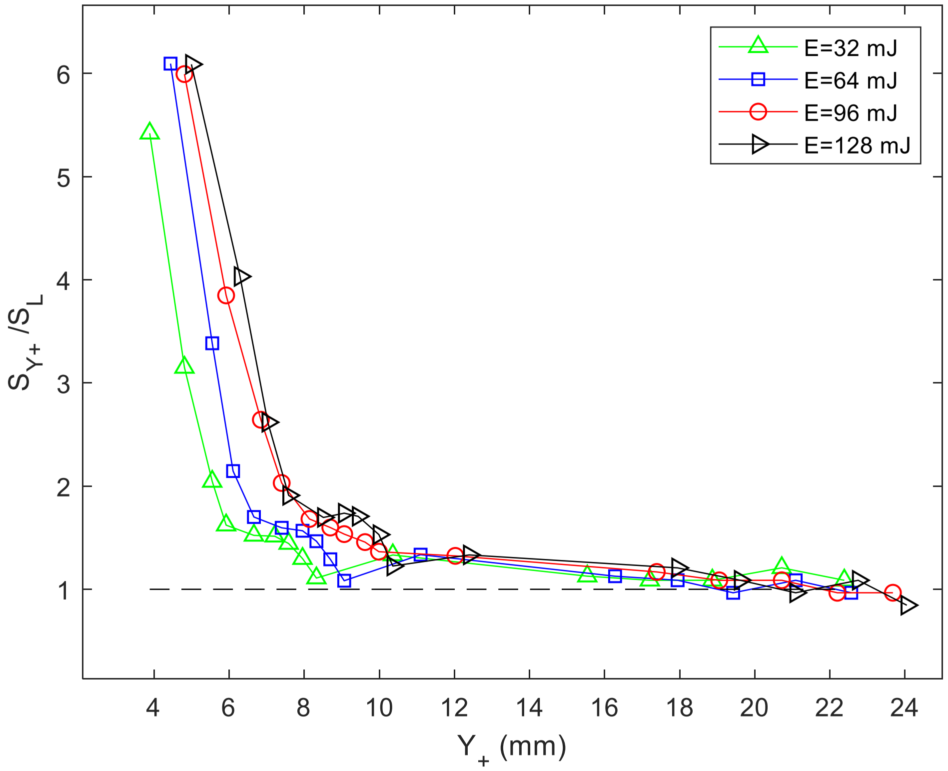

Figure 5.16: Normalised propagation rate vs displacement at changing incident pulse energy.

Figure 5.17 shows the effect of increasing pulse energy on the integrated OH* intensity. The first main observation from the results is that the value of the integrated OH* intensity falls and then rises in a non-linear fashion and the time at which the minimum integrated OH* intensity occurs is delayed with a higher pulse energy. Therefore, it can be inferred that the higher the pulse energy, the longer the chemical induction time. Following transition to an igniting kernel, the cumulative heat release rises for each case which is marked by a continuous rise in the integrated OH* intensity until a maximum value is reached. From the graphs, it is evident the mean integrated OH* intensity is highly sensitive to increase in pulse energy from 32 mJ to 64 mJ where a decrease in integrated OH* intensity was observed. Further increase in energy from 64 mJ to 128 mJ resulted an increase in the integrated OH* intensity but remained below the initial values at 32 mJ. This shows that the total heat release was increasing with energy increase but not at the optimum level.

An investigation of the variation in peak OH* intensity for different incident energies is shown in Figure 5.18. From the graph, the initial values of the peak intensity increased in accordance with the magnitude of pulse energy. However, this trend did not last beyond 500 μs, as the intensities decayed to the minimum values and then a subsequent increase which marks a growing self-sustaining flame. Following the formation of a self-sustaining flame, the peak OH* intensity decreased with energy increase from 32 to 64 mJ. Further increase in energy however did not produce any further change as observed in the kernel width.

By considering all the observation, a conclusion can be drawn that the optimal ignition energy should be decided based on the OH* production instead of the flame stretch since the initial stretch resulting from higher pulse energies did not produce bigger flame balls in the end. In the present investigation, a 32 mJ energy would be ideal, however, it will be helpful to investigate if incidents energies below 32 mJ produced more OH*. It is logical that such investigation is done since the MIE of the mixture is much lower (~0.25 mJ).

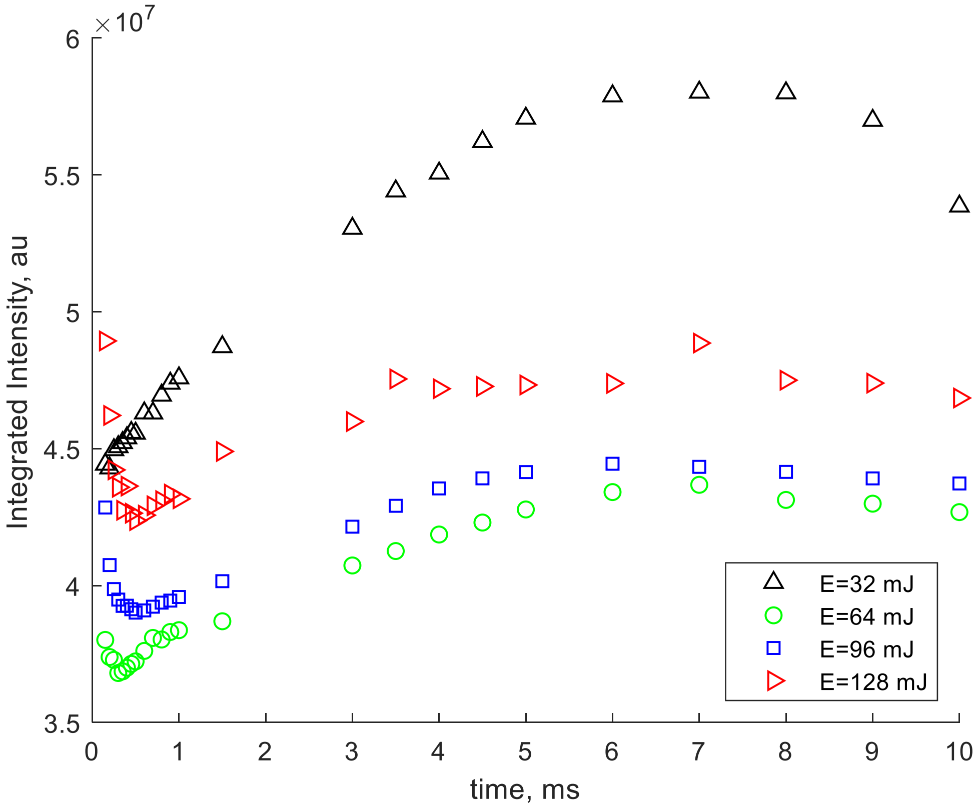

Figure 5.17: Effect of pulse energy on the mean integrated OH* intensity

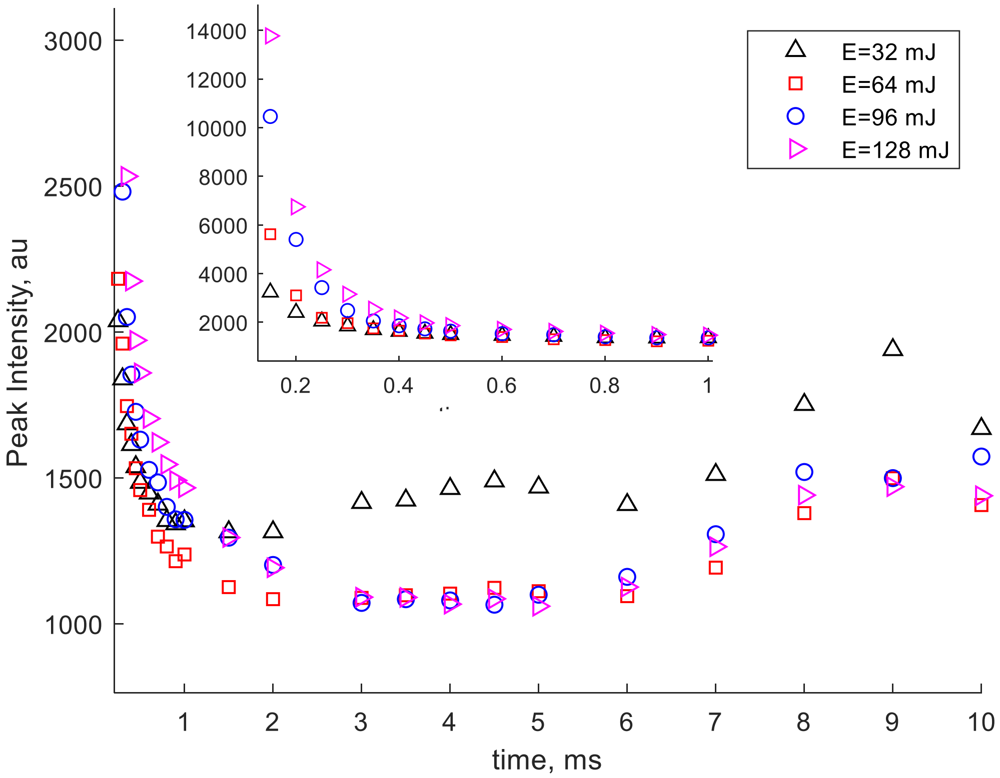

Figure 5.18: Effect of pulse energy on the mean peak OH* intensity

5.5 Effects of Flow Velocity

In this section, the effect of the gas flow velocity on the development of the flame kernel is reported. For fair comparison, experiments were conducted by maintaining a constant mixture composition and pulse energy (i.e., $\boldsymbol{\varphi} = 1.0, \mathrm{E} = 32\ \mathrm{mJ}$), while the flow velocity was varied in the following order: 1.15, 2.08, 3.0 and 3.48 m/s.

Figure 5.19 visualizes different development stages of the flame kernel (150 µs, 500 µs, 1500 µs and 3000 µs) due to variation in flow velocity. By comparing images acquired at the same ignition delays, no significant difference is observed in the kernel sizes and shapes especially at the development stage, however, the effect of increasing velocity is shown by the vertical displacement of the kernel centroid with respect to the spark position. At the developed stage, the pictures show that the kernel is under increasing amount of strain due to higher flow velocity. In addition, convective effect of the flow is shown by the fact that part of kernel is no longer within the observation window. By comparing the image colormap, it is evident that the surface of the flame front increases and becomes less defined at higher flow velocities. This is of the wrinkling of the flame front due to higher turbulence. In addition, there is hardly a noticeable change in peak OH* intensity at different flow velocities but this would be analysed further.

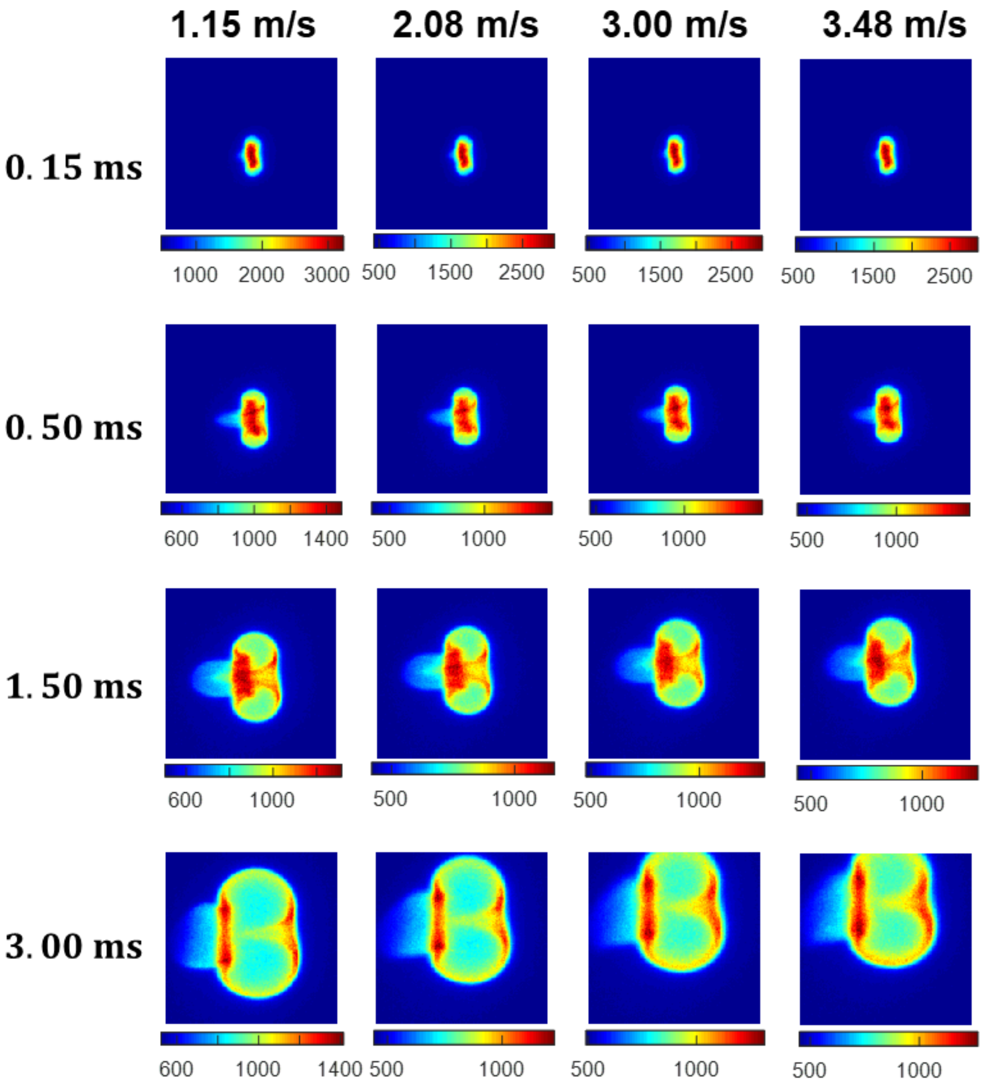

Figure 5.19: Visualisation of flow velocity effects on kernel development

To quantify the effect of increasing flow velocity on the kernel development and propagation, each kernel characteristics were extracted and shown graphically on the same timescale.

Figure 5.20 is a graphical picture of how the flow velocity influenced the displacement of the flame front tip along the axis of the flow. The figure clearly shows that the dominant effect of higher flow velocity is an increased displacement of the flame kernel centroid which in effect resulted in an increased growth downstream and decreased growth upstream. Further investigation showed that difference between the upper and lower flame front tip for different flow velocities were insignificant, hence, higher flow velocity had very little or no effect of the kernel height. Another effect of high flow velocity is that of the increased strain on the lower flame front. A clearer picture of the axial motion of the FF tips is shown by the 2D scatter plot in Figure 5.21 which shows the displacement and strain effect of increasing flow velocity on the flame kernel. Due to increasing strain resulting from a higher flow velocity, further growth of the flame front upstream is prevented resulting in a slightly wider kernels at higher flow velocities as shown by Figure 5.22.

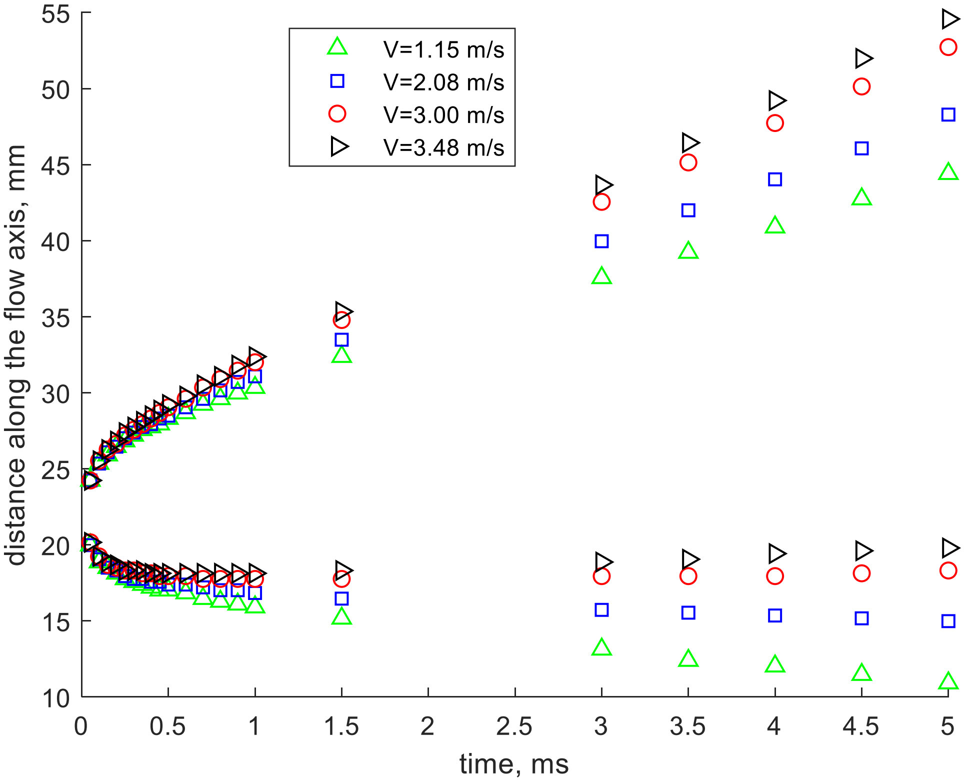

Figure 5.20: Axial FF tip locations at varying Flow velocity

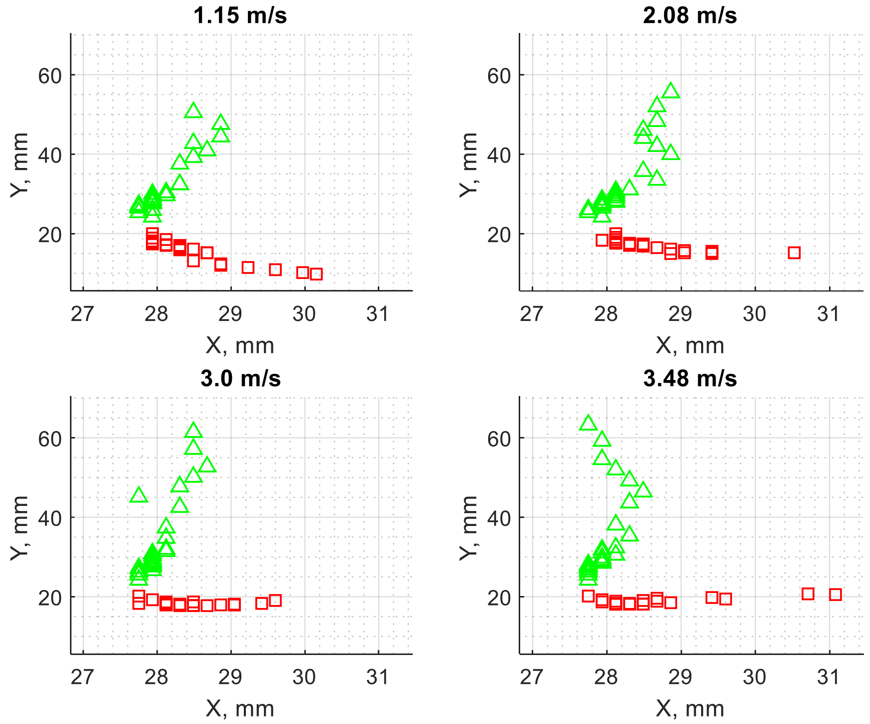

Figure 5.21: Scatter plot of Axial tip location for varying velocity of flow

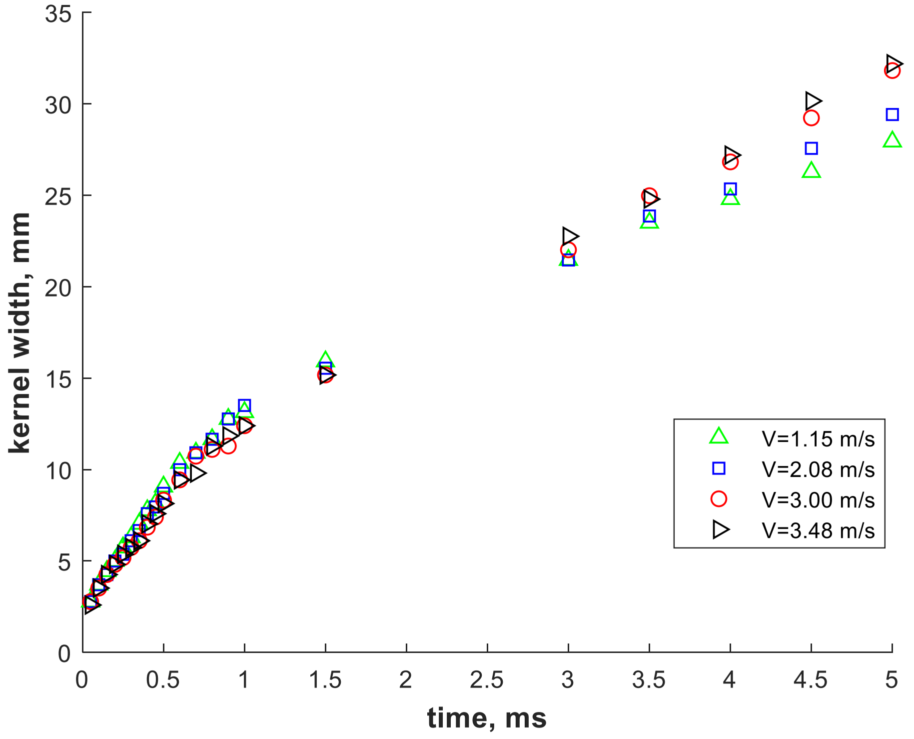

Figure 5.22: Kernel width at varying velocity of flow

Figure 5.23 shows the effect of flow velocity on the flame front tip displacement along the flow axis. As shown, the general trend in propagation rates indicates decay from a highly stretched value to an asymptotic value irrespective of the velocity of the flow. The asymptotic values of S_{y+} were 0.63, 0.79, 0.95, 1.02 m/s at respective flow velocity U_0 values of 1.15, 2.08, 3.0, 3.48 m/s. Hence, an 80% increase in U_0 produce about 25% increase in S_{y+}. In contrast, the asymptotic values of S_{y-} were -0.25, -0.09, 0.02, 0.07 m/s at respective flow velocity U_0 values of 1.15, 2.08, 3.0, 3.48 m/s which represent a 64% decrease in S_{y-} for similar increase in flow velocities. The loss in propagation rates of the upstream flame front the result of higher aerodynamic strain on the flame kernel at higher flow velocities. The graphs also shows that a higher flow velocity had little or no influence on the propagation velocity of the flame front in the early stage up to about 0.5 ms. In addition, the the higher velocity flows were characterised by fluctuation in propagation rate before reaching the asymptotic values.

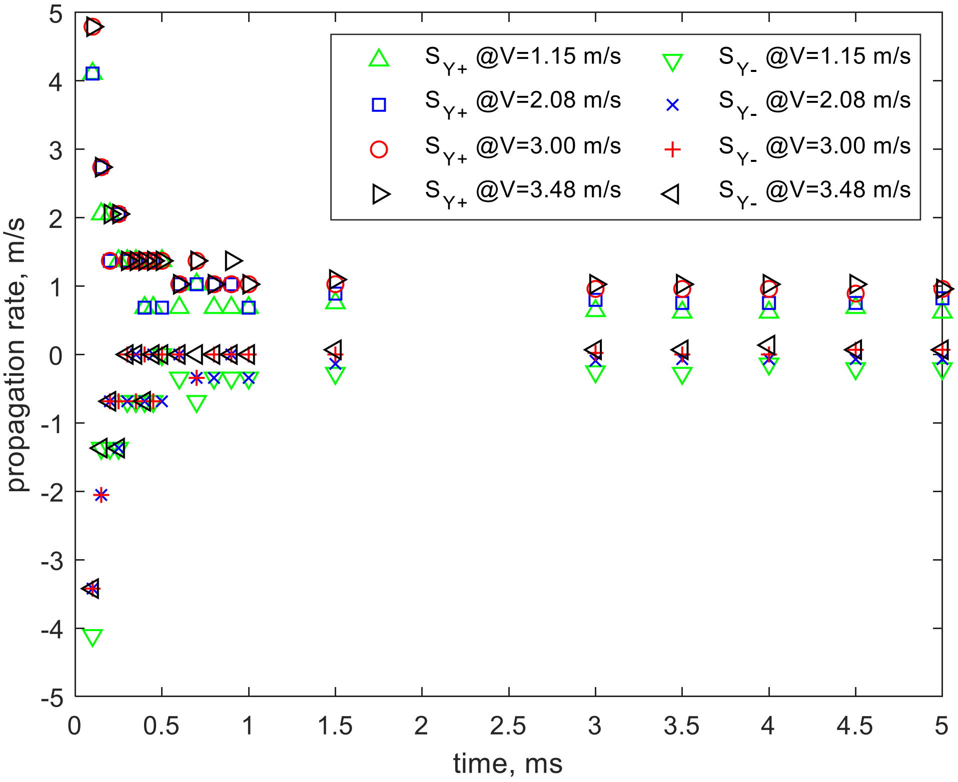

Figure 5.23: Flow velocity effect on S_{y+} and S_{y-}

Figure 5.24 shows the evolution of spatially integrated OH* intensity for varying flow velocities. The observed trend for each flow velocity is similar to earlier observation with an initial decrease during chemical induction and a constant rise afterwards. From results of the integrated OH* intensities, it was difficult to determine the particular order of influence due to fluctuating output, hence a further investigation of the fluctuations from each ignition event is recommended. A unique observation from the graph is that the duration of chemical induction (which represents the time at which minimum value was obtained) tends to increase with an increase in flow velocity which might be interpreted as the result of cooling effect.

Similarly, the integrated OH* intensity, the observed trend in peak OH* intensity shown in Figure 5.25 did not provide adequate information on its sensitivity to increasing flow velocity. The inconsistency in the observed sensitivity of OH* intensity could be linked to many factors. The first reason may be related to the displacement effect of high flow velocities on location of the flame kernel centroid, which means that a corresponding displacement in the observation window may be necessary for a fair comparison. The second reason may be linked to possible differences in spark efficiency due to the stochastic nature of breakdown process.

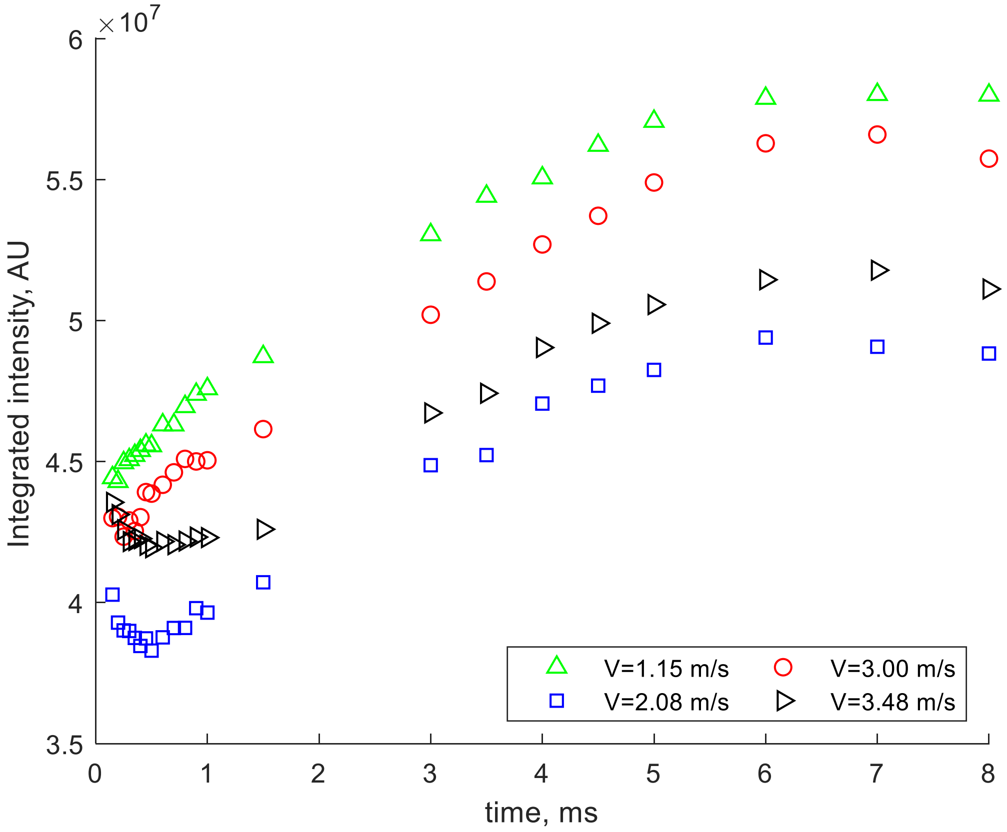

Figure 5.24: Flow velocity effect on Integrated OH* intensity

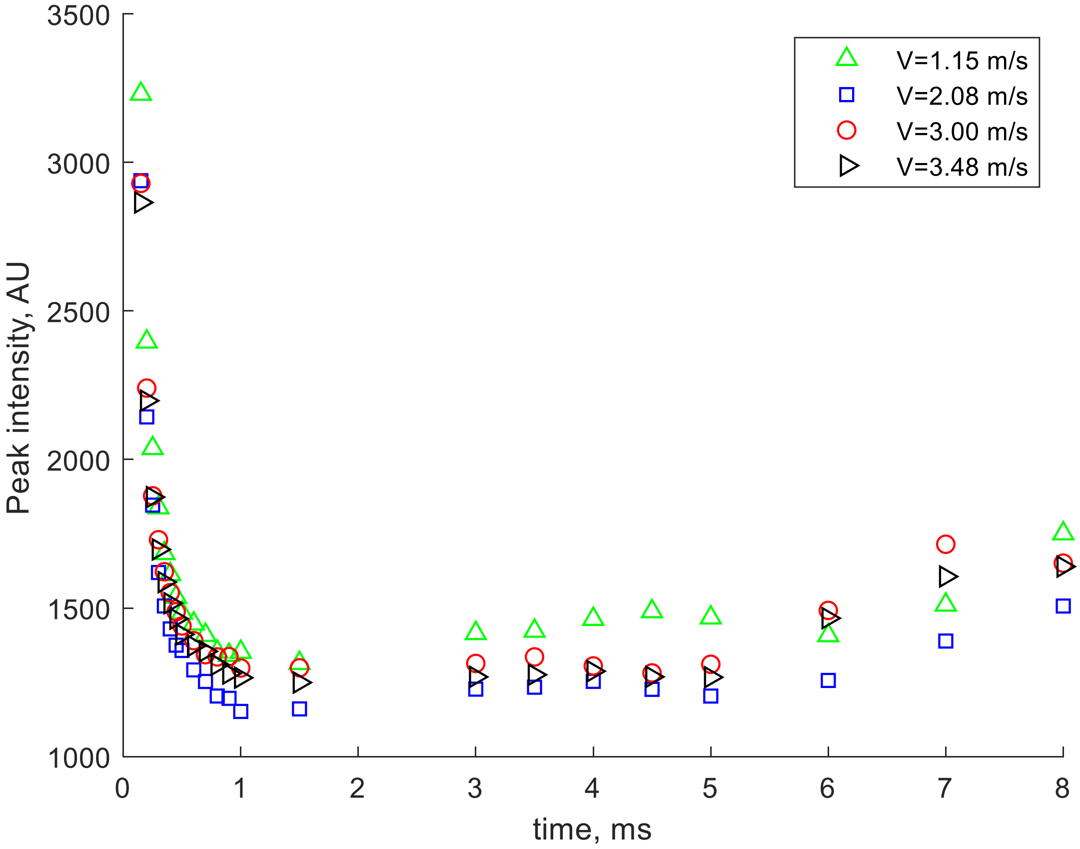

Figure 5.25: Flow velocity effect on Peak OH* intensity

5.6 Conclusions

The development of the flame kernel employing LISI has been characterized experimentally in a lab-scale atmospheric burner with flowing stoichiometric CH4/Air mixtures. This was made possible through analysis of captured 2D projection images resulting from the kernel OH* chemiluminescence. The major findings are summarised below:

- Flame kernel visualisation using the OH* chemiluminescence revealed similar geometric features observed in earlier from tomographic images. By 50 µs, the kernel shape has evolved into a two-lobe symmetric toroid. This was followed by the appearance of a front lobe before 100 µs. Finally, a self-sustained propagating flame ball resulted following the disappearance of the front lobe.
- Analysis of the image frames following a geometric edge extraction showed that the growth of the upstream flame front along the flow axis is characterised by non-linear decay growth during the first 0.8 ms, followed by a steady linear growth until it reached a maximum displacement of 12 mm in about 7 ms. On the other hand, the transverse growth of the flame front towards the laser is characterised by relatively stable growth in the first 1.5 ms, with sudden change in slope due to local quenching at the front lobe and then a steady linear growth onwards. The resulting flame kernel therefore differs in its spatial dimension (i.e., height greater than width) which may be attributable to the asymmetry in the dimensions of the initial spark kernel. Under the condition, it takes about 2 ms for the kernel height (Y) to grow to a spatial scale about the size of the burner diameter (i.e., 22 mm) and kernel width reached a spatial scale about the size of the burner diameter in just above 2 ms.

- Analysis of the flame front propagation rate along the three lobe directions showed it decayed from a highly stretched value to a steady asymptotic value close to the unstretched laminar flame speed. Based on these observations, inference can be made that the initial kernel growth is the result of both induced gas flows and chemical reactions while the steady growth in the late kernels relies entirely on heat release due to chemical reactions. It also highlighted the existence of three key development stages. From a decaying kernel of hot gas, the kernel reached an initial steady speed of about 11 m/s in 0.15 ms. This was the first phase of growth dominated by induced gas velocity of the shock waves. A second decay occurred between 0.2 and 0.25 ms, when the kernel reached a second stable speed of 7.5 m/s due to formation of an igniting kernel. This marked the second stage of development when the kernel propagates due to combined influence of chemical reactions and induced gas velocity. The third and final decay occurred between 0.8 ms beyond which a steady velocity of 3.5 m/s was maintained. From this point onwards, the kernel propagated with minimum velocity variation from its unstretched laminar value of 3.06 m/s.

- Further visualisation of the image colourmap revealed that during its development, the reaction zone of the flame kernel (indicated by the OH* intensity distribution) evolved from an isotropic to anisotropic flame front. In the self-sustained flame, the reaction zones were concentrated at the edges. These observations gave an idea of the different stages of the development and the two-way interaction involving the flame-flow mixture and flame-burnt products.

- Analysis of the luminous intensity of OH* intensity provided an indication of the reactivity and heat release rate during development of the flame kernel. Transition to a self-sustained flame kernel is characterized by decay in peak OH* intensity to a minimum value which must be sustained for the kernel to survive. The integrated OH* intensity initially decreased to a minimum trough value which occurred at 0.2 ms in the base case study, followed by a non-linear continuous rise to a maximum value in the fully developed flame. The time elapsed before this minimum value was interpreted as the chemical induction time which representing transition between a quenching kernel of hot gas and formation of an igniting flame kernel. The rising trend after an initial drop in integrated OH* intensity indicates that the kernel is more likely to survive since cumulative heat release increased during kernel expansion.

- A comparison of the kernel development at different incident energies (i.e., 32, 64, 96 and 128 mJ) reveals that the early growth of the kernel is enhanced by a higher energy, but this happens within a limiting threshold energy. In the fully developed kernel however, the size of the kernel is not influence by the energy. A comparison of the peak OH* intensities reveals that the reactivity was unaffected by the energy of the incident beam except in the first 0.5 ms. A comparison of the integrated OH* intensities shows that the chemical induction duration increased for higher energies. An interesting insight from this analysis is the fact that the maximum integrated OH* intensity decreased greatly by 25% with energy increase from 32 to 64 mJ, however, however, further increase in energy resulted a reduction in the the negative effect. Based on the observations, the optimal ignition energy should be decided based on the OH* production, however further investigation with lower ignition energies is recommended. Further details of the sensitivity analysis can be seen in Table 0.1 of Appendix E: Sensitivity Analysis.

- A comparison of the kernel development at different bulk flow velocities (i.e., 1.15, 2.08, 3.0 and 3.48 m/s) reveals and increased displacement of the kernel centroid with higher flow velocity due to convective effects and as well as an increased strain on the flame front upstream. Overall, there is no remarkable increase in growth rate of the kernel due to increased velocity. The combined effect of convection and increased turbulence at higher bulk velocities resulted in a faster propagation of the flame front downstream.

There were fluctuations in both the peak OH* intensity and maximum integrated intensity which made difficult to understand the influence of increased velocity on reactivity. Also, the duration of chemical induction appears to be longer for higher bulk velocity flows.

Chapter 6 Effects of fuel properties on the development characteristics of Laser-ignited Flame Kernel

6.1 Introduction

The demand for fuel flexibility and a shift towards lean combustion are the key motivations to study the fuel composition effect on laser-ignited flame kernels. The advantages of lean combustion are increased fuel efficiency and reduced NOx emissions due to lower maximum combustion temperatures. Despite these benefits, combustion initiation under lean conditions is challenging and even after ignition initiation, incomplete combustion may result due to slow propagation. Hence, the need to understand the impact of leaning on combustion initiation and propagation. The desire for fuel flexible combustors is to increase energy sustainability. However, the impact of the wide variety of available fuel types and sources on the engine performance remain an issue of concern. Combustion variation is caused by differences in the thermochemical properties of fuels such as the laminar burning velocities (S_L), adiabatic flame temperatures (Tad) as well as the Lewis Number (*Le*). It is therefore necessary to investigate the effects of these properties on the ignition dynamics.

In this chapter, the aim is to investigate the effect of the thermochemical properties of the fuel mixture on the development characteristics of the laser-ignited flame kernel. The study is divided into three main sections. In the first section, the composition of mixture is varied in terms of changing equivalence ratios of methane/air mixture which also represents changing values of S_L or Tad. In this investigation, the methane/air mixtures were selected to include flows within the laminar and turbulent flow regimes. In the second section the mixture composition is varied in terms of changing fuel types with constant adiabatic flame temperature while in the third section different fuel types with constant S_L are compared. In both sections two and three, differences in flame kernel characteristics are viewed from the angle of differences in the fuel type since either a constant S_L or Tad is maintained. These studies were achieved using the same experimental setup as in chapter 5. The major difference is the introduction two new fuels (i.e., propane and ethylene) in addition to methane.

6.2 Effects of change in fuel mixture composition

In this section, the effect of changing fuel-air ratio on the development characteristics of methane flame kernel is reported. Three φ values (1.0, 0.9 and 0.8) were selected in the laminar flow region and another three φ values (1.0, 0.9 and 0.8) in the turbulent flow region making a total of six test cases. The corresponding T_{ad} values are 2226 K, 2134 K and 1996 K respectively[110]. Table 6.1 is summary of the selected flow conditions and the properties. As shown in the table, the compared mixtures all have nearly the same bulk flow velocity. In addition, all experimental conditions except mixture ratios were kept constant.

Table 6.1: Summary of flow conditions with varying equivalent ratios

Test Case	**φ**	**Flow Rate (lpm)**		**U_0 (m/s)**	**R_e (Pa.s)**	**T_{ad} [110] (K)**	**u_L [112] (cm/s)**	**$\frac{\rho_u}{\rho_b}$**
		Air	**CH_4**					
Laminar flows	1	23.8	2.5	1.15	1694	2226	41	7.47
	0.9	24.3	2.3	1.17	1718	2134	36	7.16
	0.8	25.0	2.1	1.19	1750	1996	29	6.70
Turbulent flows	1	101.0	10.6	4.89	7184	2226	41	7.47
	0.9	101.6	9.6	4.87	7169	2134	36	7.16
	0.8	102.4	8.6	4.87	7165	1996	29	6.70

Figure 6.1 visualizes the effect of reducing fuel/air ratios on flame kernel evolution from the mean OH* chemiluminescence images. By comparing mean images acquired at the same ignition delays, the developing kernels showed no significant

difference in their sizes except that the leanest mixture was more stretched leading an earlier quenching at the front lobe. At the developed stage, the kernel sizes were clearly distinct from each other as the kernel become smaller at lower **φ** values. A similar trend is observed with the kernels developing in turbulent mixture environment as shown in Figure 6.2. As shown by the image colour scales, the OH* intensity at the kernel boundaries are more clearly separated from that of the hot gases in the stoichiometric mixture than the lean mixtures while in the turbulent FF, the OH* intensity seem to indicate a wider thickness as the mixture equivalence ratio decreases.

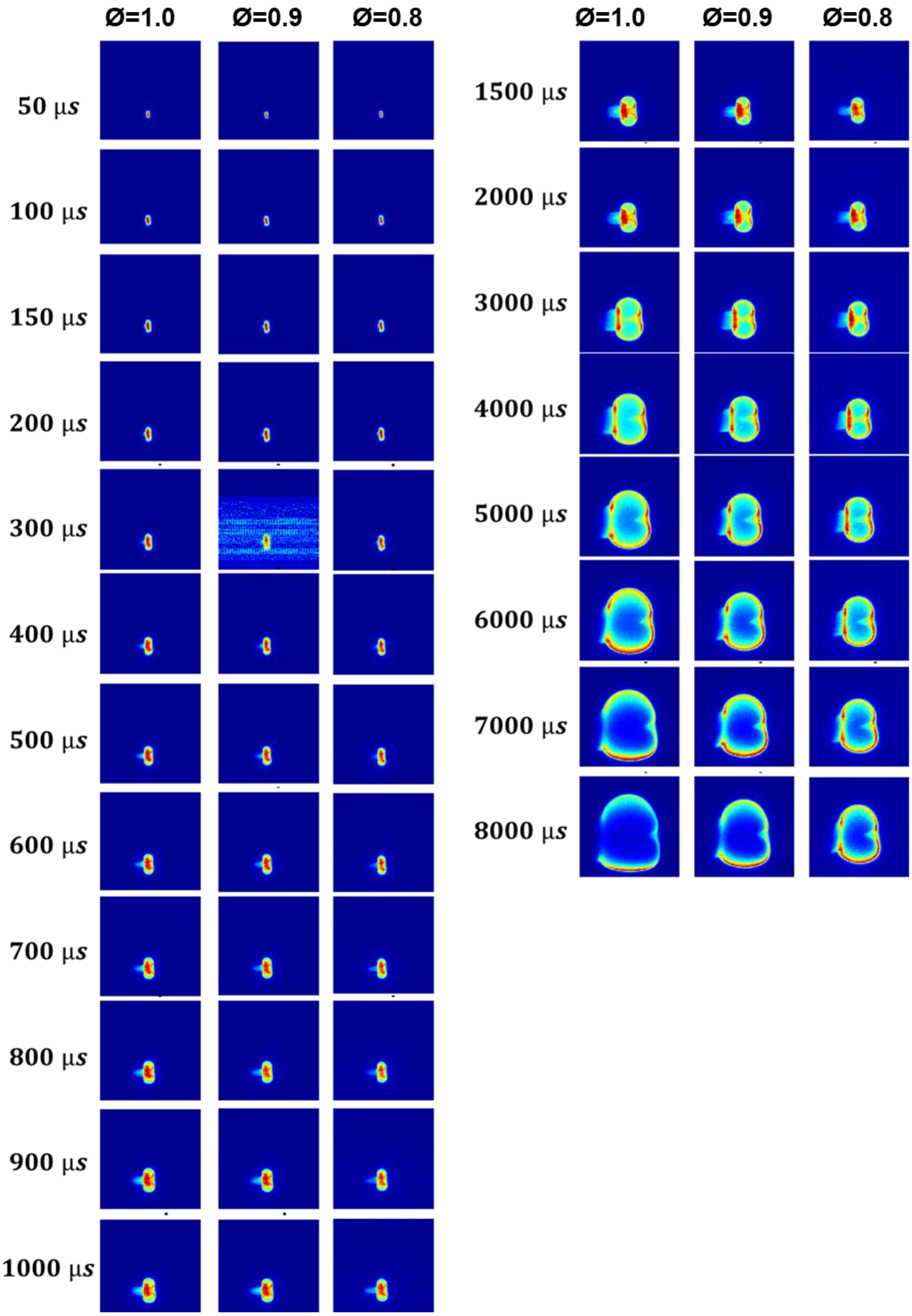

Figure 6.1: Equivalence Ratio Dependence of Flame Kernel in Laminar Mixtures (FOV: 56X56 mm^2)

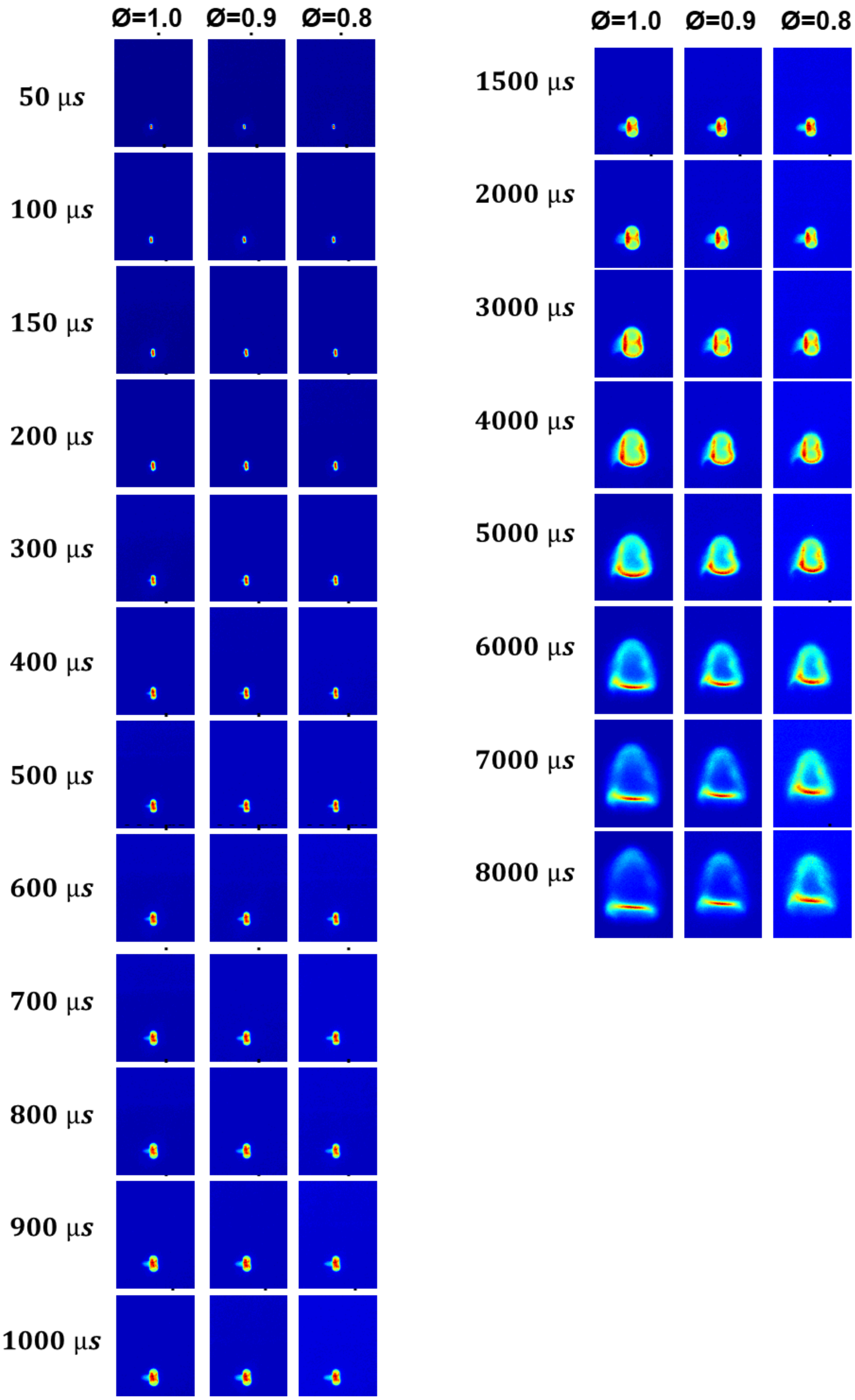

Figure 6.2: Equivalence Ratio Dependence of Flame Kernel in Turbulent Mixtures (FOV: 56X56 mm^2)

Figure 6.3 - Figure 6.4 compares the observed peak OH* intensities with changing equivalence ratios (**φ**=1.0, 0.9, 0.8) for different CH_4/Air mixtures. As in previous observations (see Chapter 5), the peak OH* intensity for each mixture follows an asymptotic trajectory which indicates cooling rate resulting from an imbalance between production and consumption of the OH* radicals. In the present investigation, the general trend is that higher OH* intensity peak is synonymous with higher adiabatic temperature which is dependent on the mixture equivalence ratio. In the self-sustained flame kernels (1.5 – 10 ms) obtained for laminar mixtures, the highest average peak of 1400 AU is obtained in the stoichiometric mixture (i.e., **φ**=1.0) while lowest average peak of 800 AU is obtained in the stoichiometric mixture (i.e., **φ**=0.8). This indicates higher reactivity for near stoichiometric mixtures (i.e., **φ**=1.0 and **φ**=0.9) due to higher adiabatic flame temperatures and lower reactivity in lean mixtures (i.e., **φ**=0.8) due to lower adiabatic flame temperatures. By comparing peak OH* intensities of the three turbulent flow mixtures, the same trend is observed as in the laminar cases having the same equivalent ratios but slightly lower reactivity. This relationship between equivalent ratio and peak OH* intensity is consistent with previous studies [50] ,[158],[159] where reactivity is associated with the rate of heat release. An interesting result from the sensitivity analysis is that the variation is linear in laminar flows but non-linear in the turbulent case.

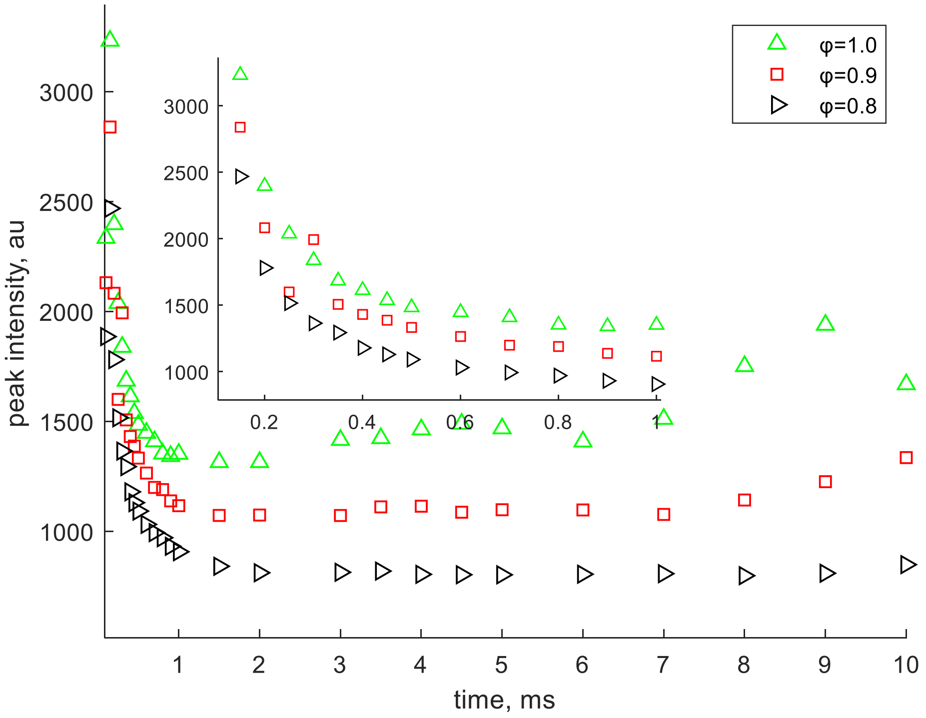

Figure 6.3: Peak OH* Intensities at varying Equivalence Ratios (Laminar Mixtures)

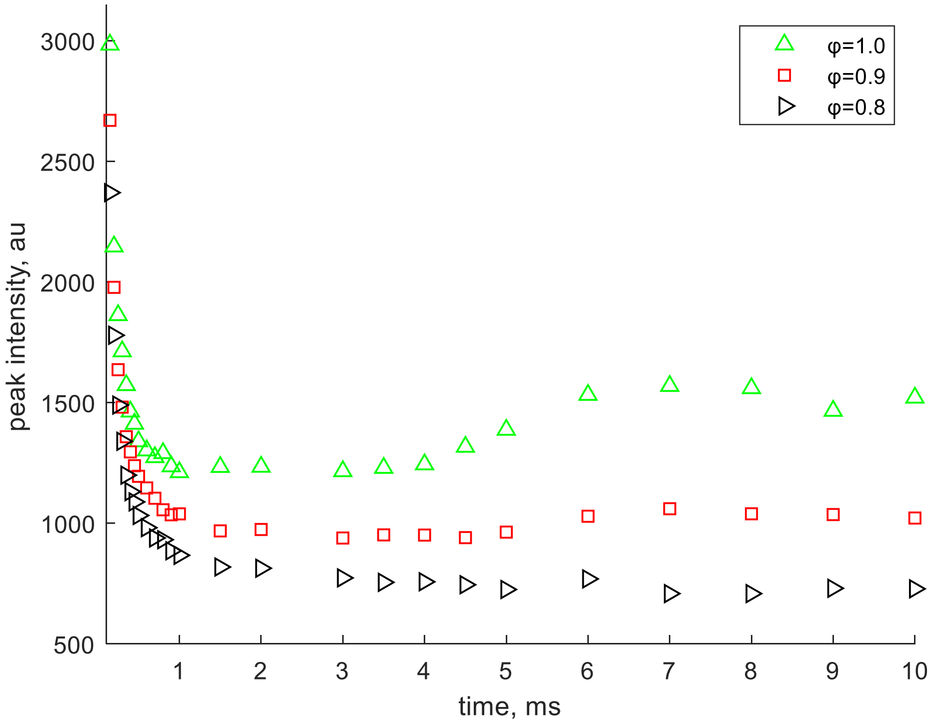

Figure 6.4: Peak OH* Intensities at varying Equivalence Ratios (Turbulent Mixtures)

Figure 6.5 - Figure 6.6 compares the spatially integrated OH* intensity with equivalence ratios (**φ**=1.0, 0.9, 0.8) for different CH_4/Air mixtures. For the laminar mixtures, the initial order of magnitude of integrated OH* intensity did not give any indication, however the time of transition from a decreasing trend to an increasing trend happened in the following order: **φ**=1.0< **φ**=0.9< **φ**=0.8. This may be an indication that chemical induction duration is shorter at **φ**=1.0 (i.e., 0.2 ms) and longer at **φ**=0.8 (i.e., 0.45 ms). Following ignition, the relative increase in production level of OH* radical was highest for the mixture with **φ**=1.0 and least for the mixture with **φ**=0.8 as indicated by the slope of the graphs. Similar trend is observed in the turbulent flows shown in Figure 6.6 with chemical induction being completed at 0.35 ms for the near stoichiometric mixtures while that of φ=0.8 was completed after 0.4 ms. From the plots, the initial order of integrated OH* intensity was 1.0< φ<0.8, however the relative production rate increased in the reverse order (i.e., 1.0> φ>0.8) until they converged at 2 ms. Beyond 2 ms, the effect of increase in fuel-air ratio was clearly marked by higher OH* intensity as well as an increasing rate of OH* production until about 6 ms when no further increase in relative OH* intensity could be observed. The sensitivity analysis further shows the variation is linear in laminar flows but non-linear in the turbulent case.

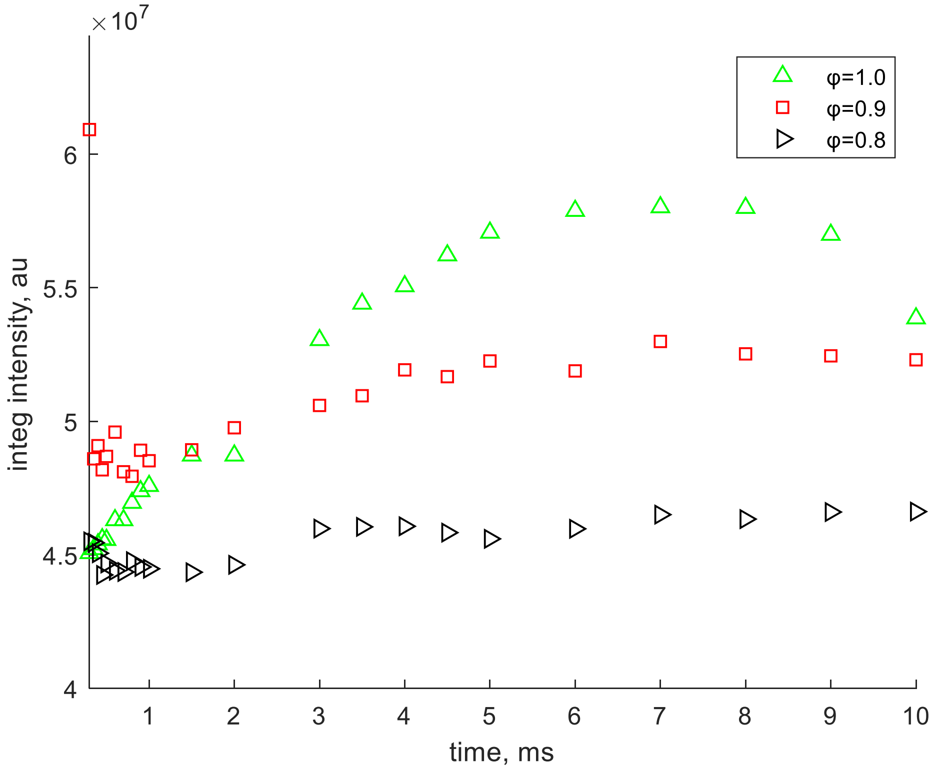

Figure 6.5: Integrated OH* Intensities at varying Equivalence Ratios (Laminar Mixtures)

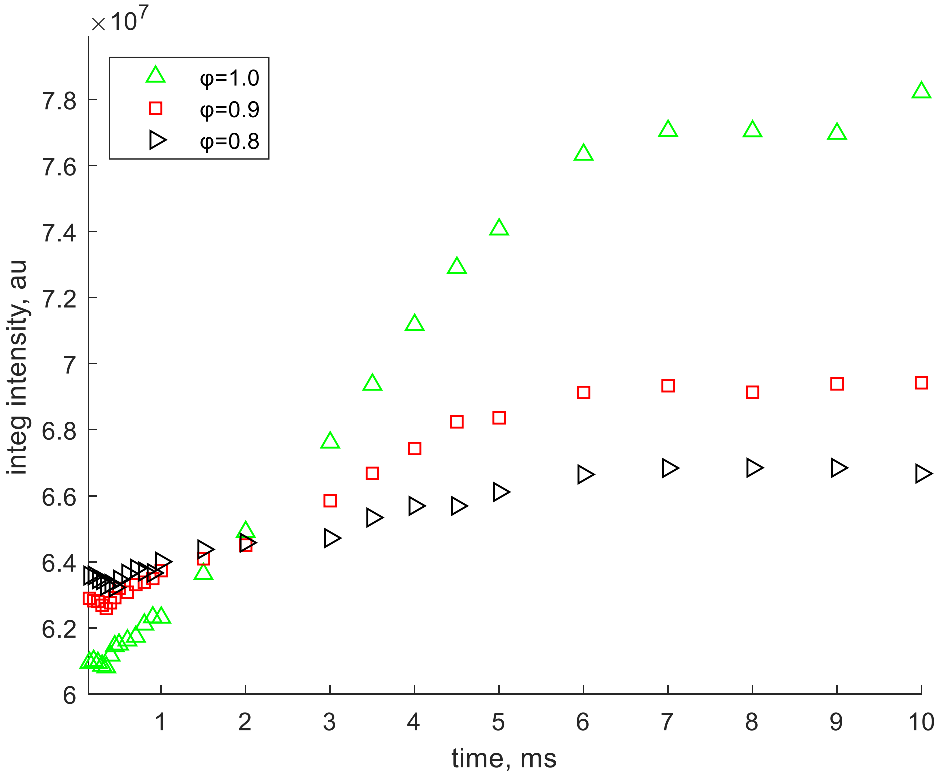

Figure 6.6: Integrated OH* Intensities at varying Equivalence Ratios (Turbulent Mixtures)

Figure 6.7 - Figure 6.8 compares the evolution of the axial flame tip locations with φ values (i.e., 1.0, 0.9, 0.8) for different CH_4/Air mixtures. A common trend from both plots is that the FF tip displacement (in both upstream and downstream directions) decreased from φ=1.0 to φ=0.8 and this was more prominent in the late developed stage (i.e., above 1 ms). According to Figure 6.7, the leanest flame kernel required 9 ms to travel 28 mm upstream compared to 7 ms required by the stoichiometric flame. An obvious distinction between both plots is that in the laminar flows the growth is nearly symmetric about the laser axis while in turbulent flows the growth symmetry is lost. The asymmetry in kernel growth under turbulent environment is due to convective effect of high flow velocity which results in a displacement of the kernel centroid from the initial location. It is also seen that the impact of high flow velocity is more prominent in lean mixtures than the stoichiometric. Further investigation of the 2D-scatter plot (see Figure 6.9) of the laminar mixtures did not show any peculiar variation in the horizontal location of the axial FF tip. The plot shows that stabilization of the upstream flames

produced in all the mixtures would more likely stabilize in the direction away from the laser source while the downstream flame would stabilize if the flame holder were placed along a horizontal axis as the ignition point. Unlike the laminar flows, the turbulent flow cases (Figure 6.10) show a tendency to blow-out, however the trends remain similar.

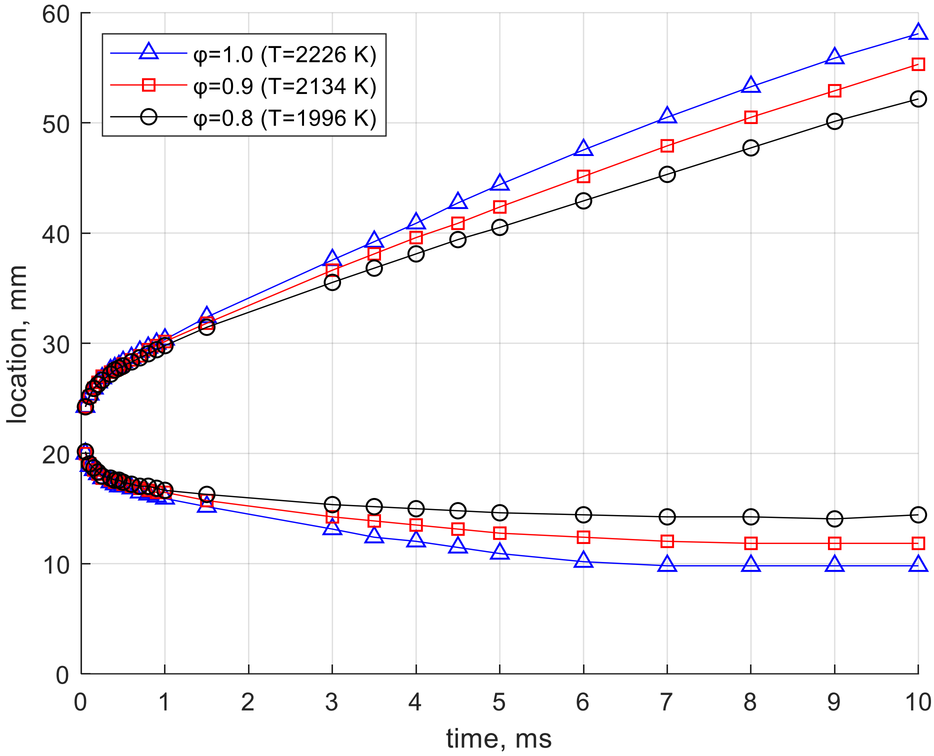

Figure 6.7: Axial Flame Front Locations at varying Equivalence Ratios (Laminar Mixtures)

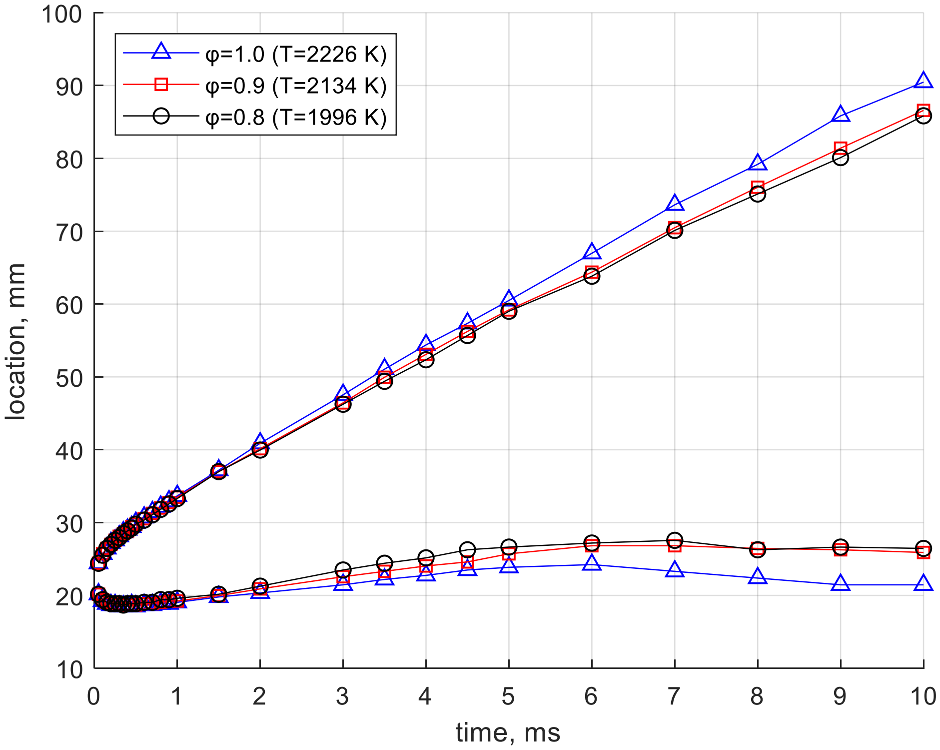

Figure 6.8: Axial Flame Front Locations at varying Equivalence Ratios (Turbulent Mixtures)

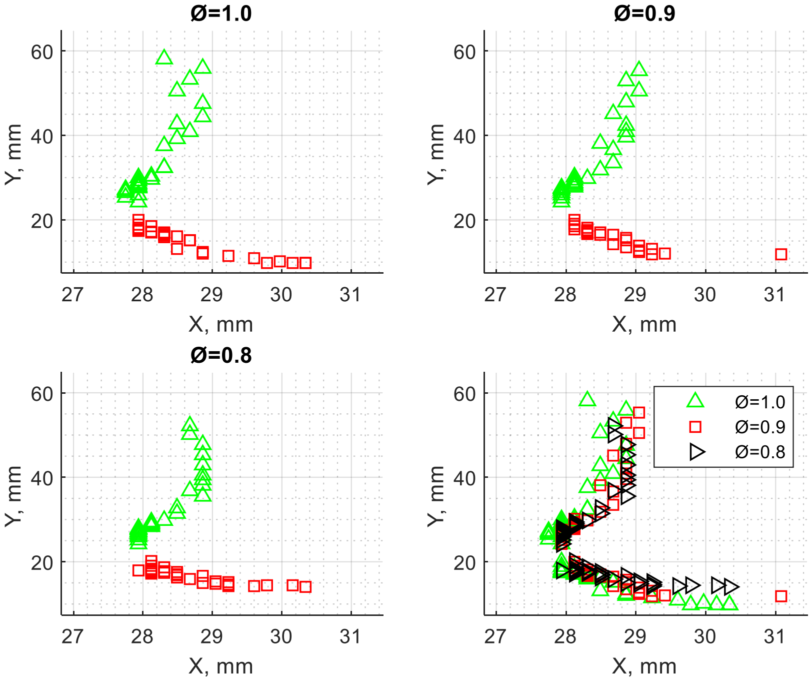

Figure 6.9: 2D Scatter Plot of Axial Flame Front Locations at varying Equivalence Ratios (Laminar Mixtures)

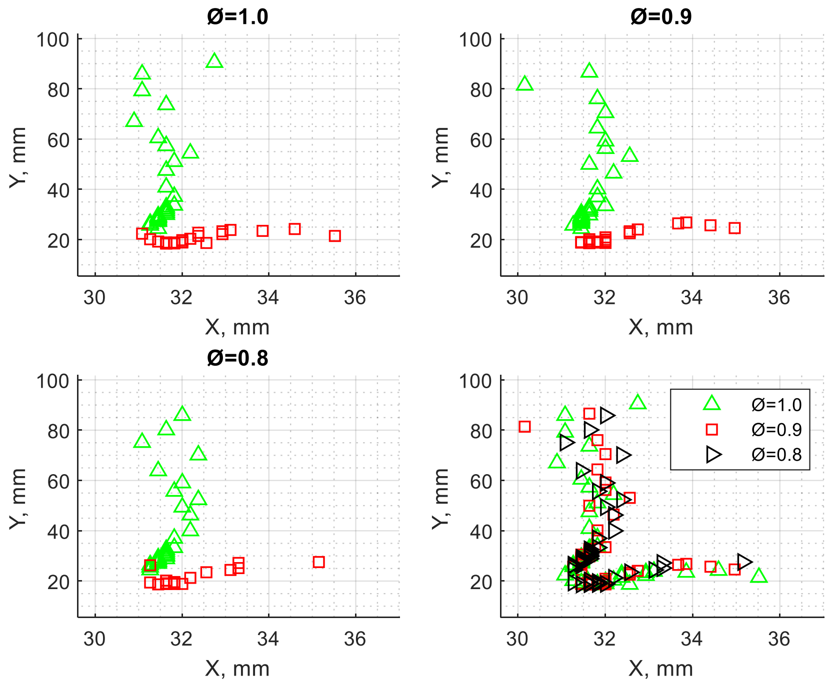

Figure 6.10: 2D Scatter Plot of Axial Flame Front Locations at varying Equivalence Ratios (Turbulent Mixtures)

Figure 6.11 - Figure 6.12 shows the variation of flame front propagation speed (S_y) with equivalent ratios (i.e., φ = 1.0, 0.9, 0.8) in CH_4/Air. The general trend is that S_y decreases asymptotically from a highly stretched initial propagation speed to a value close to the laminar growth rate (S_L). S_L is calculated from the product of the unstretched laminar flame velocity ($\mathbf{u}_L$) and the expansion coefficient ($\frac{\rho_u}{\rho_b}$):

$$S_L = \frac{\rho_u}{\rho_b} * u_L \qquad 6.1$$

where: ρ_u and ρ_u are the densities of the unburnt and burnt gas, respectively.

It is also evident from Figure 6.11 that the flame kernel development to a stable flame front evolved in three key transition stages as observed previously. For example, in the laminar mixture with φ=0.9, the first transition (which results from the front lobe development) was marked by stable S_{y+} value of 11 m/s at 200 μs, while the second transition (which marks the end of chemical induction) was indicated by another stable speed of 4 m/s at 350 μs. In the last stage of development, which began at 1.5 ms, a steady state value of 2.96 m/s was maintained. Contrary to expectations from mixtures of different S_L values, there was no noticeable variation S_{y+} with changing φ until about 1.5 ms. The same trend is observed in the kernel development for the turbulent mixtures as shown in Figure 6.12. This behaviour could be linked to the different level of stretch experienced by different mixture flame kernels. From 1.5 ms onwards, the variation of propagation speed with equivalence ratio occurred in the correct order of magnitude as the laminar unstretched growth rate, S_L of each mixture. A similar trend is observed in the turbulent flow mixtures as shown in in Figure 6.12. Just like the laminar flow mixtures, the decay from a high initial velocity to a more stable velocity involved two transition phases before reaching a stable velocity of about 7 m/s within 350 µs. Unlike the laminar mixtures, all the three equivalence ratios were marked by velocity fluctuations between 7 m/s and 11 m/s from this point until 700 µs before travelling steadily at 7 m/s. There were also no noticeable differences in the magnitude of S_y until 1.5 ms when it decreased due to reduction in φ values. In addition, S_{y+} was marked by some degree of fluctuations unlike the laminar mixtures.

To better understand the relative variation in growth rate with equivalence ratios, the axial flame front propagation speed is normalised by the unstretched laminar flame speed. Figure 6.13 - Figure 6.14 compares the normalised propagation speed of the axial flame front with the corresponding equivalent ratios (i.e., φ = 1.0, 0.9, 0.8) in laminar and turbulent mixtures, respectively. The deviation in S_y from the dashed lines gives the measure of the stretch experienced by the flame front. The Geometric Stretch (K) values for an outwardly propagating spherical flame of radius (r), can be evaluated using the below equation [90]:

$$K = \frac{2}{r} * \frac{dr}{dt} \qquad 6.2$$

In the present case, r could be replaced by Y_+ or Y_- while $\frac{dr}{dt}$ could be replaced with S_{Y+} or S_{Y-}. Analysis of the downstream flame front shows that the propagation rate, S_{y+} decreased from an initially stretched value until it converges to a steady value close to the unstretched laminar value, S_L. For the kernels propagating in laminar mixtures, measurement reveals that the most stretch occurred in the leanest mixture with adiabatic flame temperature of 1996 K (i.e., S_{Y+} @ 0.8φ =

$1.33S_L$) while the least stretch occurred in the stoichiometric mixture with adiabatic flame temperature of 2226 K (i.e., S_{Y+} @ $1.0\varphi = 1.08S_L$). A similar trend is observed in the flame kernels propagating in turbulent mixtures but with negative stretch impact such that the normalised S_{y+} values at steady state lie below the 1.0 line. Analysis of the upstream flame front shows that the propagation rate, S_{y-} continues to decrease after reaching the unstretched value S_L before converging to its asymptotic values. In both laminar and turbulent flame kernels, the stretch sensitivity to leaning appear in the reverse order with the leanest mixture being the most negatively stretched.

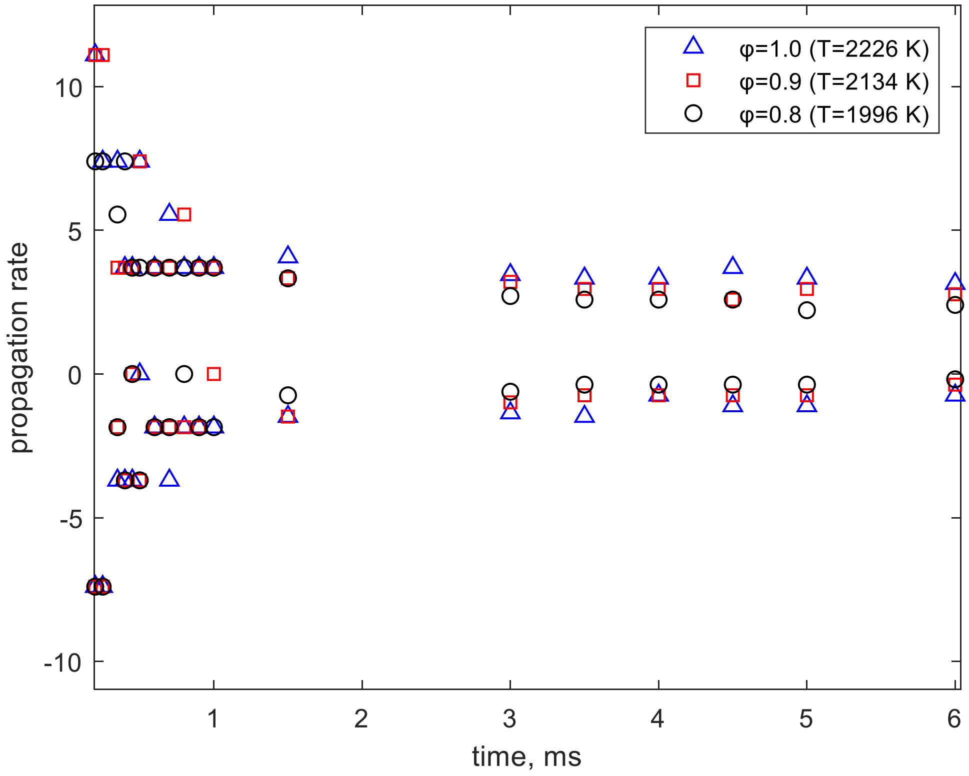

Figure 6.11: S_{y+} for varying φ (Laminar Mixtures)

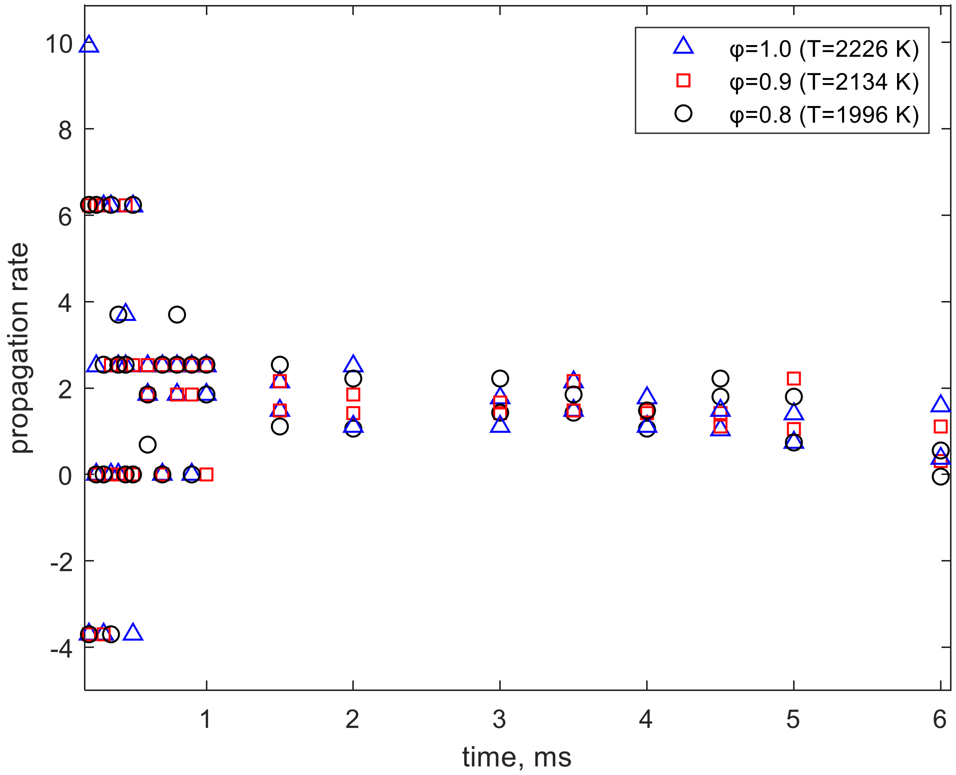

Figure 6.12: S_{y+} for varying φ (Turbulent Mixtures)

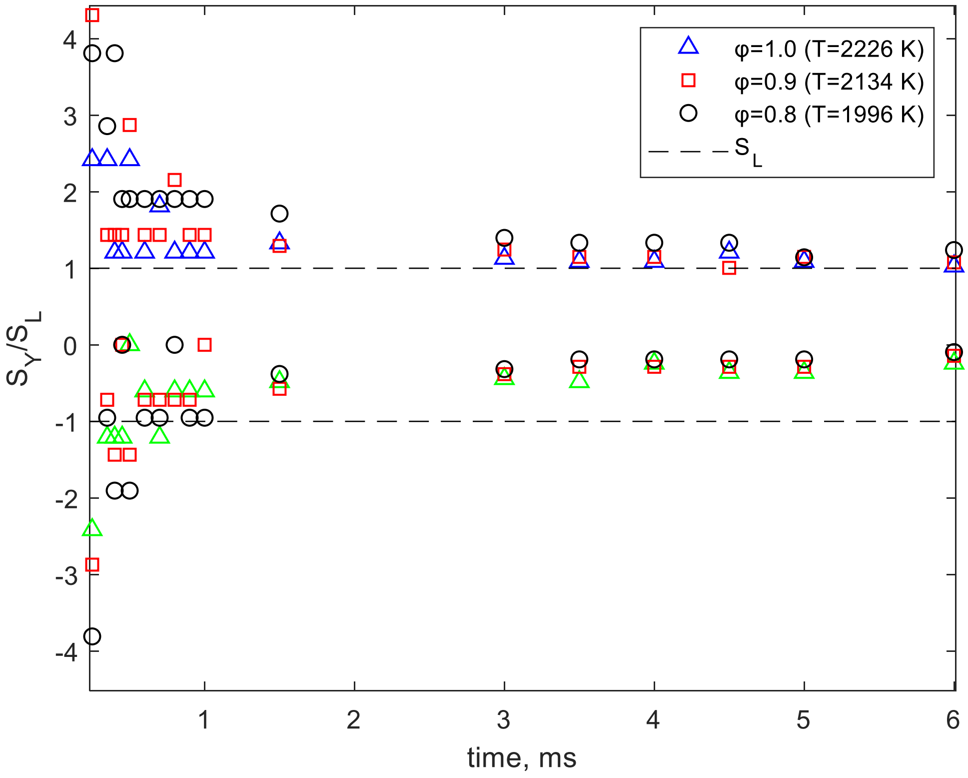

Figure 6.13: S_{y+}/S_L for varying φ (Laminar Mixtures)

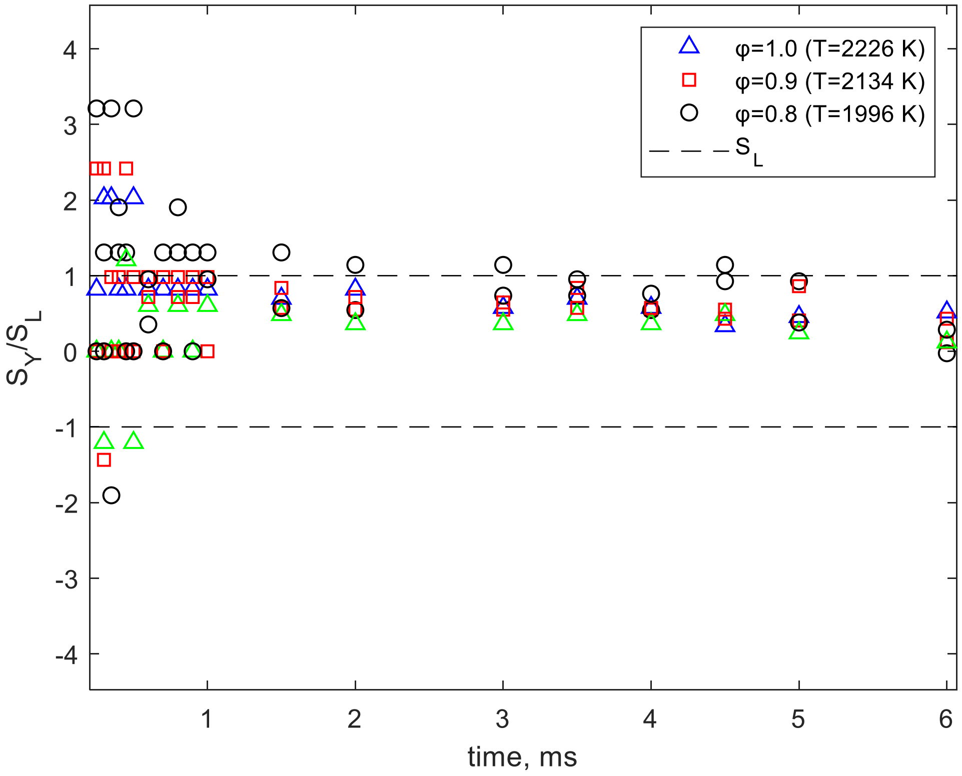

Figure 6.14: S_{y+}/S_L for varying φ (Turbulent Mixtures)

6.3 Fuel effects based on constant adiabatic flame temperature.

It is well known that the adiabatic flame temperature, T_{ad} through the Arrhenius kinetics exerts a dominant influence on the burning velocity since it is directly linked with the heat of combustion of the fuels [109]. Therefore, a means to experimentally determine the actual influence of the selected fuel on the propagation of the flame is by comparing fuel/air mixtures with different chemical composition but constant flame temperature. In this section, the effect of fuel on the flame kernel characteristics of three gaseous fuels (methane, propane and ethylene) with constant T_{ad} is investigated. The investigation is approached systematically from two angles. First, three laminar mixtures (i.e., CH_4/air @ $\varphi=1.0$, C_3H_8/air @ $\varphi=0.94$ and C_2H_4/air @ $\varphi=0.84$) with constant Tad (i.e., 2226 K) were first selected and their kernel characteristics compared to quantify the differences due to fuel type. This is followed by further investigation of the observed flame kernel characteristics under leaner mixtures (i.e., CH_4/air @ $\varphi=0.9$, C_3H_8/air @ $\varphi=0.86$ and C_2H_4/air @ $\varphi=0.78$) with a constant reduced Tad (2134 K). Overall, a total of six (6) flow conditions were compared as given in Table 6.2. The mixture ratios were selected based on the T_{ad} vs. φ plot obtained using GASEQ chemical equilibrium software [110] as shown in Figure 6.15. Besides T_{ad} being constant, the mixtures were selected such that all experimental conditions including the bulk flow velocity were kept constant.

Table 6.2: Summary of selected Laminar Flow conditions based on constant T_{ad}.

Test Case	φ	Flow Rate (lpm)				U_0 (m/s)	R_e (Pa.s)	T_{ad} [110] (K)	u_L [112] (cm/s)	$\frac{\rho_u}{\rho_b}$
		Air	CH_4	C_3H_8	C_2H_4					
Laminar mixture @ 2226 K	1.00	23.8	2.5	0.00	0.00	1.15	1694	2226	41.0	7.47
	0.94	25.3	0.0	1.00	0.00	1.17	1718		41.6	8.71
	0.84	25.5	0.0	0.00	0.90	1.19	1750		51.8	7.47
Laminar mixture	0.9	24.3	2.3	0.00	0.00	1.17	1718	2134	36.0	7.16
	0.86	26.3	0.0	0.95	0.00	1.19	1859		37.2	8.35

@ 2134 K	0.78	25.9	0.0	0.00	0.85	1.17	1777		45.0	7.16

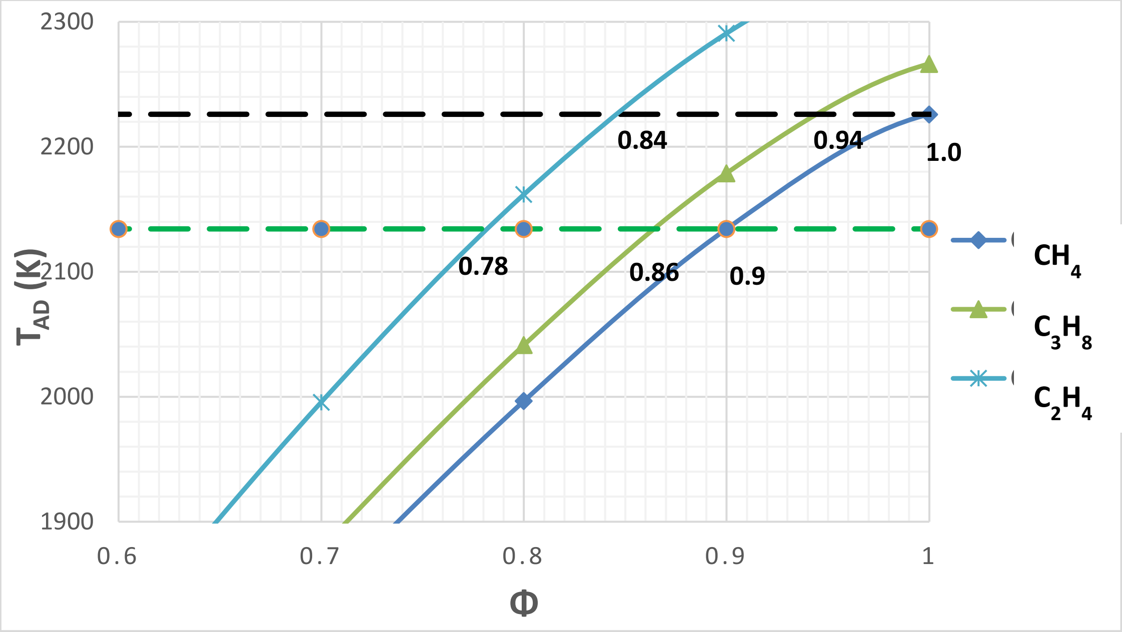

Figure 6.15: Selected flow conditions on T_{ad} – φ plots [110].

Figure 6.16 are sequences of mean OH* chemiluminescence images which visualizes the comparative characteristics of the three laminar fuel/air mixtures (i.e., CH_4/air @ φ=1.0, C_3H_8/air @ φ=0.94 and C_2H_4/air @ φ=0.84) with the same T_{ad} value of 2226 K. As expected, all the flame kernels exhibit common geometric features in their development (i.e., evolved from a two-lobe symmetric toroid to a three-lobe asymmetry and finally to a flame ball). However, there are significant differences in their growth which is obvious from 1 ms onwards. The first observation from the sizes of the late kernels is that propane experiencing the slowest growth while methane experienced the fastest growth. Another difference shown by the images is that between 0.5 and 3 ms, the front lobe of the propane flame kernel was the most stretched leading to an early local quenching which may have affected its growth rate compared to those of methane and ethylene. Comparing the flame kernels of both methane and ethylene, it appears that the difference in growth rate is mostly significant in the upstream flame front with higher strain effect on ethylene flame than the methane flame.

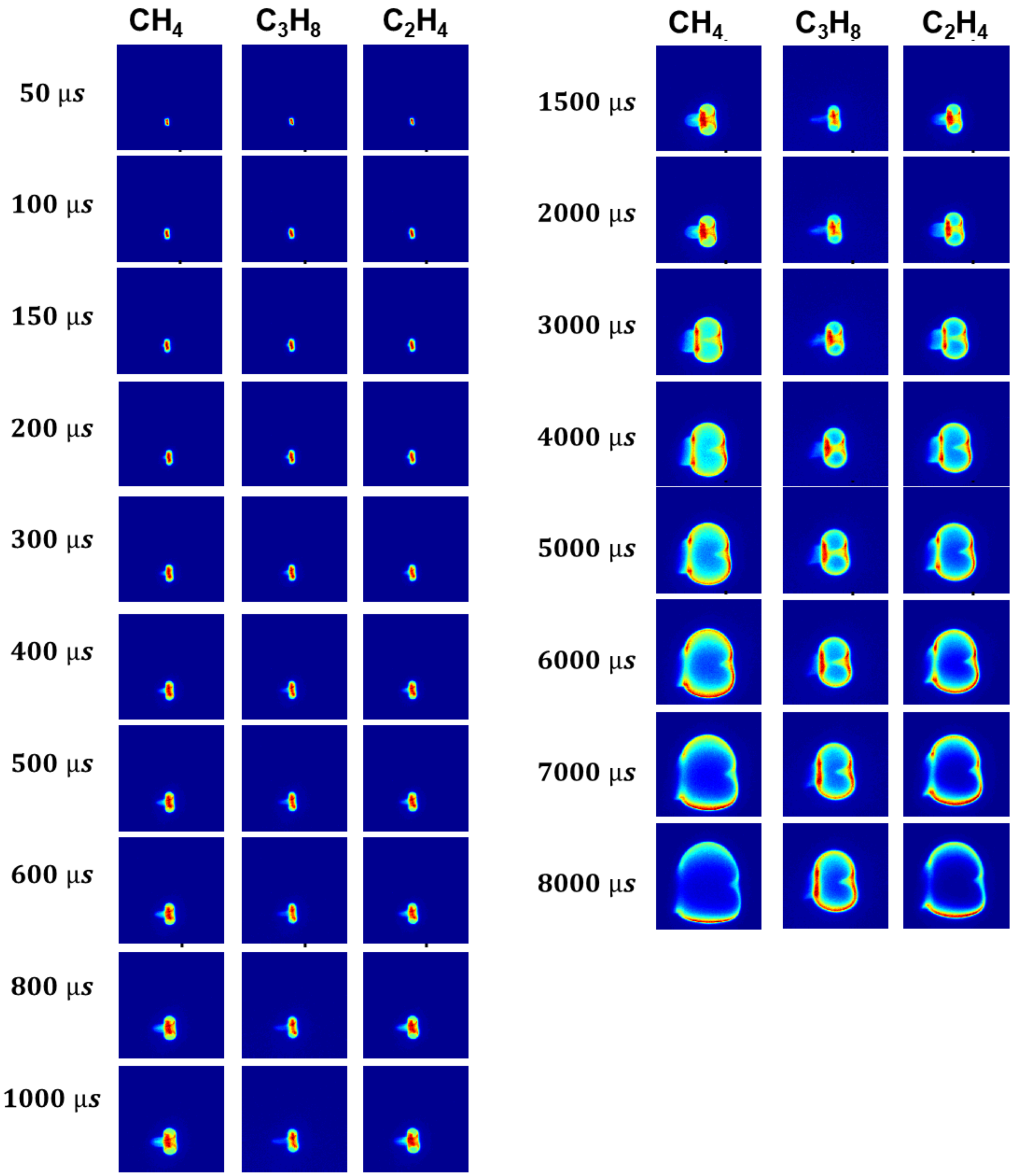

Figure 6.16: Visualization of Flame Kernel Development in mixtures at 2226 K (Image FOV: 56x56 mm^2)

Figure 6.17 - Figure 6.18 compares the peak OH* intensities obtained from the flame kernels of the three fuels at 2226 K and 2134 K respectively. Similar to the results reported in section 6.2, the peak intensity of the flame kernel for each fuel dropped at lower adiabatic flame temperature. The main observation from both graphs is that for the same adiabatic temperature, the order of peak intensity values is C_2H_4>CH_4>C_3H_8. Therefore, it can be inferred that ethylene produced the most reactive flame kernel while propane produced the least reactive flame kernel. Although the CH_4 and C_3H_8 kernels has similar initial values at 150 µs, the CH_4-flame kernel recovered more quickly from the initial rapid cooling, thus its peak intensity became higher than the C_3H_8 flame kernel. Based on the C/H ratios, it is expected that methane with lower C/H will be more reactive than propane just as observed. While the C/H may be higher for ethylene than the rest, the unstable double bonds present no doubt played a role in its high reactivity. In addition, the slow reactivity of the propane kernel could be associated with heat losses due to excessive stretching of the front lobes which persisted until 2 ms.

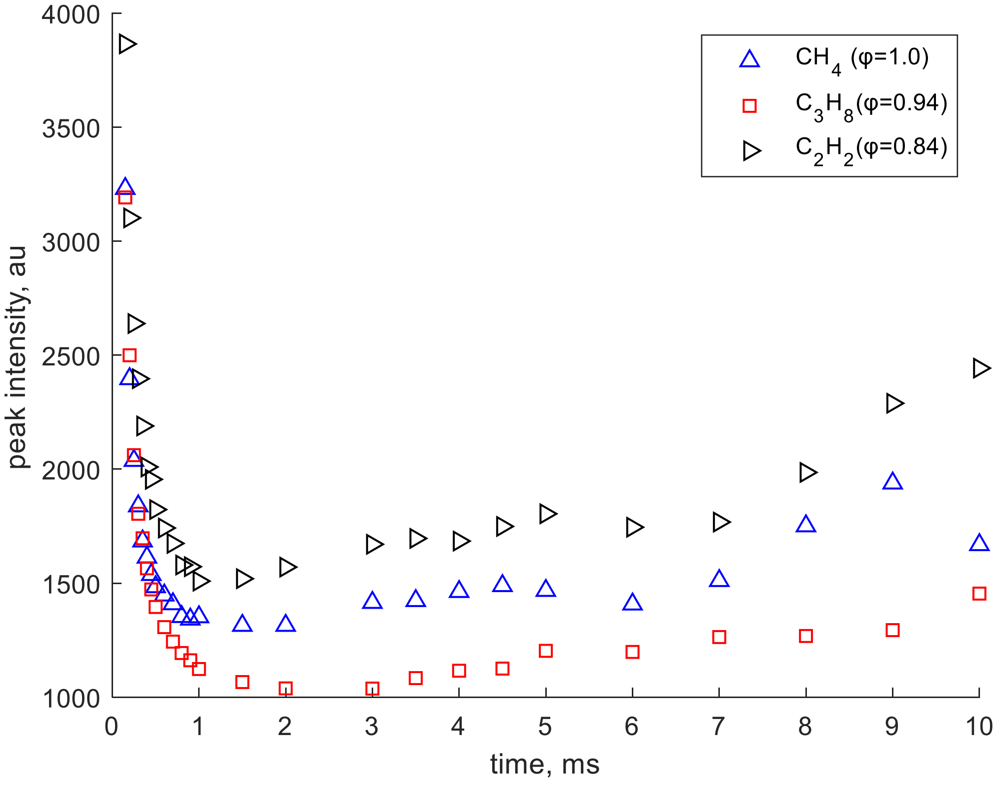

Figure 6.17: Peak OH* Intensity at 2226 K

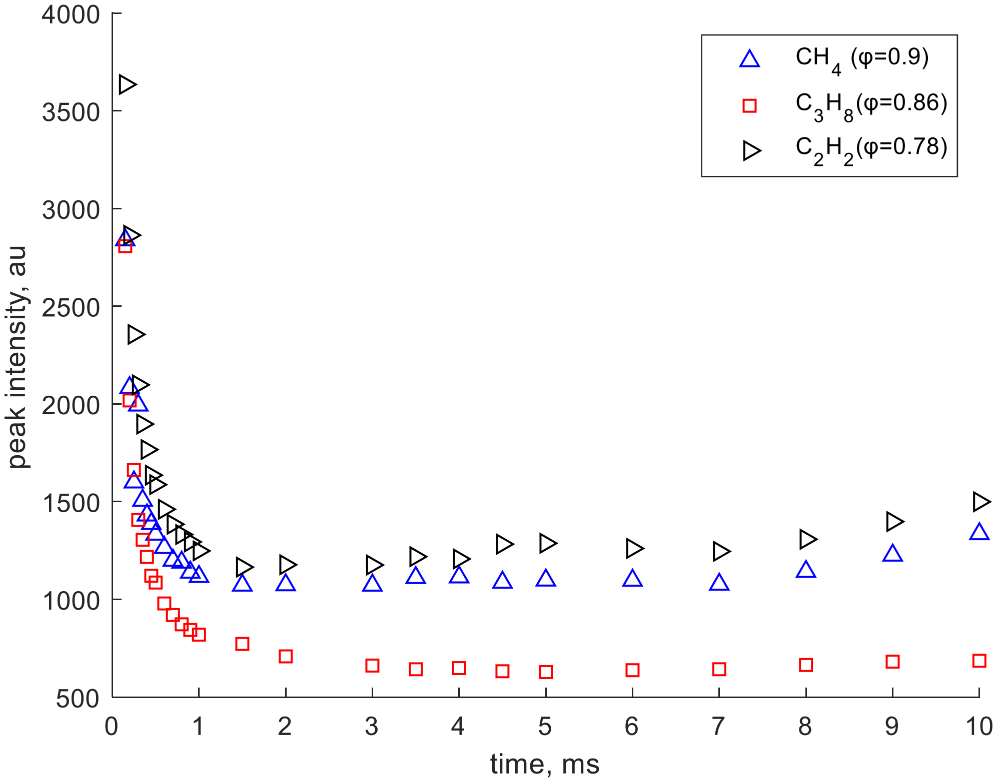

Figure 6.18: Peak OH* Intensity at 2134 K

Figure 6.19 - Figure 6.20 compares the spatially integrated OH* intensities obtained from the flame kernels of the three fuels at 2226 K and 2134 K respectively. Similar to the peak intensities, the relative order of magnitudes of integrated intensities is C_2H_4>CH_4>C_3H_8. Therefore, it can be inferred that the rate of heat release was highest in the ethylene flame kernel and lowest in the propane flame kernel. A second noticeable difference is the time it takes for the integrated OH* intensity values to drop to its minimum before rising again which had earlier been referred as the possible duration of chemical induction. According to Figure 6.19, the duration of chemical induction occurred in the following order: 200 µs in CH_4, 300 µs in C_3H_8 and 500 µs in C_2H_4. Although, chemical induction in propane ended much earlier than in ethylene, the radical generation rate is counterbalanced by losses resulting from rapid cooling of the overstretched kernel until 1 ms, hence the wider gap between the two. In the methane kernel the losses

is minimal, hence the closer gap between methane and ethylene despite having the initial value of integrated intensity being similar to the propane kernel at 150 μs.

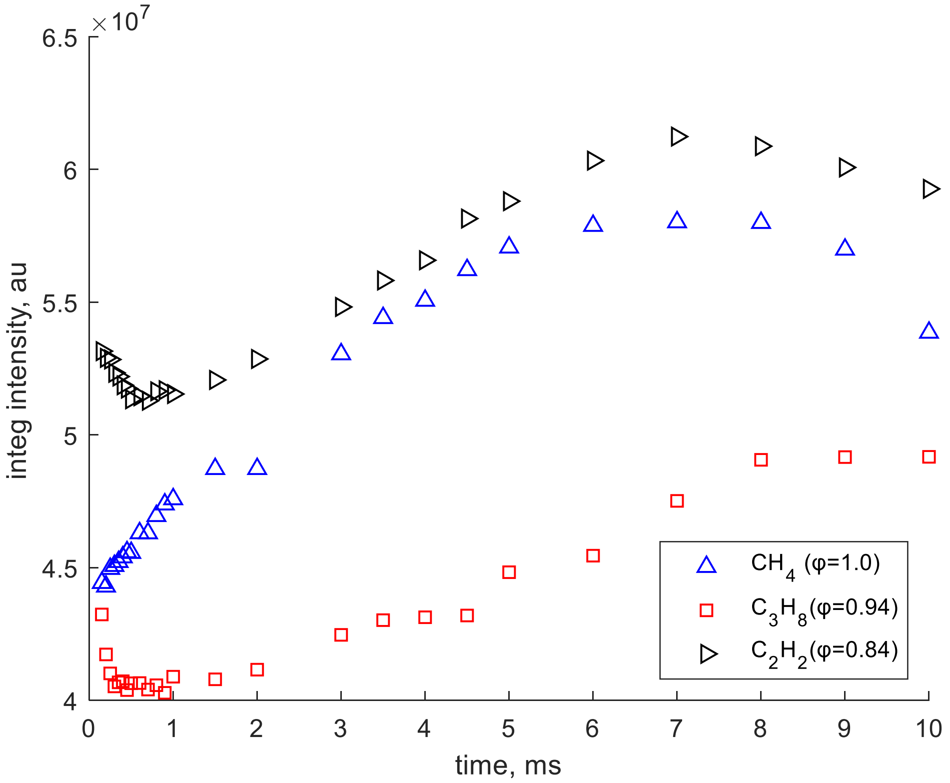

Figure 6.19: Integrated OH* Intensity at 2134 K

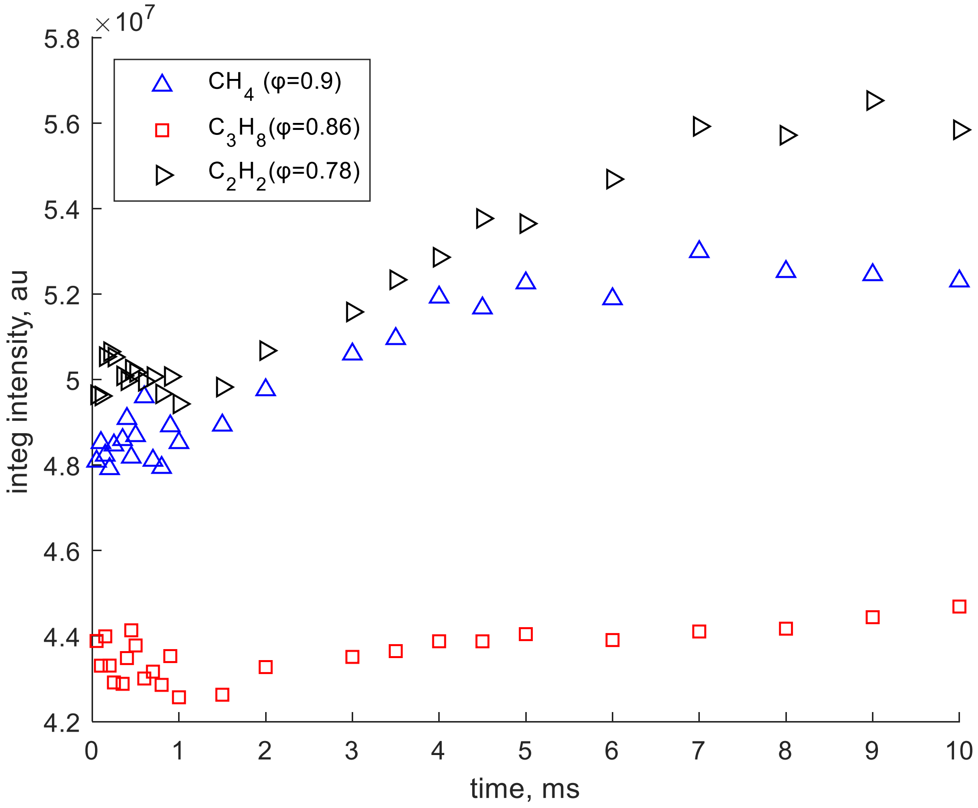

Figure 6.20: Integrated OH* Intensity at 2134 K

Figure 6.21 - Figure 6.22 compares the displacement of the flame front tip along the flow axis for the three fuel mixtures at 2226 K and 2134 K, respectively. As noted previously, the general trend in flame front displacement evolved from a decaying growth pattern in the 1 ms to a steady linear growth pattern onwards. Although flame kernels with the same adiabatic flame temperature were involved, clear differences can be seen beyond 1 ms when steady growth of the flame front is observed both upstream and downstream. Downstream, the propane kernel experienced the least growth while methane and ethylene grew at the same rate. Upstream the respective order in magnitudes was methane>ethylene>propane with maximum flame front displacement limits of 12.3, 9.9 and 6.7 mm respectively. The observed differences show the variation in stretch level of the upstream flame front due to the strain imposed by the flow. Also, the differences in growth of the flame kernels may be attributed to the differences in the mixture

Lewis Number (Le) values of the flow which in turn is inversely proportional to the unburnt mixture density. The Lewis number (Le) is defined as the ratio of thermal diffusivity (α) to mass diffusivity (D) and it's given by the equation [160]:

$$Le = \frac{\alpha}{D} = \frac{\lambda}{\rho_u * c_p * D_m} \qquad 6.3$$

where: λ is the thermal conductivity, ρ_u is density of the unburnt mixture, c_p is the specific heat capacity at constant pressure, and D_m is the mixture-averaged diffusion coefficient.

Of the three mixtures (i.e., CH_4/air @ φ=1.0, C_3H_8/air @ φ=0.94 and C_2H_4/air @ φ=0.84) with AFT of 2226 K, methane is the only fuel lighter than air and the Le value of stoichiometric CH_4/air mixture is unity (i.e., φ=1.0, Le=1). In contrast, propane is the heaviest of the three fuels and the Le value of C_3H_8/air mixture (φ=0.94, Le=1.4) is the highest of the three. In [161], it was noted that mixtures with higher Le values would require a larger critical radius to be achieved for the flame to be sustained. Likewise, in the current investigation, the CH_4/air mixture with the least Le value would require lower **MIE** and less time to develop into a self-sustained flame kernel compared with the C_3H_8/air mixture. Hence, the order of duration in reaching a self-sustainable flame kernel is methane, ethylene, propane. A similar trend in axial FF distances is observed in leaner fuel/air mixtures (CH_4/air @ φ=0.9, C_3H_8/air @ φ=0.86 and C_2H_4/air @ φ=0.78) with Tad=2134 K as shown by Figure 6.22. However, the differences become wider which is in accordance with their Le values. For fuels heavier than air (e.g., C_3H_8, C_2H_4) Le values increases with reduced φ values while the reverse is the case for fuels lighter than air (e.g., H_2, CH_4)[162].

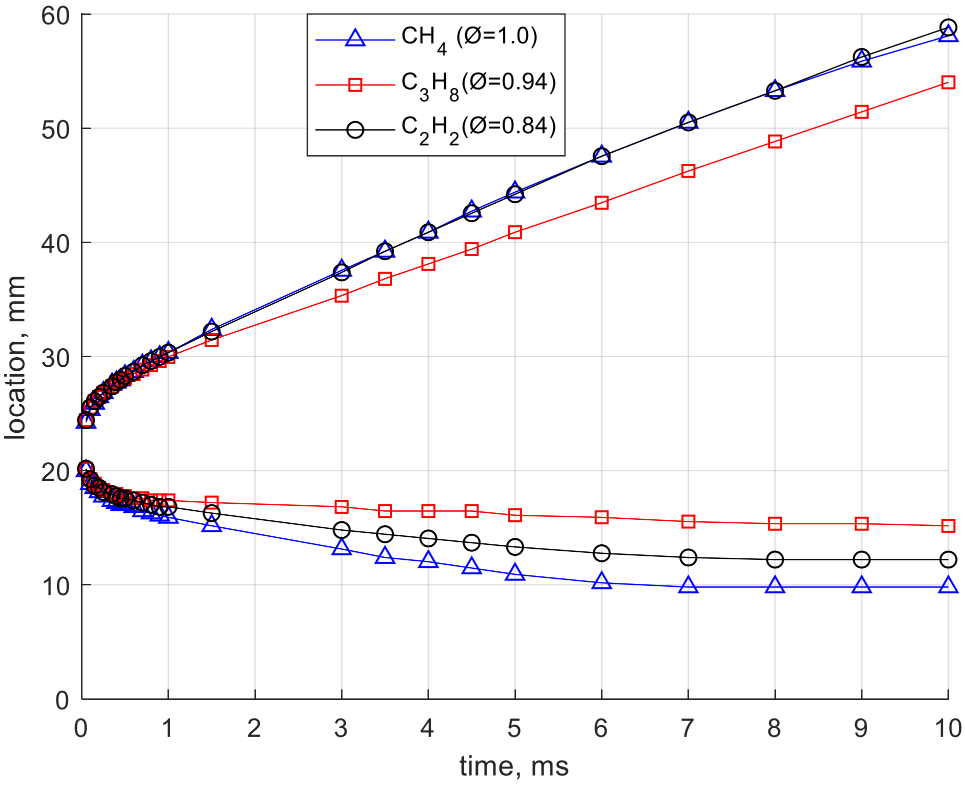

Figure 6.21: Axial Flame Front Locations at 2226 K

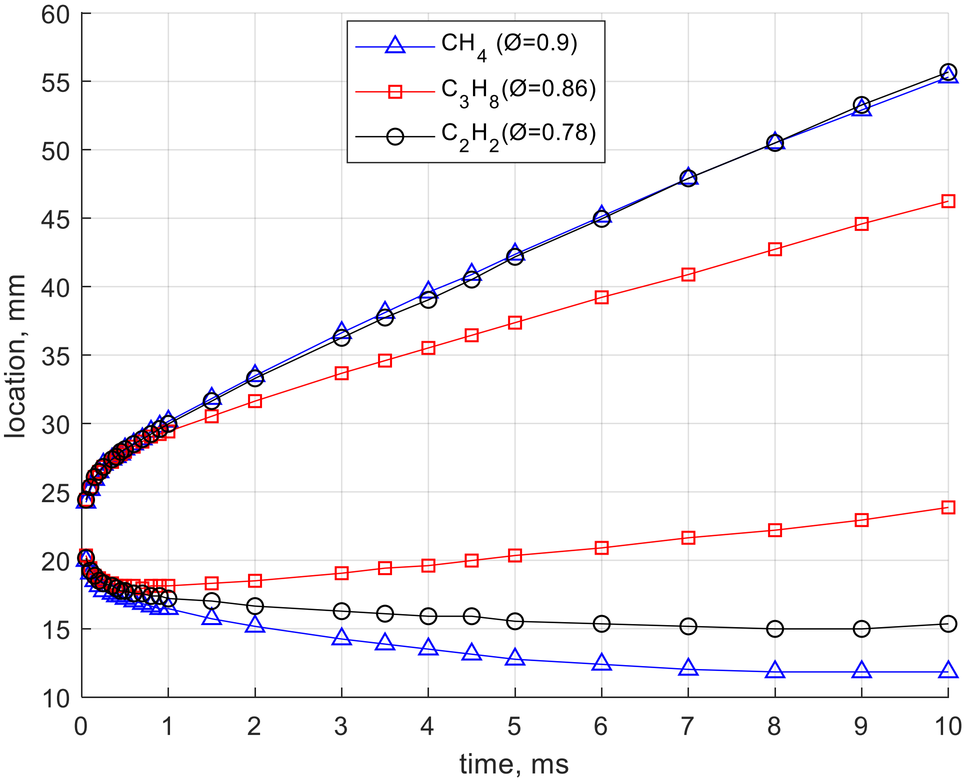

Figure 6.22: Axial Flame Front Locations at 2134 K

Figure 6.23 - Figure 6.24 compares the axial flame front propagation speed of the three mixtures at 2226 K and 2134 K adiabatic flame temperatures, respectively. As noted previously, the general trend for all the mixtures is that S_y decreases asymptotically from an initially stretched value to a steady value close to the unstretched laminar flame speed. However, obvious differences can be seen in the steady state propagation rates of each flame kernels. For example, at 2226 K flame temperature, the respective steady state S_{y+} values were 3.45, 3.45 and 2.49 m/s for methane, ethylene, and propane while the S_{y-} values were 1.35, 0.98 and 0.24 m/s respectively. Based on the S_{y-} comparison, it can be deduced that the propane mixture produced the slowest growing kernel while the methane mixture produced the fastest growing kernel despite having the same adiabatic flame temperature. This is unexpected because ethylene has the highest estimated laminar flame speed (i.e., S_L = 3.87 m/s for C_2H_4/air) while methane has the least value (i.e., S_L = 3.06 for CH_4/air). By igniting leaner mixtures with reduced flame temperature of 2134 K, a similar trend is repeated with the respective S_{y-} values

of methane, ethylene and propane reduced by 32, 62 and 329% respectively. This behaviour reaffirms the earlier assertion that flame kernels of the different fuels may be stretched differently by the same amount of flow-imposed strain despite having the same flame temperature and the stretch may increase at lower flame temperatures.

To better illustrate the relative differences in growth rate, the axial flame front propagation speed is normalised by the unstretched laminar flame speed. Figure 6.25 - Figure 6.26 compares the normalised propagation speed of the axial flame front for the three fuel blends with adiabatic flame temperatures of 2226 K and 2134 K respectively. The first observation from the results is that as the kernels grew in in size, the propagation rate of the downstream flame front decreases until it converges to a value close to the unstretched laminar value, S_L. In contrast, the propagation rate of the upstream flame front continues to decrease after reaching the unstretched value S_L before converging to its asymptotic values. This is shown by the fact that the normalised S_{y-} values lie farther above the -1.0 line unlike the normalised S_{y+} which lie somewhat around the 1.0 line. This behaviour indicates a negatively stretched flame front which could be due to several factors. One of the factors noted previously is that the flame front is impacted by flow-induced strain. The impact flow-induced strain could be in the form of wrinkling which could lead to differences in the surface area between the upper and lower flame front [163]. It could also be that the local S_L values have changed due to varying compression of the mixture in both the upstream and downstream region by the expanding flame kernel [90]. Another factor responsible for different stretching of the upper and lower flame fronts is the different curvature of the flame surface. Overall, the stretch increased when the mixtures were leaned (i.e., lowered flame temperature). A second feature observed from the results is the differences in stretch sensitivity of the flame kernels due to different fuel composition despite having the same flame temperature. For example, at 2226 K flame temperature, S_{y+} variation from S_L were +8.7%, -13.9% and -28.5% for methane, ethylene, and propane respectively while the respective S_{y-} variation from S_L were -64%, -81% and -100%. Following a reduction in flame temperature from 2226 K to 2134 K, wider differences were observed. For example, at 2134 K flame temperature, S_{y+}

variation from S_L were -4%, -24% and -49% for methane, ethylene, and propane respectively while the respective S_{y-} variation from S_L were -76%, -91% and -120%. Therefore, it can be deduced that propane kernel is the most sensitive to stretch while methane kernel is the least sensitive to stretch. The measure of flame sensitivity to stretch is given by the Markstein Length (ℓ) which in turn depends on the Effective Lewis Number, Le of the mixture. This is shown by equation 6.4, in which the stretched flame speed (S_f) is expressed as the difference between unstretched laminar value, S_L and the product of Markstein Length, ℓ and the stretch rate, K [162].

$$S_f = S_L - \ell * K \qquad 6.4$$

Just like Le, the variation of ℓ with mixture composition widens as the flow becomes leaner. The reason is that in the lean range, Le increases for fuels heavier than air (e.g., C_3H_8, C_2H_4) and decreases for fuels lighter than air (e.g., H_2, CH_4). By comparing both plots, it is obvious the variation of Sy- from S_L (or the stretch level) is widened by a decrease in mixture AFT from 2226 K to 2134 K.

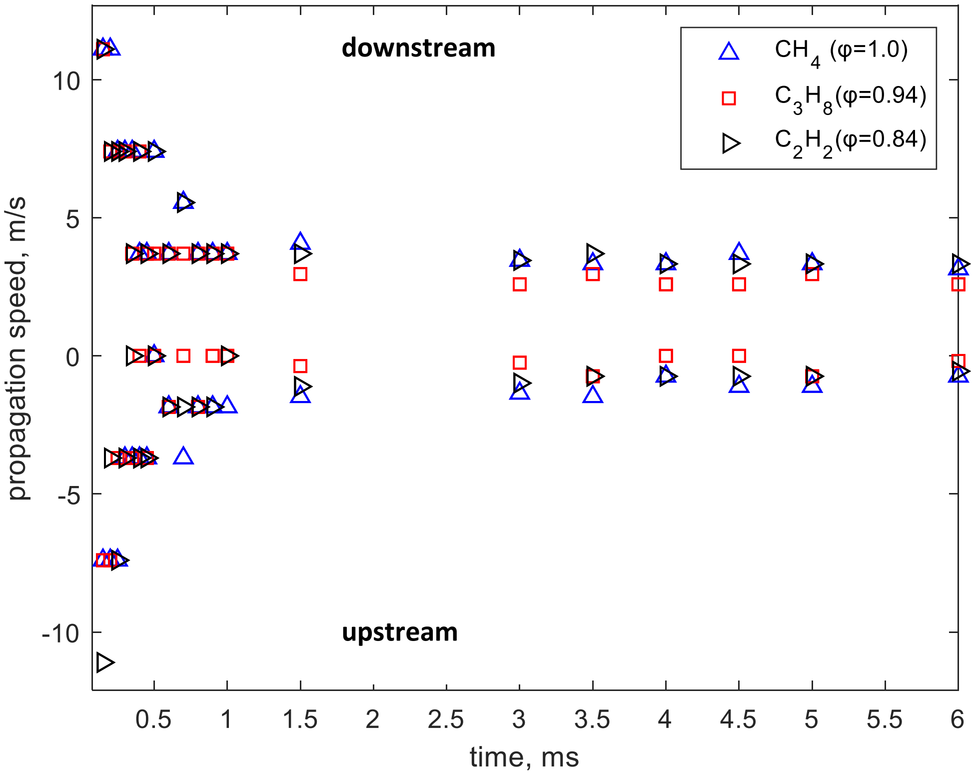

Figure 6.23: Axial flame front propagation rate at 2226 K

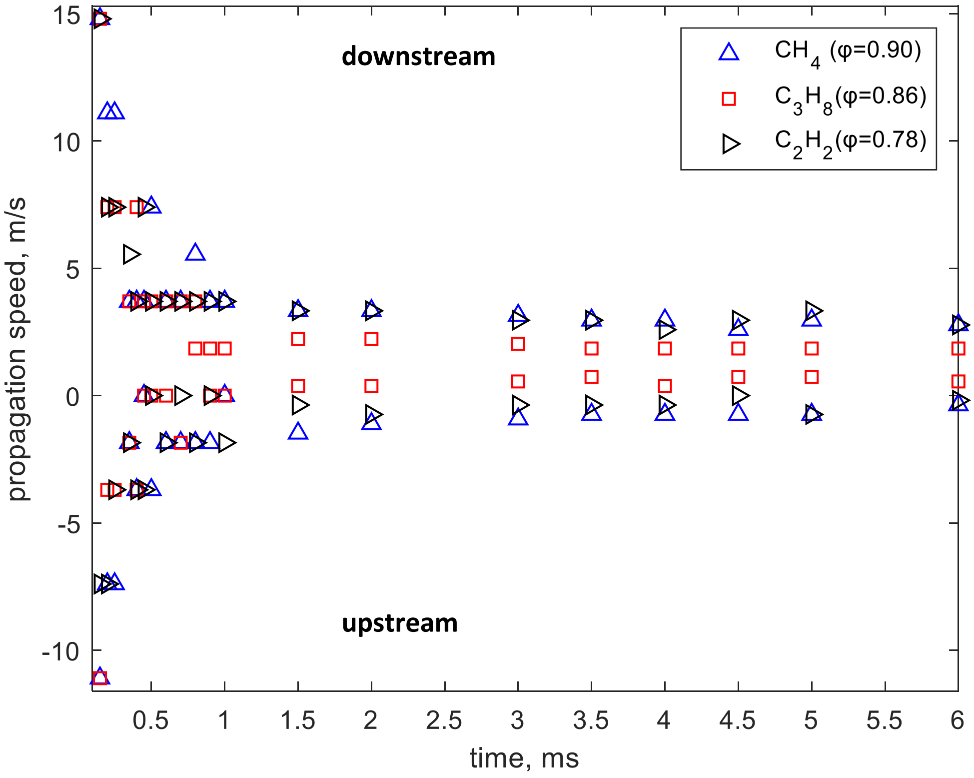

Figure 6.24: Axial flame front propagation rate at 2134 K

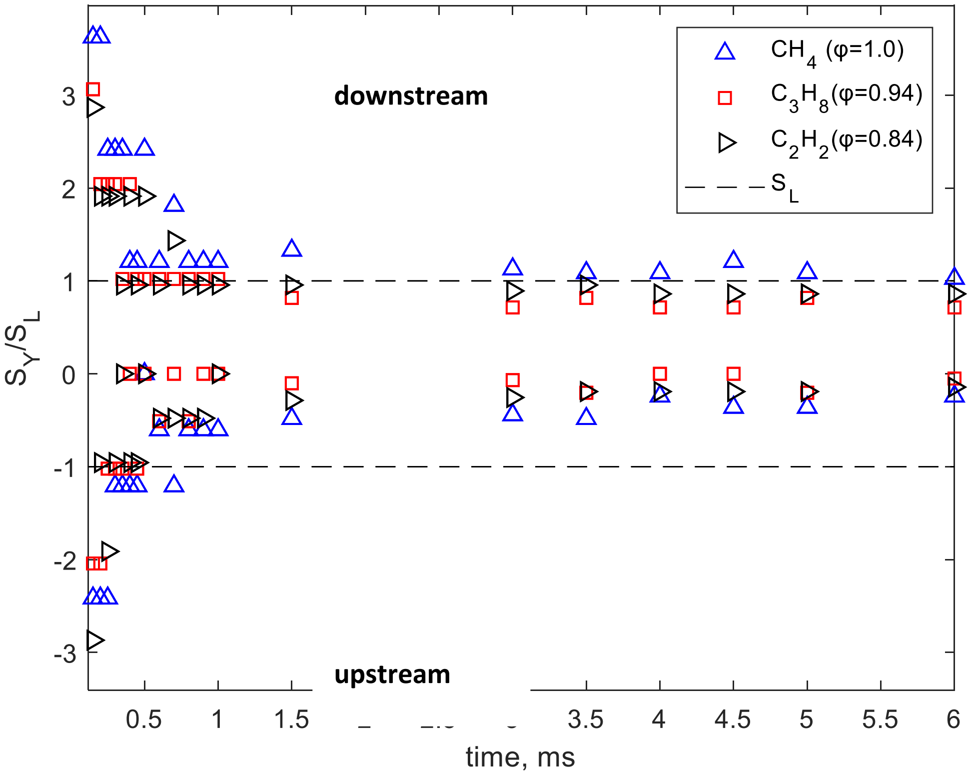

Figure 6.25: Normalised flame propagation rate at 2226 K

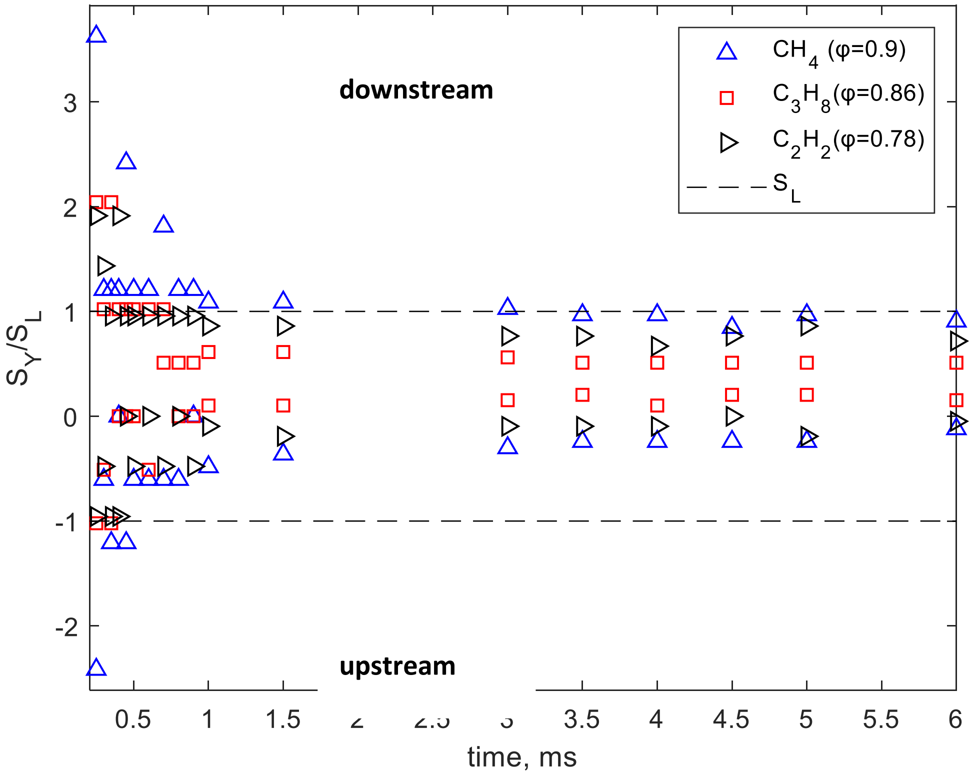

Figure 6.26: Normalised flame propagation rate at 2134 K

6.4 Fuel effects based on constant unstretched laminar flame velocity.

To further establish the influence of fuel properties on the propagation of the laser-ignited flame kernel, flow mixtures with different chemical composition are varied in such a way that a constant laminar flame velocity (LFV) is maintained. In this section, the effect of the fuel on the characteristics of the flame kernel is reported for three gaseous fuel/air mixtures (CH_4/air, C_3H_8/air, and C_2H_4/air) with the same LFV. At first, OH* chemiluminescence images of the flame kernels of three laminar mixtures (i.e., CH_4/air @ $\varphi=1.0$, C_3H_8/air @ $\varphi=0.92$ and C_2H_4/air @ $\varphi=0.74$) with a LFV of 41 m/s were obtained and their characteristics compared to quantify the differences due to fuel type. This was followed by further investigation of the characteristics under leaner mixtures (i.e., CH_4/air @ $\varphi=0.9$, C_3H_8/air @ $\varphi=0.84$ and C_2H_4/air @ $\varphi=0.7$) with SL value of 29 cm/s. Overall six (6) flow conditions were investigated which are given in table 6.3. From the table, it is evident that mixtures with the same LFV may have varying AFT. A graph showing the selected mixture composition in the S_L vs φ curve is given in Figure 6.27. Besides S_L being constant, the mixtures were selected such that all experimental conditions including the bulk flow velocity were kept constant.

Table 6.3: Summary of selected Laminar Flow conditions based on constant S_L.

Test Case	φ	Flow Rate (lpm)				U_0 (m/s)	R_e (Pa.s)	T_{ad} (K)	u_L (cm/s)	$\frac{\rho_u}{\rho_b}$
		Air	CH_4	C_3H_8	C_2H_4					
Laminar mixture @ 41 m/s	1	23.8	2.5	0	0	1.15	1694	2226	41	7.47
	0.92	23.8	0	1	0	1.15	1839	2196		8.60
	0.74	25.9	0	0	0.9	1.18	1978	2062		6.92
Laminar mixture @ 29 m/s	0.8	25.0	2.1	0	0	1.19	1750	1966	29	6.60
	0.76	25.0	0	0.85	0	1.19	1865	1976		7.74
	0.64	26.6	0	0	0.75	1.20	1894	1882		6.31

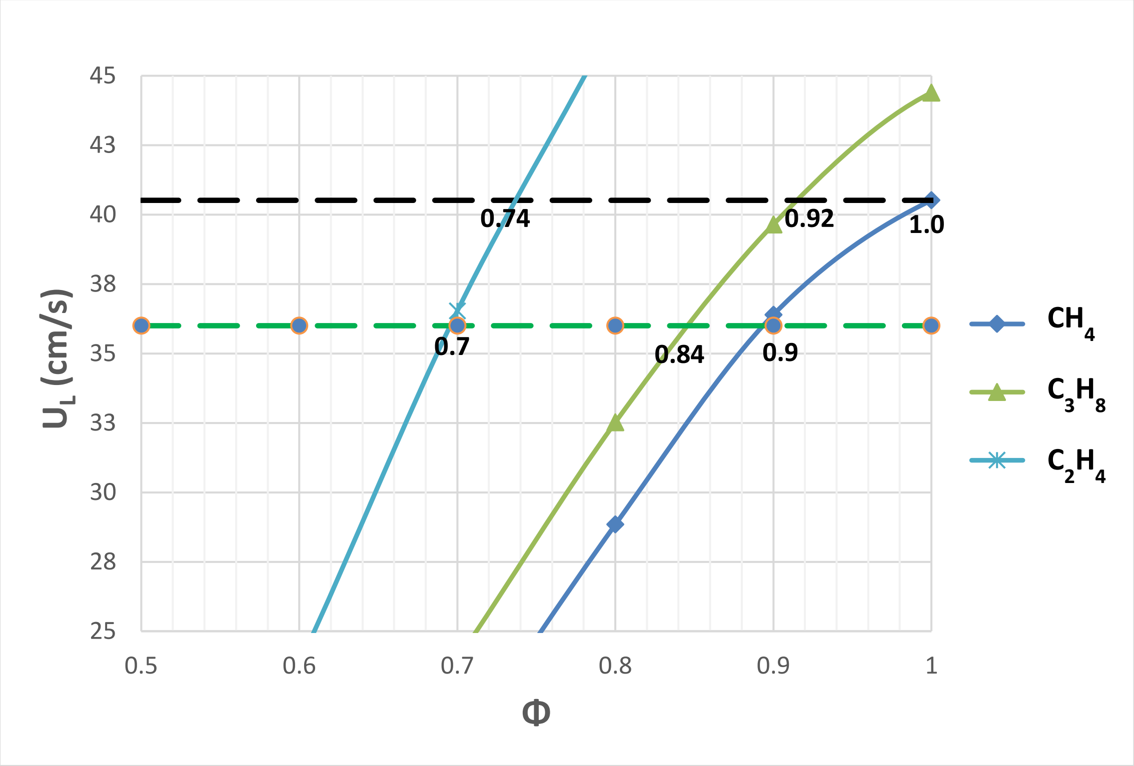

Figure 6.27: Selected flow conditions on LFV – φ plots

Figure 6.28 are sequences of mean OH* chemiluminescence images which visualizes the comparative characteristics of the flame kernels developing in different laminar fuel/air mixtures (i.e., CH_4/air @ φ=1.0, C_3H_8/air @ φ=0.92 and C_2H_4/air @ φ=0.74) with a constant LFV of 41 cm/s. As expected, all the flame kernels exhibit common geometric features in their development (i.e., evolved from a two-lobe symmetric toroid to a three-lobe asymmetry and finally to a flame ball). However, there are noticeable differences in their growth especially for the propane mixture which produced the smallest kernel. From the pictures, it is seen that in the first 400 μs, the kernels initially grow at the same rate in all directions, however from 500 μs to 2 ms, the propane kernel experienced more elongation of the front lobe which in turn affected the overall growth. On the other hand, both methane and ethylene kernels grew at nearly the same rate producing bigger flame kernels than propane. Comparing the shape of the upstream flame front in late kernels, it is obvious the difference in growth rate is mostly influenced by flow-induced strain which is expected to be highlighted through analysis of the images.

In addition, the reactivity and strength of each kernel would be highlighted through analysis of the OH* intensities.

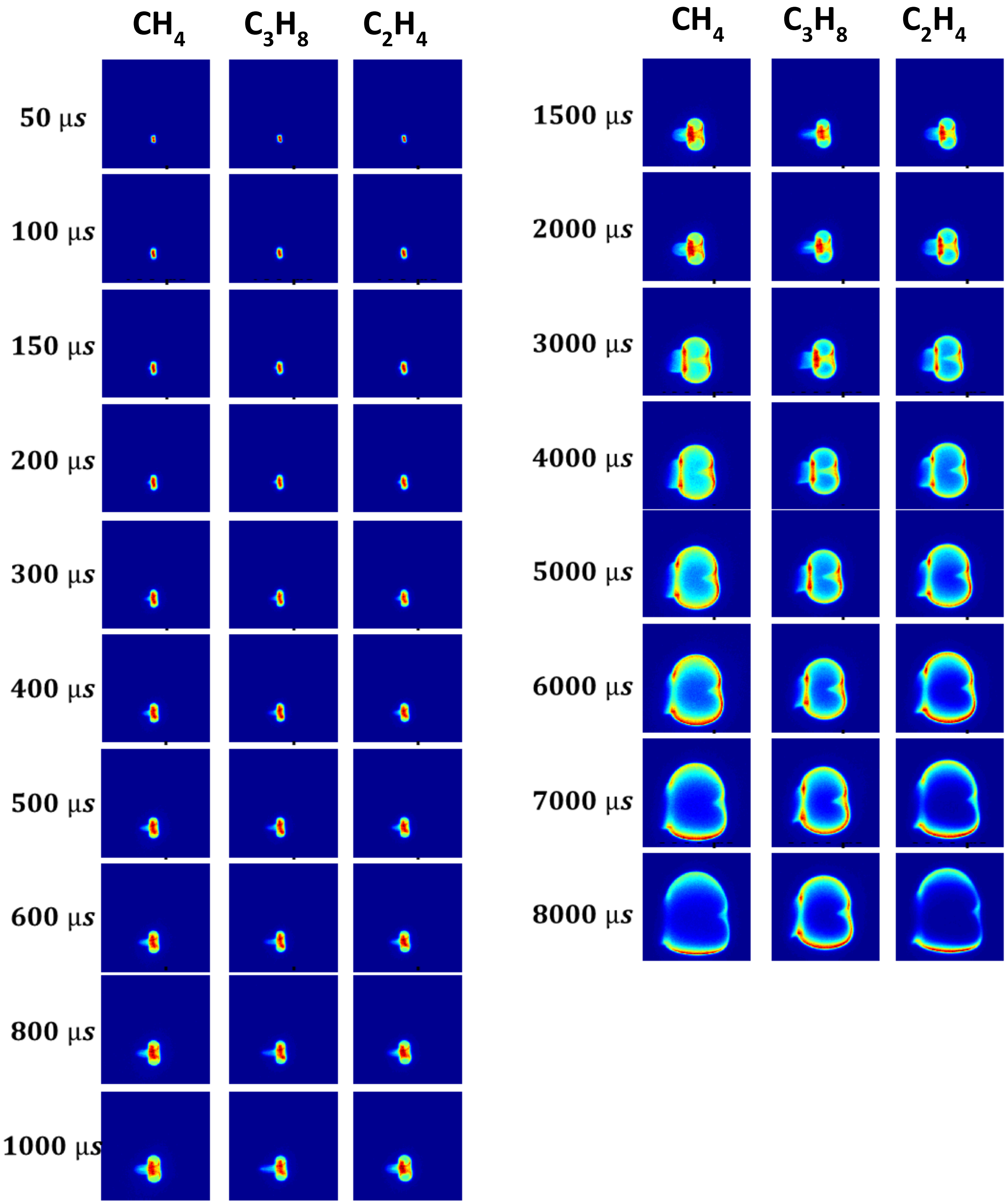

Figure 6.28: Visualization of fuel composition effects of fuels at constant LFV (Image FOV: 56x56 mm^2)

Figure 6.29 - Figure 6.30 compares the peak OH* intensities obtained from the flame kernels of the three fuels at 41 cm/s and 29 m/s unstretched laminar flame velocities, respectively. By comparing both results, it appears the peak OH* intensities followed the similar trend as it did when a constant flame temperature was maintained. For example, in the mixtures with LFV of 41 cm/s, the peak OH* intensities seem to reveal that the most reacting mixture was ethylene, while propane and methane had similar reactivity. However, a closer look at the decay from the initial peak OH* intensity, it is evident that the propane kernel decayed much faster than the rest which explains the smaller size of at the developed stage. In the leaner mixtures with LFV of 29 cm/s, both methane and ethylene kernels produced a higher steady peak OH* intensity of 800 AU at 2 ms following the initial decay while the propane kernel produced the lowest steady peak OH* intensity of 500 AU at 3.5 ms following an initial decay. This trend in reactivity is unexpected by considering the flame temperatures estimated. As shown in Table 6.3, the order of reactivity with respect to the AFT should be methane>propane>ethylene for the in the mixtures with LFV of 41 cm/s while that of the lean mixtures (with LFV of 29 cm/s) should be propane>methane>propane. This behaviour may be linked to the fact that the actual flame temperature deviates from the AFT in a proportion similar to the stretching of the flame front [162]. The stretch effect in turn depends on Lewis number of the deficient component (i.e., the Fuel) as noted previously.

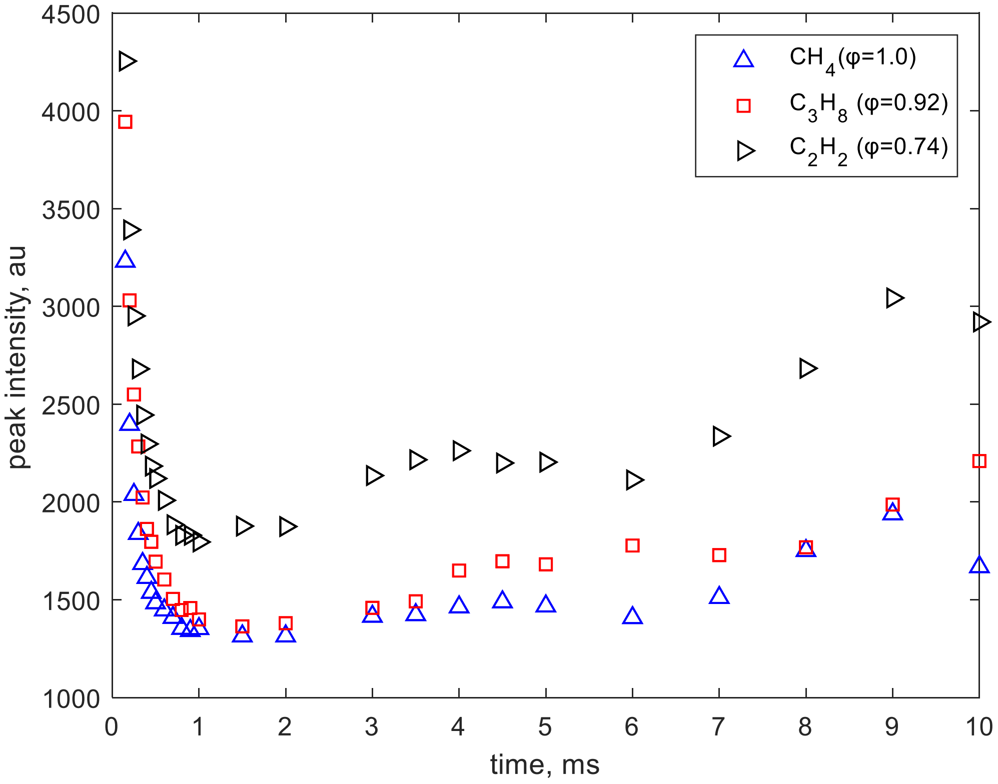

Figure 6.29: Peak OH* Intensity at 41 cm/s

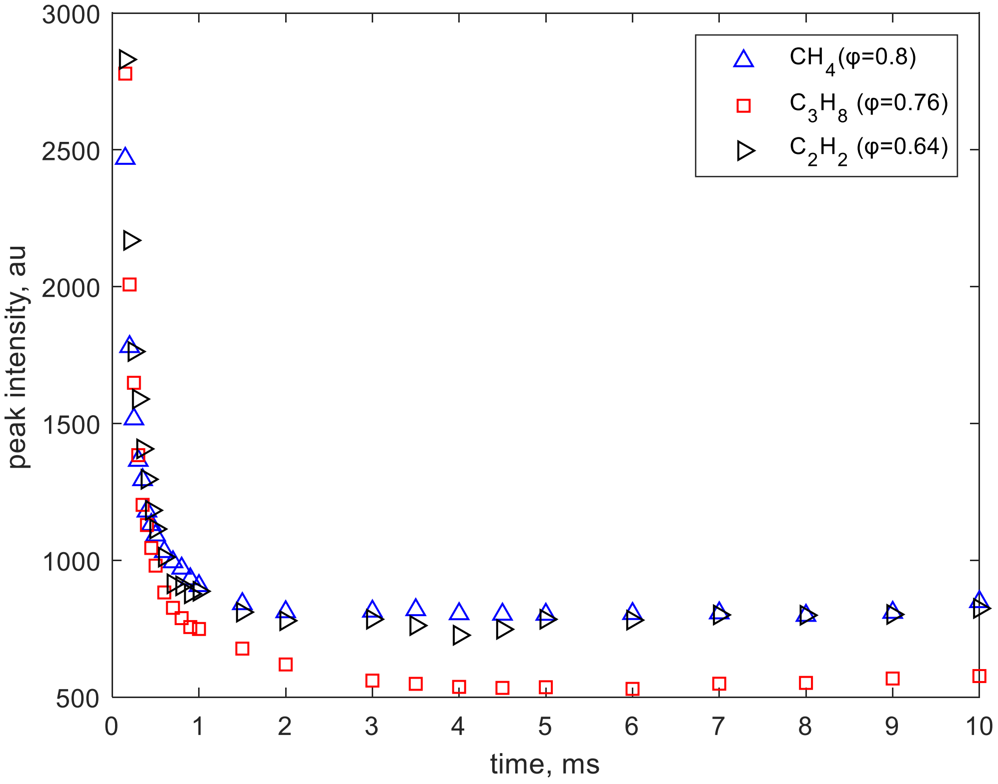

Figure 6.30: Peak OH* Intensity at 29 cm/s

Figure 6.31 - Figure 6.32 compares the spatially integrated OH* intensities obtained from the flame kernels of the three fuels with LFV of 41 cm/s and 29 cm/s, respectively. From the results, the magnitudes of integrated intensities occur in the following order: C_2H_4>CH_4>C_3H_8. Therefore, it can be inferred that under the given flow conditions the rate of heat release was highest in the ethylene flame kernel and lowest in the propane flame kernel. A second noticeable difference is the time it takes for the integrated OH* intensity values to drop to its minimum before rising again which had earlier been referred as the possible duration of chemical induction. For the mixtures with LFV of 41 m/s, the duration of chemical induction occurred in the following order: 200 µs in CH_4, 400 µs in C_3H_8 and 250 µs in C_2H_4. Comparing the kernel development in the two Figures shows that at lower LFV, more time was required to see a rise in integrated OH* intensity. Also, the late kernels were marked by wider difference in integrated OH* intensity for the leaner mixtures.

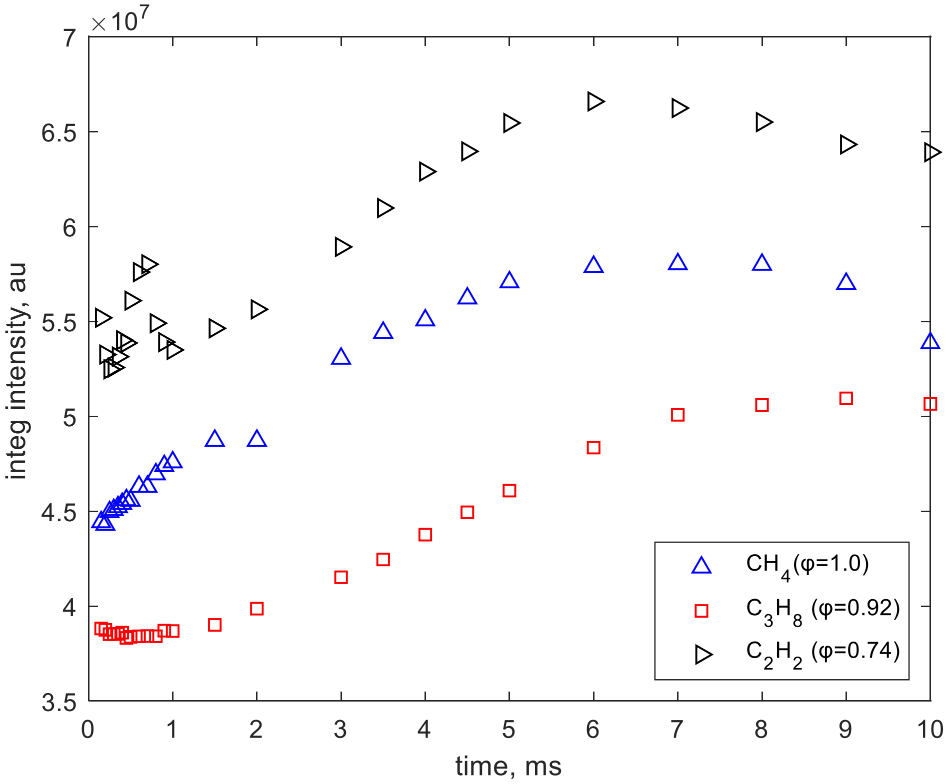

Figure 6.31: Integrated OH* Intensity at 41 cm/s

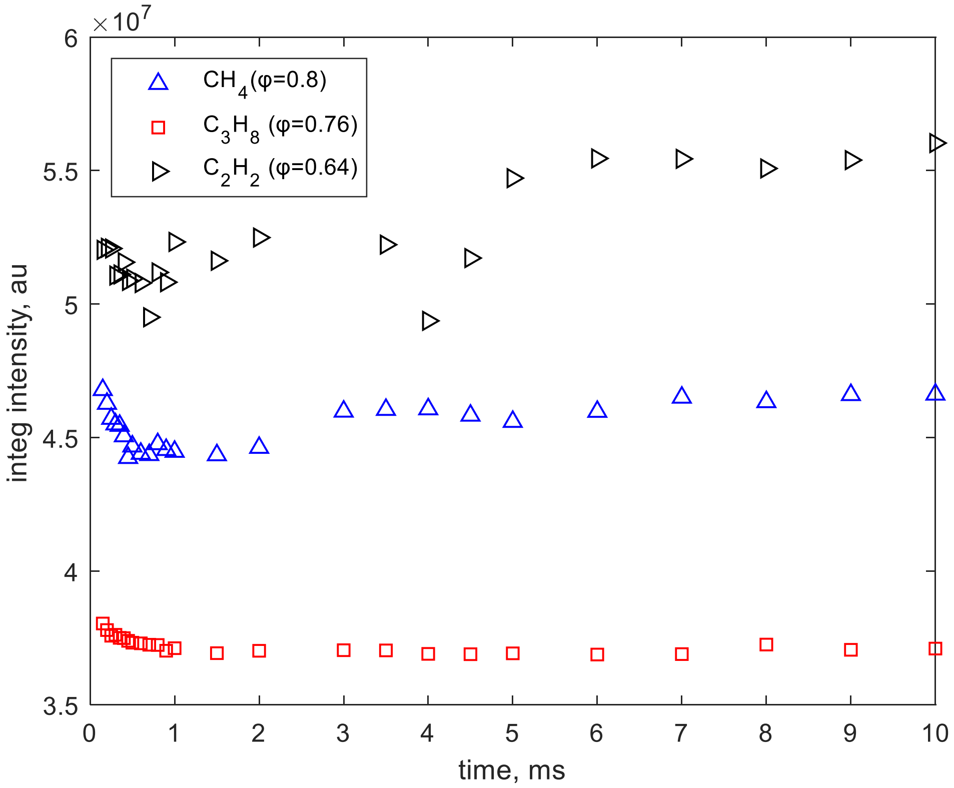

Figure 6.32: Integrated OH* Intensity at 29 cm/s

Figure 6.33 - Figure 6.34 compares the displacement of the flame front tip along the flow axis for the three fuel mixtures with at LFV of 41 cm/s and 29 cm/s, respectively. As noted previously, the general trend in flame front displacement evolved from a decaying growth pattern in the 1 ms to a steady linear growth pattern onwards. The general trend in all the graph is a symmetric axial growth with propane mixture having the slowest growth. Under the first condition, the influence of the fuel composition is clearly shown by the distances travelled in each kernel in both the upstream and downstream direction. For example, under mixture conditions with LFV of 41 cm/s, the respective Y_+ values at 7 ms delay was 31, 29 and 33 mm in methane, propane, and ethylene. Although, there is hardly a noticeable difference in the kernel height between CH_4/air and C_2H_4/air mixtures; the height of the propane kernel clearly supports the fact that higher *Le* values leads to slower growth in mixtures heavier than air. For the second condition in which the three mixtures are further leaned with a lower LFV of 29 cm/s, a remarkable difference is seen in the growth of each kernel in both the upstream and downstream directions. This is also in line with the variation of mixture

effective *Le* values which in the lean flammability range increase for heavier than air (e.g., C_3H_8, C_2H_4) but decreases for fuels lighter than air (e.g., H_2, CH_4).

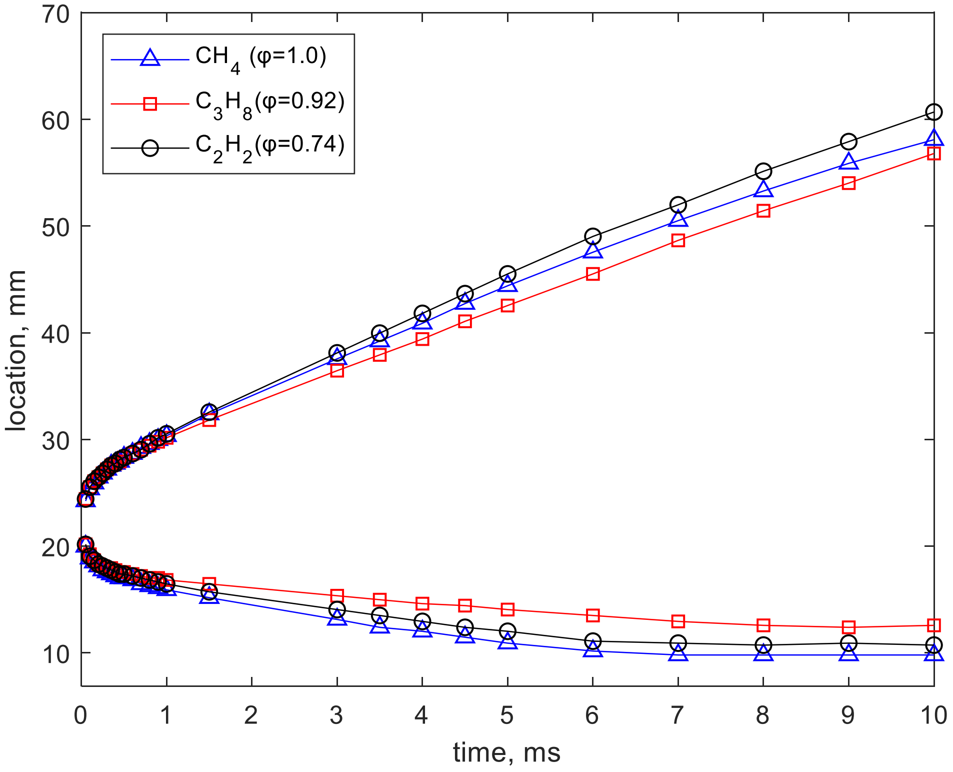

Figure 6.33: Axial flame tip locations at 41 cm/s

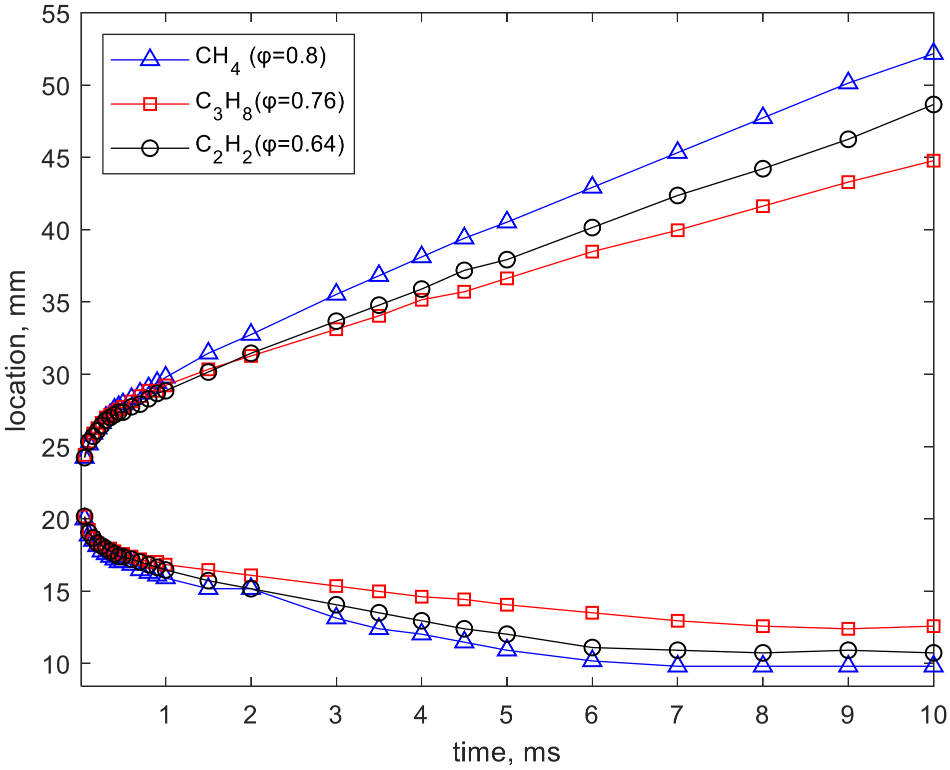

Figure 6.34: Axial flame tip locations at 29 cm/s

Figure 6.35 - Figure 6.36 compares the axial flame front propagation speed of the three mixtures with at LFV of 41 cm/s and 29 cm/s, respectively. As noted previously, the general trend for all the kernels is that S_y decreases asymptotically from an initially stretched value to a steady value close to the unstretched laminar flame speed. However, obvious differences can be seen in the steady state values of the propagation rates of each flame kernel with the propane kernel being the slowest while the ethylene kernel was the fastest. For example, with mixture LFV of 41 cm/s, the steady state S_{y+} values were 3.33 m/s in methane (a 9% increase in S_L), 3.70 m/s in ethylene (a 30% increase in S_L), and 2.96 m/s in propane (a 16% decrease in S_L). Based on the S_{y+} comparison, it can be deduced that the propagation rate of the kernels did not follow the correct order expected based on the S_L values which is 3.06 m/s for methane, 2.84 m/s for ethylene, and 3.52 m/s for propane. It is however in agreement with the earlier observed trend in heat release rate which is indicated by the integrated OH* intensity. Further leaning the mixtures resulted in a slightly different outcome in which the fasted growing kernel was that of methane while the propane kernel remained the slowest. For

example, at LFV of 29 cm/s, the steady state S_{y+} values were 2.59 m/s in methane (a 35% increase in S_L), 2.22 m/s in ethylene (a 21% increase in S_L), and 1.85 m/s in propane (a 17% decrease in S_L) when the unstretched laminar values were 1.91, 1.83 and 2.24 m/s respectively. In this result, the measured flame front propagation rate is not in agreement with the estimated unstretched laminar flame velocity of the flame and the observed trend is not in agreement with the integrated OH* intensity. This behaviour reaffirms the earlier assertion that flame kernels were stretched differently depending on the fuel.

To better illustrate the relative differences in growth rate, the axial flame front propagation speed is normalised by the unstretched laminar flame speed. Figure 6.37 - Figure 6.38 compares the normalised propagation speed of the axial flame front for the three fuel blends with mixture LFV of 41 cm/s and 29 cm/s, respectively. Analysis of the downstream flame front shows that the propagation rate, S_{y+} decreased from an initially stretched value until it converges to a value close to the unstretched laminar value, S_L. The ethylene mixture was the first to reach a stable value $1.3S_L$ at 3 ms, followed by methane (i.e., $1.09S_L$ at 3.5 ms) and finally propane (i.e., $0.84S_L$ at 3.5 ms) which was the least stretched. In the leaner mixtures at 29 cm/s, methane became more stretched than ethylene (i.e., $1.35S_L$: $1.21S_L$) while propane remained the least stretched (i.e., $0.83S_L$). Analysis of the upstream flame front shows that the propagation rate, S_{y-} continues to decrease after reaching the unstretched value S_L before converging to its asymptotic values. The difference between the two flame fronts is that while it is positively stretched downstream, the flame front upstream is negatively stretched. This explains the rational for S_{y+} lying above the 1.0 line and for S_{y-} lying above the -1.0 line. As previously explained, the difference may be due to the variations in surface area for the flame front as well as the varied compression effect of flame expansion on flow ahead of the flame which could be revealed through further analysis. With respect to the stretch sensitivity of the flame kernel, the results show that the ethylene fuel had the most influence while propane had the least influence for mixtures with LFV of 41 cm/s. However, at a lower LFV of 29 cm/s, methane was the most influential while propane had the least influence. As suggested earlier, this behaviour may be due to a higher variation of C_2H_4/air flame temperature from the AFT which can be linked to stretch dependence on Lewis number of the deficient component (i.e., the Fuel).

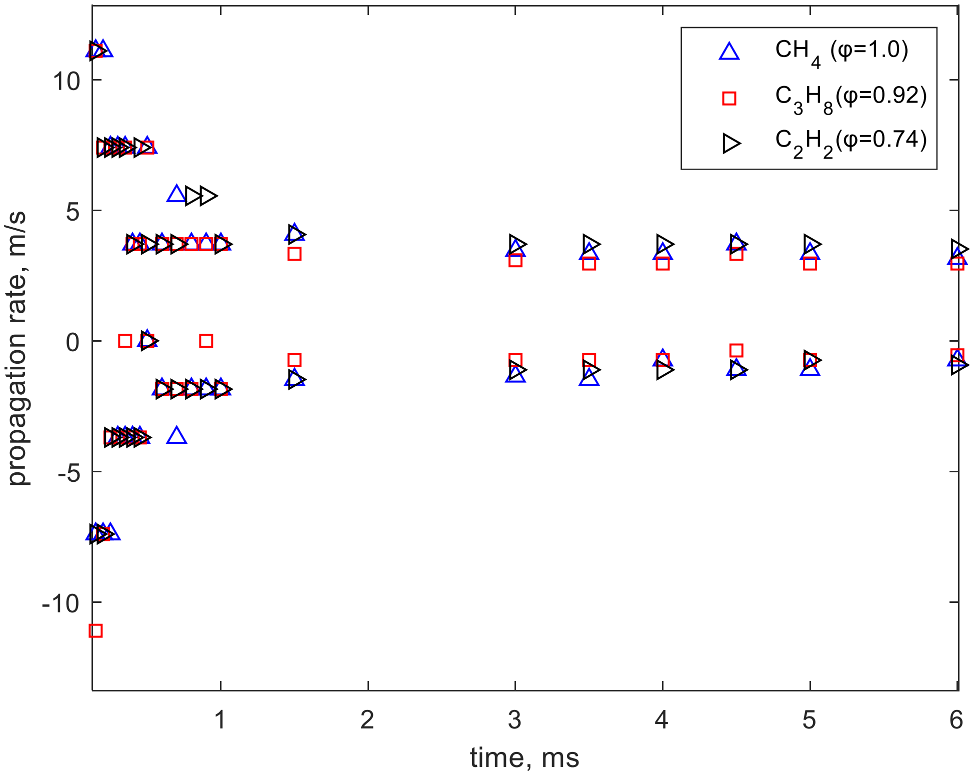

Figure 6.35: Axial propagation rate at 41 cm/s

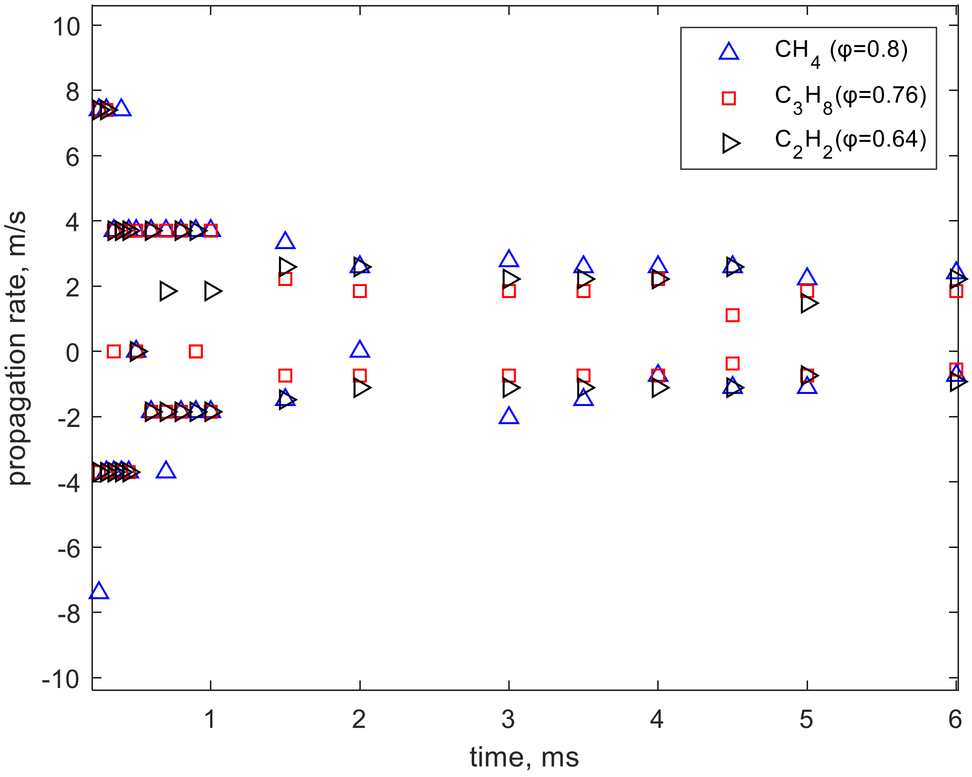

Figure 6.36: Axial propagation rate at 29 cm/s

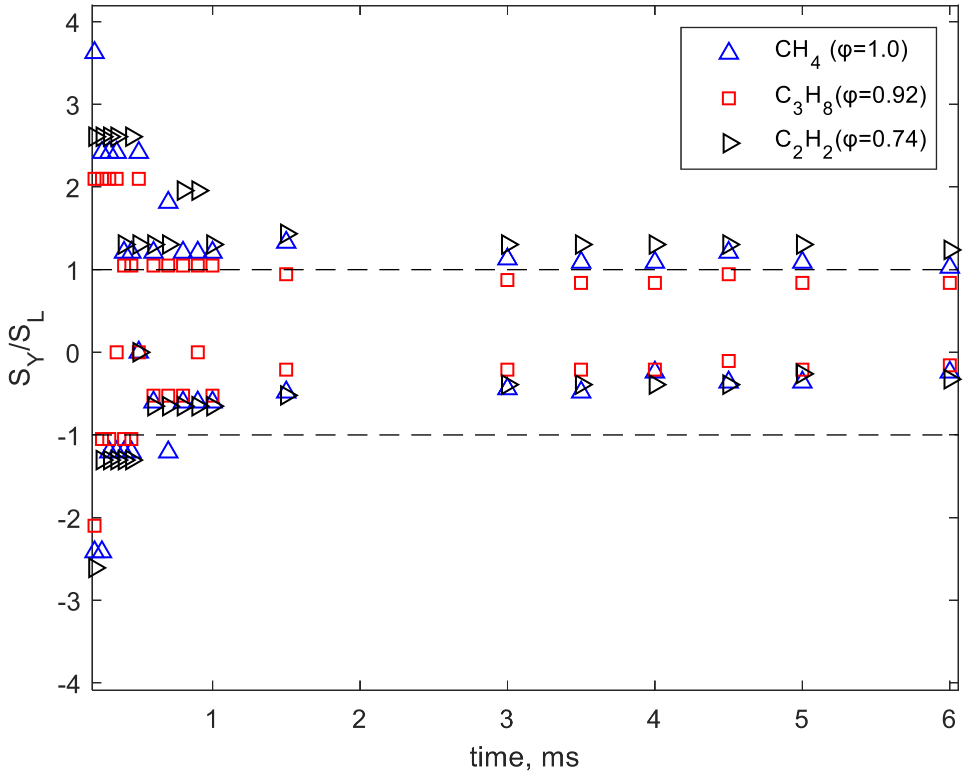

Figure 6.37: S_{y+}/ S_L at 41 cm/s

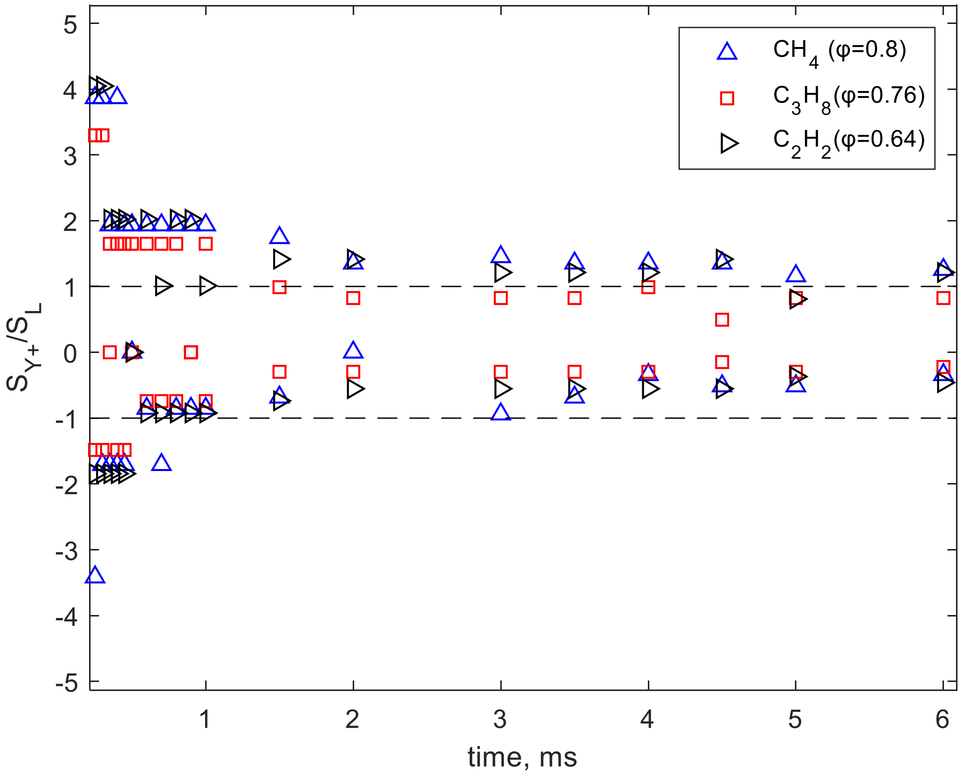

Figure 6.38: S_{y+}/S_L at 29 cm/s

6.5 Conclusions

The effect of the fuel properties on the development characteristics of the LISI flame kernel has been investigated through analysis of the mean OH* chemiluminescence images. First, the flame kernel development was compared at changing equivalence ratios while maintaining a constant flow velocity in both laminar and turbulent flow environment. Also, a second and third comparison was made at constant AFT and LFV, respectively to investigate the sensitivity to the selected fuel mixture. All the experiments were performed by repeated laser ignition of different Fuel/Air mixtures (CH_4/Air, C_3H_8/Air and C_2H_4/Air) in a co-flow burner made of smoothly contoured nozzle with contraction and the acquired images included both kernel development and initial propagation covering a temporal range of 0.05 – 10 ms. A summary of the findings based on both qualitative visualization and quantitative analysis are as follows:

Effects of variation in Mixture Equivalence Ratio

1. Visualisation observation of the kernel development in lean and stoichiometric mixtures (i.e., $\varphi=1.0$ to $\varphi=0.8$) produced similar features, however there were noticeable differences in the size and reactivity of the developing flame kernels.
2. The peak OH* intensities showed that a unit reduction in φ produced a similar reduction in the kernel peak OH* intensity during its development. This indicates more heat losses in kernels at lower φ values which could hinder its development to a stable flame kernel. At the developed kernel stage, the peak intensities increased for the near stoichiometric mixture kernels but remained constant at $\varphi=0.8$ which means lower heat release rates.
3. Also, the integrated OH* intensities showed that lower equivalence ratios produced both weaker kernels and increased chemical induction duration.
4. the kernel growth is slower when lean mixtures (i.e., $\varphi = 0.9, 0.8$) are compared with the stoichiometric mixture. Analysis showed the leanest flame

kernel required 9 ms to travel 28 mm upstream compared to 7 ms required by the stoichiometric flame.

5. The tip displacement of the flame front in laminar flow mixtures, reveals a nearly symmetric growth curve in which the distance travelled decreased from $\varphi=1.0$ to $\varphi=0.8$. Analysis shows the leanest flame kernel required 9 ms to travel 28 mm upstream compared to 7 ms required by the stoichiometric flame. In the turbulent flow mixtures, the distance travelled increased in a non-symmetric manner which led to reduction in the gap between the flame fronts.
6. For all φ values, the general trend shows that the flame front growth rate during kernel development decreases asymptotically from a highly stretched value to a value close to S_L after which a nearly constant speed is maintained. During development, the mixture with the least φ value experienced the most stretch. In the developed kernels, the steady state values of S_{y+} increased in order of the equivalence ratios (from $\varphi=0.8$ to $\varphi=1.0$).
7. Further sensitivity analysis reveals that the decreasing trend in all parameters moving from $\varphi=1.0$ to $\varphi=0.8$ follows a linear relationship for laminar flows. This, however, was not the case in turbulent flows.

Effects of variation in Fuels with constant AFT

1. For selected mixtures of 2226 K AFT (i.e., methane/air, propane/air and ethylene/air), propane produced the slowest growing flame kernel while methane and ethylene kernels were growing at the nearly the same rate.
2. Analysis of the peak OH* intensities showed that the slower growth in the propane kernel was due to faster cooling. This could be observed in the excessive stretch and local quenching at the front lobe. The peak intensities of the developed kernels also showed that the lowest heat release rates occurred in propane/air and highest in the ethylene/air.
3. The spatially integrated OH* intensity indicate that the ethylene/air mixture produced the strongest flame kernel while propane/air mixture produced the weakest flame kernel. This also showed that the duration of chemical induction was shorter in methane/air mixture than the rest.

4. Analysis of the axial flame front locations showed that the upstream propagation (Y_-) differed for all the three mixtures. The order of magnitude of Y_- was methane>ethylene>propane which could be linked to the mixture Lewis Number or Density. This affected the expected symmetry in axial growth curve of laminar flame kernel.

5. From the S_{y-} plots, the general trend showed that the propagation rate of the flame front decreases asymptotically from a highly stretched value to a value below S_L. Contrary to expectation, the CH_4/air flame kernel with LFV of 41 cm/s grew faster than the C_2H_4/air kernel with LFV of 51 cm/s. From the normalized propagation speed S_{y-}/S_L, it was observed CH_4/air experienced the most stretch at development stage and least stretch at the late kernel stage.

6. At lower flame temperature (i.e., 2134 K AFT), the observed fuel impact on Y_- increased which agrees with the mixture Lewis Numbers. This observation also agrees with previous research conclusion that mixtures with higher Lewis Number would require a larger critical radius to development into a sustained flame kernel [49].

7. It was also observed that at lower flame temperature (i.e., 2134 K AFT), S_{y-}/S_L shows that the sensitivity to stretch widened between CH4/air and the rest mixtures due to wider variation in both the Markstein length and effective Lewis Numbers.

Effects of variation in Fuels with constant LFV

1. For selected mixtures with LFV of 41 cm/s (i.e., methane/air, propane/air, and ethylene/air), propane kernel developed at slightly lower rate than methane and ethylene kernels which grew at the same rate.

2. Analysis of the image peak OH* intensities at LFV of 41 cm/s showed that ethylene was the most reactive, while methane and propane was about the same. Dilution of the flows (i.e., at LFV of 29 cm/s), resulted in an overall drop in intensity, however the decay was more significant in propane and ethylene. The higher loss in propane and ethylene may be due to an increased stretch on

the flame temperature away from the AFT which results from wider variation of Le of the fuel in the lean range [162].

3. Analysis of the integrated OH* intensity at LFV of 41 cm/s showed ethylene/air mixture to have the strongest kernel while propane/air mixture had the weakest kernel. As earlier, the decay in diluted mixtures with LFV of 29 cm/s was more significant in propane and ethylene.
4. Analysis of the axial tip locations of the flame fronts showed a symmetric growth curve at all mixture conditions investigated with propane kernel having the least growth. At 41 cm/s, the propagation of methane and ethylene was nearly the same, however the methane kernel propagated faster under leaner mixtures at the LFV of 29 cm/s. This change in characteristics may be due to the increased differences in their Lewis Numbers.
5. The general trend in S_{y+} shows that the propagation rate of the flame front decreases asymptotically from a highly stretched value to a value below SL with propane kernel having the lowest value. From the normalized propagation speed (S_{y+}/S_L) of mixtures at LFV of 41 cm/s, the kernel in CH_4/air was more stretched than that of C2H4/air at the development stage. At a lower LFV of 29 cm/s, the CH_4/air kernel became more stretched than the C_2H_4/air kernel. This change in trend may have resulted from higher stretching of the C_2H_4/air flame temperature from the AFT which is also depends on the Lewis number of the deficient component (i.e., the Fuel).

Chapter 7 Discussion of Overall Results

7.1 Introduction

As stated in the introductory chapter, this PhD work involves detailed investigation of the development characteristics of a LISI flame kernel in premixed fuel/air mixtures. The goal is to show the key development characteristics of the LISI flame kernel and possibly link them to ignition success or failure. It is also anticipated that the data from this investigation could be used for development and validation of laser ignition models. This goal is accomplished through several experimental campaigns the results of which were used for both visual characterisation and parametric study. The parametric study also involves dynamic analysis of the kernel geometric growth, the flow velocity field, and the intensity of the emitted OH* all of which have been reported in chapter 4, 5 and 6. The purpose of this chapter is to collectively discuss all the results from the investigation in a coherent and insightful manner.

7.2 Visual characteristics of the Flame Kernel development

The development of the LISI flame kernel from the ignition point to 1667 μs time delay is captured by tomographic images shown in Figure 4.1a - Figure 4.1b. Further visualisation of the kernel development is also obtained for 50 μs to 10 ms time delays using the mean OH* chemiluminescence images shown in Figure 5.1 - Figure 5.2. Both visualisations reveal that the LISI flame kernel starts as an elliptically shaped plasma of hot gas which then evolves into a two-lobe toroidal flame front, followed by the appearance of a front lobe leading to toroidal asymmetry and finally a self-sustaining flame ball. They also provided a clearer picture of both the fluid dynamics and reactivity of a developing LISI flame kernel.

Dynamics of the Kernel geometry

At the start of ignition, the first feature observed from the tomographic images is an elliptically shaped plasma of hot gas formed within the mixture. This hot plasma usually between 1-3 μs and is accompanied with shock waves. Many authors [92],[20][100] observed that the plasma usually extends more towards the direction of laser beam and the shockwave centroid is usually displaced from that of the plasma.

The second feature observed at 50 μs from both image sets is a two-lobe toroidal flame kernel propagating symmetrically above and below the laser axis. Previous studies observed similar shape for both laser ignition and electric spark ignition [92],[100]. The origin of this feature has been attributed to an induced inward flow resulting from an over-expansion of the shock wave, emanating outward from the region of the discharge at a very high velocity [138]. Figure 2.8a - Figure 2.8b provides an illustration of the transformation from ellipsoidal spark kernel to a toroidal flame kernel from 1 to 50 μs. As shown by the figure, two contra-rotating vortex rings (indicated by velocity streamlines of magnitude 25 m/s) are generated in the upstream and downstream regions via a complex process of interaction of the shock waves and rarefaction waves from the hot plasma. The inward flow from these vortices leads to the formation of the toroidal flame front. The figure also suggests that the leading-edge vortices (directed towards the laser) is smaller in size which implies it decays more rapidly than the trailing edge vortices.

The third feature observed at 100 μs is the appearance of a front lobe which propagates in the direction of the laser, thus leading to an asymmetric toroidal flame front. Previous studies [92] has suggested that this is a unique feature of laser ignition. Although observed by several authors, it is not yet clear how this feature develops. For example, Spiglanin *et al.*, 1995 [92] suggested that it might be due to the initial flow field created by the propagation of a radiation transport wave up the laser beam, arising from the high rate of energy transfer at the leading edge of the plasma. While it is true that the plasma kernel created by laser breakdown can result in an ionized front propagating toward the laser [155],[20] this is not expected to continue long after the laser pulse had ceased, hence, there is no evidence of this. Following from the differences in decay rate between the leading edge and trailing edge vortices, Bradley *et al.*, 2004 [20] suggested this phenomenon is capable of producing a centreline velocity towards the laser source, leading to generation of the front lobe. Figure 4.3 Figure 2.10clearly illustrates this transformation in the superposed kernel edges formed between 50 and 166 µs. As shown in the figure, after the weak leading-edge toroid has dissipated, the induced gas velocity to the left, up the laser beam, can be high. This results in a flow of hot gas close to the centreline to the left and its displacement by cold gas from the right. The elongated hot gas kernel comprises the third lobe. This displacement of the centreline hot gases by the cold gases is clearly shown in the observation images following the appearance of the front lobe.

The final shape of the propagating flame front is that of a typical flame ball following local quenching at the front lobe. This is shown in Figure 5.2 which represents the sequence of mean OH* chemiluminescence images acquired between 3 and 10 ms time delays. As shown by the figure, propagation of the flame front is marked by changing radius of curvature in both the upstream and downstream directions.

Dynamics of the Kernel reactivity and reaction zones distribution

An investigation of the colour scales of the OH* chemiluminescence images (Figure 5.1 - Figure 5.2) reveals that the reaction intensity changes progressively during transition to a self-sustained flame front. Between 50 µs and 100 µs, the peak intensity of OH* dropped from 3800 AU to 2300 AU due to cooling of the hot gases which make up the initial kernel. At 150 µs, a new peak in OH* intensity occurs which is the first indication of the kernel survival. Subsequent kernels showed a continuous decay in peak OH* until a minimum peak is attained beyond which the peak rises again following the formation of a self-sustaining flame. These would be shown further by quantitative analysis of the OH* intensity.

In addition, the image colourmaps also reveal that the distribution of reaction zone changes at different stages of development. At the initial stages (50 - 300 µs), the OH* is evenly distributed, hence the kernel is composed of an isotropic reaction zone. A possible explanation for this is that initial kernel growth is predominantly due to the presence of hot gases which originated from the initial hot plasma. At the mid stage of development (450 - 1500 µs), the distribution of OH* reveals the kernel is composed of anisotropic reaction zones with peak intensity within the middle region. A possible explanation for this is that kernel growth during this period is the result of both induced gas flows and chemical reactions. This could also be the result of mixing of the reaction zone with the flow due to vortex induced motion which may lead to multiple flame fronts within the kernel. As shown in Figure 5.2, the colourmap of the late kernels (3 – 10 ms) shows that the reaction zones (i.e., flame fronts) were concentrated at the edges. Unlike the early kernels, the inner region of low intensity may indicate the presence of burnt gases. These observations also give an idea of the two-way interaction involving the flame-flow mixture and flame-burnt products.

7.3 Analysis of the Flame Kernel growth and propagation

The first output from geometric measurements following edge extraction of the tomographic images is the initial plasma radius. The result reveals that following generation of the spark at ignition, there is nearly an instantaneous growth of the plasma to an initial finite size. This growth has been attributed to the sudden energy deposition at breakdown which generates high pressure in the kernel leading to a rapidly expanding wave[90]. Therefore, the growth of the plasma at this stage can be predicted using the spherical blast wave theory [91], with the assumption that heat release due to chemical reactions is negligible. Table 4.2, compares the measured plasma radii and prediction at 1 µs based on spherical blast wave model (equation 2.15), assuming 70% spark energy deposition efficiency. From this analysis, it was shown that the predicted plasma radius was 13.9% more than the measurement laminar case and 4% less than measurement in turbulent case. The observed differences in the initial sizes of the kernel for both conditions despite having similar pulse energy highlights the fact that laser induced gas breakdown is a stochastic process, hence similar pulse energies can produce different spark energies, although the same spark efficiency of 70% has been assumed in the prediction.

The second output from the measurements is the displacement of the flame front tip along opposite directions of the flow axis. Figure 5.6 shows that the downstream flame front of stoichiometric CH_4/Air is characterised by non-linear decay growth during the first 0.8 ms, followed by a steady linear growth onwards. Similarly, the upstream flame front follows the same trend until a maximum displacement of 12 mm at 7 ms is reached. The combined history of both measurement (i.e., Y_+ and $Y\_$) reveals a nearly symmetric growth curve about the laser axis, however this did not appear to be the case in the 2D scatter shown in Figure 5.5. A comparison of the axial growth curve at different flow velocities (i.e., 1.15, 2.08, 3.0 and 3.48 m/s) is shown in Figure 5.20, which reveals that the loss of symmetry is due to displacement of the kernel centroid by the flow which means symmetric growth should be obtained if ignited in quiescent mixture flows. When fuel lean mixtures (i.e., $\varphi = 0.9, 0.8$) are compared with the stoichiometric mixture, the kernel growth is slower in lean mixtures and the maximum displacement reached by the flame front upstream is lower as shown in Figure 6.7. This expected considering the differences in laminar flame speed of the mixtures. It also shows a higher strain effect of the flow on the flame front of leaner mixtures. An interesting result is the comparison between three fuels (methane, propane, and ethylene) with the same AFT (T_{ad}=2226 K) in which propane experienced the slowest growth while methane was the fasted. This is unexpected because ethylene has the highest estimated laminar flame speed (i.e., S_L = 3.87 m/s for C_2H_4/air) while methane has the least value (i.e., S_L = 3.06 for CH_4/air). It is possible the observed differences may be the result of preferential diffusion effects which occurs in mixtures with non-unity Lewis number values. As shown by the results, propane with the highest Lewis number (φ=0.94, Le=1.4) is the experiences the slowest growth while methane with unity Lewis number (i.e., φ=1.0, Le=1) experiences the fastest growth. This is in agreement with observation by past authors [161], that mixtures with higher Le values would require a larger critical radius for the flame to be sustained. In order words, the CH_4/air mixture with the least Le value would require lower **MIE** and less time to develop into a self-sustained flame kernel compared with the C_3H_8/air mixture. Hence, the order of duration in reaching a self-sustainable flame kernel is methane, ethylene, propane. A similar trend in axial flame tip displacement is observed in leaner fuel/air mixtures

(CH_4/air @ φ=0.9, C_3H_8/air @ φ=0.86 and C_2H_4/air @ φ=0.78) with T_{ad}=2134 K as shown by Figure 6.22. However, the differences become wider which is in accordance with their *Le* values. For fuels heavier than air (e.g., C_3H_8, C_2H_4) *Le* values increases with reduced φ values while the reverse is the case for fuels lighter than air (e.g., H_2, CH_4)[162]. Further analysis revealed that at lower AFT (T_{ad}=2134 K), the differences in displacement between the three mixtures widened which is in accordance with their *Le* profiles the fuels.

Unlike the two axial flame fronts, Figure 5.6 shows that the displacement of flame front towards the laser is characterised by sudden change in slope at 1.5 ms due to local quenching at the front lobe, followed by a steady linear growth onwards. As a result, measurements of the kernel dimensions reveal that the height of the flame kernel (which was measured along the flow axis) is always greater than the width (which was measured along the laser axis). This can be seen in Figure 5.7 which further reveals there is small differences between them in the first 1.5 ms due to the presence of the front lobe and the asymmetry in the initial spark dimensions [97]. Beyond 1.5 ms, the difference increases due to variation how the flow velocity affects growth along different directions. Based on the orientation of the laser and the flow condition investigated, the kernel expanded to reach the size of the burner (i.e., diameter =22 mm) in 2.5 ms, whereas it would have taken about 1.5 ms to cover the same space if it were oriented transversely. A comparison of the transverse dimensions of the kernel (W) at different pulse energies is shown in Figure 5.14 which reveals an enhanced early growth due to higher energy, however no significant changes were observed in the fully developed kernels. It is worth noting how W increased significantly during the first 1 ms when the incident energy increased from 32 mJ to 64 mJ, however, further increase in energy had little or no effect in the size. This shows the existence of a threshold incident energy beyond which increase in pulse energy had no impact on the growth. The observation agrees with previous authors that spark energy deposition has a limiting efficiency depending on the lens focal length [90],[157]. At 10 ms time delay, no significant changes were observed in the kernel growth irrespective of the magnitude of the incident pulse energy. Further details of the sensitivity analysis can be found in Table 0.1 (see Appendix E: Sensitivity Analysis).

Another common characteristic evidenced in all the cases studied is that the propagation rate of the flame fronts is marked by decay from a highly stretched initial value to a steady asymptotic value close to the unstretched laminar flame speed. Figure 5.8 reveals that as the kernels develops, the propagation rate of the downstream flame front decreases until it converges to a value slightly above the unstretched laminar value, S_L. In contrast, the propagation rate of the upstream flame front continues to decrease after reaching the unstretched value S_L before converging to its asymptotic values. The difference in growth rate between the two flame fronts implies different levels of stretch which could be due to several factors. One of the factors could be differences in the surface area of the flame fronts as a result of wrinkling induced by flow turbulence [163]. Another factor could be that the local S_L values have changed due to varying compression of the mixture in both the upstream and downstream region by the expanding flame kernel [90]. This figure also highlights the existence of three key phases of steady growth. For example, the first steady growth of the downstream flame front was observed between 150 to 200 μs, when the flame front propagation rate was 11 m/s following the appearance of the front lobe. This growth dominated by induced gas velocity of the shock waves. The second steady growth occurred between 250 and 500 μs, when the kernel propagation rate was 7.5 m/s which marked the formation of an igniting kernel. This growth is due to combined influence of chemical reactions and induced gas velocity. The third steady growth occurred from 800 μs onwards when the flame front propagated at its asymptotic velocity of 3.5 m/s. At this stage, the growth is purely by chemical reactions when variation from its laminar unstretched value (i.e., 3.06 m/s) is at its minimum. A comparison of the growth rate at different incident energies (Figure 5.15) reveals that increase in energy of the incident beam only enhanced the early kernel growth before 1 ms. A clearer picture of stretch effects due to increase in pulse energy is shown in a plot of the normalised value versus the downstream displacement (Figure 5.16). This reveals that for a displacement of 8 mm, the respective stretched speed at 32, 62 and 128 mJ were 20, 20, 30, and 50% more than the upstretched laminar value. The similar stretch between the two flame fronts at 96 and 128 mJ further confirms the existence of a threshold incident energy above which further increase has no impact on the growth. As shown in Figure 6.11 - Figure 6.12 the axial propagation rate of the flame fronts is slower in lean mixtures (i.e., φ = 0.9, 0.8) compared with the stoichiometric mixture. Analysis reveals that the effect on dilution on the steady state S_{y+} values is a linear decline in laminar flow situation (i.e., 11% drop per unit reduction in φ between φ=1.0 to φ=1.0), however, the variation is non-linear in turbulent mixtures. It was also observed that the stretched flame speed appears to be slightly higher under lean conditions. Further analysis of the growth rate normalised by the unstretched laminar flame speed (Figure 6.13 - Figure 6.14) showed higher stretch rates in leaner mixtures compared with the stoichiometric. the mixture with the least φ value experienced the most stretch. This may be due to the fact that the *Le* values of lean CH_4/air mixtures are slightly below unity, therefore preferential diffusion may affect growth. The clearest evidence of the effect of preferential diffusion on growth rate is observed when is compared for three different fuels at constant AFT (Figure 6.25 - Figure 6.26). The results clearly shows that fuels with higher *Le* values were marked with higher variation from the upstretched laminar flame speed.

7.4 Analysis of the OH* Intensity Characteristics

Analysis of the spatially integrated OH* intensity provided information about the heat release strength of the flame kernel as well as further evidence of an important transition point in the lifecycle of the kernel. Figure 5.10 shows the integrated OH* intensity history of the kernel for stoichiometric CH_4/air in laminar flow condition. An important feature of this graph which appears in all cases studied is that it involves an initial decline to a minimum trough value. This occurred within 200 µs in the stoichiometric CH_4/air mixture with a trough value of 44000000 AU. This initial trough could be interpreted as the transition point between a quenching flame kernel and the formation of an igniting kernel. The time elapsed before this transition can be interpreted as the chemical induction period [92]. The results show that the duration changes systematically depending on the incident energy, equivalence ratio and the fuel mixture. For example, the induction time increased with higher incident energy leading to lower trough values. For different equivalence ratio (i.e., φ = 1.0, 0.9, 0.8), the duration also increased in leaner mixtures but did not lead to lower trough values. Of the three fuels investigated, the shortest duration occurred in methane despite ethylene having higher values.

As the kernel continues to develop beyond this transition point, the cumulative heat release rises which is marked by a continuous rise in the integrated OH* intensity. A rising trend in the integrated OH* intensity also shows that the developing kernel has a higher chance of survival. In all the cases studied, the rising trend reaches a peak and is followed by a downward trend which may be due to heat losses resulting from interaction of the flame kernel with the Nitrogen used as blow-off gas. In the stoichiometric CH_4/air mixture, this peak appeared in the form of a plateau with intensity value of 6000000 AU which occurred between 6 ms and 8 ms. Sensitivity analysis shows that the peak integrated OH* intensity differs systematically depending on the incident energy, equivalence ratio and the fuel mixture. For example, the maximum integrated OH* intensity decreased when the incident energy from 32 to 64 mJ, however, further increase in energy produced an increase but not at the same as the initial peak with 32 mJ. Based on this observation, the optimal ignition energy should be decided based on the OH* production. In the present investigation, a 32 mJ energy would be ideal, however, it will be helpful to investigate lower incidents energies since this is much higher than the MIE of the mixture (~0.25 mJ). For different equivalence ratio (i.e., φ = 1.0, 0.9, 0.8), the maximum integrated OH* intensity decreased in leaner mixtures. Of the three fuels investigated, the maximum integrated OH* intensity was obtained in ethylene, followed by methane and then propane. This shows that a higher heat release was occurring in ethylene kernel despite the faster growth from the methane kernel.

Further analysis of the peak OH* intensity history revealed that transition to a self-sustained flame kernel is characterized by decay from an initial high peak OH* intensity to a minimum value which must be sustained for the kernel to survive. This is shown in Figure 5.11 and is also evident in all the cases investigated. According to the figure, after reaching its minimum value at 1.5 ms, a slow recovery stage is observed with subsequent peak OH* intensity reaching a maximum trough value of 1500 AU at 4.5 ms and a second maximum trough value of 2000 AU at 9 ms. The high decay rate in peak OH* intensity during the early development of the kernel is indicative of the cooling resulting from high stretch on the kernel. The recovery indicates continuous heat release resulting from chemical reaction at the flame fronts. Just like most of the parameters, sensitivity analysis showed that the minimum peak OH* intensity changed systematically depending on the incident energy, equivalence ratio and the fuel mixture. As observed in the integrated OH* intensity, the values of the peak OH* intensity decreased with energy increase from 32 to 64 mJ following the formation of a self-sustaining flame. However, further increase in energy however did not produce any further change as observed in the kernel width. As expected, the magnitude of peak OH* intensity decreased in leaner mixtures (i.e., $\varphi = 0.9, 0.8$) compared to the stoichiometric mixture (i.e., $\varphi = 1.0$). Of the three fuels investigated, the values of peak OH* intensity shows ethylene was the most reactive while propane was the least reactive. However, the reactivity of methane kernel approached that of ethylene when the mixtures were leaned further.

Chapter 8 **Conclusions and Recommendations**

8.1 Conclusions

This thesis report investigated key development characteristics of laser induced spark-ignited flame kernels propagating in gaseous premixed fuel/air mixtures. The goal was to show the link between the characteristic parameters and ignition success with the hope that the results could be used as validation data for laser ignition models. Two main studies of the kernel development were explored through visualisation of flow field features (Laser tomography) and flame chemiluminescence. The third investigation was done mainly to show the sensitivity of the parameters to changes in the fuel properties. As a result, two experimental measurement solutions were developed. The first setup consists of a co-axial straight tube burner in which flowing mixture of Methane and Mie-scattered Air was illuminated by a laser-sheet and then ignited by a single pulse laser beam of 1064 nm wavelength and 7 ns pulse width. High-speed imaging of the combustion region allowed simultaneous measurement of the flame kernel development as well as its flow field structures. The second setup consists of an axial contracting-nozzles burner in which different flowing fuel/air mixtures were repeatedly ignited using a focussed laser beam of 1064 nm wavelength and 2 Hz frequency. Direct imaging of the flame kernel OH* chemiluminescence using intensified CCD camera. Conclusions from the findings are summarised below:

- High speed flow visualization study revealed that on ignition, an elliptically shaped plasma of hot gas was formed, which developed into a two-lobe toroidal kernel by 50 μs, followed by the appearance a front lobe before 167 μs, thus resulting in an asymmetric toroidal flame kernel. The images also reveal an induced motion of a centreline jet flow, generated by contra-rotating upstream and downstream vortices which was responsible for the front lobe appearance. Analysis of the initial plasma reveal an instantaneous growth, the radius of which is comparable to that predicted by the Blast wave theory at 1 μs with some differences depending on the flow (i.e., 13.9% less in the laminar flow case, and 4% more in the turbulent flow case). Analysis of the spatial growth revealed that in the laminar flow case, it took about 0.7 ms for the kernel height to grow to a size about the burner diameter (i.e., 10 mm) and while in the turbulent flow, it took only 0.3 ms to reach this height. Further analysis of the growth rate revealed it decayed in stages from an initial shock speed 23 times the unstretched laminar value (S_L) to a stable speed close to S_L in about 1 ms.

- Prior to ignition, PIV analysis reveal an axisymmetric structure in the axial flow velocity vectors, with peaks in the potential core region which decreased radially to its minimum values near the flow edges. From the radial profiles, a constant velocity peak was observed throughout the flow in the laminar flow case, while in the turbulent flow the velocity peak decreased moving from upstream to downstream. Unlike the flow velocity, the turbulence intensity was stronger near the flow edges than in the potential core region with an increasing trend in magnitude from upstream to downstream. Analysis of the flow field after ignition show an increased peak velocity in the downstream flow ahead of the flame front and reduced peak velocity in the upstream flow behind the flame front. Further investigation of the radial profiles of the axial velocity revealed that this variation in velocity peak existed only within certain distances (below 2.5 mm) from the flame fronts.
- Flame kernel visualisation using the OH* chemiluminescence revealed transition from a toroidal shaped kernel at 50 μs, to a toroid with front lobe at 100 μs and lastly a self-sustained propagating flame ball after disappearance of the front lobe. The displacement curve of the flame fronts reveals two stages in growth: a non-linear decay growth in the first 0.8 ms, and a steady (linear) growth onwards. The dimensions of the kernel were different with the height always greater than the width. In the base case, it takes about 2 ms for the kernel height (H) to grow to a spatial scale about the size of the burner diameter (i.e., 22 mm) and kernel width (W) reached a spatial scale about the size of the burner diameter in just above 2 ms. The propagation rate of the flame front decays from a highly stretched initial value to a steady asymptotic value close to the unstretched laminar flame speed. It also highlights three key

stages in development of the kernel. In the base case (i.e., laminar CH_4/Air at $\varphi=1.0$), the first steady velocity of 11 m/s dominated by induced gas flow was observed between 150 to 200 μs. The second steady velocity of 7.5 m/s was observed between 250 and 500 μs due to combined influence of chemical reactions and induced gas flows. The third steady velocity of 3.5 m/s, observed from 800 μs and beyond was purely due to chemical reactions.

- Further visualisation of the image colourmap revealed the spatial distribution of OH* produced inside the reaction zone evolved from isotropic to anisotropic flame front during its development. In the self-sustained flame, the reaction zones were concentrated at the edges. Transition to a self-sustained flame kernel is characterized by decay in peak OH* intensity to a minimum value which must be sustained for the kernel to survive. The kernel development involves transition from a quenching kernel of hot gas to the formation of an igniting flame kernel which is marked by a minimum integrated OH* intensity. The time elapsed before this minimum value was interpreted as the chemical induction time [92]. In the base case, this transition occurred at 0.2 ms. Following this transition, the kernels with a high chance of survival is characterised by a continuous rise in integrated OH* intensity attaining a maximum value when the kernel becomes fully developed.
- A comparison of the kernel development at different incident energies (i.e., 32, 64, 96 and 128 mJ) reveals that the early growth of the kernel is enhanced by a higher energy, but this happens within a limiting threshold energy. In the fully developed kernel however, the size of the kernel is not influence by the energy. A comparison of the peak OH* intensities reveals that the reactivity was unaffected by the energy of the incident beam except in the first 0.5 ms. A comparison of the integrated OH* intensities shows that the chemical induction duration increased for higher energies. An interesting insight from this analysis is the fact that the maximum integrated OH* intensity decreased greatly by 25% with energy increase from 32 to 64 mJ, however, further increase in energy resulted a reduction in the negative effect. Therefore, in choosing the energy, the OH* production is very important since stretch effect only last for a short time. For the current investigation, 32 mJ would be the best choice, on the

observations, should be decided based on, however further investigation with lower ignition energies is advised in order to decide the optimal ignition energy. Further details of the sensitivity analysis are shown in Table 0.1 of Appendix E: Sensitivity Analysis.

- A comparison of the kernel development at different bulk flow velocities (i.e., 1.15, 2.08, 3.0 and 3.48 m/s) reveals an increased displacement of the kernel centroid with higher flow velocity due to convective effects and as well as an increased strain on the flame front upstream. Overall, there is no remarkable increase in growth rate of the kernel due to increased velocity. The combined effect of convection and increased turbulence at higher bulk velocities resulted in a faster propagation of the flame front downstream. There were fluctuations in both the peak OH* intensity and maximum integrated intensity which made difficult to understand the influence of increased velocity on reactivity. Also, the duration of chemical induction appears to be longer for higher bulk velocity flows.

- A sensitivity study of the effect of equivalence ratio on kernel development reveals a linear decline in the characteristic parameters moving from $\varphi=1.0$ to $\varphi=0.8$ with higher stretch rates in leaner mixtures. For example, the steady state values of S_{y+} in the laminar mixtures were 3.3, 2.96 and 2.59 m/s, which represents 11% drop per unit reduction in φ, moving from stoichiometric to lean. Also, the minimum peak OH* intensities were lowered by 18% per unit reduction in φ during its development. In addition, the integrated OH* intensities showed that lower equivalence ratios produced weaker kernels (9% per unit reduction in φ) and experienced longer chemical induction duration. It is worth noting that the linear relationship did not occur in turbulent flows.

- A sensitivity study of the variation in kernel development characteristics for fuels with the same AFT showed significant differences depending on the mixture Lewis number, *Le*. Of the three fuels investigated, the kernel experienced the slowest growth in propane fuel with the higher *Le*. Contrary to expectation, kernel growth was faster in methane (with LFV of 41 cm/s) than in ethylene (with LFV of 51 cm/s) due to preferential diffusion that occurs in mixture with non-unity *Le*. From the normalized propagation speed S_{y-}/S_L, it was observed CH4/air experienced the most stretch. The differences in stretch widened with lowering of the AFT from 2226 K to 2134 K due to wider variation in both the Markstein length and effective Lewis Numbers. Both peak OH* intensity and the spatial integrated OH* intensity measurements showed the ethylene kernel was the most reactive while propane was the least reactive. Likewise, the duration of chemical induction followed the same order with ethylene kernel taking longer than the rest.

- Sensitivity study using fuels with constant LFV showed some difference both geometric stretch and reactivity. At 41 cm/s LFV, the ethylene kernel was the most stretched while the propane kernel was the least stretched. However, further dilution resulted in methane becoming more stretched. The same trend is observed in reactivity as shown by both the peak OH* intensities and integrated OH* intensities. This behaviour may be explained by the fact that there is more heat losses as the flame temperature difference is expected to widen in line with wider variation of Le of the fuels in the lean range [162].

8.2 Recommendations and Further Work

- Laser tomography was employed for simultaneous visualization of the flame kernel and its flow field. From this the flame kernel characteristics such as flame tip positions and displacement speed were quantified. To effectively describe the flame kernel, a complete mapping of the characteristics of the entire kernel geometry at different times is necessary. In addition, repeated imaging of the flame kernel at the same condition would be helpful in statistically defining the reproducibility.
- High Speed PIV was employed to obtain the flow field structure before and during ignition. In the isothermal case, the velocity fields were based on an average velocity, however only instantaneous velocity field were obtained during reaction. To statistically define the reproducibility of change in velocity field during ignition, it is necessary to acquire more high-speed images at the same condition and then fine the mean using phase averaging technique. In

addition, a more realistic picture of the flow structures could be obtained by multi-camera PIV technique.

- OH* chemiluminescence was employed as flame marker to characterise the flame kernel as well as to indicate the relative measure of heat release. To effectively characterise the flame kernel, it would be helpful to measure the chemiluminescence of other radical (e.g., CH*, CO_2) produced in the reaction. In addition, a better picture of the 2D geometry of the flame kernel could be obtained from more sophisticated techniques like PLIF.
- Differences in the flame kernel characteristics due to changing pulse energy and flow velocity were observed in this work. Characterising the sparks produced by the laser beam under these conditions would be helpful in explaining the reason for these differences since the actual energy utilized in laser ignition comes from the spark.
- Differences in the flame kernel characteristics for different fuels were observed in this work. It would be interesting to look at the actual effect of the chemical components such as the carbon size and bond type. In addition, studies on a wider range of low emission fuels would be helpful in developing more robust laser ignition models and the work towards engine-relevant conditions.
- This research was conducted with the hope that it will produce useful data for improved modelling of laser ignition process. Further research in this area would be more useful if there is close collaboration with modellers such that specific data required to validate existing codes could be produced.

References

[1] Ø. Buhaug, J. J. Corbett, Ø. Endresen, V. Eyring, and K. Yoshida, “Second IMO Greenhouse Gas Study 2009,” 2009.

[2] IMO, “Third IMO Greenhouse Gas Study 2014,” *Int. Marit. Organ.*, 2014.

[3] D. K. Pritchard, D. J. Freeman, and P. W. Guilbert, “Prediction of explosion pressures in confined spaces,” *J. Loss Prev. Process Ind.*, vol. 9, no. 3, 1996.

[4] “EU Emission Standards: Cars and Light Trucks.” [Online]. Available: https://dieselnet.com/standards/eu/ld.php#stds.

[5] S. Pischinger, M. Umierski, and B. Hüchtebrock, “New CNG concepts for passenger cars: High torque engines with superior fuel consumption,” in *SAE Technical Papers*, 2003.

[6] DNV-GL, “MARITIME LNG regulatory update SUPPLY : Brief status on uptake of LNG as fuel,” no. April, 2018.

[7] “Liquefied petroleum gas, LPG.” [Online]. Available: https://www.iea-amf.org/content/fuel_information/lpg.

[8] Z. Abdul Latiff, A. Abdul Aziz, B. Suptiyano, and M. Said, “Viability study of ethylene (C2H4) as an alternative fuel for gasoline engine,” *J. Mek.*, no. 26, 2008.

[9] S. M. Correa, “A review of NOx formation under gas-turbine combustion conditions,” *Combust. Sci. Technol.*, 1993.

[10] P. D. Ronney, “Laser versus conventional ignition of flames,” *Opt. Eng.*, vol. 33, no. 2, p. 510, 1994.

[11] F. Paschen, “Ueber die zum Funkenübergang in Luft, Wasserstoff und Kohlensäure bei verschiedenen Drucken erforderliche Potentialdifferenz,” *Ann. Phys.*, vol. 273, no. 5, pp. 69–96, 1889.

[12] J. D. Dale and A. K. Oppenheim, “Enhanced ignition for I. C. Engines with premixed gases,” *SAE Tech. Pap.*, vol. 90, pp. 606–621, 1981.

[13] M. H. Morsy, “Review and recent developments of laser ignition for internal combustion engines applications,” *Renewable and Sustainable Energy Reviews*. 2012.

[14] G. Herdin, J. Klausner, E. Wintner, M. Weinrotter, J. Graf, and K. Iskra, “Laser Ignition: A New Concept to Use and Increase the Potentials of Gas Engines,” 2008.

[15] C. G. Morgan, “Laser-induced breakdown of gases,” *Reports Prog. Phys.*, 1975.

[16] D. L. Mcintyre, “A Laser Spark Plug Ignition System for a Stationary Lean-Burn Natural Gas Reciprocating Engine,” 2007.

[17] B. E. Forch and A. W. Miziolek, “Laser-based ignition of H2 O2 and D2 O2 premixed gases through resonant multiphoton excitation of H and D atoms near 243 nm,” *Combust. Flame*, 1991.

[18] B. E. Forch and A. W. Miziolek, “Oxygen-atom two-photon resonance effects in multiphoton photochemical ignition of premixed H_2/O_2 flows,” *Opt. Lett.*, 1986.

[19] D. Bradley, C. G. W. Sheppard, I. M. Suardjaja, and R. Woolley, “Fundamentals of high-energy spark ignition with lasers,” *Combust. Flame*, vol. 138, no. 1–2, pp. 55–77, 2004.

[20] D. L. McIntyre, S. D. Woodruff, and J. S. Ontko, “Lean-Burn Stationary Natural Gas Reciprocating Engine Operation With a Prototype Fiber Coupled Diode End Pumped Passively Q-Switched Laser Spark Plug,” 2009.

[21] B. Bihari, S. B. Gupta, R. R. Sekar, J. Gingrich, and J. Smith, “Development of Advanced Laser Ignition System for Stationary Natural Gas Reciprocating Engines,” 2008.

[22] G. Liedl *et al.*, “Laser-induced ignition of gasoline direct-injection engines,” in *XV International Symposium on Gas Flow, Chemical Lasers, and High-Power Lasers*, 2005.

[23] R. Osborne, J. Wehrmeyer, H. Trinh, and J. Early, “Evaluation and Characterization Study of Dual Pulse Laser-Induced Spark (DPLIS) for Rocket Engine Ignition System Application,” 2012.

[24] N. Khan, Z. Saleem, and A. A. Mirza, “Ignition study of a petrol/CNG single cylinder engine,” in *Intelligent Systems in Design and Manufacturing VI*, 2005, vol. 5999.

[25] M. Weinrotter *et al.*, “Optical diagnostics of laser-induced and spark plug-assisted hcci combustion,” in *SAE Technical Papers*, 2005.

[26] J. Tauer, H. Kofler, and E. Wintner, “Laser-initiated ignition,” *Laser Photonics Rev.*, vol. Rev. 4, no. No. 1, pp. 99–122, 2010.

[27] “Jean Boulet Archives - This Day in Aviation.” [Online]. Available:

https://www.thisdayinaviation.com/tag/jean-boulet/.

[28] H. El-Rabii and G. Gaborel, “Laser ignition of flammable mixtures via a solid core optical fiber,” *Appl. Phys. B Lasers Opt.*, 2007.

[29] M. Boileau, G. Staffelbach, B. Cuenot, T. Poinsot, and C. Bérat, “LES of an ignition sequence in a gas turbine engine,” *Combust. Flame*, vol. 154, no. 1–2, 2008.

[30] T. Marchione, “Effectiveness of localized spark ignition in recirculating n-heptane spray flames,” *21st ICDERS*, no. September 2015, pp. 1–6, 2007.

[31] M. Tsunekane and T. Taira, “High peak power, passively Q-switched Yb:YAG/Cr:YAG micro-lasers,” *IEEE J. Quantum Electron.*, 2013.

[32] H. Kofler, E. Schwarz, and E. Wintner, “Experimental development of a monolithic passively Q-switched diode-pumped Nd:YAG laser,” *Eur. Phys. J. D*, 2010.

[33] M. Weinrotter, H. Kopecek, and E. Wintner, “Laser ignition in internal combustion engines-A novel approach based on advanced lasers,” in *Optics InfoBase Conference Papers*, 2005.

[34] T. X. Phuoc, “Laser-induced spark for simultaneous ignition and fuel-to-air ratio measurements,” *Opt. Lasers Eng.*, vol. 44, no. 6, pp. 520–534, 2006.

[35] a P. Yalin, M. DeFoort, B. Willson, Y. Matsuura, and M. Miyagi, “Use of hollow-core fibers to deliver nanosecond Nd:YAG laser pulses to form sparks in gases.,” *Opt. Lett.*, vol. 30, no. 16, pp. 2083–2085, 2005.

[36] A. P. Yalin *et al.*, “Development of a fiber delivered laser ignition system for natural gas engines,” in *Proceedings of the Spring Technical Conference of the ASME Internal Combustion Engine Division*, 2006.

[37] A. P. Yalin *et al.*, “Laser ignition of natural gas engines using fiber delivery,” in *2005 Fall Technical Conference of the ASME Internal Combustion Engine Division*, 2005.

[38] S. Joshi, A. P. Yalin, and A. Galvanauskas, “Use of hollow core fibers, fiber lasers, and photonic crystal fibers for spark delivery and laser ignition in gases,” in *Applied Optics*, 2007.

[39] A. Clarke, “Calculation and consideration of the Lewis number for explosion studies,” *Process Saf. Environ. Prot. Trans. Inst. Chem. Eng. Part B*, 2002.

[40] J. B. Heywood, *Internal Combustion Engine Fundementals*, vol. 21. 1988.

[41] G. Wang, M. Boileau, D. Veynante, and K. Truffin, “Large eddy simulation of a growing turbulent premixed flame kernel using a dynamic flame surface

density model," *Combust. Flame*, 2012.

[42] M. S. Mansour, A. M. Elbaz, and M. F. Zayed, "Flame kernel generation and propagation in turbulent partially premixed hydrocarbon jet," in *Combustion Science and Technology*, 2014.

[43] A. G. Gaydon, *The spectrocopy of flames*. 1974.

[44] J. Kojima, Y. Ikeda, and T. Nakajima, "Basic aspects of OH(A), CH(A), and C2(d) chemiluminescence in the reaction zone of laminar methane-air premixed flames," *Combust. Flame*, vol. 140, no. 1–2, 2005.

[45] B. D. Stojkovic, T. D. Fansler, M. C. Drake, and V. Sick, "High-speed imaging of OH* and soot temperature and concentration in a stratified-charge direct-injection gasoline engine," *Proc. Combust. Inst.*, 2005.

[46] R. W. Schefer, "Flame Sheet Imaging Using CH Chemiluminescence," *Combust. Sci. Technol.*, 1997.

[47] C. Dumitrache, R. Vanosdol, C. M. Limbach, and A. P. Yalin, "Control of Early Flame Kernel Growth by Multi-Wavelength Laser Pulses for Enhanced Ignition," *Sci. Rep.*, 2017.

[48] N. Docquier and S. Candel, "Combustion control and sensors: A review," *Prog. Energy Combust. Sci.*, vol. 28, no. 2, pp. 107–150, 2002.

[49] B. Higgins, M. Q. McQuay, F. Lacas, and S. Candel, "An experimental study on the effect of pressure and strain rate on CH chemiluminescence of premixed fuel-lean methane/air flames," *Fuel*, 2001.

[50] Y. Ikeda, M. Kaneko, and T. Nakajima, "Local A/F Measurement by Chemiluminescence OH*, CH* and C2* in SI Engine," in *SAE Technical Paper Series*, 2001.

[51] I. Glassman, R. A. Yetter, and N. G. Glumac, *Combustion 5th ed*. 2014.

[52] I. A. Mulla, A. Dowlut, T. Hussain, S. R. Chakravarthy, N. Swaminathan, and R. Balachandran, "Heat release rate estimation in laminar premixed flames using laser-induced fluorescence of CH2O and H-atom," *Combust. Flame*, 2016.

[53] P. H. Paul and H. N. Najm, "Planar laser-induced fluorescence imaging of flame heat release rate," in *Symposium (International) on Combustion*, 1998.

[54] F. V. Tinaut, A. Melgar, B. Giménez, and M. Reyes, "Characterization of the combustion of biomass producer gas in a constant volume combustion bomb," *Fuel*, 2010.

[55] R. B. Price, I. R. Hurle, and T. M. Sugden, “Optical studies of the generation of noise in turbulent flames,” in *Symposium (International) on Combustion*, 1969, vol. 12, no. 1.

[56] C. J. Lawn, “Distributions of instantaneous heat release by the cross-correlation of chemiluminescent emissions,” *Combust. Flame*, vol. 123, no. 1–2, 2000.

[57] R. Balachandran, B. O. Ayoola, C. F. Kaminski, A. P. Dowling, and E. Mastorakos, “Experimental investigation of the nonlinear response of turbulent premixed flames to imposed inlet velocity oscillations,” *Combust. Flame*, vol. 143, no. 1–2, 2005.

[58] B. O. Ayoola, R. Balachandran, J. H. Frank, E. Mastorakos, and C. F. Kaminski, “Spatially resolved heat release rate measurements in turbulent premixed flames,” *Combust. Flame*, 2006.

[59] Y. Hardalupas and M. Orain, “Local measurements of the time-dependent heat release rate and equivalence ratio using chemiluminescent emission from a flame,” *Combust. Flame*, 2004.

[60] B. Gillet, Y. Hardalupas, C. Kavounides, and A. M. K. P. Taylor, “Infrared absorption for measurement of hydrocarbon concentration in fuel/air mixtures (MAST-B-LIQUID),” in *Applied Thermal Engineering*, 2004, vol. 24, no. 11–12.

[61] V. N. Nori and J. M. Scitzman, “CH* chemiluminescence modeling for combustion diagnostics,” *Proc. Combust. Inst.*, vol. 32 I, no. 1, 2009.

[62] V. N. Nori and J. M. Seitzman, “Chemiluminescence measurements and modeling in syngas, methane and jet-a fueled combustors,” in *Collection of Technical Papers - 45th AIAA Aerospace Sciences Meeting*, 2007, vol. 8.

[63] H. N. Najm, P. H. Paul, C. J. Mueller, and P. S. Wyckoff, “On the Adequacy of Certain Experimental Observables as Measurements of Flame Burning Rate,” *Combust. Flame*, vol. 113, no. 3, 1998.

[64] B. Kim, M. Kaneko, Y. Ikeda, and T. Nakajima, “Detailed spectral analysis of the process of HCCI combustion,” *Proc. Combust. Inst.*, vol. 29, no. 1, 2002.

[65] J. Ballester and T. García-Armingol, “Diagnostic techniques for the monitoring and control of practical flames,” *Progress in Energy and Combustion Science*, vol. 36, no. 4. 2010.

[66] P. D. Maker and R. W. Terhune, “Study of optical effects due to an induced polarization third order in the electric field strength,” *Phys. Rev.*, vol. 137, no. 3, pp. A801–A818, 1965.

[67] A. Starikovskiy and N. Aleksandrov, "Plasma-assisted ignition and combustion," *Progress in Energy and Combustion Science*. 2013.

[68] T. X. Phuoc, "Laser-induced spark ignition fundamental and applications," *Optics and Lasers in Engineering*, vol. 44, no. 5. pp. 351–397, 2006.

[69] V. E. Mitsuk, I. Savoskin, and V. A. Chernikov, "Breakdown at Optical Frequencies in the Presence of Diffusion Losses," *Journal of Experimental and Theoretical Physics Letters*, vol. 4, no. 4. pp. 129–131, 1966.

[70] C. H. Chan, C. D. Moody, and W. B. McKnight, "Significant loss mechanisms in gas breakdown at 10.6 μ," *J. Appl. Phys.*, vol. 44, no. 3, pp. 1179–1188, 1973.

[71] R. Hickling and W. R. Smith, "Combustion bomb tests of laser ignition," in *SAE Technical Papers*, 1974.

[72] Ş. Yalçin, D. R. Crosley, G. P. Smith, and G. W. Faris, "Influence of ambient conditions on the laser air spark," *Appl. Phys. B Lasers Opt.*, vol. 68, no. 1, 1999.

[73] A. W. Miziolek, V. Palleschi, and I. Schechter, "Laser-induced breakdown spectroscopy (LIBS): fundamentals and applications," *booksgooglecom*, vol. 6, p. 620, 2006.

[74] D. A. Cremers and L. J. Radziemski, *Handbook of Laser-induced Breakdown Spectroscopy*. 2006.

[75] T. Minowa, T. Kawata, H. Katsuragawa, and H. K. Uematsu, "Initial phase of laser-induced air optical breakdown: a new picture," *Appl. Opt.*, vol. 37, no. 6, 1998.

[76] I. Dors, C. Parigger, and J. W. L. Lewis, "Fluid dynamics effects following laser-induced optical breakdown," in *38th Aerospace Sciences Meeting and Exhibit*, 2000.

[77] F. J. Weinberg and J. R. Wilson, "A Preliminary Investigation of the Use of Focused Laser Beams for Minimum Ignition Energy Studies," *Proc. R. Soc. A Math. Phys. Eng. Sci.*, vol. 321, no. 1544, pp. 41–52, 1971.

[78] R. G. Kingdon and F. J. Weinberg, "The effect of plasma constitution on laser ignition energies," *Symp. Combust.*, 1977.

[79] J. A. Syage, E. W. Fournier, R. Rianda, and R. B. Cohen, "Dynamics of flame propagation using laser-induced spark initiation: Ignition energy measurements," *J. Appl. Phys.*, vol. 64, no. 3, pp. 1499–1507, 1988.

[80] T. X. Phuoc, "Laser spark ignition: Experimental determination of laser-induced breakdown thresholds of combustion gases," *Opt. Commun.*, vol. 175, no. 4, pp. 419–423, 2000.

[81] J. L. Beduneau, B. Kim, L. Zimmer, and Y. Ikeda, “Measurements of minimum ignition energy in premixed laminar methane/air flow by using laser induced spark,” *Combust. Flame*, vol. 132, no. 4, pp. 653–665, 2003.

[82] J. Huang, P. G. Hill, W. K. Bushe, and S. R. Munshi, “Shock-tube study of methane ignition under engine-relevant conditions: Experiments and modeling,” *Combust. Flame*, 2004.

[83] S. S. Shy, W. T. Shih, and C. C. Liu, “More on minimum ignition energy transition for lean premixed turbulent methane combustion in flamelet and distributed regimes,” in *Combustion Science and Technology*, 2008.

[84] C. Cardin, B. Renou, G. Cabot, and A. M. Boukhalfa, “Experimental analysis of laser-induced spark ignition of lean turbulent premixed flames: New insight into ignition transition,” *Combust. Flame*, vol. 160, no. 8, pp. 1414–1427, 2013.

[85] D. R. Ballal and A. H. Lefebvre, “The influence of flow parameters on minimum ignition energy and quenching distance,” *Symp. Combust.*, 1975.

[86] D. R. Ballal and A. H. Lefebvre, “Flame quenching in turbulent flowing gaseous mixtures,” *Symp. Combust.*, 1977.

[87] H. Kopecek, H. Maier, G. Reider, F. Winter, and E. Wintner, “Laser ignition of methane-air mixtures at high pressures,” *Exp. Therm. Fluid Sci.*, 2003.

[88] M. Weinrotter, H. Kopecek, E. Wintner, M. Lackner, and F. Winter, “Application of laser ignition to hydrogen-air mixtures at high pressures,” *Int. J. Hydrogen Energy*, vol. 30, no. 3, pp. 319–326, 2005.

[89] D. A. Santavicca, C. Ho, B. J. Reilly, and T. W. Lee, “Laser induced spark ignition of methane-oxygen mixtures,” no. September, 1991.

[90] G. Taylor, “The Formation of a Blast Wave by a Very Intense Explosion . II . The Atomic Explosion of 1945 The formation of a blast wave by a very intense explosion . 11 . The atomic explosion of 1945,” *R. Soc. London, Ser. A, Maths Phys. Sci.*, vol. 201, no. 1065, pp. 175–186, 1950.

[91] T. A. Spiglanin, A. Mcilroy, E. W. Fournier, R. B. Cohen, and J. A. Syage, “Time-resolved imaging of flame kernels: Laser spark ignition of H2/O2/Ar mixtures,” *Combust. Flame*, vol. 102, no. 3, pp. 310–328, 1995.

[92] T. X. Phuoc and F. P. White, “Laser-induced spark ignition of CH4/air mixtures,” *Combust. Flame*, 1999.

[93] C. V. Bindhu, S. S. Harilal, M. S. Tillack, F. Najmabadi, and A. C. Gaeris, “Laser propagation and energy absorption by an argon spark,” *J. Appl. Phys.*, vol. 94, no. 12, pp. 7402–7407, 2003.

[94] M. Lackner, S. Charareh, F. Winter, H. Kopecek, and E. Wintner, “Investigation of the early stages in laser-induced ignition by Schlieren photography and laser-induced fluorescence spectroscopy.,” *Opt. Express*, vol. 12, no. 19, pp. 4546–4557, 2004.

[95] J. L. Beduneau and Y. Ikeda, “Application of laser ignition on laminar flame front investigation,” in *Experiments in Fluids*, 2004, vol. 36, no. 1, pp. 108–113.

[96] J. L. Beduneau, N. Kawahara, T. Nakayama, E. Tomita, and Y. Ikeda, “Laser-induced radical generation and evolution to a self-sustaining flame,” *Combust. Flame*, 2009.

[97] D. K. Srivastava, K. Dharamshi, and A. K. Agarwal, “Flame kernel characterization of laser ignition of natural gasair mixture in a constant volume combustion chamber,” *Opt. Lasers Eng.*, 2011.

[98] K. Dharamshi, D. K. Srivastava, and A. K. Agarwal, “Combustion characteristics and flame-kernel development of a laser ignited hydrogen-air mixture in a constant volume combustion chamber,” *Int. J. Hydrogen Energy*, 2014.

[99] I. A. Mulla, S. R. Chakravarthy, N. Swaminathan, and R. Balachandran, “Evolution of flame-kernel in laser-induced spark ignited mixtures: A parametric study,” *Combust. Flame*, vol. 164, pp. 303–318, 2016.

[100] Y. Yu, X. Li, R. Fan, D. Chen, and R. Sun, “Stabilization of a premixed methane-air flame with a high repetition nanosecond laser-induced plasma,” *Opt. Laser Technol.*, 2017.

[101] B. Almansour, L. Thompson, J. Lopez, and S. S. Vasu, “Laser ignition and burning velocity measurements in natural gas/air mixtures,” 2015.

[102] J. X. Ma, D. R. Alexander, and D. E. Poulain, “Laser spark ignition and combustion characteristics of methane-air mixtures,” *Combust. Flame*, 1998.

[103] D. K. Srivastava, E. Wintner, and A. K. Agarwal, “Effect of focal size on the laser ignition of compressed natural gas-air mixture,” *Opt. Lasers Eng.*, 2014.

[104] D. K. Srivastava, E. Wintner, and A. K. Agarwal, “Effect of laser pulse energy on the laser ignition of compressed natural gas fueled engine,” *Opt. Eng.*, 2014.

[105] B. R. Munson, T. H. Okiishi, W. W. Huebsch, and A. P. Rothmayer, *Fundamentals of Fluid Mechanics*. 2012.

[106] S. B. Pope, “Turbulent premixed flames,” *Turbul. Premixed Flames*, pp. 1–437, 1987.

[107] F. Y. Hagos, A. Rashid, A. Aziz, and S. A. Sulaiman, “Study of syngas combustion parameters effect on internal combustion engine,” *Asian J. Sci. Res.*, 2013.

[108] C. K. Law, *“Combustion Physics.”* 2006.

[109] C. Morley, “Gaseq: A chemical equilibrium program for Windows.” 2005.

[110] M. Burke, X. Qin, Y. Ju, and F. Dryer, “Measurements of hydrogen syngas flame speeds at elevated pressures,” *5th US Combust. Meet.*, 2007.

[111] C. K. Law, “A Compilation of Experimental Data on Laminar Burning Velocities,” in *Reduced Kinetic Mechanisms for Applications in Combustion Systems*, 2008.

[112] S. Kondo, K. Takizawa, A. Takahashi, K. Tokuhashi, and A. Sekiya, “A study on flammability limits of fuel mixtures,” *J. Hazard. Mater.*, vol. 155, no. 3, 2008.

[113] H. S. Homan and W. A. Sirignano, “Minimum mass of burning aluminum particles for ignition of methane/air and propane/air mixtures,” *Symp. Combust.*, 1981.

[114] R. A. Hill, “Ignition-delay times in laser initiated combustion,” *Appl. Opt.*, 1981.

[115] W. M. Trott, “CO2-laser-induced deflagration of fuel/oxygen mixtures,” *J. Appl. Phys.*, 1983.

[116] R. A. Hill and G. A. Laguna, “Laser initiated combustion of CH4 + O2 mixtures,” *Opt. Commun.*, 1980.

[117] B. Raffel, J. Warnatz, and J. Wolfrum, “Experimental study of laser-induced thermal ignition in O2/O3 mixtures,” *Appl. Phys. B Photophysics Laser Chem.*, 1985.

[118] U. Maas, B. Raffel, J. Wolfrum, and J. Warnatz, “Observation and simulation of laser induced ignition processes in O2-O3 and H2-O2 mixtures,” *Symp. Combust.*, 1986.

[119] M. A. Tanoff, M. D. Smooke, R. E. Teets, and J. A. Sell, “Computational and experimental studies of laser-induced thermal ignition in premixed ethylene-oxidizer mixtures,” *Combust. Flame*, 1995.

[120] D. Lucas, D. Dunn-Rankin, K. Hom, and N. J. Brown, “Ignition by excimer laser photolysis of ozone,” *Combust. Flame*, 1987.

[121] M. Lavid and J. G. Stevens, “Photochemical ignition of premixed hydrogen oxidizer mixtures with excimer lasers,” *Combust. Flame*, 1985.

[122] M. Lavid, Y. Nachshon, S. K. Gulati, and J. G. Stevens, “Photochemical Ignition

of Premixed Hydrogen/Oxygen Mixtures With ArF Laser," *Combust. Sci. Technol.*, 1994.

[123] M. S. Chou and T. J. Zukowski, "Ignition of H2/O2/NH3, H2/air/NH3 and CH4/O2/NH3 mixtures by excimer-laser photolysis of NH3," *Combust. Flame*, 1991.

[124] R. G. W. Norrish, "The study of combustion by photochemical methods," in *Symposium (International) on Combustion*, 1965.

[125] I. E. Forch and A. W. Miziolek, "Ultraviolet laser ignition of premixed gases by efficient and esonant multiphoton photochemical formation of ilicroplasmas," *Combust. Sci. Technol.*, 1987.

[126] G. Dearden and T. Shenton, "Laser ignited engines: progress, challenges and prospects," *Opt. Express*, 2013.

[127] M. Weinrotter, "Laser Ignition of Internal Combustion Engines: Basic Laser and Ignition Optics Developments, Engine Application and Optical Diagnostics," Vienna University of Technology, 2006.

[128] B. Lewis and G. von Elbe, "Combustion Waves in Laminar Flow," *Combust. Flames Explos. Gases*, pp. 215–417, 1987.

[129] D. E. Lencioni, "The effect of dust on 10.6-μm laser-induced air breakdown," *Appl. Phys. Lett.*, vol. 23, no. 1, pp. 12–14, Jul. 1973.

[130] J. REILLY, P. SINGH, and G. WEYL, "Multiple pulse laser propagation through atmospheric dust at 10.6 microns," in *10th Fluid and Plasmadynamics Conference*, American Institute of Aeronautics and Astronautics, 1977.

[131] L. J. Radziemski, *Lasers-Induced Plasmas and Applications*. 2020.

[132] A. Gold and H. B. Bebb, "Theory of Multiphoton Ionization," *Phys. Rev. Lett.*, vol. 14, no. 3, pp. 60–63, Jan. 1965.

[133] R. M. DAVIES and S. G. TAYLOR, "The mechanics of large bubbles rising through extended liquids and through liquids in tubes," *Dyn. Curved Front.*, pp. 377–392, 1950.

[134] M. H. Morsy and S. H. Chung, "Numerical simulation of front lobe formation in laser-induced spark ignition of CH4/air mixtures," *Proc. Combust. Inst.*, vol. 29, no. 2, pp. 1613–1619, 2002.

[135] T. X. Phuoc and F. P. White, "An optical and spectroscopic study of laser-induced sparks to determine available ignition energy," *Proc. Combust. Inst.*, 2002.

[136] R. B. Edmonson, H. L. Olsen, and E. L. Gayhart, "Application of ideal gas

theory to the gaseous expansion from an electric spark," *J. Appl. Phys.*, vol. 25, no. 8, pp. 1008–1013, 1954.

[137] K. Gkagkas, R. P. Lindstedt, and T. S. Kuan, "Transported PDF modelling of a high velocity bluff-Body stabilised flame (HM2) using detailed chemistry," *Flow, Turbul. Combust.*, 2009.

[138] M. Kono, K. Niu, T. Tsukamoto, and Y. Ujiie, "Mechanism of flame kernel formation produced by short duration sparks," *Symp. Combust.*, 1989.

[139] S. R. Turns, "An introduction to combustion: concepts and applications," *System*, vol. 499. 2000.

[140] V. Babrauskak, *Ignition Handbook*. 2003.

[141] A. Dowlut, "Simultaneous OH and Formaldyde PLIF imaging in Laminar and turbulent premixed flames," 2015.

[142] R. W. Bilger, "Conditional moment closure for turbulent reacting flow," *Phys. Fluids A*, vol. 5, no. 2, 1992.

[143] V. Stetsyuk, "Experimental study of combustion and scalar mixing in swirling jet flows Declaration of Originality," no. December, 2013.

[144] F. Picano, F. Battista, G. Troiani, and C. M. Casciola, "Dynamics of PIV seeding particles in turbulent premixed flames," *Exp. Fluids*, vol. 50, no. 1, 2011.

[145] L. Boyer, "Laser tomographic method for flame front movement studies," *Combust. Flame*, vol. 39, no. 3, 1980.

[146] A. Melling, "Tracer particles and seeding for particle image velocimetry," *Meas. Sci. Technol.*, vol. 8, no. 12, 1997.

[147] B. R. Masters, "Lord Rayleigh: A Scientific Life," *Opt. Photonics News*, vol. 20, no. 6, 2009.

[148] L. E. Drain, "The laser-Doppler technique.," 1980.

[149] G. Mie, "Contributions to the optics of turbid media, particularly of colloidal metal solutions." pp. 377–445, Feb-1976.

[150] C. Brossard *et al.*, "Principles and applications of particle image velocimetry Principles and applications," *Opt. Diagnostics Flow*, 2015.

[151] I. Grant, "Particle image velocimetry: A review," *Proc. Inst. Mech. Eng. Part C J. Mech. Eng. Sci.*, vol. 211, no. 1, 1997.

[152] Insight 4G, "Particle Image Velocimetry Part - 5 Post processing of PIV measurements," vol. 027, 2020.

[153] N. Otsu, "THRESHOLD SELECTION METHOD FROM GRAY-LEVEL

HISTOGRAMS.," *IEEE Trans Syst Man Cybern*, vol. SMC-9, no. 1, 1979.

[154] T. Endo, Y. Takenaka, Y. Sako, T. Johzaki, S. ichi Namba, and D. Shimokuri, "An experimental study on the ignition ability of a laser-induced gaseous breakdown," *Combust. Flame*, 2017.

[155] Y. P. Raĭzer, "Optical discharges," *Sov. Phys. - Uspekhi*, vol. 23, no. 11, 1980.

[156] M. S. Uberoi, A. M. Kuethe, and H. R. Menkes, "Flow field of a bunsen flame," *Phys. Fluids*, 1958.

[157] J. L. Beduneau and Y. Ikeda, "Spatial characterization of laser-induced sparks in air," *J. Quant. Spectrosc. Radiat. Transf.*, 2003.

[158] D. S. Dandy and S. R. Vosen, "Numerical and experimental studies of hydroxyl radical chemiluminescence in methane-air flames," *Combust. Sci. Technol.*, 1992.

[159] M. De Leo, A. Saveliev, L. A. Kennedy, and S. A. Zelepouga, "OH and CH luminescence in opposed flow methane oxy-flames," *Combust. Flame*, 2007.

[160] F. P. Incropera, D. P. DeWitt, T. L. Bergman, and A. S. Lavine, *Fundamentals of Heat and Mass Transfer 6th Edition*. 2007.

[161] Z. Chen, M. P. Burke, and Y. Ju, "On the critical flame radius and minimum ignition energy for spherical flame initiation," *Proc. Combust. Inst.*, 2011.

[162] M. Matalon, "Flame dynamics," *Proc. Combust. Inst.*, vol. 32 I, no. 1, 2009.

[163] T. Tsuruda and T. Hirano, "Local Flame Front Disturbance Development Under Acceleration." 1991.

[1] Ø. Buhaug, J. J. Corbett, Ø. Endresen, V. Eyring, and K. Yoshida, "Second IMO Greenhouse Gas Study 2009," 2009.

[2] IMO, "Third IMO Greenhouse Gas Study 2014," *Int. Marit. Organ.*, 2014.

[3] D. K. Pritchard, D. J. Freeman, and P. W. Guilbert, "Prediction of explosion pressures in confined spaces," *J. Loss Prev. Process Ind.*, vol. 9, no. 3, 1996.

[4] "EU Emission Standards: Cars and Light Trucks." [Online]. Available: https://dieselnet.com/standards/eu/ld.php#stds.

[5] S. Pischinger, M. Umierski, and B. Hüchtebrock, "New CNG concepts for passenger cars: High torque engines with superior fuel consumption," in *SAE Technical Papers*, 2003.

[6] DNV-GL, "MARITIME LNG regulatory update SUPPLY : Brief status on uptake of LNG as fuel," no. April, 2018.

[7] “Liquefied petroleum gas, LPG.” [Online]. Available: https://www.iea-amf.org/content/fuel_information/lpg.

[8] Z. Abdul Latiff, A. Abdul Aziz, B. Suptiyano, and M. Said, “Viability study of ethylene (C2H4) as an alternative fuel for gasoline engine,” *J. Mek.*, no. 26, 2008.

[9] S. M. Correa, “A review of NOx formation under gas-turbine combustion conditions,” *Combust. Sci. Technol.*, 1993.

[10] P. D. Ronney, “Laser versus conventional ignition of flames,” *Opt. Eng.*, vol. 33, no. 2, p. 510, 1994.

[11] M. Weinrotter, “Laser Ignition of Internal Combustion Engines: Basic Laser and Ignition Optics Developments, Engine Application and Optical Diagnostics,” Vienna University of Technology, 2006.

[12] F. Paschen, “Ueber die zum Funkenübergang in Luft, Wasserstoff und Kohlensäure bei verschiedenen Drucken erforderliche Potentialdifferenz,” *Ann. Phys.*, vol. 273, no. 5, pp. 69–96, 1889.

[13] J. D. Dale and A. K. Oppenheim, “Enhanced ignition for I. C. Engines with premixed gases,” *SAE Tech. Pap.*, vol. 90, pp. 606–621, 1981.

[14] M. H. Morsy, “Review and recent developments of laser ignition for internal combustion engines applications,” *Renewable and Sustainable Energy Reviews*. 2012.

[15] G. Herdin, J. Klausner, E. Wintner, M. Weinrotter, J. Graf, and K. Iskra, “Laser Ignition: A New Concept to Use and Increase the Potentials of Gas Engines,” 2008.

[16] C. G. Morgan, “Laser-induced breakdown of gases,” *Reports Prog. Phys.*, 1975.

[17] D. L. Mcintyre, “A Laser Spark Plug Ignition System for a Stationary Lean-Burn Natural Gas Reciprocating Engine,” 2007.

[18] B. E. Forch and A. W. Miziolek, “Laser-based ignition of H2 O2 and D2 O2 premixed gases through resonant multiphoton excitation of H and D atoms near 243 nm,” *Combust. Flame*, 1991.

[19] B. E. Forch and A. W. Miziolek, “Oxygen-atom two-photon resonance effects in multiphoton photochemical ignition of premixed H_2/O_2 flows,” *Opt. Lett.*, 1986.

[20] D. Bradley, C. G. W. Sheppard, I. M. Suardjaja, and R. Woolley, “Fundamentals of high-energy spark ignition with lasers,” *Combust. Flame*, vol. 138, no. 1–2, pp. 55–77, 2004.

[21] D. L. McIntyre, S. D. Woodruff, and J. S. Ontko, “Lean-Burn Stationary Natural Gas Reciprocating Engine Operation With a Prototype Fiber Coupled Diode End

Pumped Passively Q-Switched Laser Spark Plug,” 2009.

[22] B. Bihari, S. B. Gupta, R. R. Sekar, J. Gingrich, and J. Smith, “Development of Advanced Laser Ignition System for Stationary Natural Gas Reciprocating Engines,” 2008.

[23] G. Liedl *et al.*, “Laser-induced ignition of gasoline direct-injection engines,” in *XV International Symposium on Gas Flow, Chemical Lasers, and High-Power Lasers*, 2005.

[24] R. Osborne, J. Wehrmeyer, H. Trinh, and J. Early, “Evaluation and Characterization Study of Dual Pulse Laser-Induced Spark (DPLIS) for Rocket Engine Ignition System Application,” 2012.

[25] N. Khan, Z. Saleem, and A. A. Mirza, “Ignition study of a petrol/CNG single cylinder engine,” in *Intelligent Systems in Design and Manufacturing VI*, 2005, vol. 5999.

[26] M. Weinrotter *et al.*, “Optical diagnostics of laser-induced and spark plug-assisted hcci combustion,” in *SAE Technical Papers*, 2005.

[27] J. Tauer, H. Kofler, and E. Wintner, “Laser-initiated ignition,” *Laser Photonics Rev.*, vol. Rev. 4, no. No. 1, pp. 99–122, 2010.

[28] “Jean Boulet Archives - This Day in Aviation.” [Online]. Available: https://www.thisdayinaviation.com/tag/jean-boulet/.

[29] H. El-Rabii and G. Gaborel, “Laser ignition of flammable mixtures via a solid core optical fiber,” *Appl. Phys. B Lasers Opt.*, 2007.

[30] M. Boileau, G. Staffelbach, B. Cuenot, T. Poinsot, and C. Bérat, “LES of an ignition sequence in a gas turbine engine,” *Combust. Flame*, vol. 154, no. 1–2, 2008.

[31] T. Marchione, “Effectiveness of localized spark ignition in recirculating n-heptane spray flames,” *21st ICDERS*, no. September 2015, pp. 1–6, 2007.

[32] M. Tsunekane and T. Taira, “High peak power, passively Q-switched Yb:YAG/Cr:YAG micro-lasers,” *IEEE J. Quantum Electron.*, 2013.

[33] H. Kofler, E. Schwarz, and E. Wintner, “Experimental development of a monolithic passively Q-switched diode-pumped Nd:YAG laser,” *Eur. Phys. J. D*, 2010.

[34] M. Weinrotter, H. Kopecek, and E. Wintner, “Laser ignition in internal combustion engines-A novel approach based on advanced lasers,” in *Optics InfoBase Conference Papers*, 2005.

[35] T. X. Phuoc, “Laser-induced spark for simultaneous ignition and fuel-to-air ratio measurements,” *Opt. Lasers Eng.*, vol. 44, no. 6, pp. 520–534, 2006.

[36] a P. Yalin, M. DeFoort, B. Willson, Y. Matsuura, and M. Miyagi, “Use of hollow-core fibers to deliver nanosecond Nd:YAG laser pulses to form sparks in gases.,” *Opt. Lett.*, vol. 30, no. 16, pp. 2083–2085, 2005.

[37] A. P. Yalin *et al.*, “Development of a fiber delivered laser ignition system for natural gas engines,” in *Proceedings of the Spring Technical Conference of the ASME Internal Combustion Engine Division*, 2006.

[38] A. P. Yalin *et al.*, “Laser ignition of natural gas engines using fiber delivery,” in *2005 Fall Technical Conference of the ASME Internal Combustion Engine Division*, 2005.

[39] S. Joshi, A. P. Yalin, and A. Galvanauskas, “Use of hollow core fibers, fiber lasers, and photonic crystal fibers for spark delivery and laser ignition in gases,” in *Applied Optics*, 2007.

[40] A. Clarke, “Calculation and consideration of the Lewis number for explosion studies,” *Process Saf. Environ. Prot. Trans. Inst. Chem. Eng. Part B*, 2002.

[41] J. B. Heywood, *Internal Combustion Engine Fundementals*, vol. 21. 1988.

[42] G. Wang, M. Boileau, D. Veynante, and K. Truffin, “Large eddy simulation of a growing turbulent premixed flame kernel using a dynamic flame surface density model,” *Combust. Flame*, 2012.

[43] M. S. Mansour, A. M. Elbaz, and M. F. Zayed, “Flame kernel generation and propagation in turbulent partially premixed hydrocarbon jet,” in *Combustion Science and Technology*, 2014.

[44] A. G. Gaydon, *The spectrocopy of flames*. 1974.

[45] J. Kojima, Y. Ikeda, and T. Nakajima, “Basic aspects of OH(A), CH(A), and C2(d) chemiluminescence in the reaction zone of laminar methane-air premixed flames,” *Combust. Flame*, vol. 140, no. 1–2, 2005.

[46] B. D. Stojkovic, T. D. Fansler, M. C. Drake, and V. Sick, “High-speed imaging of OH* and soot temperature and concentration in a stratified-charge direct-injection gasoline engine,” *Proc. Combust. Inst.*, 2005.

[47] R. W. Schefer, “Flame Sheet Imaging Using CH Chemiluminescence,” *Combust. Sci. Technol.*, 1997.

[48] C. Dumitrache, R. Vanosdol, C. M. Limbach, and A. P. Yalin, “Control of Early Flame Kernel Growth by Multi-Wavelength Laser Pulses for Enhanced Ignition,” *Sci. Rep.*, 2017.

[49] N. Docquier and S. Candel, “Combustion control and sensors: A review,” *Prog. Energy Combust. Sci.*, vol. 28, no. 2, pp. 107–150, 2002.

[50] B. Higgins, M. Q. McQuay, F. Lacas, and S. Candel, “An experimental study on

the effect of pressure and strain rate on CH chemiluminescence of premixed fuel-lean methane/air flames," *Fuel*, 2001.

[51] Y. Ikeda, M. Kaneko, and T. Nakajima, "Local A/F Measurement by Chemiluminescence OH*, CH* and C2* in SI Engine," in *SAE Technical Paper Series*, 2001.

[52] I. Glassman, R. A. Yetter, and N. G. Glumac, *Combustion 5th ed*. 2014.

[53] I. A. Mulla, A. Dowlut, T. Hussain, S. R. Chakravarthy, N. Swaminathan, and R. Balachandran, "Heat release rate estimation in laminar premixed flames using laser-induced fluorescence of CH2O and H-atom," *Combust. Flame*, 2016.

[54] P. H. Paul and H. N. Najm, "Planar laser-induced fluorescence imaging of flame heat release rate," in *Symposium (International) on Combustion*, 1998.

[55] F. V. Tinaut, A. Melgar, B. Giménez, and M. Reyes, "Characterization of the combustion of biomass producer gas in a constant volume combustion bomb," *Fuel*, 2010.

[56] R. B. Price, I. R. Hurle, and T. M. Sugden, "Optical studies of the generation of noise in turbulent flames," in *Symposium (International) on Combustion*, 1969, vol. 12, no. 1.

[57] C. J. Lawn, "Distributions of instantaneous heat release by the cross-correlation of chemiluminescent emissions," *Combust. Flame*, vol. 123, no. 1–2, 2000.

[58] R. Balachandran, B. O. Ayoola, C. F. Kaminski, A. P. Dowling, and E. Mastorakos, "Experimental investigation of the nonlinear response of turbulent premixed flames to imposed inlet velocity oscillations," *Combust. Flame*, vol. 143, no. 1–2, 2005.

[59] B. O. Ayoola, R. Balachandran, J. H. Frank, E. Mastorakos, and C. F. Kaminski, "Spatially resolved heat release rate measurements in turbulent premixed flames," *Combust. Flame*, 2006.

[60] Y. Hardalupas and M. Orain, "Local measurements of the time-dependent heat release rate and equivalence ratio using chemiluminescent emission from a flame," *Combust. Flame*, 2004.

[61] B. Gillet, Y. Hardalupas, C. Kavounides, and A. M. K. P. Taylor, "Infrared absorption for measurement of hydrocarbon concentration in fuel/air mixtures (MAST-B-LIQUID)," in *Applied Thermal Engineering*, 2004, vol. 24, no. 11–12.

[62] V. N. Nori and J. M. Scitzman, "CH* chemiluminescence modeling for combustion diagnostics," *Proc. Combust. Inst.*, vol. 32 I, no. 1, 2009.

[63] V. N. Nori and J. M. Seitzman, "Chemiluminescence measurements and modeling in syngas, methane and jet-a fueled combustors," in *Collection of*

Technical Papers - 45th AIAA Aerospace Sciences Meeting, 2007, vol. 8.

[64] H. N. Najm, P. H. Paul, C. J. Mueller, and P. S. Wyckoff, “On the Adequacy of Certain Experimental Observables as Measurements of Flame Burning Rate,” *Combust. Flame*, vol. 113, no. 3, 1998.

[65] B. Kim, M. Kaneko, Y. Ikeda, and T. Nakajima, “Detailed spectral analysis of the process of HCCI combustion,” *Proc. Combust. Inst.*, vol. 29, no. 1, 2002.

[66] J. Ballester and T. García-Armingol, “Diagnostic techniques for the monitoring and control of practical flames,” *Progress in Energy and Combustion Science*, vol. 36, no. 4. 2010.

[67] P. D. Maker and R. W. Terhune, “Study of optical effects due to an induced polarization third order in the electric field strength,” *Phys. Rev.*, vol. 137, no. 3, pp. A801–A818, 1965.

[68] A. Starikovskiy and N. Aleksandrov, “Plasma-assisted ignition and combustion,” *Progress in Energy and Combustion Science*. 2013.

[69] T. X. Phuoc, “Laser-induced spark ignition fundamental and applications,” *Optics and Lasers in Engineering*, vol. 44, no. 5. pp. 351–397, 2006.

[70] V. E. Mitsuk, I. Savoskin, and V. A. Chernikov, “Breakdown at Optical Frequencies in the Presence of Diffusion Losses,” *Journal of Experimental and Theoretical Physics Letters*, vol. 4, no. 4. pp. 129–131, 1966.

[71] C. H. Chan, C. D. Moody, and W. B. McKnight, “Significant loss mechanisms in gas breakdown at 10.6 μ,” *J. Appl. Phys.*, vol. 44, no. 3, pp. 1179–1188, 1973.

[72] R. Hickling and W. R. Smith, “Combustion bomb tests of laser ignition,” in *SAE Technical Papers*, 1974.

[73] Ş. Yalçin, D. R. Crosley, G. P. Smith, and G. W. Faris, “Influence of ambient conditions on the laser air spark,” *Appl. Phys. B Lasers Opt.*, vol. 68, no. 1, 1999.

[74] A. W. Miziolek, V. Palleschi, and I. Schechter, “Laser-induced breakdown spectroscopy (LIBS): fundamentals and applications,” *booksgooglecom*, vol. 6, p. 620, 2006.

[75] D. A. Cremers and L. J. Radziemski, *Handbook of Laser-induced Breakdown Spectroscopy*. 2006.

[76] T. Minowa, T. Kawata, H. Katsuragawa, and H. K. Uematsu, “Initial phase of laser-induced air optical breakdown: a new picture,” *Appl. Opt.*, vol. 37, no. 6, 1998.

[77] I. Dors, C. Parigger, and J. W. L. Lewis, “Fluid dynamics effects following laser-induced optical breakdown,” in *38th Aerospace Sciences Meeting and Exhibit*, 2000.

[78] F. J. Weinberg and J. R. Wilson, “A Preliminary Investigation of the Use of Focused Laser Beams for Minimum Ignition Energy Studies,” *Proc. R. Soc. A Math. Phys. Eng. Sci.*, vol. 321, no. 1544, pp. 41–52, 1971.

[79] R. G. Kingdon and F. J. Weinberg, “The effect of plasma constitution on laser ignition energies,” *Symp. Combust.*, 1977.

[80] J. A. Syage, E. W. Fournier, R. Rianda, and R. B. Cohen, “Dynamics of flame propagation using laser-induced spark initiation: Ignition energy measurements,” *J. Appl. Phys.*, vol. 64, no. 3, pp. 1499–1507, 1988.

[81] T. X. Phuoc, “Laser spark ignition: Experimental determination of laser-induced breakdown thresholds of combustion gases,” *Opt. Commun.*, vol. 175, no. 4, pp. 419–423, 2000.

[82] J. L. Beduneau, B. Kim, L. Zimmer, and Y. Ikeda, “Measurements of minimum ignition energy in premixed laminar methane/air flow by using laser induced spark,” *Combust. Flame*, vol. 132, no. 4, pp. 653–665, 2003.

[83] J. Huang, P. G. Hill, W. K. Bushe, and S. R. Munshi, “Shock-tube study of methane ignition under engine-relevant conditions: Experiments and modeling,” *Combust. Flame*, 2004.

[84] S. S. Shy, W. T. Shih, and C. C. Liu, “More on minimum ignition energy transition for lean premixed turbulent methane combustion in flamelet and distributed regimes,” in *Combustion Science and Technology*, 2008.

[85] C. Cardin, B. Renou, G. Cabot, and A. M. Boukhalfa, “Experimental analysis of laser-induced spark ignition of lean turbulent premixed flames: New insight into ignition transition,” *Combust. Flame*, vol. 160, no. 8, pp. 1414–1427, 2013.

[86] D. R. Ballal and A. H. Lefebvre, “The influence of flow parameters on minimum ignition energy and quenching distance,” *Symp. Combust.*, 1975.

[87] D. R. Ballal and A. H. Lefebvre, “Flame quenching in turbulent flowing gaseous mixtures,” *Symp. Combust.*, 1977.

[88] H. Kopecek, H. Maier, G. Reider, F. Winter, and E. Wintner, “Laser ignition of methane-air mixtures at high pressures,” *Exp. Therm. Fluid Sci.*, 2003.

[89] M. Weinrotter, H. Kopecek, E. Wintner, M. Lackner, and F. Winter, “Application of laser ignition to hydrogen-air mixtures at high pressures,” *Int. J. Hydrogen Energy*, vol. 30, no. 3, pp. 319–326, 2005.

[90] D. A. Santavicca, C. Ho, B. J. Reilly, and T. W. Lee, “Laser induced spark ignition of methane-oxygen mixtures,” no. September, 1991.

[91] G. Taylor, “The Formation of a Blast Wave by a Very Intense Explosion . II . The Atomic Explosion of 1945 The formation of a blast wave by a very intense

explosion . 11 . The atomic explosion of 1945," *R. Soc. London, Ser. A, Maths Phys. Sci.*, vol. 201, no. 1065, pp. 175–186, 1950.

[92] T. A. Spiglanin, A. Mcilroy, E. W. Fournier, R. B. Cohen, and J. A. Syage, "Time-resolved imaging of flame kernels: Laser spark ignition of H2/O2/Ar mixtures," *Combust. Flame*, vol. 102, no. 3, pp. 310–328, 1995.

[93] T. X. Phuoc and F. P. White, "Laser-induced spark ignition of CH4/air mixtures," *Combust. Flame*, 1999.

[94] C. V. Bindhu, S. S. Harilal, M. S. Tillack, F. Najmabadi, and A. C. Gaeris, "Laser propagation and energy absorption by an argon spark," *J. Appl. Phys.*, vol. 94, no. 12, pp. 7402–7407, 2003.

[95] M. Lackner, S. Charareh, F. Winter, H. Kopecek, and E. Wintner, "Investigation of the early stages in laser-induced ignition by Schlieren photography and laser-induced fluorescence spectroscopy.," *Opt. Express*, vol. 12, no. 19, pp. 4546–4557, 2004.

[96] J. L. Beduneau and Y. Ikeda, "Application of laser ignition on laminar flame front investigation," in *Experiments in Fluids*, 2004, vol. 36, no. 1, pp. 108–113.

[97] J. L. Beduneau, N. Kawahara, T. Nakayama, E. Tomita, and Y. Ikeda, "Laser-induced radical generation and evolution to a self-sustaining flame," *Combust. Flame*, 2009.

[98] D. K. Srivastava, K. Dharamshi, and A. K. Agarwal, "Flame kernel characterization of laser ignition of natural gasair mixture in a constant volume combustion chamber," *Opt. Lasers Eng.*, 2011.

[99] K. Dharamshi, D. K. Srivastava, and A. K. Agarwal, "Combustion characteristics and flame-kernel development of a laser ignited hydrogen-air mixture in a constant volume combustion chamber," *Int. J. Hydrogen Energy*, 2014.

[100] I. A. Mulla, S. R. Chakravarthy, N. Swaminathan, and R. Balachandran, "Evolution of flame-kernel in laser-induced spark ignited mixtures: A parametric study," *Combust. Flame*, vol. 164, pp. 303–318, 2016.

[101] Y. Yu, X. Li, R. Fan, D. Chen, and R. Sun, "Stabilization of a premixed methane-air flame with a high repetition nanosecond laser-induced plasma," *Opt. Laser Technol.*, 2017.

[102] B. Almansour, L. Thompson, J. Lopez, and S. S. Vasu, "Laser ignition and burning velocity measurements in natural gas/air mixtures," 2015.

[103] J. X. Ma, D. R. Alexander, and D. E. Poulain, "Laser spark ignition and combustion characteristics of methane-air mixtures," *Combust. Flame*, 1998.

[104] D. K. Srivastava, E. Wintner, and A. K. Agarwal, "Effect of focal size on the

laser ignition of compressed natural gas-air mixture," *Opt. Lasers Eng.*, 2014.

[105] D. K. Srivastava, E. Wintner, and A. K. Agarwal, "Effect of laser pulse energy on the laser ignition of compressed natural gas fueled engine," *Opt. Eng.*, 2014.

[106] B. R. Munson, T. H. Okiishi, W. W. Huebsch, and A. P. Rothmayer, *Fundamentals of Fluid Mechanics*. 2012.

[107] S. B. Pope, "Turbulent premixed flames," *Turbul. Premixed Flames*, pp. 1–437, 1987.

[108] F. Y. Hagos, A. Rashid, A. Aziz, and S. A. Sulaiman, "Study of syngas combustion parameters effect on internal combustion engine," *Asian J. Sci. Res.*, 2013.

[109] C. K. Law, *"Combustion Physics."* 2006.

[110] C. Morley, "Gaseq: A chemical equilibrium program for Windows." 2005.

[111] M. Burke, X. Qin, Y. Ju, and F. Dryer, "Measurements of hydrogen syngas flame speeds at elevated pressures," *5th US Combust. Meet.*, 2007.

[112] C. K. Law, "A Compilation of Experimental Data on Laminar Burning Velocities," in *Reduced Kinetic Mechanisms for Applications in Combustion Systems*, 2008.

[113] S. Kondo, K. Takizawa, A. Takahashi, K. Tokuhashi, and A. Sekiya, "A study on flammability limits of fuel mixtures," *J. Hazard. Mater.*, vol. 155, no. 3, 2008.

[114] H. S. Homan and W. A. Sirignano, "Minimum mass of burning aluminum particles for ignition of methane/air and propane/air mixtures," *Symp. Combust.*, 1981.

[115] R. A. Hill, "Ignition-delay times in laser initiated combustion," *Appl. Opt.*, 1981.

[116] W. M. Trott, "CO2-laser-induced deflagration of fuel/oxygen mixtures," *J. Appl. Phys.*, 1983.

[117] R. A. Hill and G. A. Laguna, "Laser initiated combustion of CH4 + O2 mixtures," *Opt. Commun.*, 1980.

[118] B. Raffel, J. Warnatz, and J. Wolfrum, "Experimental study of laser-induced thermal ignition in O2/O3 mixtures," *Appl. Phys. B Photophysics Laser Chem.*, 1985.

[119] U. Maas, B. Raffel, J. Wolfrum, and J. Warnatz, "Observation and simulation of laser induced ignition processes in O2-O3 and H2-O2 mixtures," *Symp. Combust.*, 1986.

[120] M. A. Tanoff, M. D. Smooke, R. E. Teets, and J. A. Sell, "Computational and experimental studies of laser-induced thermal ignition in premixed ethylene-

oxidizer mixtures," *Combust. Flame*, 1995.

[121] D. Lucas, D. Dunn-Rankin, K. Hom, and N. J. Brown, "Ignition by excimer laser photolysis of ozone," *Combust. Flame*, 1987.

[122] M. Lavid and J. G. Stevens, "Photochemical ignition of premixed hydrogen oxidizer mixtures with excimer lasers," *Combust. Flame*, 1985.

[123] M. Lavid, Y. Nachshon, S. K. Gulati, and J. G. Stevens, "Photochemical Ignition of Premixed Hydrogen/Oxygen Mixtures With ArF Laser," *Combust. Sci. Technol.*, 1994.

[124] M. S. Chou and T. J. Zukowski, "Ignition of H2/O2/NH3, H2/air/NH3 and CH4/O2/NH3 mixtures by excimer-laser photolysis of NH3," *Combust. Flame*, 1991.

[125] R. G. W. Norrish, "The study of combustion by photochemical methods," in *Symposium (International) on Combustion*, 1965.

[126] I. E. Forch and A. W. Miziolek, "Ultraviolet laser ignition of premixed gases by efficient and esonant multiphoton photochemical formation of ilicroplasmas," *Combust. Sci. Technol.*, 1987.

[127] G. Dearden and T. Shenton, "Laser ignited engines: progress, challenges and prospects," *Opt. Express*, 2013.

[128] B. Lewis and G. von Elbe, "Combustion Waves in Laminar Flow," *Combust. Flames Explos. Gases*, pp. 215–417, 1987.

[129] D. E. Lencioni, "The effect of dust on 10.6-μm laser-induced air breakdown," *Appl. Phys. Lett.*, vol. 23, no. 1, pp. 12–14, Jul. 1973.

[130] J. REILLY, P. SINGH, and G. WEYL, "Multiple pulse laser propagation through atmospheric dust at 10.6 microns," in *10th Fluid and Plasmadynamics Conference*, American Institute of Aeronautics and Astronautics, 1977.

[131] L. J. Radziemski, *Lasers-Induced Plasmas and Applications*. 2020.

[132] A. Gold and H. B. Bebb, "Theory of Multiphoton Ionization," *Phys. Rev. Lett.*, vol. 14, no. 3, pp. 60–63, Jan. 1965.

[133] R. M. DAVIES and S. G. TAYLOR, "The mechanics of large bubbles rising through extended liquids and through liquids in tubes," *Dyn. Curved Front.*, pp. 377–392, 1950.

[134] M. H. Morsy and S. H. Chung, "Numerical simulation of front lobe formation in laser-induced spark ignition of CH4/air mixtures," *Proc. Combust. Inst.*, vol. 29, no. 2, pp. 1613–1619, 2002.

[135] T. X. Phuoc and F. P. White, "An optical and spectroscopic study of laser-

induced sparks to determine available ignition energy," *Proc. Combust. Inst.*, 2002.

[136] R. B. Edmonson, H. L. Olsen, and E. L. Gayhart, "Application of ideal gas theory to the gaseous expansion from an electric spark," *J. Appl. Phys.*, vol. 25, no. 8, pp. 1008–1013, 1954.

[137] K. Gkagkas, R. P. Lindstedt, and T. S. Kuan, "Transported PDF modelling of a high velocity bluff-Body stabilised flame (HM2) using detailed chemistry," *Flow, Turbul. Combust.*, 2009.

[138] M. Kono, K. Niu, T. Tsukamoto, and Y. Ujiie, "Mechanism of flame kernel formation produced by short duration sparks," *Symp. Combust.*, 1989.

[139] S. R. Turns, "An introduction to combustion: concepts and applications," *System*, vol. 499. 2000.

[140] V. Babrauskak, *Ignition Handbook*. 2003.

[141] A. Dowlut, "Simultaneous OH and Formaldyde PLIF imaging in Laminar and turbulent premixed flames," 2015.

[142] R. W. Bilger, "Conditional moment closure for turbulent reacting flow," *Phys. Fluids A*, vol. 5, no. 2, 1992.

[143] V. Stetsyuk, "Experimental study of combustion and scalar mixing in swirling jet flows Declaration of Originality," no. December, 2013.

[144] F. Picano, F. Battista, G. Troiani, and C. M. Casciola, "Dynamics of PIV seeding particles in turbulent premixed flames," *Exp. Fluids*, vol. 50, no. 1, 2011.

[145] L. Boyer, "Laser tomographic method for flame front movement studies," *Combust. Flame*, vol. 39, no. 3, 1980.

[146] A. Melling, "Tracer particles and seeding for particle image velocimetry," *Meas. Sci. Technol.*, vol. 8, no. 12, 1997.

[147] B. R. Masters, "Lord Rayleigh: A Scientific Life," *Opt. Photonics News*, vol. 20, no. 6, 2009.

[148] L. E. Drain, "The laser-Doppler technique.," 1980.

[149] G. Mie, "Contributions to the optics of turbid media, particularly of colloidal metal solutions." pp. 377–445, Feb-1976.

[150] C. Brossard *et al.*, "Principles and applications of particle image velocimetry Principles and applications," *Opt. Diagnostics Flow*, 2015.

[151] I. Grant, "Particle image velocimetry: A review," *Proc. Inst. Mech. Eng. Part C J. Mech. Eng. Sci.*, vol. 211, no. 1, 1997.

[152] Insight 4G, "Particle Image Velocimetry Part - 5 Post processing of PIV

measurements," vol. 027, 2020.

[153] N. Otsu, "THRESHOLD SELECTION METHOD FROM GRAY-LEVEL HISTOGRAMS.," *IEEE Trans Syst Man Cybern*, vol. SMC-9, no. 1, 1979.

[154] T. Endo, Y. Takenaka, Y. Sako, T. Johzaki, S. ichi Namba, and D. Shimokuri, "An experimental study on the ignition ability of a laser-induced gaseous breakdown," *Combust. Flame*, 2017.

[155] Y. P. Raĭzer, "Optical discharges," *Sov. Phys. - Uspekhi*, vol. 23, no. 11, 1980.

[156] M. S. Uberoi, A. M. Kuethe, and H. R. Menkes, "Flow field of a bunsen flame," *Phys. Fluids*, 1958.

[157] J. L. Beduneau and Y. Ikeda, "Spatial characterization of laser-induced sparks in air," *J. Quant. Spectrosc. Radiat. Transf.*, 2003.

[158] D. S. Dandy and S. R. Vosen, "Numerical and experimental studies of hydroxyl radical chemiluminescence in methane-air flames," *Combust. Sci. Technol.*, 1992.

[159] M. De Leo, A. Saveliev, L. A. Kennedy, and S. A. Zelepouga, "OH and CH luminescence in opposed flow methane oxy-flames," *Combust. Flame*, 2007.

[160] F. P. Incropera, D. P. DeWitt, T. L. Bergman, and A. S. Lavine, *Fundamentals of Heat and Mass Transfer 6th Edition*. 2007.

[161] Z. Chen, M. P. Burke, and Y. Ju, "On the critical flame radius and minimum ignition energy for spherical flame initiation," *Proc. Combust. Inst.*, 2011.

[162] M. Matalon, "Flame dynamics," *Proc. Combust. Inst.*, vol. 32 I, no. 1, 2009.

[163] T. Tsuruda and T. Hirano, "Local Flame Front Disturbance Development Under Acceleration." 1991.

Appendices

Appendix A: Experimental Procedures

{Note: These procedures were developed for a broader research work including spark ignition work not reported in this thesis}

Prior to conducting the experiments:

- A leakage test is done by opening the gas supply line (air, methane, hydrogen or carbon dioxide) and applying a leak identifying agent to potential leaking points like connections between pipes.
- A visual scan is then performed to make sure there are no flammable objects near the ignition location.
- The Extraction system is positioned above the burner to suck any unburnt fuel out of the laboratory.
- A confirmatory test should be performed to ensure the electrode gap can produce consistent sparks in open air (electric ignition).
- Ensure the laser beam is optically aligned and a confirmatory test should be performed to ensure consistent sparks in open air (laser ignition).

The experimental procedure is based on the flowchart presented in Figure. Based on this flowchart, the sequence of activities to be performed are described below:

Start up

1. Ensure the Ignition unit (or Laser system), control and measurement Instruments are switch ON with the correct settings.
2. Open the gas cylinder regulator valves and set delivery pressures to 1 bar.

Gas flow setup

3. Open the Nitrogen valve to purge the system of combustion products and unburnt gases accumulated from the last experiment. Turn off the Nitrogen.
4. Open the Air Flow Meter to supply the desired amount of Air. Record the air flow rate.
5. With the Solenoid Valve (SV-1) ON, open fuel valves to set the correct fuel flow rates for the desired mixture equivalence ratio and exit flow velocity.

Safety check

6. With the flow rates correctly set, quickly turn OFF the Solenoid valve (SV-1 in Figure 1) to stop the fuel flow.
7. If using electric ignition source, ensure high voltage warning sign is placed at the door.
8. If using laser ignition source, ensure the door safety interlock switch is activated and a laser warning sign is placed at the door.

Gas mixing, Ignition and measurement

9. With the air flow ON, switch ON the Solenoid valve to initiate the fuel flow.

10. Wait for 15 seconds for the air and fuel to mix.

11. Ignite the mixture and initiate measurements by pressing the Spark Trigger button.

    Spark Energy: the spark energy is obtained from the oscilloscope display of the transient Voltage and Current triggered by the spark signal. The pulse energy output from the laser is recorded by using an Energy meter.

    Image acquisition: The development of the flame kernel is recorded by the TSI camera.
12. Switch OFF the Solenoid valve to stop the fuel flow.
13. If the gas mixture is ignited by spark (as observed through visual observation or chemiluminescence) then, purge system with Nitrogen (step 3) and repeat experiments with fresh gas air mixture (steps 16, 17, 18) for specified number of runs (say 20 runs)
14. If the gas mixture did not ignite, then increase the spark energy either by increasing the pulse width (electric ignition) or reducing the Q-Switch delay (laser ignition)
15. Repeat process for different equivalent ratios, flow velocity and mixture composition.

16. Shutdown

17. Switch OFF the Ignition unit (or Laser system), control and measurement Instruments.
18. Close the gas cylinder regulator valves and de-pressurize lines.

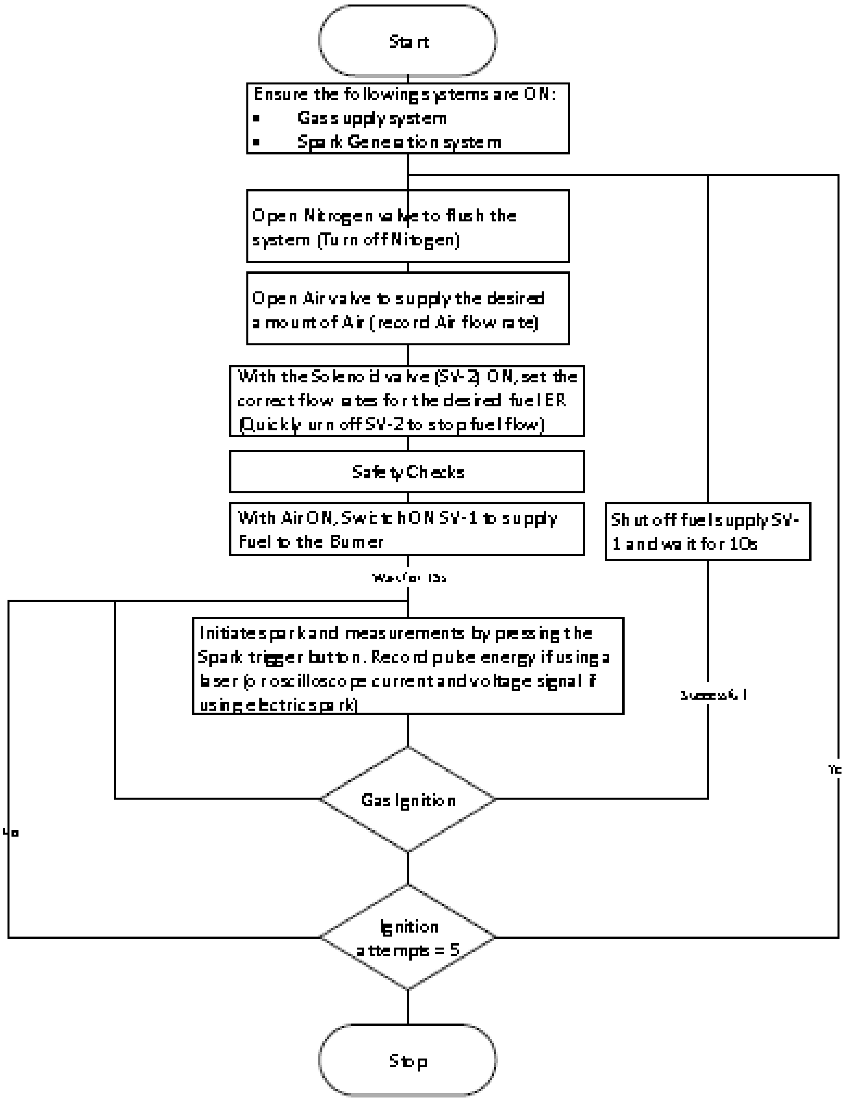
Start
Ensure the following systems are ON:
▪ Gas supply system
▪ Spark Generation system
Open Nitrogen valve to flush the system (Turn off Nitrogen)
Open Air valve to supply the desired amount of Air (record Air flow rate)
With the Solenoid valve (SV-2) ON, set the correct flow rates for the desired fuel ER (Quickly turn off SV-2 to stop fuel flow)
Safety Checks
With Air ON, Switch ON SV-1 to supply Fuel to the Burner
Wait for 15s
Initiate spark and measurements by pressing the Spark trigger button. Record pulse energy if using a laser (or oscilloscope current and voltage signal if using electric spark)
Gas Ignition
Successful
Shut off fuel supply SV-1 and wait for 10s
Ignition attempts = 5
No
Yes
Stop

Appendix B: Risk Assessment

{Note: This Risk Assessment was developed for a broader research work including spark ignition work not reported in this thesis}

Activities, Hazards, Controls

Reference: RA015952/1

1. **Laser ignition experiment in Thermodynamics Laboratory**

Sign-off Stat

Description of Activity:	This is an experiment where different Hydrocarbon-Air mixtures are ignited in a Co-flow Burner using both a laser and electrical ignition systems. The laser system comprises a Q-switched Nd-YAG laser (Class 4) focused on the Burner exit via a collection of optics in space. The electrical spark is generated between two electrodes (at the burner exit) from the high voltage side of an ignition coil which is powered by a 12 volts car battery.

Hazard 1. Laser beam

Risks: - Eye injury/damage, Skin burns, etc from contact with lasers and diffuse reflections - Ignition of flammable materials - heating/vaporization of materials causing hazardous fumes Risk level: - Medium	**Existing Control Measures** - Beam dump to terminate beam at the end of its useful path - Black Shield cover to conceal and absorb the area from stray radiations - Door interlock system in place - The laser equipment is supported on a fixed platform so as avoid toppling - Beam paths kept below eye level. - Adherence to instructions on the Operational Manual - Eye protection to be worn during operation - Notices and sign placed outside the door

<table>
<tr><td colspan="2">Hazard 2. Compressed Gases (e.g. Methane, Hydrogen, Nitrogen and Carbon dioxide)</td></tr>
<tr><td>Risks: -Methane: Methane is a colorless and odorless gas. It forms flammable and explosive mixture with air between 5%-15% concentration. Asphyxia may result if the oxygen concentration is reduced below 18% by displacement. - Hydrogen: Hydrogen is a colorless and odorless gas. It forms flammable and explosive mixture over a wide range of concentration (5%-75%). It burns with almost an invisible blue flame. Primary health hazard is Asphyxiation by displacement of Oxygen. - Over-exposure to inhaled aerosol Risk level: -Medium</td><td>Existing Control Measures
- Fumes/Gas detection and extraction systems are installed - Solenoid valves, flashback arresters are installed on the fuel delivery line - Gases are stored in isolated and well ventilated cupboards - Only small quantities of flammable gases will be used for experiment - The fuel lines are operated at atmospheric pressure such that only minor leaks is envisaged in case of valve malfunction
Leakage test is done at potential leakage points - Visual scan to ensure no flammable objects nearby - safety valves, flow regulators and flash back arresters are in place</td></tr>
<tr><td colspan="2">Hazard 3. Hot surfaces (e.g Gas Burner, Electrodes)</td></tr>
<tr><td>Risks: - Burns from contact with hot surfaces - Explosion through contact with flammable gases
Risk level: -Medium</td><td>Existing Control Measures
- System is ignited and turned off in a controlled manner - Hot surfaces/materials allowed to cool before handling</td></tr>
</table>

Hazard 4. Electrical Hazards (e.g. Power supply units including high voltage power to Laser)

Risks: - electrical shock from electrical equipment and exposed cables - death from electrocution - fire and burnsRisk Level: - Low	**Existing Control Measures** Both the Laser and Electric ignition systems are operated in a controlled manner The electrical cables are carefully checked for signs of wear/tear, etc. The earth connection is connected for all the electrical equipment. Appropriate fuses are placed in each piece of equipment The room is an explosion proof room. Facilities controlled by UCL staff

Hazard 5. Environment

Risk: Risk level -Slip, trips and falls : medium risk - Inhalation of poisonous fumes or particulate matter: medium risk -Hearing damage due	**Existing Control Measures** - Proper house keeping - Extraction system and ventilation system in place - PPE (Ear plugs)

Hazard 6. Spark Radiations

Risks - Retina damage due to intense spark light - cataracts, cornea damage due to infrared radiation - skin burn, blurred vision due to UV radiations Risk level: Medium	**Existing Control Measures** Wearing proper eye protection

Hazard 7. Manual handling

Risk: back injuries, shoulder pain due to occasional movement of burner, imaging and optical equipment Risk level: low	**Existing Control Measures** proper lifting; not working in one position for long periods of time

Hazard 8. Lone/out-of-hours working

Risk: -delay in getting help in the event of emergency, - being attacked by intruders. Risk level: low	**Existing Control Measures** Avoid lone or out-of-hours working

Risk Level

With Existing Controls:

Risk Level	**C- Medium / Moderate**

Appendix C: MATLAB Codes Used to Analyse Laser Tomography Images and PIV Data

C1: This code was written to enable visualisation of the tomographic images of the flame kernel in pseudo-coloured form.

```
clc
close all
clear all
tic
folderpath='E:\21032019_PIV\LAM_TIF\New folder';% Current working folderpath (no more than 2 subfolder)
imagetype='\*.TIF';% type of image in the folder
file=fullfile(folderpath,imagetype);
directory=dir(file);
Numimage=numel(directory);
delt=round([1 51 167.67:166.67:(1+166.67*10)]);



for k=1:Numimage
ff= fullfile(folderpath,directory(k).name);
  Raw_image_x=imread(ff);
 M=double(rgb2gray(Raw_image_x));
%  M1=M(1:end-25,:);
M2=flip(M,1);
% M2=imrotate(M,-180);
% M2=flip(M1,2);
%  M1=imcrop(M,[50 100 300 300]);
 [ax,ay]=size(M2);

a=52e-3;
  x=1:ax;
    y=1:ay;
    [X,Y]=meshgrid(y,x);

    max_pix=max(max((M2)));
    %max_pix=1;
    min_pix=0;

 if k<10, continue; end

figure(1),
% hold on;
subplot(1,3,k-9),
pcolor (a*X,a*Y,(M2)), axis on, %axis equal;
shading flat, caxis([min_pix max_pix]),title([num2str(delt(k)), ' µs']),%colorbar ('vert')
% hold on;
% imtool(figure(),[num2str(delt(k)) '.jpeg'],'jpeg');
end
```

C2: This code was written to extract the kernel edges from the Laser tomography image and to obtain the flame tip locations and propagation rate

```
clear all
close all
clc


tic
folderpath='E:\New folder\Kernel Xtics\Laminar\New folder';% Current working folderpath (no
more than 2 subfolder)
imagetype='\*.TIF';% type of image in the folder
file=fullfile(folderpath,imagetype);
directory=dir(file);
Numimage=numel(directory);

delt=round([51:166.67:166.67*12]);

for k=1:length(delt)
  % for k=1:Numimage
  ff= fullfile(folderpath,directory(k).name);
  Mask_image_x=imread(ff);
  M=im2double(Mask_image_x);
  M1=M(250:600,100:250);
%    M4=flip(M1,1);
  M2=imcomplement(M1);
  M3=edge(M2,'canny',0.0001);

  DF=diff(sum(M3'));

  [peaks, locs]=findpeaks(DF);
  DF1=diff(M3(min(locs),:));
  findpeaks(diff(M3(min(locs),:)))
%    %Yt(fi,di)=min(find(diff(sum(KP'))==max(peaks))); % higher point on the kernel
  Yt(k,:)=min(locs);
%    indexxt=find(M3(min(locs)+1,:)==1);
%    Xt=ceil(mean(indexxt));
  [peaks1, locs1]=findpeaks(-1*DF);
  % Yb(fi,di)=max(find(-1*diff(sum(KP'))==max(peaks1))); % lowest point on the kernel
  Yb(k,:)=max(locs1);

%    if k>3, stop; end
%
%    figure(1),
%    subplot(1,3,k), imshow(M3), title([num2str(delt(k)), ' µs']),axis on, %axis equal;
% %     subplot(1,3,k), imshow(edgematrix), title([num2str(delt(k)), ' µs']), colorbar verti, axis
equal;
%

end

Yt1=351-Yt;
Yb1=351-Yb;
Y=Yt1-Yb1;
```

```
figure(100),plot(delt,52e-3.*Yt1,'ko-'); hold on; plot((delt),52e-3.*Yb1,'r--*'); xlabel('time, µs'),
ylabel('location, mm');
legend('downstream location', 'upstream location');
figure(101),scatter(delt,52e-3.*Y,'ko'); xlabel('time, µs'), ylabel('location, mm');
```

C3: This code was written to visualize the flow field velocity from the PIV data

```
close all
clc

%%%%%Reads Multiple excel file%%%%%%
 folderpath='E:\21032019_PIV\LAM_VEC';%14F11A VECTOR FILES
 filetype='*.xls';
 file=fullfile(folderpath,filetype);
directory=dir(file);
N=numel(directory);
u=cell({});
v=cell({});
n=N;
% data{k}=cell({});
us=[];
vs=[];

ux=[];
vy=[];

for k=1:n
    data{k}=xlsread(fullfile(folderpath,directory(k).name));
  cv=folderpath;directory(k).name
 x=data{k}(1:end,1);
 y=data{k}(1:end,2);
 ux=[ux,x];
 vy=[vy,y];
%  if k==1
   u=data{k}(1:end,3);
    v=data{k}(1:end,4);
    us=[us,u];
    vs=[vs,v];

rgx=min(ux(:,k)):0.5:max(ux(:,k));
rgy=min(vy(:,k)):0.5:max(vy(:,k));
% grd=griddata(rgx,rgy,ux(:,k),vy(:,k),us(:,k),vs(:,k));

xmin=min(ux(:,k));
xmax=max(ux(:,k));

ymin=min(vy(:,k));
ymax=max(vy(:,k));

y1=ymin:0.05:ymax;
x1=xmin:0.05:xmax;

[x2d,y2d] = meshgrid(x1,y1);
velu = griddata(ux(:,k),vy(:,k),us(:,k),x2d,y2d);
velv = griddata(ux(:,k),vy(:,k),vs(:,k),x2d,y2d);
velmag = griddata(ux(:,k),vy(:,k),sqrt(us(:,k).^2+vs(:,k).^2),x2d,y2d);
```

```
figure()
pcolor(x2d,y2d,velv), axis image,   colormap jet,  colorbar verti, shading flat
hold on
quiver(ux(:,k),vy(:,k),us(:,k),vs(:,k),1.5,'filled', 'k'),set(gca, 'color', [1 1 1]);

end
%% ========================================
```

Appendix D: MATLAB Code Used to Analyse Chemiluminescence Data

This MATLAB code visualises the pseudo-colour chemiluminescence image of the kernel, extracts image edges and outputs OH* kernel tip locations and propagation rates

```
clc;
clear all;
close all;
CurrentPath=pwd;
%% ========================================
prefix_FolderName=['aS29Test'];
startF=15; endF=15; %starting and ending folder number
%outfile name




%delta t - time delay from laser ignition, for all cases following delay
%used; the values are in microseconds

delt=([50:50:500 600:100:1000 1500:500:2000 3000:500:5000 6000:1000:10000]);
delts= delt*1e-6; % converted to seconds



for fi=startF:endF
  FolderName=[prefix_FolderName num2str(fi)];
  cd(FolderName) % change the working folder
  pwd
  dirinfo=dir('a*.SPE');
  name_list={dirinfo.name};
  for di=1:length(delt) %#ok<ALIGN>
%
  for fii=1:length(name_list)
  if contains(char(strcat(name_list(fii))),['T' num2str(delt(di))]), filename=strcat(name_list(fii));
  end
   if fii==18, continue; end
 end %fii % getting filename for loading
filename=char(filename);
filename1=filename(1:end-4); % name without suffix



a=readSPE(char(filename)); % load SPE file into matrix
mean_a=mean(a,3); % mean image from the raw chemi images
[mx, my]=size(mean_a);

%region of intest definition
%top left, bottom right
```

```
t=167; b=mx-45; sr=320;sl=20;
% t=67; b=mx-45; sr=320;sl=20;

%
% ROI=imcrop(mean_a,[1 167 300 300]);
ROI=mean_a(t:b,sl:sr);
% ROI=mean_a(1:my,1:mx);



TL=20;
aLevel=multithresh(ROI,TL); % multilevel threshold, here TL=1
seg_a=imquantize(ROI,aLevel);
%PV=seg_a-1; % progress variable based on thresholding.. requires modification to include inside area of kernel
if delt(di)<8000, customlevel=4; else, customlevel=4; end
M1=imbinarize(ROI,aLevel(customlevel));
filtersize=7;
PV=medfilt2(M1,[filtersize filtersize]);%% progress variable based on thresholding.. requires modification to include inside area of kernel



TMa=ROI.*(seg_a-1); %this will generate a thresholded mean iamge
TMa(TMa<0)=0;
% figpv=figure(2),imagesc(PV), colorbar hori, axis equal
KP=edge(PV); %edge on PV gives kernel perimeter
% figkp=figure(3),imagesc(KP), colorbar hori, axis equal

DF=diff(sum(KP'));
%
[peaks, locs]=findpeaks(DF);
DF1=diff(KP(min(locs),:));
findpeaks(diff(KP(min(locs),:)))
%Yt(fi,di)=min(find(diff(sum(KP'))==max(peaks))); % higher point on the kernel
Yt(fi,di)=min(locs);
indexxt=find(KP(min(locs)+1,:)==1);
Xt(fi,di)=ceil(mean(indexxt));
[peaks1, locs1]=findpeaks(-1*DF);
%  Yb(fi,di)=max(find(-1*diff(sum(KP'))==max(peaks1)));  % lowest point on the kernel
Yb(fi,di)=max(locs1);
indexxb=find(KP(max(locs),:)==1);
Xb(fi,di)=ceil(mean(indexxb));

Itotal(fi,di)=sum(sum(ROI));
Imax(fi,di)=max(max(ROI));

edgematrix=zeros(size(KP));
edgematrix(Yt(fi,di),:)=1;
edgematrix(Yb(fi,di),:)=1;



% figure (1),
% subplot(4,4,di), imagesc(ROI), title([num2str(delt(di)), ' µs']), colormap jet, axis equal; axis off
% subplot(4,4,di), imagesc(ROI), title([num2str(delt(di)), ' µs']), colormap jet, %axis equal,  %axis off,
% colorbar verti, set(gca, 'Fontsize', 18),set(gca, 'Fontsize', 2),
% subplot(3,3,di), imagesc(M1), title([num2str(delt(di)), ' µs']), colorbar verti, axis equal;
% subplot(3,3,di), imagesc(PV), title([num2str(delt(di)), ' µs']), colorbar verti, axis equal;
```

```
% subplot(3,3,di), imagesc(KP), title([num2str(delt(di)), ' µs']), colorbar verti, axis equal;
% subplot(4,1,di), imagesc(KP+edgematrix), title([num2str(delt(di)), ' µs']), colorbar verti, axis
equal;
% pause(0.01);


end %% di, delay loop

%
cd(CurrentPath) % change it back to main folder
% %
% path=('D:\Flame_kernel_chemiluminescence\Sunny\Chapter6\delt.mat');
% save(path,'delt');



Xt1=20+Xt(fi,:);
Yt1=345-Yt(fi,:);
Xb1=20+Xb(fi,:);
Yb1=345-Yb(fi,:);
XYtop=[Xt1(:),Yt1(:)];
XYbot=[Xb1(:),Yb1(:)];

% Xt1=20+Xt; Yt1=445-Yt;
% Xb1=20+Xb; Yb1=445-Yb;
% XYtop=[Xt1(:),Yt1(:)];
% XYbot=[Xb1(:),Yb1(:)];

path3a=['E:\Flame_kernel_chemiluminescence\Sunny\Chapter6\', [prefix_FolderName
num2str(fi)], '_XYtop.mat'];
save(path3a,'XYtop');
path3b=['E:\Flame_kernel_chemiluminescence\Sunny\Chapter6\', [prefix_FolderName
num2str(fi)], '_XYbot.mat'];
save(path3b,'XYbot');
figure (3), scatter(Xt1,Yt1,'g*'), xlim([150 200]), grid on, grid minor; hold on,
scatter((Xb1),(Yb1),'r*'), xlim([150 200]), grid on, grid minor;
hold on, title('scatter plot of flame tip location'), xlabel('X, pixel'), ylabel('Y, pixel'),
legend('downstream location', 'upstream location')

figure (4), plot(delt,Itotal(fi,:),'r*'), xlabel('time, µs'), ylabel('integrated intensity, au'), grid on, grid
minor, title('integrated intensity vs time');
path4=['E:\Flame_kernel_chemiluminescence\Sunny\Chapter6\', [prefix_FolderName
num2str(fi)], '_Itotal.mat'];
save(path4,'Itotal');

figure (5), plot((delt),Imax(fi,:),'r*'), xlabel('time, µs'), ylabel('peak intensity, au'), grid on, grid
minor, title('peak intensity vs time');
path5=['E:\Flame_kernel_chemiluminescence\Sunny\Chapter6\', [prefix_FolderName
num2str(fi)], '_Imax.mat'];
save(path5,'Imax');


figure (6), scatter(delt,185e-3.*Yt1,'go'); hold on; scatter((delt),185e-3.*Yb1,'r^'); xlabel('time, µs'),
ylabel('location, mm');
legend('downstream location', 'upstream location');
path6a=['E:\Flame_kernel_chemiluminescence\Sunny\Chapter6\', [prefix_FolderName
num2str(fi)], '_Yt1.mat'];
save(path6a,'Yt1');
```

```
path6b=['E:\Flame_kernel_chemiluminescence\Sunny\Chapter6\', [prefix_FolderName num2str(fi)], '_Yb1.mat'];
save(path6b,'Yb1');

for x=1:1
Yt01=185e-6*Yt1(x,:);
Yb01=185e-6*Yb1(x,:);



Ut=diff(Yt01)./diff(delts);
Ub=diff(Yb01)./diff(delts);



figure (7), plot(delts(2:length(delts)),Ut,'go'); hold on
plot(delts(2:length(delts)),Ub,'r^'); hold on;
title('Growth rate of Torroidal flame'), xlabel('time, sec'), ylabel('flame speed, m/s'), legend('downstream flame', 'upstream flame')
path7a=['E:\Flame_kernel_chemiluminescence\Sunny\Chapter6\', [prefix_FolderName num2str(fi)], '_Ut.mat'];
save(path7a,'Ut');
path7b=['E:\Flame_kernel_chemiluminescence\Sunny\Chapter6\', [prefix_FolderName num2str(fi)], '_Ub.mat'];
save(path7b,'Ub');

end %x

end  %fi folder loop
```

Appendix E: Sensitivity Analysis

Table 0.1: Pulse Energy effect on the Kernel development parameters

Parameter	Pulse Energy (mJ)			
	32	64 (100%)	96 (200%)	128 (300%)
Dimension: W @ 1 ms (mm)	13.13	16.83 (28%)	17.94 (37%)	18.13 (38%)
Dimension: W @ 10 ms (mm)	38.48	37.00	37.18	37.37
Growth rate: $\mathbf{S}_{y+}$ @ 0.45 ms	3.70	5.55 (50%)	5.55 (50%)	5.55 (50%)
Growth rate: $\mathbf{S}_{y+}$ @ 1.0 ms	3.70	3.70	3.70	3.70
Minimum integ OH* intensity (AU)	4.43E+07	3.68E+07	3.90E+07	4.24E+07
Time @ min integ OH* intensity (μs)	200	300	500	500
Maximum integrated OH* intensity (AU)	5.80E+07	4.37E+07 (-25%)	4.45E+07 (-23%)	5.69E+07 (-2%)
Min peak intensity (AU)	1314	1084 (-18%)	1071 (-19%)	1090 (-17%)
Time @ min peak intensity (ms)	1.5	2	3	3

Table 0.2: Effects of Equivalence ratio on Kernel development parameters (Laminar flow)

Parameter	Equivalence Ratio (Laminar)		
	1.00	0.90	0.80
Y_+ @7 ms (mm)	28.405	25.815 (9%)	23.225 (18%)
Steady state $\mathbf{S}_{y+}$ (m/s)	3.33	2.96 (-11%)	2.59 (-22%)
minimum peak OH* intensity (AU)	1.31E+03	1.07E+03 (-18%)	8.11E+02 (-38%)
time at minimum peak OH* intensity (ms)	1.5	1.5	2
maximum integrated OH* intensity (AU)	5.80E+07	5.30E+07 (-9%)	4.66E+07 (-20%)
minimum integ OH* intensity (AU)	4.43E+07	4.79E+07	4.42E+07
time at minimum integrated OH* intensity (μs)	200	200	450

Table 0.3: Effects of Equivalence ratio on Kernel development parameters (Turbulent flow)

Parameter	Equivalence Ratio (Turb)		
	1.00	0.90	0.80
Y_+ @7 ms (mm)	51.53	48.385 (6%)	48.015 (7%)
Steady state S_{y+} (m/s)	2.14	2.16 (1%)	1.43 (33%)
minimum peak OH* intensity (AU)	1.21E+03	9.39E+02 (22%)	7.55E+02 (38%)
time at minimum peak OH* intensity (μs)	1	3	3.5
maximum integrated OH* intensity (AU)	7.71E+07	6.93E+07 (10%)	6.68E+07 (13%)
minimum integ OH* intensity (AU)	6.08E+07	6.26E+07	6.32E+07
time at minimum integrated OH* intensity (μs)	350	350	450

Table 0.4: Effect of the fuel on the Kernel development parameters (Constant AFT)

Parameter	T=2226 K			T=1234 K		
	CH_4	C_3H_8	C_2H_4	CH_4	C_3H_8	C_2H_4
Maximum Y_- (mm)	12.295 (0%)	6.745 (-45%)	9.89 (-20%)	10.26 (0%)	-0.10 (-101%)	7.115 (-42%)
Steady state S_{y+}/S_L	1.1275 (0%)	0.7148 (-37%)	0.8925 (-21%)	1.0269 (0%)	0.5616 (45%)	0.7650 (-26%)
minimum peak OH* intensity (AU)	1.31E+03 (0%)	1.04E+03 (-21%)	1.51E+03 (15%)	1.07E+03 (0%)	6.42E+02 (-40%)	1.16E+03 (+8%)
time at minimum peak OH* intensity (ms)	1.5	2	1			
maximum integrated OH* intensity (AU)	5.80E+07 (0%)	4.92E+07 (-15%)	6.12E+07 (+6%)	52449275 (0%)	44441798 (-15%)	56525861 (+8%)
minimum integ OH* intensity (AU)	4.43E+07	4.10E+07	5.13E+07	47913172	42883432	49973437
time at minimum integrated OH* intensity (μs)	200	250	500	200	350	400

Table 0.5: Effect of the fuel on the Kernel development parameters (Constant LFV)

Parameter	LFV=41 cm/s	LFV=29 cm/s

	CH4	C3H8	C2H4	CH4	C3H8	C2H4
Y_+ (mm) @ 7ms	31.18	29.33 (-6%)	33.03 (+6%)	23.225	17.86 (-23%)	20.265 (-13%)
Steady state $\mathbf{S}_{y+}/\mathbf{S}_L$	1.127545	0.874456 (-22%)	1.304103 (16%)	1.44984326	0.8242003 (-43%)	1.213181 (-16%)
minimum peak OH* intensity (AU)	1.31E+03	1.36E+03 (+4%)	1.80E+03 (32%)	8.11E+02	5.34E+02 (-34%)	7.26E+02 (-11%)
time at minimum peak OH* intensity (µs)	1.5	1.5	1	2	4.5	4
maximum integrated OH* intensity (AU)	5.80E+07	5.01E+07 (-14%)	6.66E+07 (33%)	46504843.8	36896883.2 (-20%)	55439766 (50%)
minimum integ OH* intensity (AU)	4.43E+07	3.85E+07	5.25E+07	44246478.4	37393897.2	49509389
time at minimum integrated OH* intensity (µs)	200	250	250	450	450	700